The Low–Temperature Properties of Boron–Implanted Diamond Materials.

WITS
UNIVERSITY

Nyiku C. Mahonisi

School of Physics

University of Witwatersrand

Thesis submitted to the Faculty of Science in fulfillment of the requirement for
the degree of Doctor of Philosophy

August 20, 2024

Declaration

I hereby declare that the work contained in this thesis is my own and has not been submitted for any degree or examination in any other institution of higher learning. Results highlighted and presented from other authors are duly acknowledged and referenced accordingly throughout this present text. This work is being submitted for the degree of Doctor of Philosophy at the University of the Witwatersrand, Johannesburg.

N.C.Mlambo

Signature

20/08/2024

Date

Abstract

The physio-chemical properties of semiconducting diamond materials under extremely low temperatures have fundamental implications in Condensed Matter Physics. Highly doped boron diamonds have been shown to reach a superconductive state at critical temperatures (T_c) ranging from $4\,\mathrm{K} - 10\,\mathrm{K}$, albeit such properties are "at the moment" only attributed to heavily boron-doped synthesized samples via HPHT and CVD growth methods. Theoretical predictions have shown that by exceeding the current solubility limit of boron in diamond, an increase in T_c beyond the $4\,\mathrm{K} - 10\,\mathrm{K}$ is possible, even close to room temperatures. However, in order to gain such a feat, an increase in active boron concentration beyond the metal-to-insulator transition (MIT) is an absolute necessity, and hence, non-equilibrium doping fabrication processes such as CVD growth and ion implantation are required. In this study, we explore carefully the properties of degenerate diamond layers with p-type impurity bands via low energy and low fluence ion implantation.

The study involves the utilization of the non-equilibrium ion implantation technique to fabricate boron layers that stretches from the diamond surface to some depth that is a few nm deep into the diamond matrix. A total of seven samples were processed uniquely with respect to ion energies, ion concentrations and annealing temperatures. Three samples (A, B and D) with varying parameters were implanted with both carbon and boron ions in regions where the carbon distribution overlaps with the boron distribution at concentrations close to the MIT level $\sim 4 \times 10^{20}\,\mathrm{ions/cm^3}$. The carbon implants were used to induce vacancy defects very close to the surface such that the boron ions that are subsequently implanted would simply diffuse into the carbon vacant sites. Furthermore, four samples (BE, ME and SE) were implanted with only boron ions also with varying processing parameters to establish a correlation between the two set of implanted samples. Lastly, one sample (C) was implanted similarly to the first set of samples , albeit, with only carbon ions in order to ascertain the boron-related defects. Initially, all the samples were annealed at 650°C in order to recover the crystalline state.

Spectral analysis clearly confirms the formation of boron-related defects for the carbon and boron implants with dynamic annealing at 200°C and at 400°C, respectively. That is, the Lorentzian-like component $\sim 1200\,\mathrm{cm^{-1}}$ and the asymmetric line shape $\sim 1300\,\mathrm{cm^{-1}}$. However, vacancy and interstitial peaks at $\sim 1500\,\mathrm{cm^{-1}}$ and $\sim 1620\,\mathrm{cm^{-1}}$, respectively, are also prevalent. Albeit, dynamic annealing limits the graphitization of the diamond structure with no detection of graphitic features. A concentration and thermal annealing dependency was also established. The second batch of samples were multi implanted with boron (i.e., within the same buried region for samples ME and SE and overlapping implanted regions for sample BE to form a box profile). Boron-related features were not wholly detected for all these samples. After multiple implantation processes it was evident that the diamond structure of samples BE and SE were adversely affected with prominent graphitic features forming. Very faint boron-related features appear for sample ME after nine multiple boron implantation processes with low energy and low fluence at room temperature (RT). However, the spectra show the onset of broadening effects associated structural damage. Expectantly, boron-related features are absent for the carbon implanted sample C with very minimum damage to the diamond spectra.

Low resistance tri-layer metal contacts of Ti/Cr/Au were deposited onto the

surfaces of the samples in a 4-point probe Van der Pauw configuration. Ohmic behavior was confirmed from electronic transport measurements. Thus, the conduction properties of the samples are also reported in this thesis. A very clear dependence on the fabrication method used to create the boron buried layers is demonstrated by the electronic response of the samples. Sample A experiences Space Charge Limited Currents (SCLCs) related to high localization effects that compensate the movement of free charge carriers through the diamond matrix such that the reported data is limited to a temperature range that is between $300\,\mathrm{K} \rightarrow 100\,\mathrm{K}$. The carrier concentration of sample B determined from Hall effect measurements indicate a contribution of both electrons and holes, likely due to the amphoteric vacancy states induced by carbon implantation. However, a careful increase in boron fluence and thermal annealing averts such effects. Samples BE and SE showcase a high level of conductivity with variable range hopping (VRH) mechanisms at low temperatures $\sim 10\,\mathrm{K}$ that suggests an increase of the localization length ξ_{loc} with low T_{ES} values. The overpopulation of boron ions within the nm−sized channels of these samples results in amorphous regions that contribute to the conduction properties of the materials. Hence, a very clear difference of the conduction properties of the samples is demonstrated.

To me...

I want to let you know that I make it. I faithfully run the race that you set in motion. Your dreams are becoming a stupendous reality. Henceforth, be bold and take courage in knowing the extraordinary possibilities that lie ahead of you at each and every waking moment. Indeed, the journey is long but success is inevitable if you stay the course and continue onward.
As Dr Martin Luther King once said "If you can't fly, run, if you can't run, walk, if you can't walk, crawl, but by all means keep moving."

"Being confident of this very thing, that he which began a good work in you will perform it until that day." Phil 1:6.

Live long and prosper,
Future self

Acknowledgements

Firstly, I'd like to express my sincere gratitude to my supervisor, Professors Mervin Naidoo, who has shown great effort and exceptional support in the completion of this thesis. He has been exceedingly helpful and encouraging in my pursuit of establishing myself as a researcher in Condensed Matter Physics. He has done so by invariably sharing from his fount of knowledge and wisdom coupled with years of experience in the field. Thank you Prof.

I'd like to thank Professor Rudolph Erasmus for constantly availing himself for all the Raman and PL measurements that were required, and for his excellent input during analysis of the results. I'd also like to acknowledge Dr Nasheeta Hanief from the Electron Microscopy Unit, University of Cape Town for the training pertaining to the use of an Electron Beam Lithography system, also for helping me with sample preparation and Fabrication of Ohmic contacts. Many thanks to Professor Mark Blumenthal and Dr Dominique Gouveia for also affording me the opportunity to expertly acquaint myself with an electronic transport measurement system at the Nano Electronics Research Laboratory, University of Cape Town. Salutations to Dr Stephane Pailhes and the CNRS ILM, Lyon, for giving me access to their state of the art research laboratories for low temperature measurements, and for the invaluable discussions we had pertaining to my research. I am also very thankful to Professor Charles Sheppard from UJ for assisting me with Hall effect measurements and for his indispensable expertise in the subject matter that he so graciously shared with me when needed. Last but not least, I'd like to thank Anthony Miller at iThemba LABS Gauteng, for helping me with ion implantation processes implemented throughout the duration of this PhD research work.

I'm also very humbled and thankful to the DSI-NRF Centre of Excellence in Strong Materials (COE–SM) for their unwavering financial support, throughout most of my postgraduate studies at WITS.

And to my family, sisters Thembi and Khanyisa Mahonisi. Thank you so much for your undying love, support and patience as I continued to pursue the pinnacle of my postgraduate studies, my PhD. And of course, my beloved late parents, Eric Mbudana Mahonisi and Tintswalo Alice Mahonisi. I am thankful for the opportunity to be raised in a principled and loving home.

And foremost, I'd like to thank and acknowledge the Lord God Almighty in Heaven for His mercy, love, grace and favor. Without Him I am nothing. He has constantly given me the faith and hope to better myself every single day. Thank you, "*Asante sana*", "*Ndza khensa*".

Contents

List of Figures

List of Tables

List of Symbols and Abbreviations

a_0	Lattice parameter	$2p$	2nd energy p-orbital
C_p	Atomic concentration	ξ_{loc}	Localization length
E_d	Displacement energy	Δ_g	Forbidden energy gap
E_A	Activation energy	Δ	Superconducting gap
E_F	Fermi energy	Ω_0	Resonant wavenumber
E_g	Band energy	Ω_f	Ion fluence
H_c	Critical magnetic field	Γ_B	Broadening parameter
n_B	Boron concentration	$N(E,\Gamma_B)$	DoS of superconductors
n_c	Critical boron concentration	$\rho(E)$	DoS of the quasi-continuum
N_p	Peak atomic concentration	μ_c	Chemical potential
N_s	Substitutional nitrogen	V_m	Matrix element
R_p	Projected range	λ_c	Coupling constant
T_c	Critical temperature	σ	Conductivity
T_e	Raman scattering amplitude of the electronic continuum	ρ	Resistivity
T_p	Raman scattering amplitude of the phonon continuum	q_a	Asymmetry parameter
ARPES	Angle-resolved photoemission spectroscopy	NA	Numerical Aperture
BDD	Boron-Doped Diamond	NDs	Nanodiamonds
CB	Conduction Band	NV	Nitrogen Vacancy
CCD	Charged Coupled Device	OD	Optical density
CCR	Closed Cycle Refrigerator	PDoS	Phonon density of states
CTF	Carbon Tube Furnaces	PL	Photoluminescence
CIRA	Cold Implantation Rapid Annealing	PSBs	Phonon Sidebands
CVD	Chemical Vapor Deposition	QIP	Quantum Information Processing
FCC	Face centered cubic	RCA	Recrystallized Alumina
FWHM	Full Width at Half Maximum	SRIM	Stopping Range of Ions in Matter
H	Hole state	TRIM	Transport Range of Ions in Matter
HPHT	High-Pressure High-Temperature	VB	Valence Band
I	Impurity state	XAS	X-ray Absorption Spectroscopy
IBA	Ion Beam Analysis	XES	X-ray Emission Spectroscopy
MIT	Metal-to-insulator transition	ZCP	Zero Center Line
Mott	Metal-to-insulator transition	ZPL	Zero Phonon Line

Chapter 1

General introduction

It has been well over a century since the experimental discovery of zero resistance for certain materials under low temperature conditions. The notable studies related to the behavioral properties of materials near absolute zero temperatures were first published by Onnes [1], in 1911. This followed after the discovery of liquid helium at a transition temperature of 4.2 K in 1908 [2], which was the last of the presumably "permanent gases" to be liquefied. This great milestone was the dawn of a new era of scientific research in Solid State Physics based on experimentally unexplored extreme low temperature measurements (~ 0 K), which became the premise of the discovery of superconductivity in certain materials. Onnes [1], while studying the dependency of electrical resistance on temperature, discovered that at near absolute zero temperatures, the electrical resistance of mercury–Hg peculiarly and suddenly vanished at a critical temperature (T_c) of 4.2 K, as seen in Fig. 1.1.

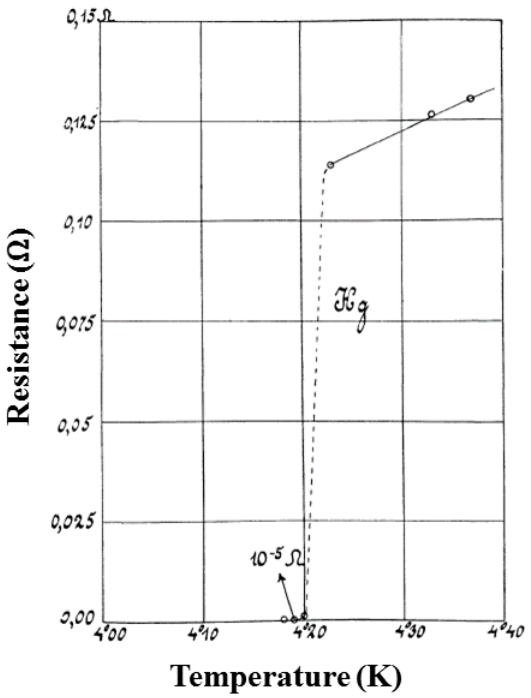

Figure 1.1: **Novel results of the resistance of Hg at liquid He temperatures.** The first resistance measurements of mercury as reported by Onnes [1], where the resistance suddenly drops to $\sim 0\,\Omega$ at a T_c of 4.2 K.

Certainly, the vanishing of resistance was surprising such that it became a fundamental property of superconductors, however, not the only one. Superconductors possess anomalous physical properties related to magnetism and thermal capacity [3]. In 1933, two decades after the inception of superconductors, Meissner and Ochsenfeld [4], found that external magnetic fields do not penetrate a material in its superconductive state, even though the magnetic flux is conserved, as shown in Fig. 1.2. This turned out to be a unique and fundamental property of superconductors referred to as the Meissner effect.

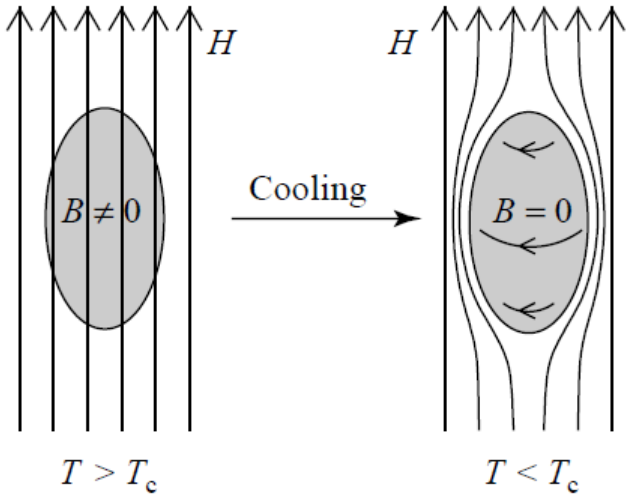

Figure 1.2: **A schematic of the Meissner effect.** The cooling down of a material from a normal state into a superconductive state induces a Meissner effect where the penetrative external magnetic fields in a material are expelled once the $T<T_c$ [5].

The discovery of superconductivity led to an avalanche of experimental studies, where many more superconducting materials were discovered with varying T_c, and their physical properties studied extensively [3]. However, almost half a century went by without a convincing theoretical description of how the superconductive phenomena appears in certain materials. Many great scientific minds at the time tried unsatisfactorily to explain the distinct properties of a superconductive state. It was only in 1957, when Bardeen et al. [6], formulated a plausible argument "dubbed" the BCS microscopic theory of superconductivity. The theory describes how a pair of electrons known as Cooper pairs flow through a superconductive material unperturbed. Albeit, this was assisted by the significant realization that the principal mechanism involved is based on the interactive process between electrons and the crystal lattice known as the isotope effect (i.e., electron-phonon scattering) [7, 8]. Maxwell [7] and Reynolds et al. [8], were the first to show experimentally that the T_c of Hg varies with the isotopic mass given by the following variable relationship:

$$T_c M^{1/2} = \text{constant}, \tag{1.1}$$

where M is the mass number of the elemental composition. This significant demonstration in the early 1950s was the foundation on which the BCS theory was built upon 7 years later.

The BCS theory illustrates how the electron-phonon interaction is responsible for the "indirect" attraction between electrons. The unusual proposition (i.e., charges

with similar polarization repel one another), was built upon the work done by Cooper [9], just a year earlier. Cooper [9], suggested that at low temperatures the energy gap (Δ) between the ground state and excited state of a one-electron energy spectrum is responsible for superconducting properties. His proposal was based on the possibility of a pair of electrons attractively interacting on the Fermi surface because of the electron-phonon scattering processes. The schematic in Fig. 1.3, demonstrates the manner at which these interactions may occur. A single transient electron distorts the positive ionic structure of the crystal lattice via attractive electric forces, resulting in a positively polarized cloud of ions surrounding the electron. If the positive charge of the resultant ionic system exceeds the screened Coulomb repulsive forces between two electrons, then a second electron is attracted to the positively charged system at an average extension of the order $\sim 10^{-4}$ cm, resulting in a bound state of electrons regardless of the weak attraction. And, due to Pauli's exclusion principle, certain quantum transitions against the coupled electron pair will not be possible, effecting a non-interacting quasi-particle system moving through the lattice with no electrical resistance, i.e., A bosonic Cooper pair of electrons.

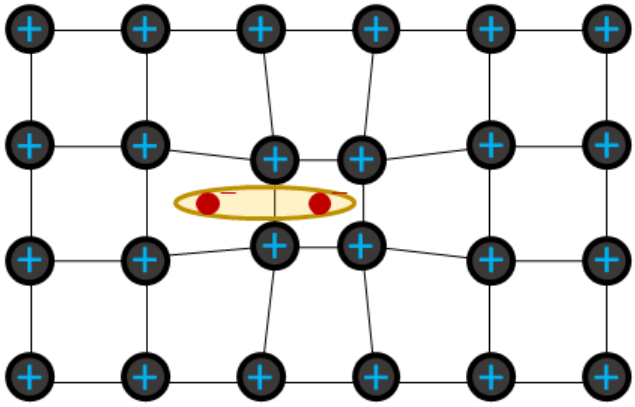

Figure 1.3: **A schematic of a Cooper pair with two bound electrons.** The minimal distortion of the crystal lattice with positive ions is due to a single transient electron. The distortion and the electron can result in a positively charged system that attracts a second electron, forming a Cooper pair of two electrons.

The non-interacting characteristic of Cooper pairs with the crystal lattice brought about necessary discussions pertaining to the existence of a "forbidden" energy gap. The appearance of an energy gap (Δ_g) as indicated by Cooper [9], is based on the effective inter-electron attraction due to the atomic vibrational modes of the lattice, and is one basic characterizing parameter for superconductivity and is also essential for measuring its magnitude [3]. A gap in the energy spectrum of a superconducting state was first observed experimentally by Glover III and Tinkham [10], through electromagnetic radiation with large wavelengths close to 1 mm corresponding to the binding energy ($\Delta_g = 10^{-3}$ eV) of the Cooper pairs. The gap was found to be dependent on the strength of a dimensionless electron-phonon coupling constant λ_c, derived from an exponential law, i.e., exp(-1/λ_c), proposed by Fröhlich [11]. The aforementioned exponential function possesses a curious property, in that it cannot be expanded mathematically by a Taylor series for small values of λ_c. This brought about significant restrictions to the establishment of a theoretical description of superconductivity, since the expansion of powers of such a small parameter is

the premise of obtaining quantities such as wave functions and energies using the much familiar perturbation expansion theory [3]. Consequently, the failure of the perturbation theory led to the discovery of the reputable BCS theory as proposed by Bardeen et al. [6].

Despite the early success of the BCS theory, unanswered questions were raised regarding the theory's limitations, since it could not qualitatively explain the absence of superconductivity in some highly conductive metals [3]. Again, three decades later after the BCS theory was highly accepted by the science community as the most viable description of superconductivity, it was also shown that such a theoretical explanation seem to apply specifically to certain types of superconductors characterized as low temperature type I superconductors [12]. This was validated by the discovery of a high temperature superconducting material in insulating ceramic compounds (i.e., lanthanum-barium-copper oxides), with a T_c of 30 K by Bednorz and Müller [12], in 1986. Many other high temperature superconductors have been discovered ever since with T_c as high as 250 K [3, 13]. Unfortunately, the origin of high temperature superconductors (HTS) or type II superconductors cannot be adequately described by the BCS theory at its current format since it relies solely on low temperature conditions.

1.1 Boron-doped diamond

The likelihood of superconductivity arising in degenerate semiconductors or semimetals has been investigated since the 1960s [14, 15], with emphasis on doped semiconductors having a many-valley band structure due to the possible increase of the attractive interactions between the transient electrons provided by the inter valley phonons. However, focus studies in superconducting semiconductors intensified only recently, particularly since the unveiling of superconducting boron-doped diamond (BDD) and silicon crystals [16–18].

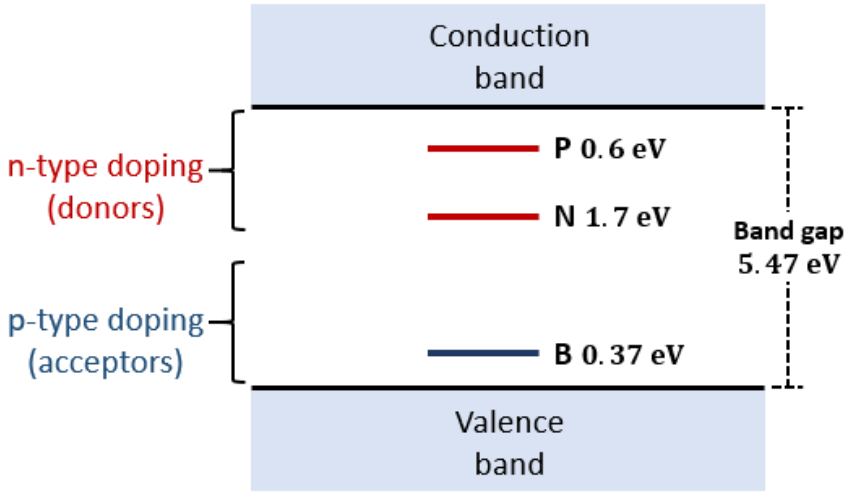

Figure 1.4: **Band gap states in diamond.** The energy states for n-type donors represented by phosphorus (P 0.6 eV) and nitrogen (N 1.7 eV) dopants below the conduction band, and a p-type donor represented by boron (B 0.37 eV) dopant above the valence band.

Figure 1.4, depicts the activation energy (E_A) levels of prominent n-type dopants phosphorus (P – 0.6 eV) and nitrogen (N – 1.7 eV) below the conduction band (CB),

and a p-type dopant boron (B – 0.37 eV) ontop of the valence band (VB). A substantial amount of boron atoms embedded in diamond behave as electron acceptors within the diamond structure where the quantity of boron has a proportional relationship with the conduction of electrons in diamond such that a superconducting state can also be achieved under specific fabrication processes. With the appearance of superconductivity in BDD synthesized at high-pressure and high-temperature (HPHT), and in BDD films engineered via microwave plasma-assisted chemical vapor deposition (MPCVD) ($\sim T_c = 4\,\mathrm{K}$), as well as in silicon crystals ($\sim T_c = 0.35\,\mathrm{K}$) [16–18], has recently renewed great interests in the properties of semiconducting materials near absolute zero temperatures [19].

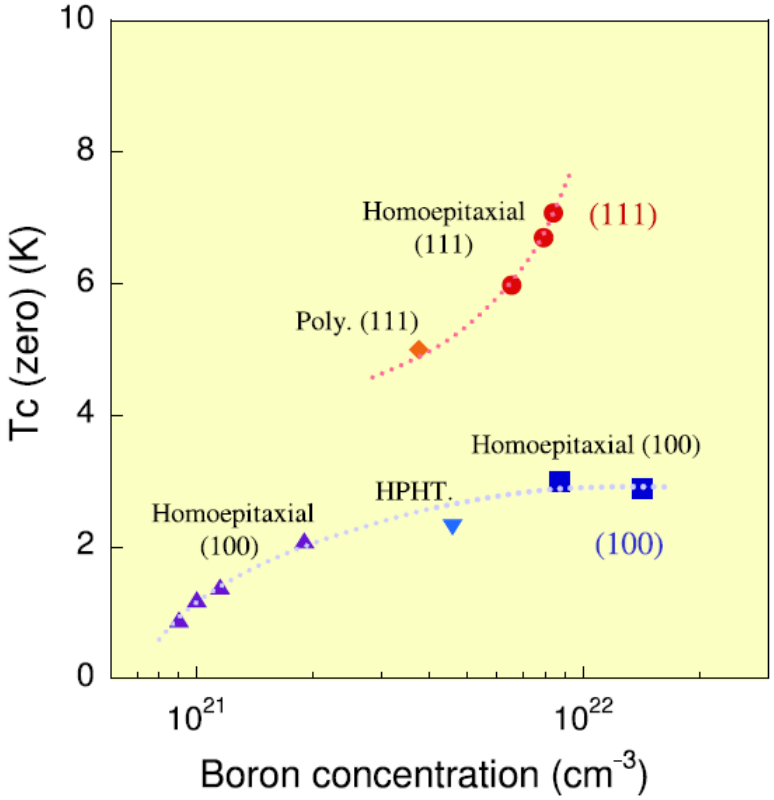

Figure 1.5: **Diamond lattice structure orientation on.** The T_c of (111)-oriented diamond samples is higher than (100)-oriented diamond samples with nominally similar boron concentrations and similar crystallinity [20].

The superconductive state in a heavily BDD arises close to the metal-to-insulator transition (MIT), related to the critical concentration of boron (n_B) ranging from $\sim 2 \times 10^{20} - 3 \times 10^{21}\,\mathrm{cm}^{-3}$ [16, 21, 22]. The many-valley band structure in a degenerate diamond material is favored to address superconductive properties due to the additional electron interactions with inter-valley phonons [14] (please refer to Fig. 2.4 (b) in Chap. 2). Although, the resistance of current flow is prominent in 'semiconducting' diamonds than in ordinary metals due to the wide energy transition for charge carriers (i.e., electrons and holes) between the energy bands [23]; the carrier density in diamond can be substantially altered via impurity carrier doping techniques, thereby affecting the Fermi-energy (E_F) level of its electronic band structure [24–26]. Consequently, such an approach modifies the conductive nature of a semiconducting diamond such that it reaches a superconductive state under suitable

conditions [27]. This behavior is remarkable for a wide band-gap semiconducting material such as a relatively pure diamond with a very high electrical resistance ($>10^{15}\,\Omega\,\mathrm{cm}$) [28].

The phase diagram depicted in Fig. 1.5, shows the significant work that has been achieved thus far due to the effective activation of boron into the diamond matrix during growth. There is a clear dependency of the critical temperature T_c of a superconductor on substrate orientation and boron concentration [20]. The crystal orientation is associated with the distortion of the crystal lattice with different growth directions resulting in different expansion rates which seems to have an impact on the T_c for various samples [20, 29]. These differences are thought to affect change in the density of states and hence the superconducting properties. On the other hand, the increase in boron concentration corresponds to the hole carrier concentration within a diamond matrix that is indicative of substitutional boron [20, 29]. There is a significant difference in superconducting transition temperatures for various diamond materials that have been fabricated and processed diversely; leaving good opportunities to study the optimal doping level of boron in diamond.

1.2 Why boron-implanted diamond?

It is imperative to bring to the reader's attention that the superconductive properties discovered in diamond are only attributed to boron doped diamonds that are synthesized via HPHT and CVD processes [16, 22]. That is, boron was only incorporated into the diamond lattice during growth. Such appealing properties are yet to be demonstrated in boron '**ion implanted**' diamond samples [30]. Despite the use of some compensating ion implanting techniques and extensive post-implant annealing studies by scientists, the boron implanted diamond with hole carrier concentration well above the MIT level has not yet reached the superconductive state. This means new experimental processes and other comprehensive techniques are required to address this predicament. With the flexibility of non-equilibrium ion implantation processes, there is a research gap to address the solubility of boron in diamond in order to improve the T_c beyond the reported level of $\sim T_c = 7.4\,\mathrm{K}$ [17]. This study aims to investigate low temperature transport properties of boron implanted layers in diamond materials with doping levels near the Fermi-energy E_F (i.e., localized states), via low energy and low fluence ion implantation with annealing.

Interestingly, there are boron associated bands that are prevalent in both superconducting and non-supercondcuting boron-doped diamonds, i.e., $500\,\mathrm{cm}^{-1}$ and $1200\,\mathrm{cm}^{-1}$ Raman bands [31]. The aforementioned bands are said to originate from the phonon density of states of diamond [32, 33]. Morever, it has been reported from Fano interaction effects that the $500\,\mathrm{cm}^{-1}$ band is related to boron dimers and boron clusters while the $1200\,\mathrm{cm}^{-1}$ band is related to boron centers (i.e., B – C bonds), which is likely to be responsible for the mechanism of superconductivity in diamond [19, 34, 35]. The very same Raman bands also appear in ion implanted and annealed samples, albeit, with a more pronounced graphitic band at $1546\,\mathrm{cm}^{-1}$, which seems to increase with increasing B concentration (refer to chapter 6). It may very well be that a relatively significant ratio of graphite related sp^2 bonds are the main compensating factor that suppresses superconductivity in boron implanted diamonds. Nonetheless, boron-doped nanocrystalline diamond with graphitic clusters near the grain boundaries was confirmed to be superconducting

[36]. Moreover, from irradiation studies of helium ions in a diamond that is already superconducting ($T_c \approx 10\,\mathrm{K}$), it is also evident that only high fluences of ion implantation ($\sim 10^{16}\,\mathrm{cm}^{-2}$), is detrimental to superconductivity [30]. While to some degree thermal annealing processes assists in recovering the superconductive state of diamond ($T_c \approx 4\,\mathrm{K}$). It is also worth noting that there is little to no degradation of superconductivity at low ion fluences ($\sim 10^{14}\,\mathrm{cm}^{-2}$).

Furthermore, the energy spectra of both superconducting (4.3% B conc.) and non-superconducting (0.25% B conc.) diamonds from XAS spectroscopy measurements looks to be very similar, with impurity in-gap states $I-$ and hole states $H-$ 0.37 eV above and 1.3 eV below the valence band, respectively [20, 37]. However, the peaks seem to broaden for superconducting diamond, likely due to high boron concentrations. In comparison, it would be very interesting to see the energy spectrum of boron 'implanted' diamond. Now, the similarities between superconducting and non-superconducting diamond from these analytical techniques indicate that other compensating defects such as the appearance of peaks associated with D ($1345\,\mathrm{cm}^{-1}$) and G ($1500 - 1600\,\mathrm{cm}^{-1}$) bands for disordered diamond or carbon interstitial bands ($1620\,\mathrm{cm}^{-1}$) after heavy boron implantation and annealing are mainly responsible for the absence of a superconducting state in boron implanted diamond [38, 39]. Clearly, this also necessitates the careful study of the evolution of all the aforementioned bands via ion implantation and annealing processes; along with the relative conduction mechanisms at low temperature regimes.

1.3 Outline

The aim of this study is to investigate the low temperature properties ($T \longrightarrow 0\,\mathrm{K}$), of heavily boron-implanted diamond nanoscale layers in proximity to the diamond surface. The study looks at various independent processes that includes sample preparation through sequential low fluence and low energy ion implantation with dynamic and thermal annealing to ascertain boron ion incorporation into carbon substitutional sites with minimal degradation of the diamond matrix (i.e., disordered graphitic phases). Whilst, using spectral analysis to study the evolution of the Raman bands that appear after ion implantation and annealing, and also to affirm the structural integrity of the diamond matrix as well as to detect boron-carbon bonds leading up to the MIT threshold. And lastly, the characterization of samples using electric transport techniques at low temperatures. This study will add to the ongoing pursuit of superconducting semiconductors with suitable control over doping parameters via Boron ion implantation.

- **Chapter 2** : Background study based on boron related defects in diamond; with a thorough investigation of the properties of boron implanted diamond samples in comparison with other doping techniques: The techniques involved in inducing boron correlated hole charge carriers within the diamond matrix.
- **Chapter 3** : The ion doping technique suitable for this particular project. A thorough consideration will be given to the ion and solid interaction processes required to successfully fabricate a controlled concentration of boron buried channels in diamond, while also giving an overview of the SRIM simulation package used in this study.
- **Chapter 4** : Experimental techniques involved with the engineering of boron

-implanted diamond samples. This include the ion implantation process and its suitability for a type IIa CVD diamond. The effects of annealing of the diamond sample and the detection of the zero phonon lines (ZPLs) associated with boron defects.

- **Chapter 5** : The SRIM/TRIM simulations of boron ion implantation. The viability of low energy keV boron ion implantation in nm-sized shallow layers below the diamond surface is demonstrated. Due to the accurate nature of the SRIM simulations the vacancy densities attained are used as basis of discussion throughout the whole thesis.

- **Chapter 6** : The spectral analysis of boron-implanted diamonds. This include the analysis of an ion implanted and thermally treated diamond sample by employing Raman and photoluminescence characterization techniques to substantiate the dynamic attribute of the defects involved in the formation of the boron buried channels.

- **Chapter 7** : The electric transport measurement. Resistivity characterization of the samples is investigated from $300\,\mathrm{K} \longleftrightarrow 2\,\mathrm{K}$. And finally, the deduction of the hole carrier concentration within the implanted samples via Hall effect and Seeback measurements.

- **Chapter 8** : Summary and conclusion of the results obtained. A brief discussion of the future work based on the enhancement of the optimum doping level of boron in diamond with minimum compensating defects that suppresses conductivity for applications in the electronic industry.

Chapter 2

Theory

In this chapter I provide a theoretical background related to this study. Firstly, I discuss the physical and atomic structure of diamond, together with the characterization techniques used for all the diamond types. This includes a discourse on the photo-physical properties of diamond with respect to the common well-studied defects that are found in the diamond matrix, particularly carbon vacancies and interstitial sites that interact with foreign atomic impurities. The second section focuses on the main properties associated with heavily boron-doped diamond materials, i.e., the optical response, lattice expansion and metal-to-insulator transition (MIT) properties due to atomic boron incorporation into the diamond matrix. In the third section, I discuss the electronic properties of boron-doped superconducting and non-superconducting diamonds.

2.1 Impurities in diamond

The ancient Greek translation for diamond is *Adámas*, which in part means 'invincible', a befitting description for a gemstone of its near indestructible and scenic physical properties. Diamonds are known for their exceptional quality and ability to symbolize wealth. When exposed to light, they display a wide range of colors, demonstrating their exceptional nature. It is commonly known that various colors result from impurities or defects that are absorbed into the diamond crystal's lattice structure [40]. The large energy band-gap of a pure diamond, 5.47 eV, should theoretically cause it to be optically isotropic, or a transparent colorless crystal [41, 42]. However, in actuality, extrinsic atoms such as nitrogen, boron, hydrogen, nickel, chromium, cobalt, titanium, zinc, tungsten, silver, and silicon, atom impurities [43, 44], embedded within the lattice structure of diamond, are the cause of more than 500 known color centers in diamond. Also, every color center in a diamond confers distinct visual and physical characteristics, some of which are essential to many areas of physics [44]. From ultraviolet to far infrared, the centers produce radiation across the spectrum. Diamond has an abundance of optical centers, more than any other material, allowing for the detection and manipulation of individual color centers at room temperature (RT). These discrete color centers are often called "artificial atoms" and are being investigated as a separate quantum system that can produce single photons on command.

Figure 2.1: **Diamond types due to defects.** Four main types of diamonds that are both natural and synthetic. The different colors are due to unique impurity types and impurity levels. [45].

2.1.1 Physical properties of diamond

A diamond is a chemically inert substance composed primarily of carbon atoms covalently bound inside its matrix structure. Its exceptionally high thermal conductivity ($\sim 25\,\mathrm{W\,cm^{-1}\,K^{-1}}$) makes it the hardest known bulk substance on Earth.

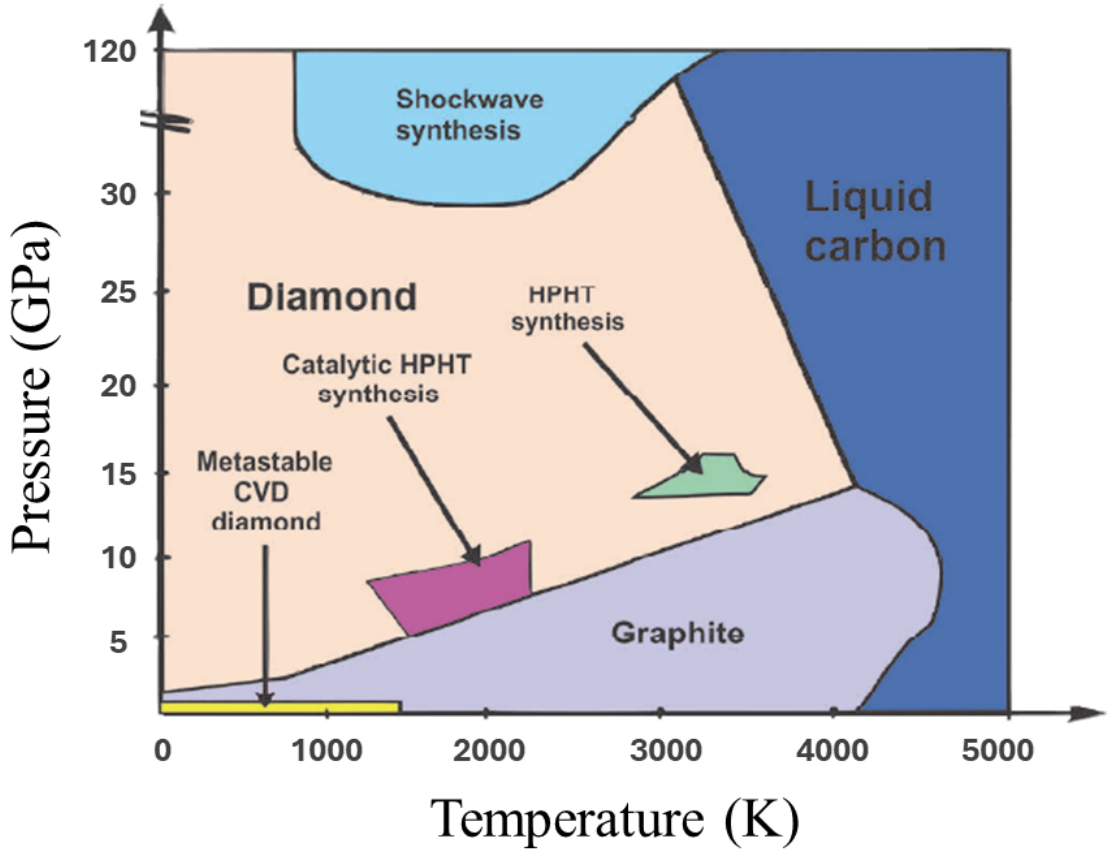

Figure 2.2: **Carbon phase diagram.** Extensions of the liquidus lines for graphite and diamond define their respective regions of metastability [46].

The two most researched and well-known carbon allotropes are diamond and graphite (refer to Fig. 2.2). The structural rearranging of a primary atom to create distinct materials with differing properties is known as allotropy. Diamond is a highly esteemed semiconductor material, primarily because of its exceptional mechanical qualities and remarkable physical attributes such as luster, hardness, high Debye temperatures, and optical transparency. A few of these properties are displayed in Tab. 2.1. Diamond is used extensively in both jewelry and industrial applications. The basic and regular arrangement of carbon atoms within the crystal lattice of diamond gives it its distinct qualities. This three-dimensional, highly symmetrical atomic arrangement within a material affects the material's fundamental characteristics. The diamond structure is sp^3 hybridized with each atom covalently bonded to four other carbon atoms via sigma ($\sigma = 1.54\,\text{Å}$) bonds, with equal angles ($\beta = 109.4°$) between them. The lattice structure of diamond is therefore crucial, in this case to fully investigate the properties of diamond.

Table 2.1: The optical, mechanical and thermal properties of diamond [47].

Properties of diamond	
Lattice structure	Cubic
Space group	$Fd3m$–O_h^7
Lattice parameter (a_0)	3.567 Å
Density	$3.515\,\text{g/cm}^3$
Thermal conductivity	$\sim 25\,\text{W cm}^{-1}\,\text{K}^{-1}$
Debye temperature	1860 K
Melting point (12.4 GPa)	$4440 - 4773$ °C
Energy band gap (E_g)	5.47 eV
Raman frequency	$1332\,\text{cm}^{-1}$
Index of refraction (visible)	2.4
Electron mobility (300 K)	$1800\,\text{cm}^2/(\text{V}\cdot\text{s})$
Hole mobility (300 K)	$1500\,\text{cm}^2/(\text{V}\cdot\text{s})$
Atomic density	$1.76 \times 10^{23}\,\text{cm}^{-3}$
Bulk modulus	$4.5 - 5.5 \times 10^{11}\,\text{Nm}^{-2}$
Dielectric constant (300 K, low frequency)	5.70
Thermal expansion coefficient (300 K)	$\sim 1 \times 10^{-6}\,\text{K}^{-1}$
Velocity of sound	$\sim 1.96 \times 10^5\,\text{cm s}^{-1}$

The cubic lattice structure of diamond is formed by unit cells periodically arrayed and stacked together, described by a face centered cubic (FCC) point lattice structure in which each site has a two atom basis, with one located at ($0\hat{x}$, $0\hat{y}$, $0\hat{z}$) and the other at ($\frac{1}{4}\hat{x}$, $\frac{1}{4}\hat{y}$, $\frac{1}{4}\hat{z}$), where $\hat{x}$, $\hat{y}$ and $\hat{z}$ are orthogonal unit vectors [48]. The structure is depicted in Fig. 2.3 (a). The unit cells consist of lattice sites housing carbon atoms, with each carbon atom surrounded by four other carbon atoms to form a tetrahedral geometry. Each unit cell has 8 atoms from 18 lattice sites with 14 shared by other unit cells. Atoms located at the corner sites are shared by 8 unit cells each and hence make up 1 atom, while the 6 face-centered atoms are shared by 2 unit cells which

then make up 3 atoms, and together with the 4 atoms inside make up 8 atoms per unit cell. The lattice parameter (a_0) or the edge length of the cubic unit cell is equal to 3.57 Å [48].

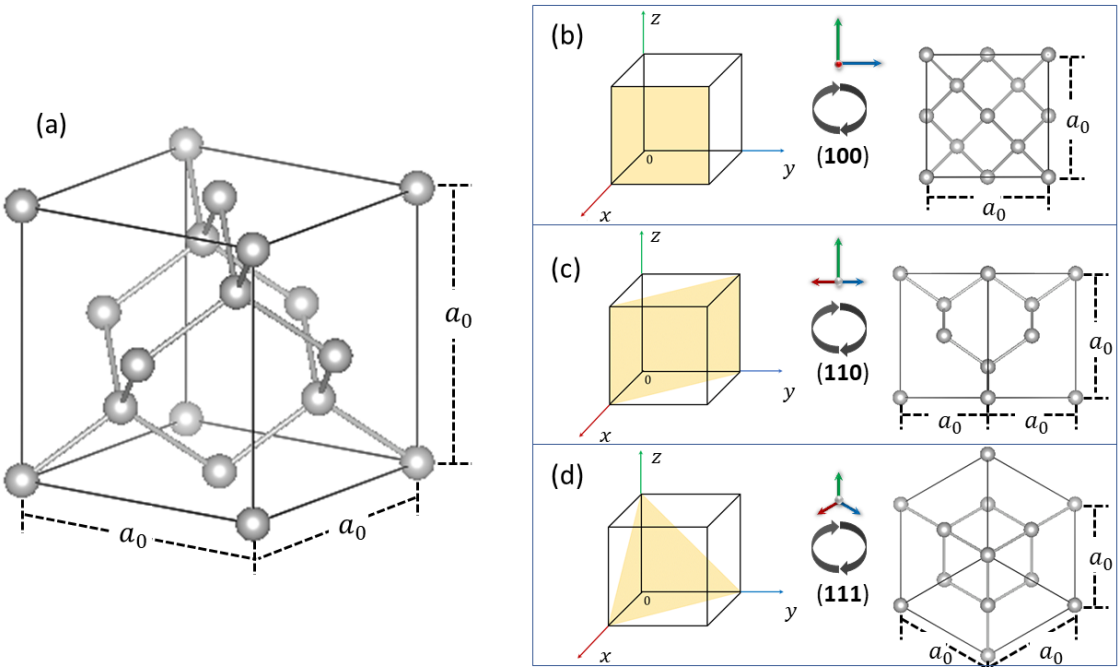

Figure 2.3: **Diamond cubic structure.** (a) The face centered cubic (FCC) crystal structure of diamond with 8 carbon atoms per unit cell, with lattice parameter 'a_0' of length 3.57 Ã. (b)-(d) Represents the diamond lattice structure oriented along the three commonly considered crystallographic planes for a cubic crystal. (b) The lattice structure is perpendicular to (111) plane, while at (b) and (c) the lattice structure is perpendicular to (001) and (110) planes, respectively.

Figure 2.3 (b-d), shows the lattice structure of diamond viewed along three commonly considered crystallographic planes. The orientation of each atomic plane is represented by the reciprocals of a set of vector intercepts along the x, y and z axes known as Miller indices (hkl). Consider Fig. 2.3 (b), where the plane is parallel to axes y and z, the intercepts can be taken as $\hat{x} = 1$, $\hat{y} = \infty$ and $\hat{z} = \infty$. The reciprocal of these intercepts then gives us the Miller indices as $h = 1$, $k = 0$ and $l = 0$, representing the plane (100). Similarly, the planes in Fig. 2.3 (c) and (d) are referred to as (110) and (111), respectively. In general, each lattice point is represented in the form $\hat{r} = n_1\hat{x}+n_2\hat{y}+n_3\hat{z}$ and lies in the direction $[n_1n_2n_3]$ from the origin. The lattice crystal structure of diamond has a high degree of symmetry, where each plane can be rotated by 90° in each of the three dimensions. All the six faces of the cubic structure are identical and have entirely equivalent (100) planes referred to as {100} set of planes. Similarly, there are sets {110} and {111} with equivalent planes (110) and (111), respectively. Furthermore, the particular direction of a plane is represented by square brackets $[hkl]$ and is perpendicular to the (hkl) plane. A variety of these crystallographic directions can also be symmetrically equivalent, therefore a set of directions are written with triangular brackets: ⟨UVW⟩. The differences in brackets is essential, and will be referred to throughout this dissertation to describe both ion orientation and growth surfaces with respect to the diamond lattice structure. The lattice structure of diamond and many other materials has

been expounded adequately in many texts over the years, hence the reader can refer to texts by Ashcroft and Mermin [48], and Kittel et al. [49], for further expatiation on the subject.

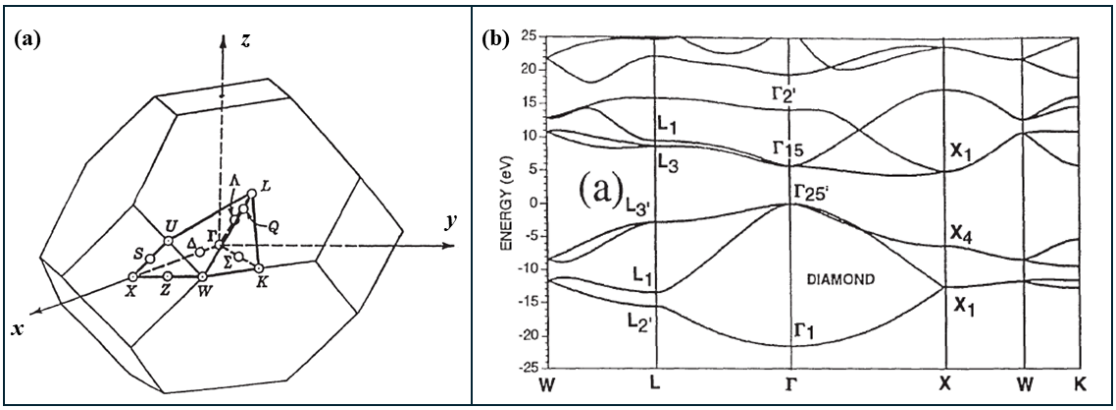

Figure 2.4: **The band structure of diamond.** (a) The first Brillouin zone (BZ) of diamond with $\vec{k}-$symmetry points (Γ, X, L, W, K, U) and symmetry lines ($\Lambda, \Delta, S, \Sigma, Q, Z$). (b) The electronic band structure of diamond calculated using the linearized-augmented-plane-wave (LAPW) method within local-density approximation (LDA). The corresponding symmetry points are represented by the vertical lines with center at Γ ($\vec{k} = 0$) [50].

The high symmetry properties of diamond in the reciprocal space is depicted by a truncated octahedron shaped Brillouin zone (BZ) as shown in Fig. 2.4 (a). The diamond structure is invariant in symmetry operations or point operations such as reflection and rotation [50]. These symmetry operations make up the point group of the diamond structure with 48 symmetry elements reflected about the first BZ. Due to the high symmetry of the diamond structure only the irreducible wedge (1/48th) of the first BZ is considered for the electronic band structure analysis of diamond materials (i.e., the electronic and vibrational properties).

The periodicity of a pristine diamond crystal structure is described by the $\vec{k}-$symmetry points: $\Gamma = 2\pi/a_0(0,0,0)$, $X = 2\pi/a_0(1,0,0)$, $L = 2\pi/a_0(\frac{1}{2},\frac{1}{2},\frac{1}{2})$, $W = 2\pi/a_0(1,\frac{1}{2},0)$, $K = 2\pi/a_0(\frac{3}{4},\frac{3}{4},0)$ and $U = 2\pi/a_0(1,\frac{1}{4},\frac{1}{4})$ [51]. The highest symmetry point is located at the zone center Γ ($\vec{k} = 0$) of the BZ and possess the same symmetry properties as the crystal. At the zone center, there are three acoustic phonon modes related to the translational geometry of the diamond crystal and three doubly degenerate optical phonon modes with different polarizations. Consequently, by considering all 9 vibrational modes, the degeneracy of the zone center point is 9. As shown in Fig. 2.4 (b), the VB of diamond has four subbands; three are degenerate at the upper edge of the band and one is non-degenerate located at the bottom of the band. Therefore, the degeneracy of Γ is 1 (i.e., there is only 1 distinct $\vec{k}-$point in the Brillouin zone center) [51].

The electronic band structure of diamond consisting of the VB (lower band) and CB (upper band) is shown in Fig. 2.4 (b); and it is obtained from solving the Schrödinger equation for an approximate one-electron model [52],

$$\left[-\frac{\hbar}{2m}\nabla^2 + V(\vec{r})\right]\phi_k(\vec{r}) = E_k\phi_k(\vec{r}), \tag{2.1}$$

where $V(\vec{r})$ represents the periodic potential energy due to the periodicity of the crystal lattice with the plane wave given by the Bloch function $\phi_k(\vec{r})$ written as follows,

$$\phi_k(\vec{r}) = e^{i\vec{k}\vec{r}} U_n(\vec{k}, \vec{r}), \tag{2.2}$$

where $\vec{k}$ is the wave vector, $U_n(\vec{k}, \vec{r})$ is a periodic function in $\vec{r}$ related to the crystal lattice and n is the band index. From Fig. 2.4 (b), the conduction band minimum (CBM) is located at different $\vec{k}-$points from the center (Γ) where the valence band maximum (VBM) is located. Therefore, the band structure of diamond is described as a many-valley band structure with an indirect energy band $E_g \approx 5.47\,\text{eV}$.

2.1.2 Charecterization of diamond types

Deep in the Earth's mantle ($\approx 150\,\text{km}$), natural diamonds are formed. The majority of diamonds that have been found were produced in environments with high pressure and temperatures millions or even billions of years ago, and they were eventually carried to the Earth's surface by volcanic eruptions. When compared to other places, diamond deposits from the same area frequently have comparable chemical and physical characteristics. All naturally occurring and artificially created diamonds have mechanical and physical qualities that are exactly the same, however they differ greatly based on the internal structure and crystal morphology. As shown in Fig. 2.3 (*b-d*), the anisotropic nature of the crystal properties is caused by the various arrangements of carbon atoms in different planes. As expected, many established authors developed a variety of diamond characterization methodologies over the last century.

It was established by Robertson et al. [40], whose research examined the absorption spectra of several diamond samples subsequently introducing an optical classification system for diamonds. They were able to successfully classify diamonds into two groups: type I and type II, based on how transparent they were to ultraviolet (UV) and infrared (IR) light, respectively. As opposed to type I diamonds with IR, type II diamonds were found to frequently show little to no birefringence from the UV light when viewed between two crossed polarizers. This finding led to the conclusion that type II crystals had to have either a nearly faultless and pure crystal structure or a minimum amount of impurities. According to [53], type I samples are indeed more defective than type II samples due to multiple chemical impurities clustered in and around the carbon lattice sites. .

Since then, a great amount of research work has been done on the availability of impurities in a carbon-based structure like diamond, yielding interesting optical absorption findings. At the time, research concentrated on relationships between the physical characteristics of each sample and the fluorescence from various samples' absorption bands. Scientists as a result started to observe systematic relationships between the optical characteristics provided by type I and type II diamonds. As described by Lang et al. [54] and Thomaz et al. [55], some of the linked properties of type I diamonds containing nitrogen impurities are the yellowish color and blueish fluorescence with distinct absorption spectra (N3 defect-415 nm). As can be seen from Tab. 2.2, this ultimately led to the sub-classification of these diamond types [42]. Through IR spectroscopy, researchers such as Dyer et al. [56] were able to distinguish between isolated nitrogen (type Ib) and clusters of nitrogen ions, also known as aggregated nitrogen (type Ia), in type I diamonds. Because nitrogen is the

Table 2.2: Categorization of diamonds based on sample characteristics [40, 42].

				Optical absorption	
Type	Impurity	Visual properties	Feature	Visible	Infrared
Ia	Aggregated nitrogen	Colorless, violet, green, brown, orange, yellow, pink	Opaque to short-wave UV; common	Secondary absorption edge at 300 nm, 415 nm	A–bands, B1 and B2 peaks
Ib	Isolated nitrogen	Brown, orange, yellow	Strong absorption increasing at higher photon energy; common	Strong absorption up to 450 nm	Peaks at 0.14 eV and 0.167 eV
IIa	None	Colorless, green, brown, pink	Transparent to short-wave UV; rare	Fundamental absorption edge, 5.5 eV	Lattice bands only
IIb	Boron	Gray, blue	Transparent to short-wave UV; electrically conductive; rare	Fundamental absorption edge, 5.5 eV, absorption at red end of spectrum	Acceptor bands, free carrier absorption

most commonly detected impurity in diamonds, it was evident at the time that its presence or absence would determine the type of diamond [41].

Over 95 % of natural diamonds were discovered to have type Ia features, but type Ib properties were found to be rare in natural diamonds [42]. Other researchers acknowledged the scarcity of type II properties in natural diamonds and suggested splitting them into type IIa and type IIb [57]. These differences in physical and electric properties (again, see Tab. 2.2), are the reason for the recommendation; the former is primarily impure-free, while the latter exhibits electrical conductivity because of boron. A schematic illustration of how nitrogen, boron, and vacancies might be embedded into the diamond carbon lattice sites is presented in Figure 2.5 [45]. Diamond is a rare natural resource that may also be created artificially in a lab. High-pressure and high-temperature (HPHT) [58] and chemical vapor deposition (CVD) [59, 60] growth procedures are widely employed experimental approaches for special characteristics. With HPHT and CVD methods, respectively, synthetically produced diamonds frequently display optical characteristics of the naturally scarce diamond types, namely type Ib and type IIa.

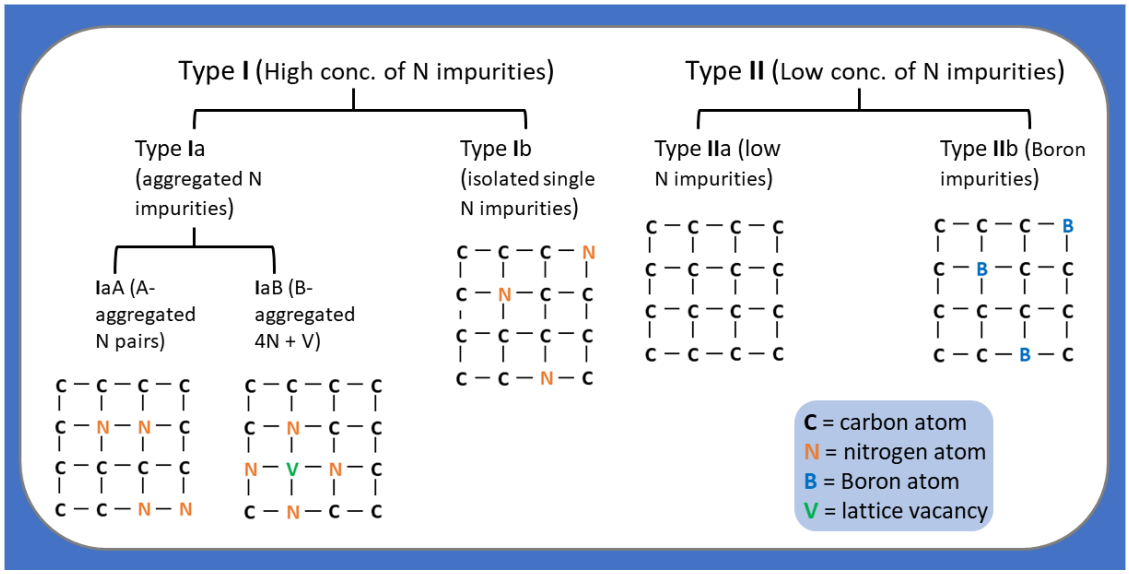

Figure 2.5: **Schematic of diamond types with host and impurity atoms.** Classification of diamond types due to the presence of nitrogen and boron impurities [44].

2.1.3 Point defects in diamond

Many characteristics of diamond are governed by the presence of point defects. Zhu [61], defines point defect as a "zero-dimensional and thermodynamic equilibrium defect present within the diamond lattice". Figure 2.6, shows a schematic of point defects that are possibly available in diamond (please refer to Tab. 2.3, for description). They include intrinsic vacancy (V) and self-interstitial (I) point defects and extrinsic (foreign atoms and impurities) substitutional or interstitial point defects. Nitrogen (N), along with a vacancy or a combination of both, are the commonly studied point defects in diamond. However, extrinsic boron (B) atom doped or injected into the diamond lattice is of significant interest in electron conduction studies.

As depicted in Fig. 2.5, foreign atom impurities can exist either in simple configurations for isolated single atomic impurities similar to type Ib and IIb diamonds or in complex configurations for aggregated impurities in type Ia diamonds. As such, a simple configuration can be a single boron atom substituting a carbon atom from its lattice site or even occupying a usually unoccupied site within the diamond crystal lattice, with both such impurities commonly referred to as substitutional and interstitial point defects, respectively, as seen in Fig. 2.6. Complex configurations include a combination of extrinsic atoms adjacent to each other or other foreign atoms coupled with intrinsic vacancies inside the diamond crystal lattice. All the different configurations of these foreign atoms in diamond induces unique physical and optical properties [42]. Most defects in diamond appear naturally, however it is also possible to engineer desired defects with specified concentrations for various studies and applications.

Since the classification of diamond types, subsitutional boron atoms have been identified as the dominant impurity in type IIb diamonds. Typically, these kind of diamonds are extremely rare in nature with atomic boron concentrations <0.5ppm. Since nitrogen related impurities are largely electron donors, only diamonds with concentrations [N]<[B] exhibit characteristics associated with type IIb diamonds,

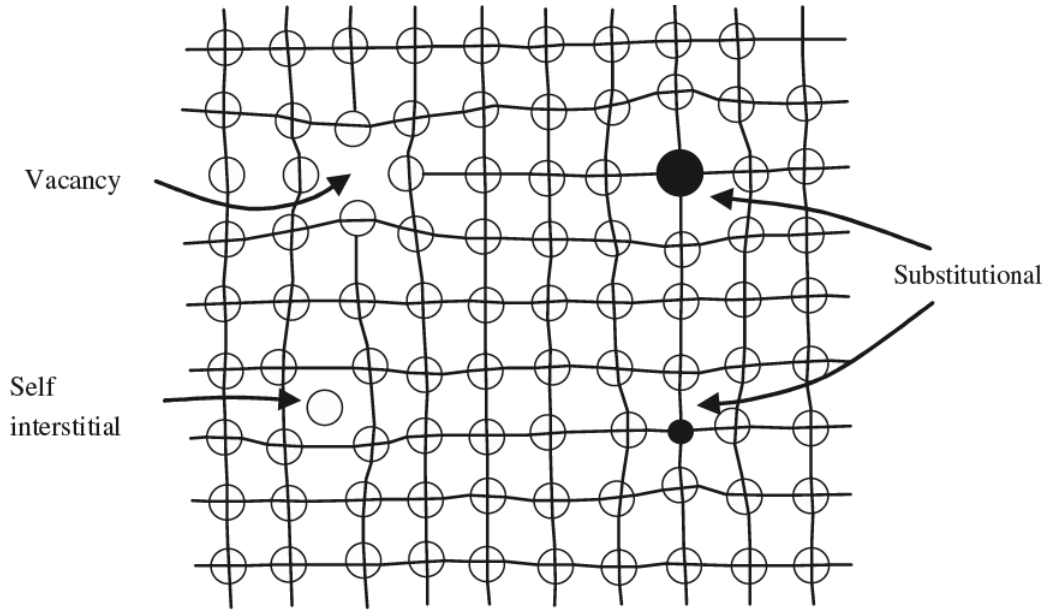

Figure 2.6: **Schematic of possible point defects.** A vacancy and a self-interstitial are intrinsic point defects, while foreign atom can exist as either an interstitial or substitutional (S) [62].

Table 2.3: Possible semiconductor defects [62].

Type of defect	Description
Point	Carbon vacant sites, substitutional foreign atoms, self- and foreign interstitials.
Line	Crystallographic dislocations.
Planar	Stacking faults with twins and grain boundaries.
Volume	Precipitates and voids

and hence the rarity of such natural specimens. However, it common to produce type IIb diamonds via HPHT and CVD growth techniques by removing nitrogen and doping with boron. Through these synthesizing processes it is possible to reach concentrations well above 1000ppm (i.e., it is at such high boron concentrations where excellent electrical properties are expected). Moreover, radiation damage is another way to introduce boron into a diamond specimen. For almost fifty years, the primary mechanism for producing vacancies and interstitials has been radiation damage. Our understanding of diamond spectroscopy has been aided by the interaction of preexisting defects with vacancies and interstitials generated through radiation damage. In this study, I use radiation damage in controlled sequences to ascertain boron incorporation into the diamond lattice structure while limiting the point defects that are known to affect the perfect conduction of electrons through the diamond matrix.

2.2 Boron-doped diamonds (BDD)

It is theoretically anticipated that the electronic nature of heavily boron-doped diamond (BDD) materials without any electronic compensatory effects could become a perfect electric conductor with no resistance (i.e., a superconductor) at high temperatures, if the substitutional concentration is sufficiently high [63]. To date, superconductivity in a BDD has been demonstrated in the past twenty years in both single crystal and nanocrystalline diamond structures [20, 36]. Up to 10% of boron can be incorporated by chemical vapour deposition (CVD) growth in the (100) direction [29]. However, a large amount of hydrogen incorporated into the crystal compensates a large % of the boron, which lowers the transition critical temperature T_c to roughly $\sim$7 K. In high quality CVD grown single-crystal diamonds that are heavily boron-doped, signs of a much higher T_c values close to 25 K have recently been reported [64]. This corresponds to a carrier concentration of $\sim 3 \times 10^{21}$ cm^3 ($\approx$1.8 at.%). It's interesting to note that their calculations suggested that low % doping may produce a T_c of about 100 K if the incorporated boron could be periodically substitutionally placed or the degree of disorder is substantially decreased.

2.2.1 In-growth boron doping

Interest in electrically conductive diamond structures was heightened in 2004 when Ekimov et al. [16], reported the first evidence of superconductivity in BDD with a T_c of 4 K, synthesized at HPHT conditions. They synthesized the BDD by reacting B_4C and graphitic carbon at 8–9 GPa and 2500–2800 K for $\sim$ 5 s. This resulted in metallic polycrystalline diamond aggregates of $\sim$ 1.5 mm in size sandwiched between the graphitic carbon and B_4C materials. Almost immediately after the successful fabrication of the first superconducting diamond, Takano et al. [17], reported a superconducting diamond thin film with a T_c of 7.4 K, synthesized via the MPCVD method. The feat was achieved through a careful process of pre-treating a silicon substrate using ultrasonic waves of diamond powder, followed by the deposition of a dilute gas mixture of methane (1% concentration in hydrogen with a B/C ratio of 2500 ppm) and trimethylboron in hydrogen. For the deposition conditions, a chamber pressure of $\sim$ 6.7 kPa was set at $\sim$1080–1180 K substrate temperature with a microwave power of 500 W for 9 h. Currently, many scientists have successfully replicated to some extent the results by Ekimov et al. [16] and Takano et al. [17], with a consensus regarding the boron concentration that is tuned well over $\sim 3 \times 10^{20}$ cm^3, which is the onset of a superconducting state coinciding perfectly with the "**metal-insulator-transition (MIT)**" phase. In terms of band theory, this is known as the Mott insulating impurity band which will be detailed explicitly in the succeeding sections.

A large T_c ranging between 140–160 K for BDD was initially estimated theoretically, by only taking into account the atomic mass of light host atoms and the strong covalent bonds within the diamond structure [65]. However, complimentary predictions later considered also the lattice disorder and the local variations of boron concentrations with local electron-phonon coupling, resulting in a $T_c \approx$ 55–80 K for 10–20% of boron that is electrically active [63]. Additional estimations by Cohen [66], suggested a possible T_c of 290 K for an ideal case with strong electron-phonon coupling strengths within a phonon-mediated superconducting diamond. Apart from lattice disorder, the main constraint on T_c for superconducting diamond is the solubility limit imposed by boron doping methods, i.e., $\sim$ 90% of boron ions incorporated in diamond

are not substitutional p-type acceptors and hence are electrically inactive [67, 68]. Now, since the HPHT doping method is highly limited by a $\sim 2.8\%$ solubility of boron in diamond, it has been suggested in literature that non-equilibrium fabrication processes such as **CVD** and **ion implantation** should be pursued in order to address this predicament [30, 63]. Although structural disorder is inevitable due to the introduction of foreign atoms in diamond using the aforementioned techniques, the structural integrity of diamond (even of specimens that have transitioned into a superconducting state) can be recovered via annealing processes [30]. However, ion implantation offers much better control of the concentration and distribution of dopants. Experimental techniques such as infrared (IR) absorption spectroscopy [67], photo-electron intensity angular distribution (PIAD) circular dichroism [69], and Nuclear Magnetic Resonance (NMR) [70], have been used to investigate the incorporation of p-type dopants within the diamond lattice.

2.3 Properties of boron-doped diamonds

Despite the superconductive nature discovered in semiconducting diamond, it is expedient to extensively study the properties that are demonstrated due boron doping into the diamond matrix. Why? because diamond that has been doped with boron finds itself as a primary candidate for future electrical devices due to the apparent unique mechanical and thermal properties that have been well-documented over the years. Lightly boron-doped diamonds are charcterized as p-type semiconductor where the extrinsic boron atoms displace and/or substitute the host carbon atoms in the diamond lattice. When boron content exceeds a critical boron concentration ($n_c \approx 2 \times 10^{20}\,\mathrm{atom/cm^3}$), a metallic-like conduction is observed. Furthermore, certain heavily boron-doped diamonds above n_c exhibit superconducting properties. Evidently, the incorporation of boron into the diamond matrix is not unambiguously established within the three phases. Now, when the boron concentration is low ($\sim$0.1 at.%), it results in a strong hybridization between (B)-2p and (C)-2p states because of the occupation of substitutional sites rather than interstitial sites in diamonds [20]. Since boron is able to readily integrate itself into the diamond lattice even at a determinable concentration range leading up to phase transitions [38], while maintaining the diamond structure with a boron activation energy of 0.37 eV; it is worth considering the properties of boron doping transitions that have been studied by many capable scientists thus far.

2.3.1 Optical nature of boron-doped diamonds

Due to the high cost of real gem stones, there is no shortage of optical spectroscopic data on diamond [71], but comparatively little optical research has been done on the darker, frequently brownish, extensively boron-doped diamond. For instance, the diamond substrates that develops a dark metallic opaque appearance due to heavy doping, cannot be adequately processed via the infrared transmission spectroscopy technique to estimate the boron content; i.e., the commonly utilized method of determining the boron content in polycrystalline or homoepitaxial doped diamond layers [72]. Consequently, these measurements have only been possible using extremely thin homepitaxial films [73]. Similar to this, the optical emission spectra obtained by cathodoluminescence on heavily boron-doped (p^{++}) diamond layers are significantly weak in intensity and provide little information than those obtained on p-type lightly boron-doped layers (p^{+}), especially in the visible range. The dominant

features, as depicted in Fig. 2.7 (a), are a peak at $4.1 \times 10^4\,\mathrm{cm}^{-1}(5.02\,\mathrm{eV})$ that extends to a low energy peak at $3.92 \times 10^4\,\mathrm{cm}^{-1}(4.86\,\mathrm{eV})$, and a much weaker and broader peak stretching from $3.31 \times 10^4\,\mathrm{cm}^{-1}(4.1\,\mathrm{eV})$ to $3.71 \times 10^4\,\mathrm{cm}^{-1}(4.6\,\mathrm{eV})$, even at ambient temperature. The $\sim 5.02\,\mathrm{eV}$ peak is typically characterized as a broadened and red shifted excitonic recombination that is boron-bound, which has also been detected in polycrystalline, and epilayers with (001) and (111) orientations [74–76]. The latter peak is likely due to boron-related centers [77]. The extinction coefficient spectrum (refer to Figure 2.7(a)) produced at $\sim 300\,\mathrm{K}$ using ellipsometry on a p^{++} epilayer exhibits a peak at $\sim 4.86\,\mathrm{eV}$ [78]. Additionally, the lines at $3.86 \times 10^4\,\mathrm{cm}^{-1}(\sim 4.78\,\mathrm{eV})$, which are linked to the 2BD defect and are thought to be caused by interstitial boron, are not visible [28].

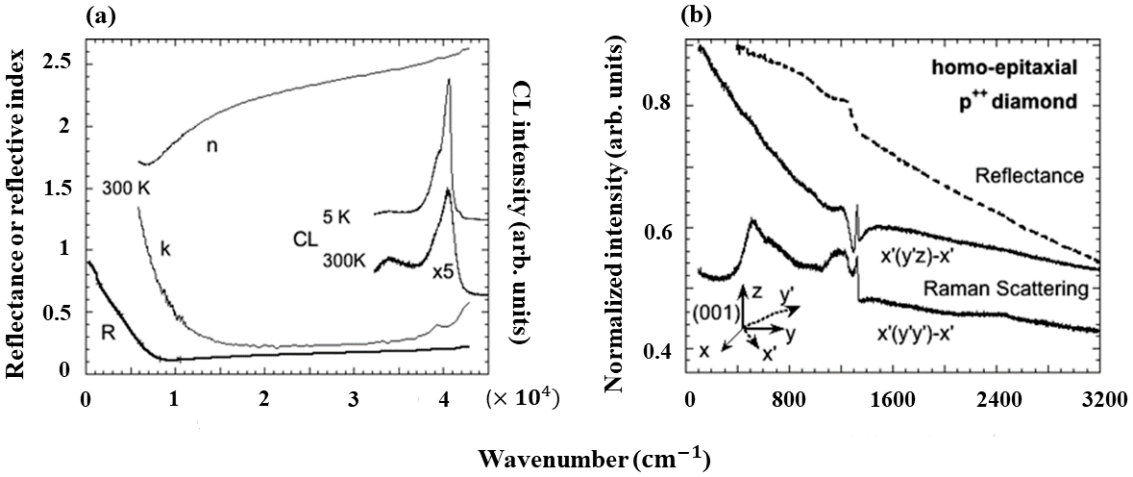

Figure 2.7: **Optical response of heavily BDD.** (a) The reflectance (R) analysis and the cathodoluminescence (CL) spectra of a BDD epilayer with a (100) orientation measured at 5 K and 300 K. k and n represent the imaginary and real components of the optical refractive index. (b) A diamond epilayer that is doped with $10^{21}\,\mathrm{B/cm}^{-3}$, oriented at (100) and with (011)-oriented polarized Raman spectra (from an edge view) and IR reflectance. The excitation wavelength for the Raman spectra was 633 nm [19].

Furthermore, spectroscopic data obtained from reflectance or ellipsometry techniques have been documented for highly doped epilayers with orientations (001) and (111) [73, 78, 79]. Figure 2.7 (a), shows the results that demonstrate the reflecting edge of free carriers in the mid-infrared band, indicating the presence of a plasma with low density. The reflectivity of a Drude metal accurately reproduces this line shape, with plasmon frequencies typically ranging between $1 \times 10^4\,\mathrm{cm}^{-1} - 2 \times 10^4\,\mathrm{cm}^{-1}$ with damping factors ranging between $3000\,\mathrm{cm}^{-1} - 8000\,\mathrm{cm}^{-1}$ [73, 78]. The optical conductivities at zero frequency have been compared to the electrical direct current conductivities. A polished polycrystalline sample has been reported to exhibit an unusual reflectivity spectrum, deviating from the expected behavior [80]. The plasmon edge is significantly affected by supplementary contributions within the spectral range between $450\,\mathrm{cm}^{-1}$ – $1350\,\mathrm{cm}^{-1}$. These contributions correspond to one-phonon energies in diamond, as previously mentioned in publications and illustrated in Fig. 2.7 (b). The current interpretation of these spectrum deviations involves a semi-quantitative analysis that assumes a scattering rate dependent on frequency. This scattering rate is attributed to a spectral function resulting from

the coupling between electrons and phonons, which exhibits two peaks close to the $600\,\mathrm{cm}^{-1}$ and $1200\,\mathrm{cm}^{-1}$ wavenumbers [79].

Figure 2.7 (b), presents additional support for the existence of a free hole gas due to the boron dopants (i.e., a model that describes the behavior of free charge carriers in a solid-state system) and a significant electron and phonon coupling. The Raman spectrum of a boron-doped diamond surface with a (110) orientation reveals a scattering tail attributed to the free holes, likely due to low energy intra-impurity band hole scattering [78]. Additionally, the spectrum exhibits a complex Fano-distorted line-shape, suggesting an interference between the continuum of the free hole carriers and certain discrete vibrational levels involving local boron-related modes (i.e., Raman modes $\sim 500\,\mathrm{cm}^{-1}$ and $\sim 1200\,\mathrm{cm}^{-1}$) [78]. Figure 2.7 (b), clearly illustrates that the parallel polarized Raman spectrum exhibits distinct characteristics. It shows a broad range of excitations, beginning with clearly defined peaks at approximately $500\,\mathrm{cm}^{-1}$ and around $1200\,\mathrm{cm}^{-1}$. These peaks are typically associated with off-center optical modes and Si-B resonant modes. Additionally, there is a narrow line at approximately $1320\,\mathrm{cm}^{-1}$, which is attributed to the zone-center phonons (ZCPs) at the $\Gamma-$point shifting due to strain; likely affecting the degeneracy of the phonon modes. Recent indications suggest that the most likely explanation for the parallel-polarized Raman peak at $500\,\mathrm{cm}^{-1}$ is the A_{1g} vibrational mode of boron–boron dimers [81, 82]. This is supported by the observation that the frequency of this peak remains unchanged regardless of an applied magnetic field or carbon isotopic substitution (i.e., $^{12}\mathrm{C}\rightarrow^{13}\mathrm{C}$). Moreover, the aforementioned features are greatly influenced by the wavelngth excitation and the polarization geometry (refer to Fig. 2.7 (b)) [82, 83]. Hence, according to Bustarret [19], attempting to interpret the lineshape and compare the many room temperature (RT) Raman spectra of heavily-doped diamond published since 1993 would be futile.

Fano line shape

BDD has been verified as an illustration of Mott's transition metal when the free carrier concentration exceeds the threshold value of $n_c = 2\text{–}3 \times 10^{20}\,\mathrm{cm}^{-3}$ (i.e., the critical boron concentration) [19, 22, 84]. The emergence of metallic conductivity leading up to superconducting properties in BDD can be observed through the shifting of the zone-center phonon (ZCP) Raman line [85]. Interference may arise in the Raman signal of BDD due to the interaction between the ZCPs and the electronic transition continuum (i.e., electron transitions between the energy bands and the impurity states introduced into the forbidden energy gap due to boron doping). Now, the phenomenon being referred to is widely known as the Fano effect as observed in Fig. 2.8 [86], which has also been observed in silicon that has been extensively doped [87]. The Fano resonance peak is commonly utilized for calibrating the boron content [16]. However, the exact source of the Fano line remains a subject of debate in BDD [19, 33]. To enhance comprehension of the aforementioned Raman modes, a thorough characterization is required. Through experimental investigations, a peculiar correlation between the wavelength and the Raman scattering amplitude of the decoupled phonon (T_p) was discovered. Furthermore, the energy of the excitation has an impact on the asymmetry of the lineshape [33, 34].

Mortet et al. [33], reported very interesting behavior of a BDD as a function of excitation wavelength and boron concentration. Figure 2.8(a), displays the Raman spectra of epitaxial diamond layers that were deposited with varying B/C ratios

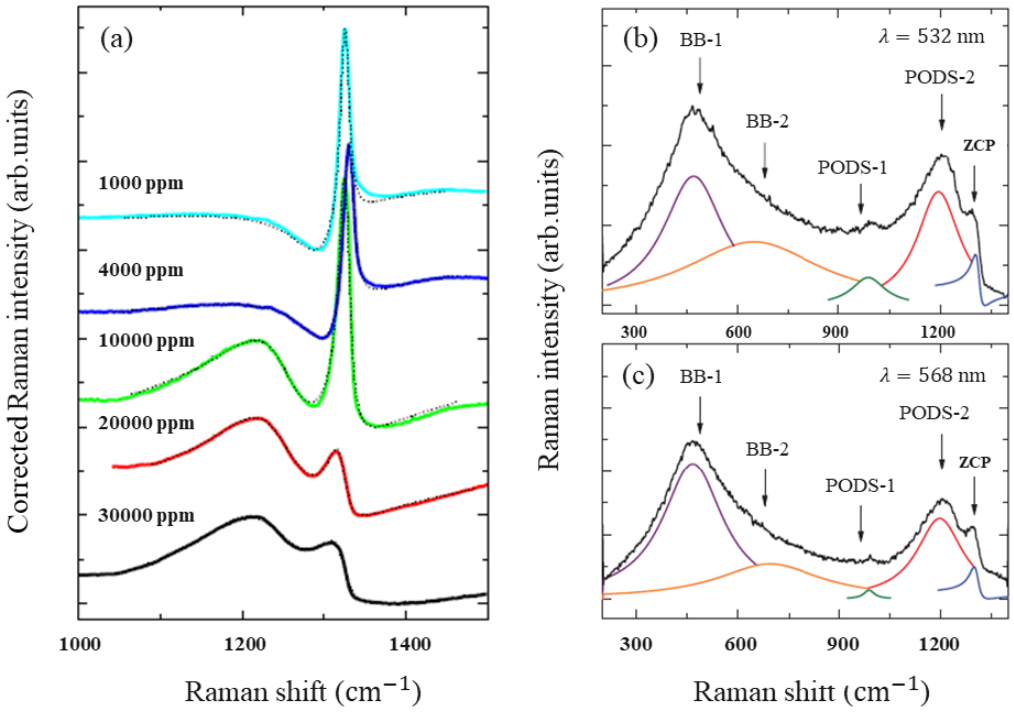

Figure 2.8: **Raman spectra of BBD.** (a) A double Fano fit for boron-doped diamond with prominent features increasing with boron concentration [33]. (b)–(c) Evidence of a Fano line shape in superconducting diamond induced by wavelengths 532 nm and 568 nm. The peaks BB–1 and BB-2 represents the boron dimers (500 cm^{-1} ∼ 660 nm) while PDoS–1 and PDoS–2 represents the phonon density of states maxima (1000 nm ∼ 1200 cm^{-1}) and ZCP is the zone center phonon (∼ 1331 cm^{-1}) [34].

and excited by a 488 nm laser. In addition to relatively similar background features, all spectra display a broad and asymmetrical band around 1200 cm^{-1}, which is associated with the maximum of the PDoS (Phonon Density of States) together with a displaced ZCP line below 1332.5 cm^{-1}. These findings are consistent with previous reports in literature [16, 19, 34, 85]. The spectrum illustrates the phenomenon of the PDoS and the ZCP lines shifting towards the red end of the spectrum, accompanied by a decrease in the relative strength of ZCP as the B/C ratio increases.

Szirmai et al. [34], also demonstrated similar attributes in a superconducting BDD structure (with a $n_B \approx 1.8 \times 10^{21}$ cm^{-3}) where the ZCP is significantly red-shifted with a notable asymmetric behavior. The Raman band at 1000 cm^{-1} (PDoS-1) is derived from the peak of the phonon density of states of diamond. The distribution of boron atoms in BDD is most likely inhomogeneous, resulting in the violation of the Raman wave vector conservation principle, producing comparable Raman spectral features for BDD and *amorphous* diamond.,i.e., the boron induced point defects in the substrate enable forbidden states to become permissible [88, 89]. The Raman spectrum at 1200 cm^{-1} exhibits two distinct features: a Lorentzian-like component at 1210 cm^{-1} and another component with the asymmetric line shape centered at 1300 cm^{-1}. The 1210 cm^{-1} (PDoS-2) mode is attributed to the existence of crystallographic faults. The mode in question arises due to boron–carbon complexes. Evidently, the peak in question demonstrates a Fano line shape as demonstrated [82]. The zone center phonon (ZCP) of diamond also known as the zero phonon line (ZPL), has a frequency of ∼ 1332 cm^{-1} and a linewidth of ∼ 1.2 cm^{-1}, is displaced

to a range between 1300–1315 cm^{-1} in BDD. Additionally, it exhibits a Fano line shape related to the existence of free charge carriers [83]. The Raman spectra in Fig. 2.8, are depicted with fitted Fano line shapes.

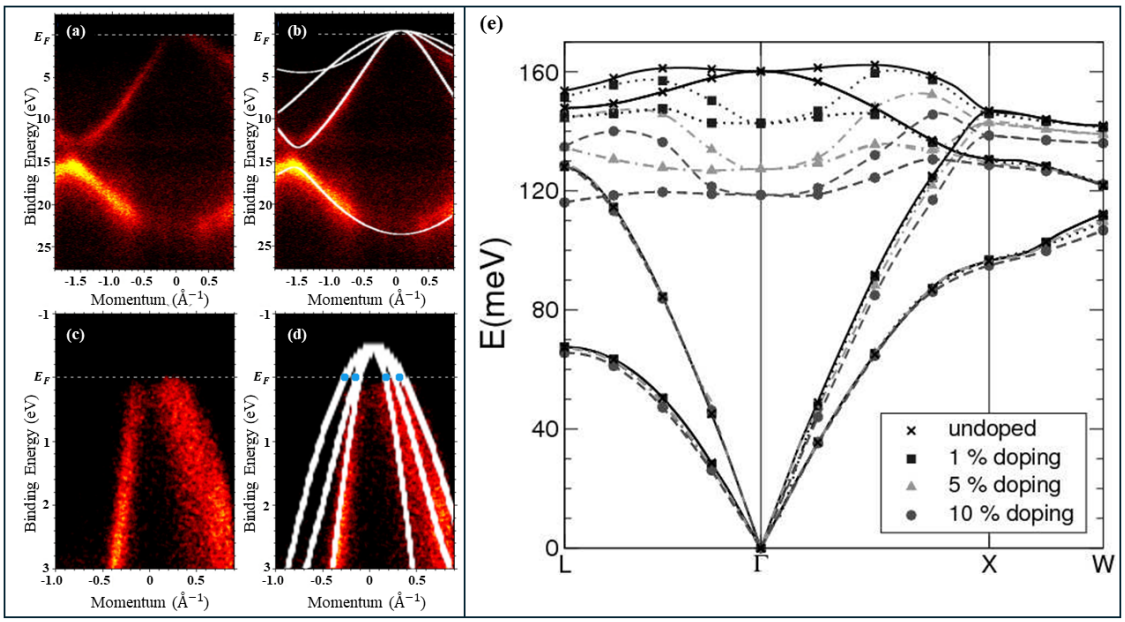

Figure 2.9: **Electronic and Phonon dispersion of BBD.** (a)–(d) The electronic dispersion of BDD by soft X-ray ARPES compared to calculated VB dispersions (solid white lines). The bands clearly disperse across the top of the VB from the reduction of intensity along E_F at the $\Gamma-$point [64]. (e) The Phonon dispersion of a pristine diamond compared with BDDs with different boron concentrations. The frequency of the ZCPs clearly softens with an increase in boron dopants. [90].

It is evident that boron doping affects the ZCP line of diamond which has significant implications to the electronic band structure of BDDs. As mentioned before the introduction of boron into diamond results in impurity levels near the band edges with activation energies of $\sim 0.37\,\mathrm{eV}$; thereby affecting the diamond material's screening properties such as electrical conductivity, charge carrier and dielectric properties of diamond [19, 34]. Such changes certainly have an effect on the frequency of the ZCPs due to the coupling of the electronic and vibrational degrees of freedom. When the boron concentration is increased the ZCP line is further red-shifted which coincides with the boron-induced impurity levels evolving into an impurity band (detailed discussion in the succeeding sections). Figure 2.9 (a)–(d), shows the modification of the electronic structure where the optical phonon modes cross the E_F at the $\Gamma-$point [64]. Moreover, the reduced intensity near the $\Gamma-$point is indicative of holes in the VB. Consequently, according to the BCS model Cooper pairs in the VB form due to the attractive interaction mediated by the quantized lattice vibrations leading to superconducting properties in diamond. The collective behavior of the Cooper pairs is analogous to Bose-Einstein Condensate (BEC) particles associated with superfluidity at low temperatures; however, these are known to be different concepts with varying mechanisms. Furthermore, the red-shifting of the zone center phonon line in BDD implies the frequency of the optical ZCPs softens and broadens due to lattice distortions and the impurity states induced by boron doping (see Fig. 2.9 (b)) [90]. This validates the electron-phonon

interactions in BDDs, i.e., the interaction of conduction electrons and the phonon modes reduces the energy of optical phonon modes [19, 90, 91].

Now, the Fano line shape arises from the quantum interference between the ZCP and the electronic transition continuum at the same energy level. The calculation can be determined as follows,

$$I(\omega) \propto \frac{[q + (\frac{\omega-\Omega_0}{\Gamma})]^2}{1 + (\frac{\omega-\Omega_0}{\Gamma})^2}, \tag{2.3}$$

where the intensity of the Raman signal is represented by $I(\omega)$. The real and imaginary contribution of the self-energy in BDD, denoted as $\hbar\Omega_0$ and $\hbar\Gamma$ respectively, are the result of the coupling between a discrete phonon transition and a continuum of states,

$$\hbar\Omega = \pi V_m^2 \rho(E) + \hbar\gamma \tag{2.4}$$

and

$$\hbar\Omega_0 = \hbar\omega_0 - V_m^2 R(E) \tag{2.5}$$

where $\rho(E)$ represents the density of states of the quasi-continuum. The variables $\hbar\omega_0$ and $\hbar\gamma$ correspond to the real and imaginary parts, respectively, of the self-energy of the phonon in a pristine diamond material. V_m is the matrix element that describes the connection between the two states. Meanwhile $\pi^{-1}R(E)$ represents the Hilbert transform of V.

The asymmetry parameter q_a is expressed as follows,

$$q_a = \frac{V_m \frac{T_p}{T_e} + V_m^2 R(E)}{\pi V_m^2 \rho(E)}, \tag{2.6}$$

where T_p and T_e are the phonon and the electronic continuum Raman scattering amplitudes, respectively [34, 87]. When the electronic continuum vanishes and q_a approaches infinity, the Fano formula simplifies to the conventional Lorentzian curve. The variation in the asymmetry parameter of both the PDoS maximum and the Fano-shaped degenerate ZCP line may be adequately described by the relationships between their predicted scattering cross-section and the concentration of boron atoms, as well as the excitation wavelength. A greater Ω_0 resonant wavenumber confirms the lower doping level, as the red-shift is associated with the incorporation of boron [85]. Note that the amount of boron in the material does not directly determine the concentration of carriers, since boron dimers do not contribute to the concentration of free carriers [19].

Photophysical properties of a boron-implanted diamond

Figure 2.10 (a), depicts the Photoluminescence (PL) of a boron implanted diamond sample from a 532 nm laser excitation [92]. The spectra exhibit dominant emission features ascribed to nitrogen related defects referred to as nitrogen vacancy (NV) centers that exist in neutral and negative charge states (i.e., NV^0 and NV^-) [93–95]. The ZPLs of these charge states are centered at 575 nm and 637 nm for NV^0 and NV^-, respectively; and hold meaningful significance in quantum information processing (QIP) applications [95]. The photo-induced electronic transitions of these centers

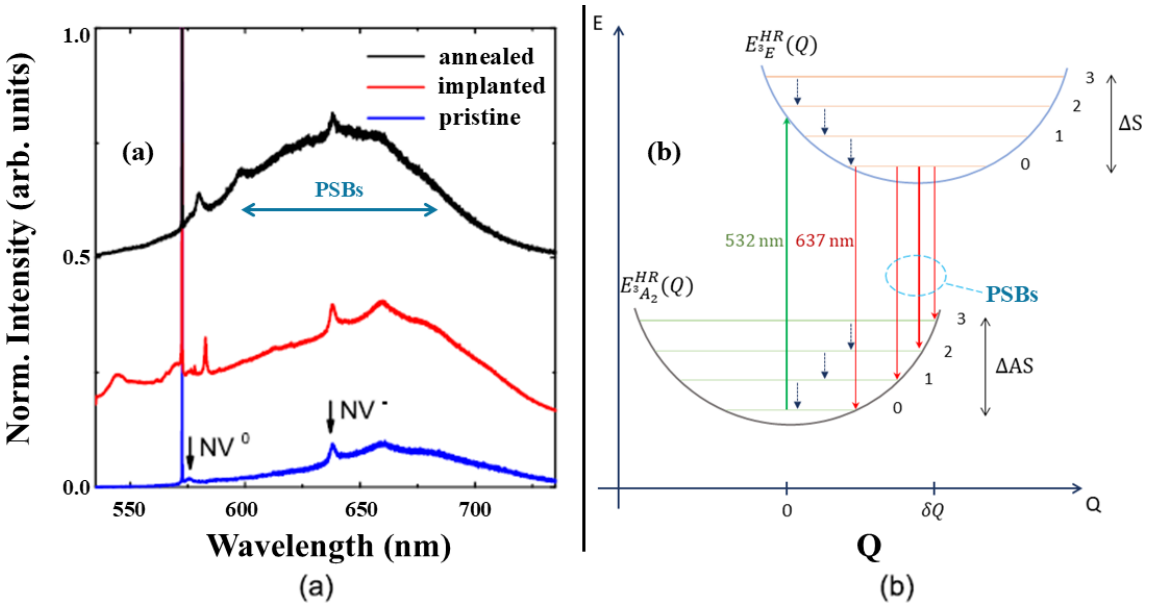

Figure 2.10: **Phololuminescence spectra of BDD with PSBs.** (a) The spectra displays the evolution of the diamond structure after boron implantation and annealing with PSBs around the NV centers NV^0 and NV^- [92]. (b) Schematic of the Frank-Condon principle with harmonic potentials describing the electronic energies (E) of the ground and excited states separated by the nuclear displacement coordinate Q [97].

couple with the vibrational modes of the diamond lattice which consequently results in phonon sides bands (PSBs) alongside the centers [95, 96].

The simplest form to approximate the vibrational structure of the NV center is detailed rather expertly using the Huang-Rhys [97]. This implies a quasi-continuum system of phonons representing a single vibrational mode within the diamond lattice, with coordinates corresponding to the nuclei displacement due to transitions within the electronic states of the NV center. By making use of the Born-Oppenheimer approximation, Fig. 2.10 (b), depicts the potential curves of the $^3A_2$ and ^3E electronic states of the NV^- center, δQ apart in the normal coordinate space. The potentials have different electronic energies (E) with vibrational levels ($n = 0, 1, 2, 3$) associated with the $^3A_2$ and ^3E states of the NV center. In this case, the Frank-Condon principle is also employed in order to account for the differences between the optical spectra of the electronic states. The Frank-Condon principle states that the highly probable transitions are at the same nuclear configuration, i.e., the vertical transitions depicted in Fig. 2.10. However, due to the overlap of the vibrational wave functions being non-zero where the probability is given by the Frank-Condon factors, other electronic transitions are also allowed with Stokes (ΔS) shifted excitation and anti-Stokes (ΔAS) shifted decay [97].

The vertical transitions implies an overlap between the two vibrational states, indicating a broader bandwidth as the excitation is most likely to be the PSBs (640 nm − 760 nm) than to the narrow ZPL (637 nm). The approximation of the potentials is described by the following quadratic function of the nuclear coordinates for the $^3A_2$ and ^3E states [98],

$$
\begin{aligned}
E^{HR}_{^3A_2} &= \frac{1}{2}m\omega^2Q^2, \\
E^{HR}_{^3E} &= E_{^3E} + \frac{1}{2}m\omega^2Q^2 + aQ + bQ^2, \\
&= E_{^3E} - E_R + (\frac{1}{2}m\omega^2 + b)(Q - \delta(Q))^2,
\end{aligned} \tag{2.7}
$$

where $E_{^3E}$ represents the electronic energy of the ^3E state at the nuclear equilibrium coordinate for the $^3A_2$ state ($Q = 0$), m is the mass of the mode, ω and $\sqrt{\omega^2 + b}$ are the frequency of the vibrational modes in the $^3A_2$ and ^3E states, respectively. The linear and quadratic electron-vibration coupling parameters to the ^3E state are represented by a and b, respectively. The equilibrium displacement of the ^3E state is given by $\delta Q = -a/(m\omega^2 + 2b)$, while its relaxation energy is given by $E_R = a^2/2(m\omega^2 + 2b)$. Mita [98], also expressed the probability integral for the optical transition for a single vibrational frequency as follows,

$$
\iint drdQ\phi^*_e(r)\chi^*_n(Q - Q_0)D\phi_g(r)\chi_0(Q), \tag{2.8}
$$

where D is the electric-dipole operator, while the wavefunction is the product of the nuclear and electric components for both states (e.g., $\psi(r, Q) = \phi_g(r)\chi_0(Q)$ for the ground state). The Franck-Condon principle approximates that the electronic coordinate is independednt of the vibrational coordinate, and hence Eq. 2.8, can be factorized,

$$
\int dr\phi^*_e(r)D\phi_g(r) \int dQ\chi^*_n(Q - Q_0)\chi_0(Q) \tag{2.9}
$$

The Franck-Condon factors are defined as,

$$
M_{0n} = \int dQ\chi^*_n(Q - Q_0)\chi_0(Q) \tag{2.10}
$$

for the harmonic states,

$$
|M_0n|^2 = \frac{e^{-S}S^n}{n!}, \tag{2.11}
$$

where $S = a^2/2m\hbar\omega^3 \equiv E_R/\hbar\omega$, is the Huang-Rhys factor measured from the fraction of the optical transition which lies in the ZPL,

$$
S = \ln\Big(\sum_{n=0}^{\infty}|M_{0n}|^2/|M_{00}|^2\Big) \tag{2.12}
$$

The model also accounts for the similarity between the absorption and luminescence transitions whenever the respective frequencies are equal ($\omega = \Omega$), resulting in the mirror images of the bands.

The treatment of Huang-Rhys model for multiple modes N is also given [25]. The harmonic nuclear potentials of the electronic states now takes the form,

$$E^{HR}_{^3A_2} = \frac{1}{2}\sum_{i=1}^{N} m_i\omega_i^2 Q_i^2,$$

$$E^{HR}_{^3E} = E_{^3E} + \frac{1}{2}m_i\omega_i^2 Q_i^2 + \sum_{i=1}^{2} a_i Q_i,$$

$$= E_{^3E} + \frac{1}{2}m_i\omega_i^2 (Q_i + a_i/(m_i\omega_i^2))^2 - \frac{1}{2}\sum_{i=1}^{N} a_i/(m_i\omega_i^2), \tag{2.13}$$

The Huang-Rhys factor is now defined as,

$$S = \sum_{i=1}^{N} S_i \text{ where } S_i = \frac{a_i^2}{2\hbar\omega_i^3 m_i} \tag{2.14}$$

Now, considering the one-phonon sideband, one vibrational mode is excited. For a single excited mode, the Franck-Condon factor is given by,

$$M^i_{01} = \int dQ_i \chi_1^{0*}(Q_1)\chi_1^0(Q_1 - Q_1^0)... \int dQ_i \chi_i^{0*}(Q_i)\chi_i^1(Q_i - Q_i^0)$$
$$\times ... \int dQ_N \chi_N^{0*}(Q_N)\chi_N^0(Q_N - Q_N^0), \tag{2.15}$$

$$|M^i_{01}|^2 = S_i \exp(-S_i)\prod_{j\neq i}\exp(-S_j) = S_i e^{-S} \tag{2.16}$$

Giving total relative intensity on the one-phonon band to be,

$$|M_{01}|^2 = \sum_i |M^i_{01}|^2 = Se^{-S} \tag{2.17}$$

and likewise for the n-phonon band, the total relative intensity is ,

$$|M_{0n}|^2 = \frac{S^n e^{-S}}{n!} \tag{2.18}$$

If the independent spectral shape of one-phonon band is known, the function for the spectral shape of the n-phonon band at frequency v can be determined as follows,

$$I_n(v) = \int_0^{\omega_m} dx I_1(x) I_{n-1}(v - x), \tag{2.19}$$

where ω_m is the frequency of the vibrational modes within the crystal defect, I_1 and I_{n-1} are the spectral form for the one-phonon band and the $(n-1)$-phonon band, respectively. The absorption frequency of $(n-1)$ is given by $(v-x)$. The shape of the one-phonon band for the NV center was determined by Stoneham [97], and it peaked $\sim 65\,\text{meV}$.

2.3.2 Lattice effects due to boron

Due to a larger atomic radius of boron (i.e., $r_B = 0.088\,\text{nm} > r_C = 0.077\,\text{nm}$), the lattice parameter of diamond is expected to expand when substitutional boron is introduced. It has been observed that this follows the linear interpolation described by Vegard's law, for boron content below 0.2 at.% in CVD epilayers or 1.5 at.% in HPHT bulk diamond [78, 99, 100]. The expansion in the homoepitaxial films is greatly restricted due to irregular growth due to compressive biaxial stress. The boron related strain along direction of growth can be easily observed in double crystal X-ray rocking and theta-2 theta Bragg reflection curves [101].

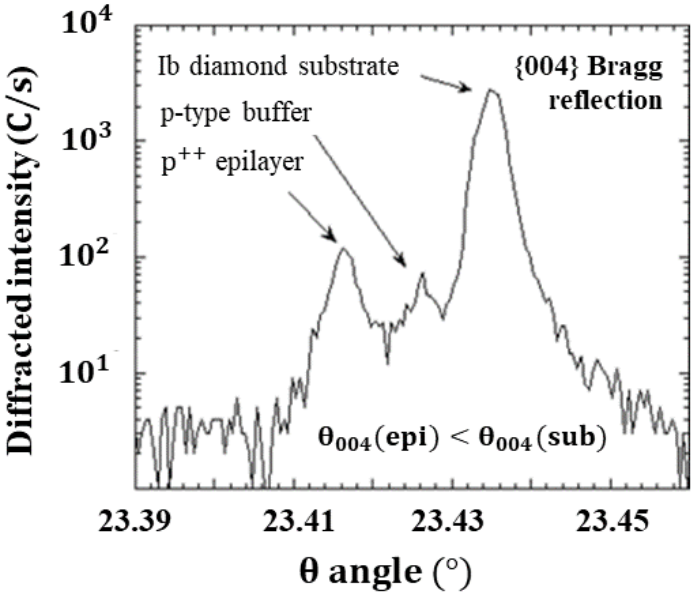

Figure 2.11: **Diffraction spectra of BDD.** The diffraction pattern displays the responses of an Ib substrate, lightly doped p-type buffer layer, and a highly boron doped (p^{++}) epilayer in a (100)-oriented diamond epilayer that is 3 µm–thick and doped with about $10^{21}\,\text{B/cm}^{-3}$ [19].

Figures 2.11–2.12, displays a standard data sets acquired from two homoepitaxial films aligned along the (100) direction. There is a similarity between lineshapes of the pristine type Ib substrate and the heavily doped epilayer which is shifted downwards by 400 units. Moreover, an unintended doped buffer layer can be observed at intermediate angles if the heavily doped epilayer is sufficiently thin. However, the distribution of the strain on the aforementioned epilayer is also comparable to that of the type Ib diamond substrate if it is a very thick film. The similarities are demonstrated by the intensity contours shown in Fig. 2.12, which depict the relationship between rocking angle θ and the diffraction angle θ–2θ.

Beyond those threshold concentrations, the degree of expansion is not as considerable, which contradicts the results of previous studies that had greatly overestimated the amount of boron present [78, 99, 100]. The reduced expansion rate can be related to the presence of holes, the negative structural distortion potentials at the top of the VB and the presence of boron substitutional pairs. Furthermore, temperature-dependent X-ray diffraction techniques confirm the thermal expansion coefficient of extensively BDD to be 2 to 4 times higher than that reported in pristine or lightly boron-doped diamond crystals [100, 102].

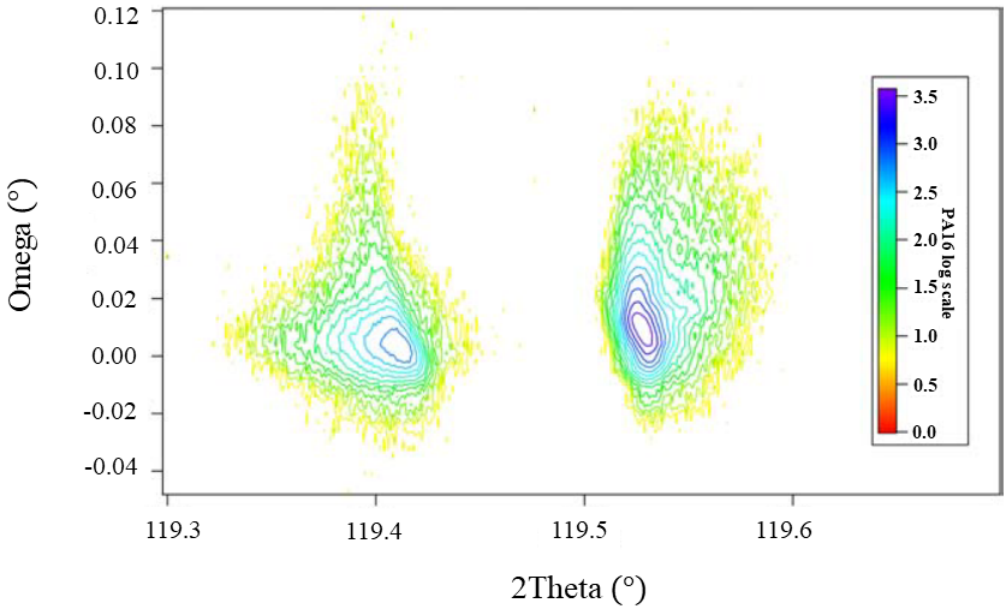

Figure 2.12: **Iso–intensity contour map.** Iso-intensity contours surrounding a 400 diffraction peak of heavily BDD epilayer that is 3 µm–thick, (100)-oriented. The relationship is between scanning the omega angle against the θ–2θ scanning direction. Utilizing a double crystal, the stimulating Cu $K_{\alpha 1}$ line was chosen [19].

Table 2.4: The lattice expansions of (111)– and (100)–oriented diamond films. They are measured parallel and perpendicular to the film [20].

	Expansion of the lattice parameter				
Sample	a: (111)	b: (111)	c: (111)	d: (100)	e: (100)
T_c^{zero}(K)	7.4	4.6	2.6	4.4	3.0
Perpendicular expansion (%)	0.48	0.44	0.44	0.51	0.46
In–plane expansion (%)	0.02	0.02	0.02	0.55	0.57

Moreover, as demonstrated in Fig. 1.5, thin films with (111) crystal orientation displayed elevated superconducting transition temperatures compared to (100) films, even when the boron content is kept constant (**NB**, the critical temperature T_c associated with each film increases boron concentrations). Conversely, the superconducting properties of (100) films were considerably diminished. Several potential factors, including the distortion of the crystal lattices or/and the boron content, have been proposed as reasons [29]. When boron is added as a dopant, the direction of growth of the crystal lattice varies between (111) and (100) orientations. The expansion rates of diamond crystal lattices that are parallel and perpendicular to a specific thin film are presented in Tab. 2.4. For the (111) films, the crystal lattices exhibit expansion exclusively in the direction perpendicular to the films, with no expansion detected within the plane. This emphasizes the presence of a distorted crystal lattice constant. Contrarily, the (100) crystal lattices expands isotropically in

all directions, both within the plane and perpendicular to it. The variations of the lattice distortions are hypothesized to cause the alterations in the density of states, potentially leading to distinct superconducting characteristics [29].

Temperature-dependent lattice expansion

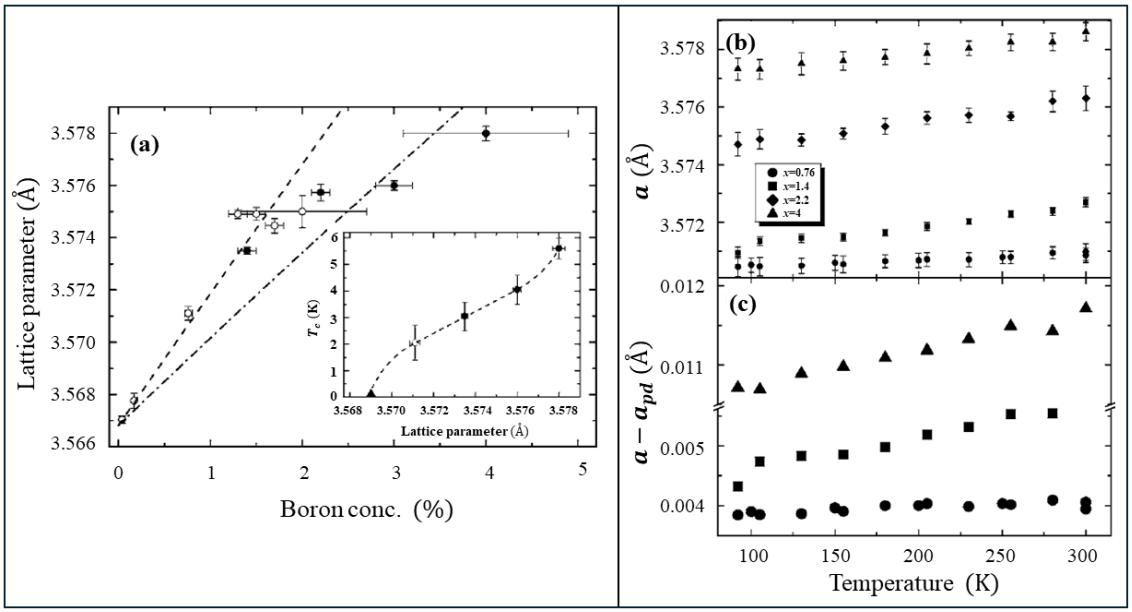

Figure 2.13: **BDD lattice parameter–a(Å).** (a) A linear relationship between the boron concentration and the lattice parameter. The insert demonstrates the dependency of T_c on the lattice parameter. (b) The temperature–dependent relation between the lattice parameter and boron concentrations. (c) Similar dependence to (b) after subtracting the lattice parameter of a relatively pure diamond–a_{pd}(T)≈3.566 Å [100].

Brazhkin et al. [100], demonstrated a linear dependence between the boron concentration and lattice parameter, with the lattice constant shifting by approximately 0.011 Å at its highest. They reported an unusually high increase in thermal expansion in superconducting BDD compared to pristine diamond samples. Additionally, they found a nearly linear relation between the lattice constant and T_c of a superconductor (please refer to Fig. 2.13).

Studies using X-ray inelastic scattering and the investigation of the influence of T_c on the doping level have shown progress in the experimental analysis of BDD samples that are superconducting [103, 104]. Information on the relationship between the concentration of boron and the lattice parameter, as well as the thermal expansion, is crucial to gaining a deeper understanding of how boron atoms are incorporated and the characteristics of heavily doped diamonds leading up to superconductivity. Specifically, studying the relationship between the boron concentration and affected lattice parameter can provide insights into how boron penetrates the diamond lattice. Additionally, analyzing thermal expansion results is valuable for understanding lattice dynamics. The difficulty of undergoing such investigations is primarily due to the challenge of independently measuring the boron concentration. Additionally, the effects measured are of relatively low magnitude.

The lattice parameter for undoped diamond is $\sim 3.5666 \pm 0.0001$ Å at low temperatures of 4.2 K, and $\sim 3.5669 \pm 0.0001$ Å at RT–300 K [102]. The resultant

low thermal expansion of diamond is a consequence of its high Debye temperature $\theta_D = 1860\,\mathrm{K}$ and a high bulk modulus $B \approx 445\,\mathrm{GPa}$ (refer to Tab. 2.1 for the physical properties of diamond). Other scientists have measured the lattice parameter of BDD at RT with slight variations in the results [100]. These differences can be attributed, in part, to the significant uncertainty in measuring the concentration of boron. From literature, an increase of 0.1% in the lattice parameter for heavily BDD ($n_\mathrm{B} \approx 10^{21}\,\mathrm{atom/cm^3}$) has been reported. Initially, a single attempt had been undertaken to study the thermal expansion of BDD with $n_\mathrm{B} \approx 10^{19}\,\mathrm{atom/cm^3}$ (i.e., a few years before the discovery of superconductivity in BBD). According Saotome et al. [102], diamonds with the doping level mentioned above, similarly for undoped diamond, the lattice parameter increases proportionally to T^4 in a temperature range that stretches between $4.2\,\mathrm{K} - 300\,\mathrm{K}$, consistent with the Debye model. He gave a mathematical description for the thermal expansion curves with lattice parameters consistent with non-doped diamond [105], beginning with the following expression,

$$a = \sum_{n=0}^{5} a_n T^n. \tag{2.20}$$

It is well established that in thermal equilibrium, a crystal such as diamond undergoes a reduction of its free energy F represented by the crystalline structure's internal energy U, temperature T, and entropy S using the following equation,

$$F = U - TS. \tag{2.21}$$

Because the frequency ω of lattice vibrations are dependent on the crystal's volume V due to the anharmonic nature of these vibrations, we get the following expression,

$$\frac{d\omega}{dV} = -\frac{\gamma\omega}{V}. \tag{2.22}$$

where γ is the Gruneisen parameter.

The elastic energy of the diamond crystal increases by $V_0(B/2)((V-V_0)/V_0)^2$ due to the change in volume ($\delta V = V - V_0$). The variable B represents the measurement of the resistance of the diamond material against compression, i.e., the bulk modulus. The reciprocal of B, denoted as $\kappa = 1/B$, represents the compressibility of the material. Therefore, the free energy increases as the elastic energy increases, while the vibrational frequencies decrease due to the expansion of the crystal. Equilibrium is achieved when the reduced vibrational energy is balanced out by the increasing elastic energy. From the Debye approximation, δV becomes [106, 107],

$$V - V_0 = \frac{9}{8}\kappa N_0 \gamma k_B \Theta_D + \frac{9\pi^4}{15}\kappa N_0 \gamma k_B \frac{T^4}{\Theta_D^3}, \tag{2.23}$$

where N_0 represents the quantity of atoms that make up a system, while k_B refers to the Boltzmann constant and Θ_D is the Debye temperature of diamond. At low temperatures the thermal expansion is expressed by the following,

$$\frac{\Delta a}{a_0} \equiv \frac{\Delta V}{3V_0} = \frac{3\pi^4 N_0 \kappa k_B}{15 V_0 \Theta_D^3}\gamma T^4. \tag{2.24}$$

Saotome et al. [102], reported that at sufficiently low temperatures, the dilation caused by the anharmonicity in vibrational motion is directly proportional to T^4. Brazhkin et al. [100], reported a slightly different relationship between temperature and the lattice parameters for BDD, with concentrations ranging from 0.76 to 4 at.%, is illustrated in Fig. 2.13 (a). All dependencies exhibit an almost linear relationship throughout their experimental temperature range of 90–300 K. They considered the uncertainties associated with the experimental data. The results deviated from the T^4–law which is often observed in pristine or slightly doped diamonds as reported by Saotome et al. [102].

In addition, the thermal expansion of pure diamond has a negligible effect on B concentrations of 1.4, 2.2, and 4 at. %. The effect of boron related and boron induced phonon modes is much more significant, as demonstrated in Figs. 2.13 (a) and (b) [100, 102]. However, for a boron concentration of x=0.76 at. %, the thermal expansion of BDD becomes comparable to that of pure diamond around RT. Hence, the thermal linear expansion coefficient of extensively doped diamonds is significantly greater than that of pristine diamonds. The thermal expansion coefficient is determined by analyzing the measured values of the lattice parameters where the linear thermal expansion coefficient is determined by,

$$\alpha = \frac{1}{a_{He}} \frac{da}{dT}, \tag{2.25}$$

where a_{He} represents the lattice parameter at helium temperature.

Results from Brazhkin et al. [100] and Saotome et al. [102] clearly demonstrate that heavily boron-doped diamonds exhibit an increased thermal expansion which seems to be linked to the presence of substitutional boron atoms and boron aggregates. The nearly constant thermal expansion coefficient observed within most practical data temperature range suggests a low effective Debye temperature of approximately $\sim 10^2$ K for the portion of the phonon spectrum impacted by boron. This indicates the presence of soft phonon modes associated with the incorporation of boron.

2.3.3 Metal-insulator transition

According to Fig. 2.14 (a), when the concentration of boron (n_{B}) is increased from $4 \times 10^{20}\,\mathrm{cm}^{-3}$ to approximately $5 \times 10^{20}\,\mathrm{cm}^{-3}$, the electronic properties of heavily boron-doped (p^{++}) layers with a (100)-orientation undergoes a significant change. The layers, which initially exhibit insulating behavior (meaning the resistivity increases infinitely as temperature approaches zero), transforms into a metallic (and possibly superconducting) state with a temperature-dependent resistivity that converges to a finite value at liquid helium temperatures. Considering the 10% margin of error in calibrations of SIMS systems, the experimental data align remarkably well with the zero–temperature model for disappearance of chemical potential (μ_c) for both metallic and insulating phases [101]. These calculations indicate a critical concentration of boron atoms, (n_{c}) of $\sim 5.2 \times 10^{20}\,\mathrm{cm}^{-3}$. The Drude technique, which considers the impact of temperature but not the impact of hopping mechanisms or weak localization, has been used to analyze these kind of systems [22, 81]. The results indicate a critical boron concentration range that is between $4 \times 10^{20}\,\mathrm{cm}^{-3} - 5 \times 10^{20}\,\mathrm{cm}^{-3}$.

According to Mott's findings, this transition occurs due to the overlapping of hydrogen-like states associated with boron, which have a Bohr radius represented by $a_{\mathrm{H}} = \epsilon a_0/m^*$. This overlap happens when the number of boron atoms n_{B} hits a critical

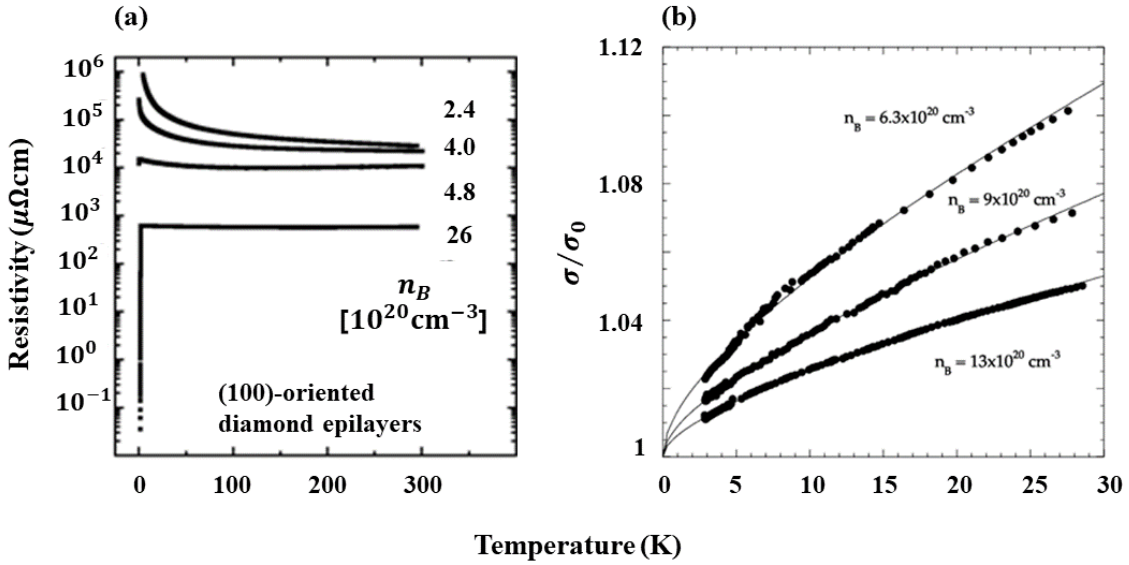

Figure 2.14: **Temperature–dependent resistivity and conductance of heavily BBD.** (a) SIMS measured boron concentrations (n_{B}) was used to assess the temperature dependent four–point resistivity of distinct diamond epilayers with (100)-orientation with respect to n_{B}. The MIT takes place between 4.0 and $4.8 \times 10^{20}\,\mathrm{cm}^{-3}$. (b) The conductivity of various (100)–oriented diamond epilayers on the metallic side of the MIT doped with the specified amounts of boron [22].

value n_{c}, which is observed to be 0.26 times the product of a_{H} and ${n_{\mathrm{c}}}^{1/3}$ in many different materials [108]. The Bohr radius a_{H} is calculated to be approximately 0.35 nm, given that the permittivity value ϵ is 5.7 for diamond and the VB effective mass m^* is 0.74 for the holes. This is reasonably consistent with values derived from the excited states of the acceptors. The current experimental and theoretical calculations for the carrier concentration n_{c} align with the experimental results obtained in polycrystalline p^{++} layers. In these layers, the value of n_{c} is less than $4.5 \times 10^{20}\,\mathrm{cm}^{-3}$ and falls between the range of $3.4{\times}10^{20}\,\mathrm{cm}^{-3}$ to $5.5{\times}10^{20}\,\mathrm{cm}^{-3}$ [27, 109]. Nevertheless, the measured values in ion-implanted diamond are significantly lower by a factor of 10 [38]. According to Bustarret [19], this discrepancy may be attributed to the reduced effectiveness of doping due to the incorporation of boron non-substitutionally.

When the concentration of boron falls below a certain critical level, the resistivity increases according to the equation,

$$\rho = \rho_0 \exp(T_0/T)^m \tag{2.26}$$

The exponent m is associated with the specific hopping transport mechanisms: where $m = 1$ when hopping occurs to the nearest neighbor site, $m = 1/4$ in the case of variable range hopping (VRH) with a reasonable constant density of states at the Fermi level (g_F), and $m = 1/2$ represents the lowering of g_F due to a Coulomb gap associated with disorder-induced localized states typically occurring at low temperatures, i.e., Efros-Shklovskii (ES) regime [84, 110]. The T_0 parameter is linked to the localization length $\xi_{loc} \approx a_H$ at regions exceeding the MIT transition [111, 112]. This occurs within a specific concentration range where the impurity- and the valence-bands are anticipated to form. Many $T_0 \sim 10^6\,\mathrm{K}$ values and transitions from VRH $\rightarrow$ ES regime, and subsequently to $m = 1$ at much lower temperatures,

have been documented for type IIb single crystals with a carrier concentration $n_{\mathrm{B}} \approx 2 \times 10^{19}\,\mathrm{cm}^{-3}$ [113]. As the MIT transition approaches, ξ_{loc} is predicted to rise, resulting in low T_0 values. This causes the VRH regime to dominate at low temperatures, as shown in Fig. 2.14 (a). In this figure, T_0 is approximately a few thousand Kelvin for a boron concentrations of $2.4 \times 10^{20}\,\mathrm{cm}^{-3}$ and several hundred Kelvin for a boron concentration of $4 \times 10^{20}\,\mathrm{cm}^{-3}$. The VRH regime extends down to 10 K [22].

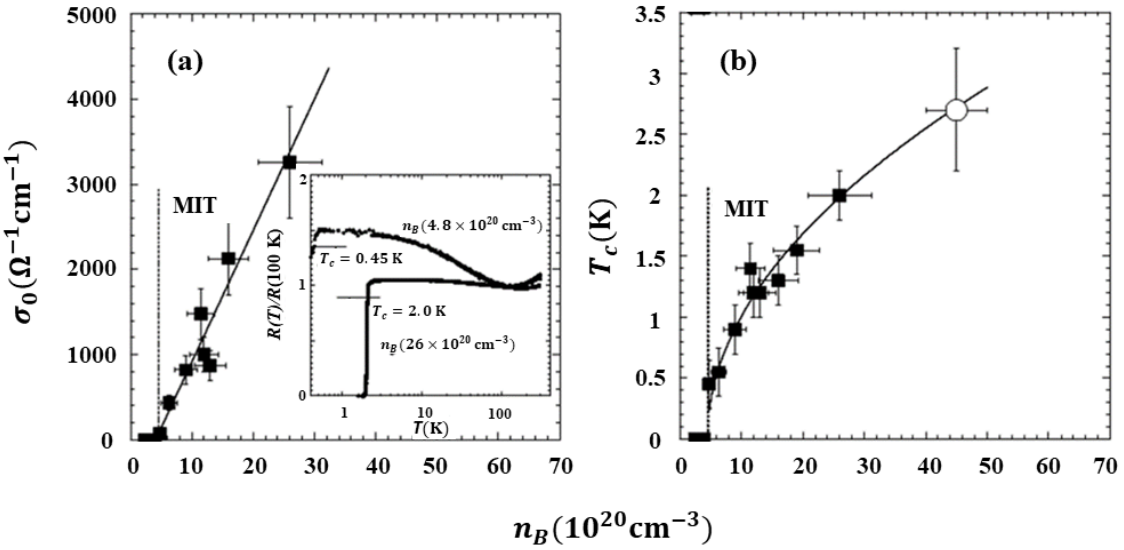

Figure 2.15: **Metal-insulator transition (MIT) of BDD.** (a) Conductivity measurements of BDD (100)–oriented epilayers as a function of concentration n_{B} ascertained from SIMS measurements. (b) T_c as a function of concentration n_{B} determined from SIMS measurements and resistivity curves [22].

When n_B exceeds n_c, the conductivity σ can be extended to a specific value σ_0 as the temperature approaches absolute zero, as shown in Fig. 2.14 (a). Indeed, as shown in the inset of Fig. 2.15 (a), when the concentration n_{B} exceeds $6 \times 10^{20}\,\mathrm{cm}^{-3}$ and the temperature is below a specific threshold where the inelastic mean free path approaches the elastic one, the resistivity exhibits a gradual increase as the temperature decreases [22]. Figure 2.14 (b), shows the measured temperature-dependent conductivity induced from the weak localization effects due electronic correlations at low temperatures. This is described by the following equation,

$$\sigma = \sigma_0 + AT^{1/2} + B_{e-ph}T, \tag{2.27}$$

within temperatures ranging from 3 K to 30 K. The parameters A and B_{e-ph} account for the weak localization effects for electron-phonon scattering [22]. Weak localization was found in both extensively boron-doped polycrystalline and nanocrystalline diamonds [109, 114]. Additionally, ion implanted samples have shown a change in conductivity relationship [38], namely,

$$\sigma = \sigma_0 + AT^{1/3} \tag{2.28}$$

The critical regime of a second order phase transition is typically characterized by two distinct exponents, ν and η [115]. The parameter ν expresses the relationship

between ξ_{loc} and n_{B} that drives the transition, according to the equation $\xi \sim 1/|n_{\mathrm{B}} - n_{\mathrm{c}}|^{\nu}$. On the other hand, the parameter η is associated to the energy E and length L of the system, following the equation $E \sim 1/L^{\eta}$. There is a suggestion by McMillan [115], that the value of η can vary between 1 and 3, depending on the significance of the electron localization, the many-body correlations, and the screening effects. There are indications that for heavily BDD diamond, η is approximately equal to 3, which aligns with the findings obtained from doped silicon [22, 38, 116]. Since σ is anticipated to change in proportion to $1/\xi$, it is predicted that σ_o is given by the following expression,

$$\sigma_0 = 0.1(e^2/\hbar)/\xi, \tag{2.29}$$

where a_{H}/ξ is equal to $(n_{\mathrm{B}}/n_{\mathrm{c}} - 1)^{\nu}$ [115]. As depicted by the solid line in Fig. 2.15 (a), σ_0 strictly adheres to the scaling theory prediction with $\nu = 1$, without the need for any additional adjustable parameter [22]. Unlike η, a distinct ν value around 1 has been calculated for all systems, regardless of the significance of the one electron and many body effects. Albeit, the previously stated value $\nu = 1.7$ for implanted diamond still requires an explanation [38].

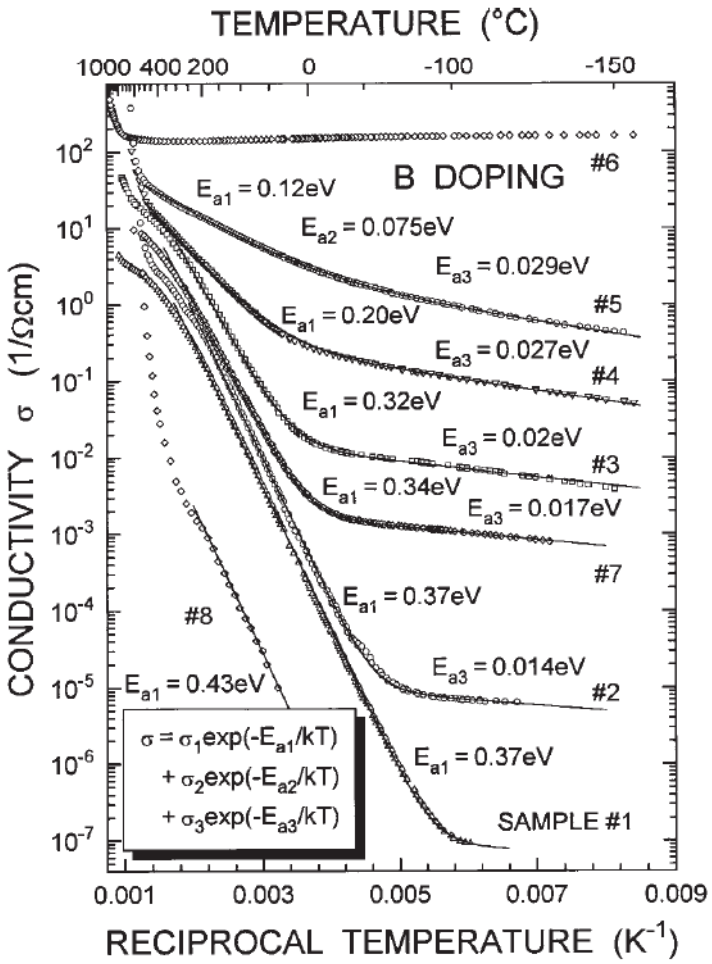

Figure 2.16: **Temperature-dependent conductivity of BDD.** Conductivity activation energies $E_{a1} \ldots E_{a3}$, of diamonds with varying boron concentrations increasing in an anticlockwise order from #8 → #6 [117].

Furthermore, the electrical conductivity of homoepitaxial CVD layers can be

characterized by the following equation that involves the sum of three Arrhenius terms,

$$\sigma = \sigma_1 . \exp(-E_{a1}/k_B T) + \sigma_2 . \exp(-E_{a2}/k_B T) + \sigma_3 . \exp(-E_{a3}/k_B T), \qquad (2.30)$$

where E_{a1}, E_{a2}, E_{a3} are the activation energies associated with Valence-Band (VB) conduction (1), excitation of the ionization process (2) and the hopping conduction (3) (see the Arrhenius plot in Fig. 2.16). k_B is the Boltzmann constant – $8.617\,333\,262 \times 10^{-5}\,\mathrm{eV/K}$ [21].

At low boron concentrations ($\sim 10^{19}\,\mathrm{cm}^{-3}$), the thermal activation energy E_{a1} corresponds to the ionization energy $E_A = 0.37\,\mathrm{eV}$ from optical experiments. For higher boron concentrations, E_{a1} decreases and eventually disappears at a boron concentration of $\sim 2 \times 10^{20}\,\mathrm{cm}^{-3}$ associated with Mott's transition. This dependency can be understood using the model previously developed by Pearson and Bardeen [118] for silicon,

$$E_A = 0.37\,\mathrm{eV} - \alpha_c . (n_A)^{1/3}, \qquad (2.31)$$

where $(n_A)^{1/3}$ represents the average distance of acceptors and α_c is the material dependent constant expressed by the following equation,

$$\begin{aligned} \alpha_c &= 1.65 \frac{q^2}{4\pi\epsilon_0\epsilon_r} (4\pi/3)^{1/3} \\ &\approx 6.7 \times 10^{-8}\,\mathrm{eV\,cm}. \end{aligned} \qquad (2.32)$$

In samples where boron concentrations approach the Mott transition, the dominant conduction mechanism is the rare impurity band conduction occurring within a temperature range typically extending from RT $\rightarrow$ 100°C (373 K) [117]. This behavior is represented by the second Arrhenius term. In this case, hole movement occurs via neutral acceptors (A^0) and is thermally activated by an energy $E_{a2}(75\,\mathrm{meV})$, which is associated with the ionization process: $A^0 + A^0 > A^+ + A^-$.

The third term E_{a3} in the sum describes hopping conduction between occupied and unoccupied acceptor sites. This type of conduction is generally observed at low temperatures in partially compensated silicon and germanium. However, it can also play a significant role in the wide-bandgap semiconductor diamond, particularly for boron, which is a relatively deep acceptor. In diamond samples where $[N_A - N_B] > 10^{19}\,\mathrm{cm}^{-3}$ [117], hopping conduction can become important even at room temperature. The temperature dependence of σ_3 led to the conclusion by Borst and Weis [117], that nearest neighbor hopping [119] is the dominant conduction mechanism, with thermally activated variable range hopping [120] playing a negligible role. Consequently, σ_3 is directly related to the overlap of impurity wave functions, which decay as $\exp(-\alpha . n_A^{-1/3})$, where α_l is the characteristic length of the overlapping ground state. Experimentally, this decay was observed with $\alpha_l = 1.086 \times a_H$. For E_{a3}, which depends on the degree of compensation, an increase with higher boron concentration has been observed, though its magnitude was about half of what theoretical models predict [21].

2.4 Electronic properties of BDD

It is now evident that within the metal-insulator-transition phase, it is possible to attain a superconducting state in diamond materials that are boron-doped during growth methods such as CVD and HPHT. Regrettably, the introduction of boron into the diamond matrix using ion implantation has not yielded many such positive results. Hence, it is crucial to elucidate, thus far, the electronic properties of a boron-embedded diamond matrix leading up to a superconducting state. This will aid to fully comprehend the electronic mechanism of the phase changes in BDD and eventually highlight the limitations of boron incorporation into the diamond lattice via current ion implantation methods.

2.4.1 Scanning tunneling spectroscopy

Following the discovery of superconductivity in diamond, scanning tunneling microscopy (STM) experiments showed an s-wave superconducting gap (Δ) with $2\Delta/k_BT_c \approx 3.5$ for a (100)-oriented sample and $2\Delta/k_BT_c \approx 3.7$ for a (111)-oriented sample, compatible to conventional BCS superconducting weak-coupling and strong-coupling mechanisms, respectively [121, 122]. At temperatures significantly lower than T_c, the spectra of dI/dV offers insight into the local density of states (DoS) of quasi-particles – $N(E, r)$, and therefore, the structure of the superconducting gap. In this context, E represents the energy of quasi-particles, whereas r denotes the position of the scanning tunneling microscope (STM) tip on the surface of the film, specifically the point being measured. An analysis of the spectrum is conducted by employing the BCS expression modified for the DoS in superconductors,

$$N(E, \Gamma_B) \propto \left| Re \frac{E - i\Gamma_B}{\sqrt{(E - i\Gamma_B)^2 - \Delta^2}} \right|, \tag{2.33}$$

where Γ_B is the broadening parameter introduced to account for the effects of pair breaking.

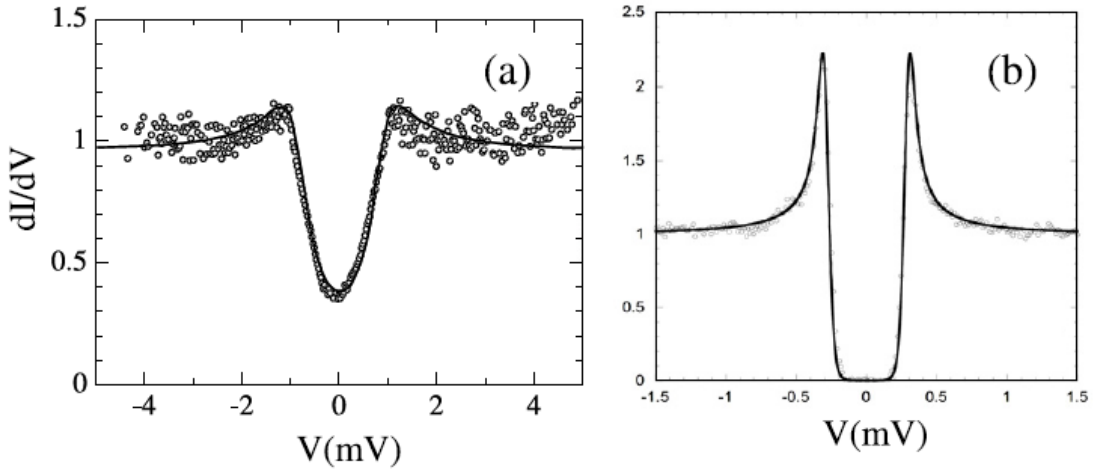

Figure 2.17: **Superconducting gap in diamond.** The dI/dV spectrum for (a) (111)- and (b)(100)-oriented homoepitaxial diamond samples [121, 122].

Figure 2.17 (a) from Nishizaki et al. [121], displays the experimental tunneling conductance spectrum of a superconducting boron-doped diamond as open circles,

together with the calculated conductance represented by a solid line. The calculation is based on the Dynes function, as defined by Eq. 2.33. The most suitable fitting for the experimental data provides the values of the parameters $\Delta = 0.87\,\text{meV}$ and $\Gamma_B = 0.38\,\text{meV}$ at a temperature of $T = 0.47\,\text{K}$ corresponding to $t \equiv T/T_c = 0.087$. The superconducting gap in the above-mentioned study aligned with the findings of investigations conducted using laser-excited photoemission spectroscopy on an MPCVD diamond ($\Delta = 0.78\,\text{meV}$ at $T = 4\,\text{K}$) and STM/STS on a polycrystalline bulk diamond ($\Delta = 0.8 - 1.0\,\text{meV}$ at $T = 0.5\,\text{K}$). By measuring the value of T_c to be $5.4\,\text{K}$ on a (111)-oriented epitaxial film with $n_B \sim 6 \times 10^{21}\,\text{cm}^{-3}$, they managed to calculate the BCS ratio to be $2\Delta/k_BT_c \approx 3.7$, as reported above. The experimental value is marginally higher compared to the theoretical value of $2\Delta/k_BT_c \approx 3.53$ calculated for a BCS superconductor with weak coupling, but significantly lower compared to strong coupling superconductors like Pb ($2\Delta/k_BT_c \approx 4.2{-}4.7$) and MgB_2 ($2\Delta/k_BT_c \approx 4.5$) [123, 124].

The tunneling spectra recorded in their study, demonstrate the presence of a wide coherence peak, a conductance with a high zero-bias, and a comparatively significant value of Γ_B. However, [122], reported a BCS weak coupling with no broadening parameter Γ_B when they investigated an MPCVD diamond film with (001)-orientation, $T_c \approx 2\,\text{K}$ and $n_\text{B} \approx 2 \times 10^{21}\,\text{cm}^{-3}$ (see fig. 2.17 (b)). Nishizaki et al. [121], argues that the significant value of Γ_B cannot be attributed to thermal effects since the experiments were conducted at extremely low temperatures. Therefore, alternative mechanisms are required to address the source of the small energy excitations. There were suggestions by Dynes et al. [125], that the widening edge of the energy gap over time is caused by the inelastic scattering of electrons and this phenomenon is intensified in disordered thin films near the MIT level.

Hence, the presence of disorder caused by doped boron is a potential cause of the of the pair breaking effect, where the variation in tunneling spectra between (001)– and (111)–oriented diamond films is attributed to differences in boron concentration and growth mode. The value of T_c increases as the boron concentration rises due to carrier doping. Moreover, the introduction of boron into the lattice of the diamond leads to disorder, which in turn boosts inelastic electron scattering. It was identified by Umezawa et al. [126], that boron-boron pairs, that cause local distortion within the lattice of diamond, are more likely to develop during (111)–growth rather than (001)–growth. The presence of heavy boron doping induces inherent disorder, which leads to the peculiar feature of the tunneling spectra in the (111)–oriented diamond film. This feature is characterized by ungapped excitations and can be explained by inelastic electron scattering. The experimental results of a high resistivity $\rho = 2.5\,\text{m}\Omega\,\text{cm}$, near T_c with a short electronic mean-free path (l) validates this scenario in superconducting boron-doped diamond and is expressed by the following equation [127],

$$l = \hbar k_F/(\rho n e^2) = 0.34\,\text{nm} \ll \xi_{GL}, \tag{2.34}$$

where k_F represents the Fermi momentum and ξ_{GL} is the Ginzburg-Landau coherence length. The results suggest that the quasiparticles undergo substantial scattering, leading to the creation of excitations within the gap. This, in turn, boosts the zero bias conductance.

Interestingly, Okazaki et al. [64], investigated the effect of a high quality diamond structure on superconductivity, with positive results indicating a higher critical

temperature ($T_c \simeq 10\,\mathrm{K}$), compared to the $T_c \approx 7\,\mathrm{K}$ of previously reported diamond films with similar carrier concentrations ($\approx 3 \times 10^{21}\,\mathrm{cm}^{-3}$); albeit, with much less crystallinity disorder according to the electronic structure measurements by soft X-ray angle-resolved photoemission spectroscopy (ARPES).

From literature, it is evident that diamond orientation [20, 29], and diamond quality [64], have been shown to have an effect on superconducting properties within a heavily boron-doped diamond matrix. Moreover, from the hole doping phase diagram (see Fig. 1.5), Umezawa et al. [126], reported the highest boron concentration of $1.42 \times 10^{22}\,\mathrm{cm}^{-3}$ in a (100)–oriented superconducting diamond sample with a degraded $T_c = 2.9\,\mathrm{K}$. It is clear that non-equilibrium doping processes results in a higher T_c for (111)–oriented films within the doping damage threshold for diamond ($\approx 1 \times 10^{22}\,\mathrm{cm}^{-3}$).

2.4.2 The electronic structure of diamond

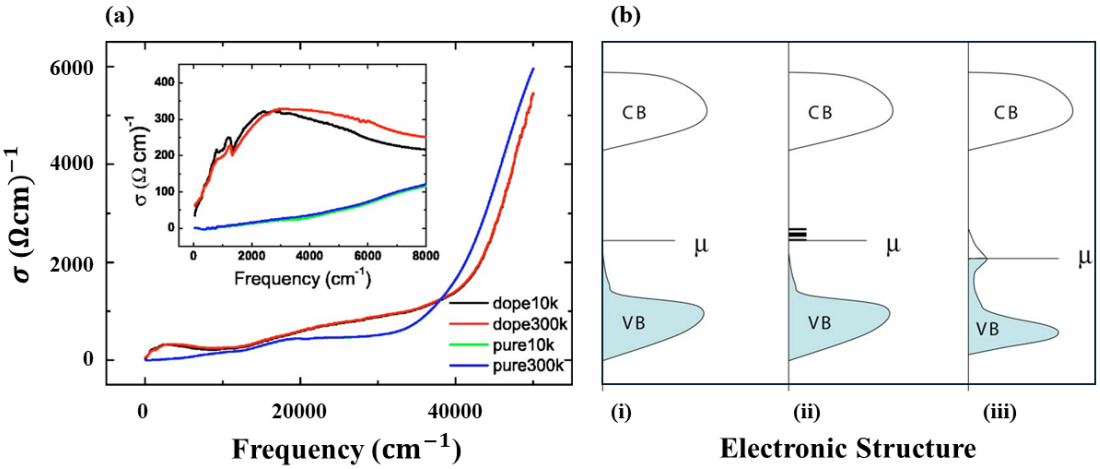

Figure 2.18: **The boron-induced impurity band.** (a) Optical conductivity with a broad-frequency of pure and boron-doped diamonds. (b) The diamond in its pure form exhibits conventional semiconductor properties. (i) The chemical potential (μ) in close proximity to the uppermost energy level of the VB. (ii) Doping with boron introduces acceptor energy levels in close proximity to the uppermost region of the VB. (iii) Increasing boron impurities induces an impurity band that can potentially overlap with the upper part of the VB. Metallic conduction takes place when the impurity band intersects μ [80].

Wu et al. [80], reported clear evidence of an acceptor impurity band above the valance band due to boron doping. Firstly, in order to study the evolution of the electronic states refer to the optical studies of boron-doped diamond, including that of fig. 2.18 (a). That is the display of the conductivity spectra across a wide range of frequencies. The spectral value at low frequencies for the pure diamond sample is very small. However, a sharp increase in σ_ω was observed at frequencies exceeding $30\,000\,\mathrm{cm}^{-1}$. This phenomenon occurs as a result of the interband transition that takes place between the valence band and the conduction band. Conversely, the boron-doped sample exhibits a noticeable spectral rise at frequencies below $7000\,\mathrm{cm}^{-1}$. Meanwhile, the onset of interband transition move towards higher frequencies. Significantly, the low energy excitations did not exhibit a Drude peak. The low frequency caused a significant reduction in conductivity,

leading to a wide peak centered at 3000 cm^{-1} ($\sim$ 0.38 eV). Consequently, the states caused by boron-doping remained highly localized. The observed energy peak aligns closely with the acceptor level of boron situated $\sim$ 0.38 eV above the valence band, as determined by numerous earlier experimental investigations [128]. The energy peak corresponds to the interband transition between the highest energy level in the valence band and the impurity states.

Now, from the optical studies in literature, Wu et al. [80], constructed a schematic illustrating the transformation of the electronic states in BDD, as depicted in fig. 2.18 (b). The pure sample is a pristine semiconductor with a fully occupied valence band and an unoccupied conduction band. The Fermi level is situated in close proximity to the uppermost region of the valence band, as depicted in fig. 2.18 (b) (i). Boron doping introduces impurities as acceptor states with a binding energy of $\sim$ 0.38 eV in close proximity to the Fermi level. At low doping levels, the energy levels are separate and distinct, and the impurity states are fully localized (see (ii) from fig. 2.18 (b)). By increasing the boron concentration, the energy levels of impurities broaden and combine to create a band. When the doping level is sufficiently enough, the impurity band and the top states of the valence band may overlap due to their closely matched energies as depicted in (iii) of fig. 2.18 (b). Metallic conduction occurs when the impurity band intersects the Fermi level. Furthermore, as the holes are formed in the valence band, it is probable that a small downward displacement of the Fermi level takes place, which accounts for the observed shift in energy of interband transitions. It has been argued that superconductivity arises from this impurity band.

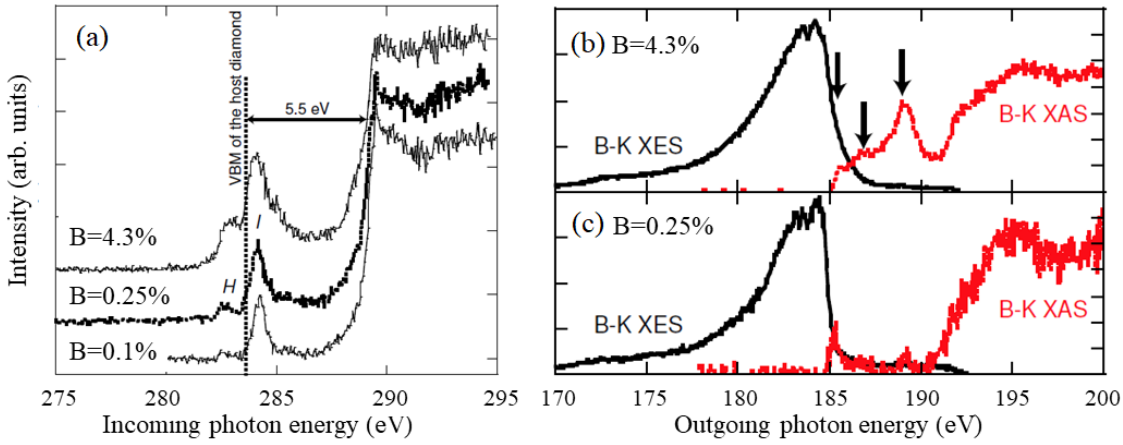

Figure 2.19: **X-ray absorption and X-ray emission spectroscopy for boron-doped diamond.** (a) C-K edge XAS spectra for superconducting diamond (B=4.3%) and non-superconducting diamonds (B=0.25% & 0.1%). (b) B-K edge XAS and XES spectra for a superconducting diamond. (c) B-K edge XAS and XES spectra for a non-superconducting diamond [37].

Moreover, Nakamura et al. [37], studied the electronic structure of both superconducting and non-superconducting diamonds. They reported a partial density of states (PDOS) of impurity boron (B)-2p and host carbon (C)-2p states using soft X-ray absorption (XAS) and X-ray emission (XES) spectroscopy near boron (B)-K and carbon (C)-K edges (see Fig. 2.19). The C-K XAS results in Fig. 2.19(a), indicates an identical impurity in-gap state I for varying concentrations of boron and

a prominent hole state H below $\sim 1.3\,\text{eV}$ for high boron concentrations. By the taking into account the band-gap of a non-doped diamond where the observed bottom of the conduction band is 289.1 eV as reported by Nakamura et al. [128]; the threshold energy (i.e., Fermi level) of I located at $\sim 283.9\,\text{eV}$, corresponds to the top of the valence band. Since I doesn't seem to change with boron concentration while H intensifies with boron concentration, these results indicate a considerable amount of hole states embedded close to the Fermi level within the C-2p valence band for superconducting diamond, and hence the state H appears to be more important for superconductivity. The B-K XES spectra of the impurity B-2p state for both superconducting and non-superconducting diamonds are relatively identical. Contrarily, the B-K XAS spectra shows a difference for different boron concentrations, i.e., in-gap states between 185 eV–190 eV with a sharp peak at $\sim$ 189 eV for the superconducting diamond. The in-gap states are attributed to interstials and/or boron clusters. The Fermi level on both B-K XAS and XES for all the samples is located at $\sim 185.3\,\text{eV}$, as seen in fig. 2.19 (b). The features close to the aforementioned Fermi level are very similar for all the samples with different boron concentrations, i.e., there is no boron concentration dependence from the XAS and XES spectra close to the Fermi energy. Significantly, Nakamura et al. [128] reports a strong hybridization between the (B)-2p and (C)-2p states for doped samples, assuming doping at subsitutional sites. It has been proposed that while the aforementioned findings demonstrate the formation of a band of impurity states in both superconducting and non-superconducting samples, the formation of holes within the valence band as reported, appears to be more significant for superconductivity due to the positioning of the Fermi level within the valence band.

2.4.3 Amorphous 'quenched' carbon

Although the complete amorphization of diamond goes beyond the scope of this thesis; it is essential to note that doping over the graphitization threshold ($\sim 10^{22}\,\text{cm}^3$) of a covalently-bonded diamond crystalline material is widely recognized to cause a collapse in the crystalline structure, resulting in the formation of an amorphous material [129]. Elevating the doping concentration to a significant extent can lead to the complete transformation of the implanted layer into an amorphous state. With respect to ion implantation, implanting at sufficiently elevated temperatures (i.e., to induce self-annealing), the process of forming an amorphous material is typically entirely prevented. Scientists have used, with some success, processes such as dynamic and thermal annealing to help preserve and recover the diamond structure after heavily implanting boron atoms into the diamond matrix in order to achieve a superconducting state [39, 130]. And as mentioned before, such a state has yet to be reported for boron implanted samples.

It was concluded that small graphitic fractions are perhaps responsible for this. However, superconducting nanocrystilline diamonds were reported with high sp^2 graphitic defects [36]. Moreover, ion implantation and thermal annealing processes were employed on a superconducting diamond sample [30]. The superconducting state of that particular sample was retained but affected by the reduction of the T_c. Ion concentration close to the graphitization limit quenched superconductivity, however, the superconducting state was recovered after thermal annealing at 1150 °C. Interestingly, this begs the question: are sp^2 graphitic defects associated with heavy ion implantation the compensating defects that prevents the formation of a

superconducting state in boron implanted diamond? It is then necessary to concisely highlight some carbon structures that are closely related to diamond for further evaluation.

There are the different carbon structures visible in a Raman spectrum ($200 - 3000\,\mathrm{cm}^{-1}$), as detailed in Tab. 2.5. The Raman spectra of amorphous carbon has two spectral regions with ranges between $1500 - 1600\,\mathrm{cm}^{-1}$ and $1320 - 1360\,\mathrm{cm}^{-1}$ known as G and D bands, respectively. The physical properties of amorphous carbon structures primarily depends on the $\mathrm{sp}^3/\mathrm{sp}^2$ ratio. Pure diamond and graphite exhibit sharp peaks at $\sim 1332\,\mathrm{cm}^{-1}$ and $\sim 1575\,\mathrm{cm}^{-1}$, respectively [131].

Table 2.5: Amorphous carbon and diamond bands [131].

Wavenumber (cm^{-1})	Description
1500	Graphite in Monocrystalline form
1546	Disordered graphite
1500–1600	G-band
1430–1470	Trans-polyacetylene laying in the grain boundaries
1345	D-band
1332	1st order Raman
1220	Disordered diamond
1150, 1237	Nanodiamond
1100–1150	Trans-polyacetylene segments at the grain boundaries

Although, this are early days but studies related to superconductivity in diamond and amorphous carbon materials have seen some steady progress with recent developments even indicating that high T_c can be achieved. Very recently, superconductivity in boron-doped amorphous quenched carbon material was reported [132]. Bhaumik et al. [132], reported the novel discovery of the non-diamond phase with a superconducting T_c of $36 \pm 0.5\,\mathrm{K}$ and upper critical field of $5.4\,\mathrm{T}$ at $0\,\mathrm{K}$ for $\sim 17\%$ boron concentration. The critical magnetic field $H_{c2}(T)$ follows $H_{c2}(0)[1 - (T/T_c)]$ temperature dependence, consistent with the BCS formalism [6]. They argue that such a high T_c is effected by a high density of states at the Fermi level due to the close packed carbon atoms of the amorphous carbon material. And, this is the result of a non-equilibrium process where an amorphous boron-doped carbon film in a supercooling state is rapidly melted by a nanosecond laser and subsequently quenched to form boron-doped diamond or a noncrystalline Q-carbon with 85% of sp^3 bonding and 15% of sp^2 bonding. Electron energy loss spectroscopy (EELS) indicates the presence of sp^3- and sp^2- hybridized states of C and B bonds.

2.5 Discussion

The superconducting structure of diamond is well elucidated in literature. However, some superconducting features are yet to be satisfactorily interpreted and concluded. Whether such perfect electron conduction properties are due to impurity states or hole states above and/or below the Valence Band Maximum (VBM), respectively, or a combination of both remains in question [37, 133]. Moreover, recent studies have shown that in certain processing conditions that are well-known to induce superconducting properties in boron-doped diamond result in non-superconducting metallic phases well-above the MIT level (i.e., superconducting transition does not coincide with the onset of MIT) [134]. Furthermore, studies have shown that superconducting diamond undergoes a softening of the optical phonon modes at T_c, near the Brillioun zone center [103, 135]. The aforementioned studies of the optical phonon modes validates the electron-phonon mechanism for superconducting diamond [134]. Howbeit, it has also recently been shown that boron doped nanocrystalline diamonds possess BCS and non-BCS superconducting grains [136]. While the limiting factors of boron ion implantation are also not yet known.

Regardless, the superconductivity phenomena in diamond has rightfully brought some needed attention to boron-doped diamonds and Condensed Matter Physics as a whole due to the excellent underlying physical properties of diamond with many possible applications in devices such as superconducting quantum interference devices (SQUID) [137], nanomechanical resonators [138], δ-doped superlattice structures yielding visible light Bragg mirrors [139], and superconducting diamond nanostructures [140]. However, despite the recent success with the fabrication of superconducting boron-doped diamonds, significant improvements are necessary to fully understand the mechanism involved and to achieve a desirable high T_c. In order to further uncover and understand the conduction mechanism of boron-doped diamonds, the succeeding chapters will discuss and exam the photo-physical and electronic transport properties of uniquely prepared *nano-scale* thin boron-implanted diamond layers in proximity to the diamond surface.

Chapter 3

Mechanisms of ion implantation

3.1 Introduction

It is now expertly known even from Chap. 2, that the controlled introduction of impurities into a relatively pure diamond structure has significant effects on the properties of the diamond. That is, ion doping can be utilized to fabricate or optimize desired characteristics that can be used for various applications and research purposes. This includes studies in quantum information processing, bio-sensing, and in this case diamond phase transitions for electron conduction studies. In this study, we investigate in part the latter by "*carefully*" introducing boron via ion irradiation damage and annealing processes. In order to ensure precise control, it is imperative to regulate the quantity and arrangement of the implied impurity atoms that are incorporated into the material through ion implantation. This chapter will discuss in detail the mechanism of these fabrication techniques that will be applied in order to establish nano-scale boron-doped layers within the diamond matrix while circumventing irreversible graphitizaion.

3.1.1 B^+ doping background

The successful synthesis of diamond in the 1950s by Bundy et al. [58], sparked extensive discussions in Semiconductor Physics on the incorporation of dopants in the solvents used as ingrowth products for artificially grown diamonds. Dopants can indeed be incorporated in this manner [141–143]. Nevertheless, regulating the ion distribution within the diamond substrate is a highly challenging task [144, 145]. Instead, the controlled insertion of ions and high energy particles into the diamond structure through radiation damage processes offers a more effective method of incorporating dopants with specified densities at specific locations within the diamond structure. Vavilov et al. [146], was the first to show that boron can be doped at low concentrations by ion implantation with annealing. This process creates p-type acceptor states in diamond, located 0.37 eV above the valence band (please refer to Fig. 1.4).

Substitutional nitrogen N_s is a commonly known n-type deep donor center in diamond. It has an ionization energy of 1.7 eV below the conduction band, as determined by electrical experiments [147, 148]. The ionization level is located at a significant depth, making it difficult to transport a sufficient number of electrons inside the conduction band at ambient temperature [149]. For electrical devices to be suitable, the dopant states must have a depth significantly less than 1.7 eV. Another feasible option for donor centers is the significantly denser phosphorus P dopant,

which is located 0.6 eV below the conduction band [150]. This depth is shallower compared to N_s donors. Nevertheless, the electrical conductivity resulting from P donors at room temperature is comparatively low [151]. The need for annealing arises from the significant radiation damage caused by the heavier P dopants, which necessitates the reconfiguration of the diamond structure. In order to fabricate P n-type dopant diamonds at different temperatures, cold implantation rapid annealing (CIRA) was implemented after standard ion implantation and annealing methods proved to be unsatisfactory [152]. The annealing process was discovered to be detrimental to the P-doped layers at elevated temperatures [153], perhaps leading to deactivation of the activated P-dopants. At lower temperatures, the residual vacancy density is high, resulting in the formation of P-doped layers of bad quality and high resistance. This high resistance makes it difficult to successfully conduct Hall-effect measurements. Therefore, there is a need for a smaller radius n-type dopant that has shallow donor levels and causes less residual damage to the substrate [151].

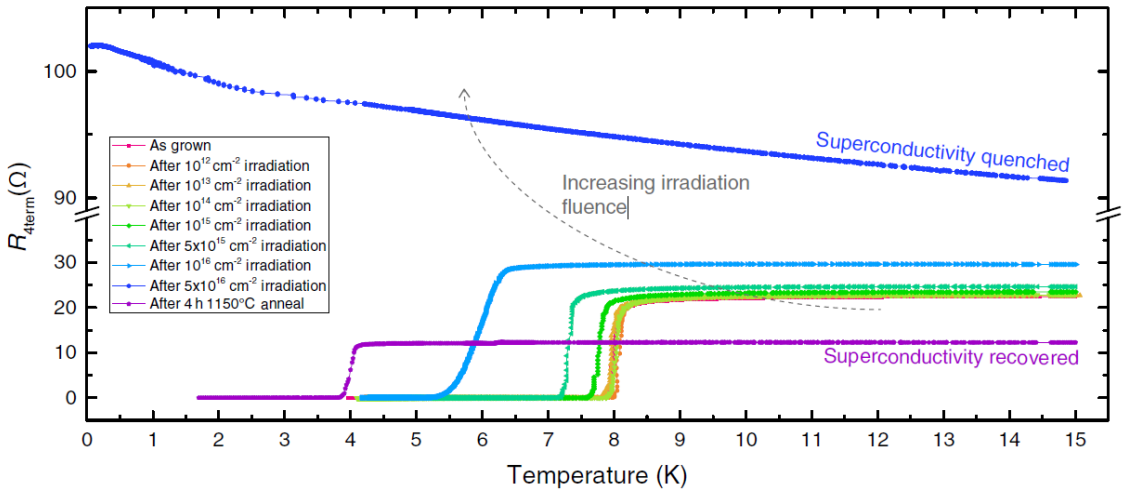

Figure 3.1: **Quenched superconducting properties via** 1 MeV **He ion implantation.** A four-terminal resistance measurement is conducted following each irradiation of the sample. The dotted line serves as a visual aid, indicating that the resistivity of the normal-conducting sample typically rises as the irradiation fluence increases, while the critical temperature of the superconducting material lowers [30].

Most recently, scientist have studied the radiation of boron in diamond in order to achieve a superconductive state. Tshepe et al. [38], investigated the MIT with boron ions implanted in multiple energy steps using the CIRA (77 K) method followed by high temperature (1200°C⟶ 1700°C) annealing in order to circumvent irreversible damage caused by heavy ion implantation. This resulted in a homogeneous non-superconducting metallic phase with an effective thickness of $\sim 0.2\,\mu$m, obtained with a critical concentration of $3.9 \times 10^{21}\,\mathrm{cm}^3$. A hot implantation scheme with dynamic annealing (900°C) and subsequent high temperature (1500°C and 1700°C) annealing was investigated by Heera et al. [39]. The dynamic annealing approach has been shown to significantly reduce radiation damage that mainly results in the undesirable graphitization of diamond [129, 154, 155]. It was shown that heavy boron ion implantation at both room temperature (27°C) and high temperature (900°C) conditions did not result in any known superconductive characteristics in

diamond even down to 40 mK, mainly due to damage induced graphitic fractions forming within the diamond matrix as indicated by the optical analysis.

Creedon et al. [30], has shown recently that superconductivity in diamond can be suppressed by exposing a single superconducting diamond sample to sequential light helium-ion irradiation damage below the vacancy critical limit ($\sim 1\times10^{22}$ vac/cm^3). The T_c was shown to decrease with increase in fluence ranging from 1×10^{12} cm^2 $\longrightarrow$ 1×10^{16} cm^2, while at 5×10^{16} cm^2 superconductivity completely vanished due a low hole compensation efficiency. Annealing the sample at 1050°C for 4 h successfully recovered the superconductive state of the diamond, albeit with a lower T_c. Bousquet et al. [134], showed for the first time the existence of an intermediate non-superconducting metallic phase above the MIT ($n_c^{MIT} \simeq 3\pm1\times10^{20}$ cm^3), and below a critical concentration limit for superconductivity ($n_c^S \simeq 1.1\pm0.2\times10^{21}$ cm^3). The report unveiled the new phase by using mesa patterns that minimizes parasitic currents induced by doping inhomogeneities.

The results reported above of the pursuit of a superconducting diamond fabricated via ion implantation, indicate a dependence on other factors other than the MIT [30, 38, 39]. The T_c of a superconducting diamond sample exposed to radiation damage has also been shown to be affected by high energy ion implantation such that superconductivity cannot be recovered wholly even after annealing the affected sample. The work by Tshepe et al. [38] and Heera et al. [39], utilized high fluences (10^{16}–10^{17} cm^{-2}) at low energies (10–300 keV), which often results in surface erosion due to sputtering [156]. Furthermore, high fluences results in major structural modifications of the implanted surface where the solubility limit of the foreign atoms is usually exceeded [156].

Also, it has been well studied that the diamond structure can be adversely affected by boron implantation [39]. Since the boron concentration range required for supercondcuting properties leads to the breaking of perfect "diamond" sp^3 bonds, and the subsequent conversion to sp^2 bonds of graphite [157]. Although, below the graphitization threshold ($\sim 10^{22}$ cm^{-3}), the diamond structure can be recovered through annealing. Raman and FTIR optical analysis have been reported for such heavily boron implanted diamond samples [39], with contrasting spectral features compared to superconducting diamonds. That is, the $\sim$ 500 cm^{-1} and $\sim$ 1200 cm^{-1} associated with boron concentration content in diamond, are less pronounced while graphitic fractions appear to dominate after annealing at high temperatures (>1800 K).

3.2 Ion beam processing

Ion beam processing of materials occurs when ions are bombarded onto the surface layer of a solid substrate, introducing atoms into it [62]. This bombardment is done using ions with energies ranging from electron-volts (eV) to mega-electron-volts (MeV). The solid-state features are extensive due to the wide variety of physical properties that are influenced by the existence of a small quantity of extrinsic foreign atoms. The presence of these foreign atoms can significantly influence and control the mechanical, optical and electronic transport properties of materials. Utilizing energetic ions allows for the introduction of a diverse array of atomic species, regardless of thermodynamic considerations. This enables the achievement of impurity concentrations and distributions that are of specific interest. In numerous instances, these distributions would be unattainable through other means.

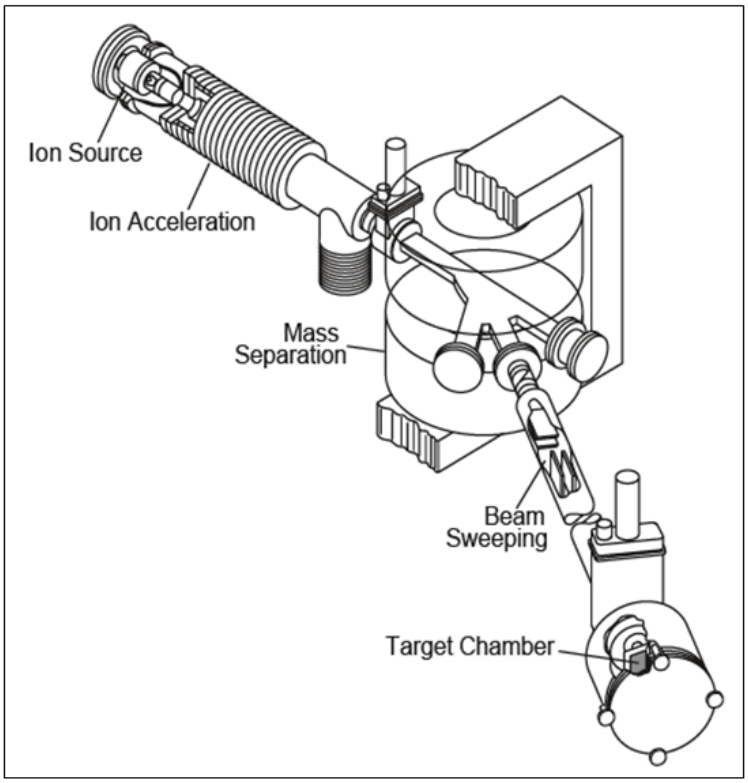

Figure 3.2: **Schematic of an ion beam processing system.** Ion species of interest are accelerated through the system, separated via a magnetic particle filter and directed towards the target chamber [62].

Furthermore, ion beam processing offers a distinct non-equilibrium and low temperature approach to incorporating dopant atoms into the lattice. In conventional scenarios, a beam of ions is accelerated with an electric potential ranging from 10–100 kV [62]. Figure 3.2, showcases the fundamental components necessary for this technique: an ion source, acceleration column, mass-separator, and target chamber. Various ion sources can generate a diverse range of beams with enough intensity for implantation even in integrated circuit technology. A typical ion dose for this purpose is typically between $10^{14} - 10^{15}$ ions/cm^2. Ion dosage is the quantity of ions/cm^2 that is implanted into a sample. Fluence will be employed as a substitute for dosage throughout this thesis. The density of the ion beam current is measured in A/cm^2. The dosage rate or flux is expressed in units of ions/s/cm^2.

3.2.1 Ion-solid interactions

When an energetic charged particle is accelerated towards a solid material, the interactions that takes place is of valuable interest in many studies study; and the phenomena is referred to as an ion-solid interaction process [156]. This process has been intensively researched in the field of material science since the early 1900s. Ernest Rutherford is recognized as one of the pioneering scientists who first observed this phenomenon using experimental means [158]. The experiment involved bombarding alpha (α) particles emitted from a Radon source onto a metal foil. This experiment provided evidence that energetic particles can be halted and deflected by matter, subsequently introducing the field of ion-solid interaction into the realm of Physics. As a result, ion beam technology was developed. Ziegler and Biersack [159], provide

an extensive examination of the mechanism, progress and evolution of the mentioned technology, showcasing different procedures and applications that have emerged over time. These include ion beam analysis (IBA), substrate sputtering, ion beam mixing, and artificially induced ion implantation. In this study, we make use of the latter (i.e., ion implantation), to fabricate metallic conduction layers inside diamond materials [62, 156].

3.2.2 Ion implantation

Ion implantation is a method that enables the introduction of various ion impurities into the shallow layers of any solid material, such as diamond, graphite, or other carbon-based substances [156]. The accelerated ions interact with the target atoms by breaking their chemical bonds and displacing them from their original positions within the lattice. As a result, the atomic structure of the target material is modified. In certain cases, the implanted ions may also cause changes in the elemental composition of the target material, particularly if the target atoms differ from the ions being implanted, thereby inducing radiation damage [156, 160]. Radiation damage refers to the alteration of the atomic structure of a lattice caused by the transfer of energy from a projectile ion to a target atom. Moreover, the collision between the highly charged ions and the host material's atoms typically leads to the formation of localized imperfections, known as point defects, that have the ability to move and cluster together, leading in the formation of larger imperfections called extended defects or dislocation loops [61, 156].

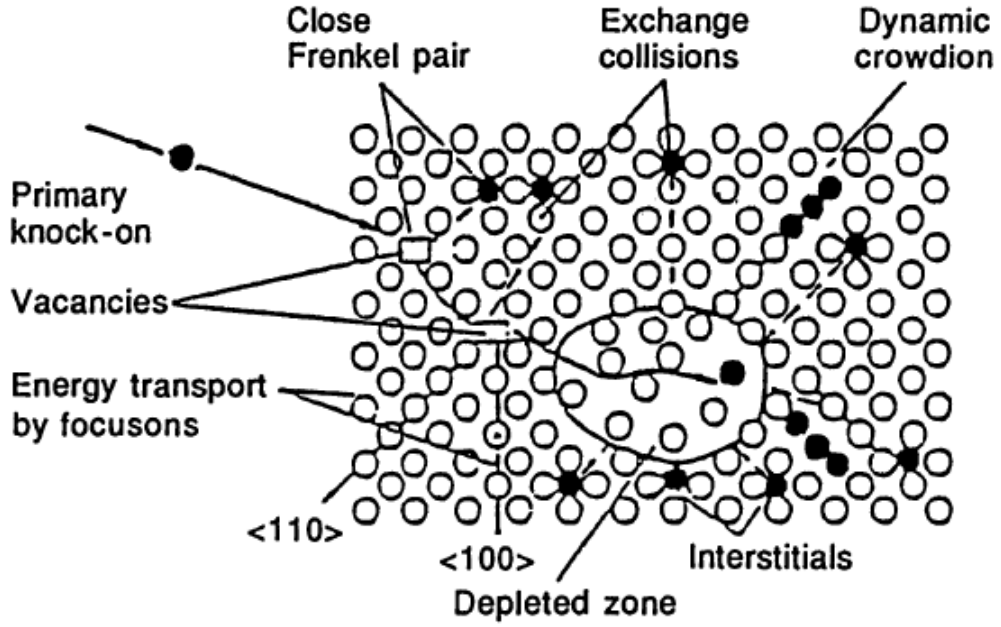

Figure 3.3: **Ion implantation interaction processes.** Illustration of possible defects induced by ion implantation [156].

Figure 3.3, illustrates the many defects that can occur as a result of ion implantation. These defects include vacancies, interstitials, and more complicated defects such as Frenkel pairs, which are created by a combination of a vacancy and an interstitial. For further comprehensive understanding of the topic, readers can consult the text authored by Dresselhaus and Kalish [156]. The principle of ion

radiation damage states that the energy of the ion (E_i) must exceed the displacement energy (E_d) of the atom being targeted. Under appropriate transient conditions, a solitary ion that possesses sufficient energy can displace several atoms in the target material. This displacement can then lead to a chain reaction where the displaced atoms continue to displace other atoms, resulting in a collision cascade [159].

3.2.3 Ion stopping process

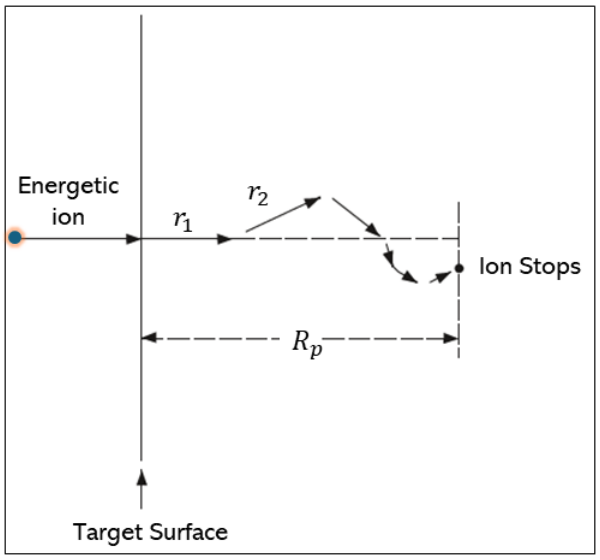

Figure 3.4: **Schematic of an accelerated ion into a solid.** The trajectory of a highly energetic ion as it traverses a solid material in an ion implantation experiment. It depicts both the total path of the ion with positions r_i and its projected range, R_p. While traversing the material, the ion collides with stationary target atoms that causes it to deviate from its original path [62].

When an incident energetic ion enters a solid material, it has a sequence of interactions with the host atoms and electrons present in the target. During these collisions, the energetic ion in transit experiences a decrease in energy at a rate of dE/dx ranging around 100 eV nm^{-1} [62]. The specific value depends on factors such as the energy, mass, and atomic number of the ion and the host material with a specific density. The subsequent section will address the energy dissipation methods. Our current focus is on the ions' penetration depth, also known as range, denoted as R (see Fig. 3.4). R is the range that is defined as the distance that an ion can travel in a solid before losing all of its energy. The rate of energy-loss along the ion's route determines this range as follows,

$$R = \int_{E_0}^{0} \frac{1}{dE/dx} dE, \tag{3.1}$$

where E_0 is the incident energy of the ion, which is the initial energy it has when it enters the solid. The sign of the derivative dE/dx is negative, indicating a decrease in energy per unit distance traveled. However, tabulated numbers are presented as positive quantities. The primary factors determining the extent of energy loss are the ion's energy E_0 and atomic number Z_1, as well as the substrate's atomic number Z_2, assuming the crystal lattice's orientation is not considered. When the

incident ion enters the material, it undergoes collisions with atoms and electrons as expected. Random processes take place such as the distance traversed between the collisions and the amount of energy lost per collision. Therefore, different ion species and different incident energies do not possess identical ranges. Instead, there is a wide variation in the depths at which specific ions are able to penetrate. The distribution of ions inside specific ranges is commonly known as the range distribution or straggling. The focus in ion implantation is not on the whole distance R that the ion travels, but rather on the projection of R perpendicular to the surface. This projection is known as the penetration depth or projected range R_p as depicted in Fig. 3.4.

3.2.4 Energy-loss mechanism

The rate of loss of energy by an incident ion, dE/dx, while passing through a solid is dictated by the interactions it has with the atoms and electrons of the host material, and this interactions are affected by screening Coulomb forces. There are often two distinct methods of energy loss, namely: (1) **nuclear collisions**, when energy is transferred as translational motion to an entire host atom, and (2) **electronic collisions**, where an incident ion in transit ejects electrons of the host atoms [62, 156]. The separation between the collisions is a practical and useful one, even though it is not quite accurate. However, it serves as a reliable approximation. The energy-loss rate, represented as dE/dx, can be mathematically written as equation,

$$\frac{dE}{dx} = \left(\frac{dE}{dx}\right)_n + \left(\frac{dE}{dx}\right)_e \tag{3.2}$$

where e and n indicate the electronic and nuclear collisions, respectively.

Nuclear collisions can result in substantial discrete energy losses and notable angular deviation of the ion's course (refer to Fig. 3.5). This process induces lattice disorder by causing atoms to be displaced from their original positions in the lattice. Electronic collisions exhibit significantly lower energy losses per collision, minimal deviation of the ion's path, and minor disruption to the crystal lattice. The energy-loss mechanisms varies fast with the energy E and atomic number Z_1 of the ion. Nuclear stopping prevails for low E and high Z_1, while electronic stopping becomes dominant for high E and low Z_1 (please see Fig. 3.6). Furthermore, with the rate of energy-loss, it is normal to refer to the stopping cross-section, denoted as S, which is precisely described as

$$S \equiv \frac{dE/dx}{N} \tag{3.3}$$

with N representing the atomic density. The stopping cross-section can be conceptualized as the rate at which energy is lost per scattering center.

An accurate comprehension of the processes by which energy is lost is crucial for managing the distribution of implanted dopant atoms and for defining the type of lattice disorder that occurs when a solid is subjected to ion implantation or ion irradiation. During the deceleration process within the host material, the implanted ions experience intense collisions with certain atoms in the lattice, resulting in the displacement of those atoms from their original positions.

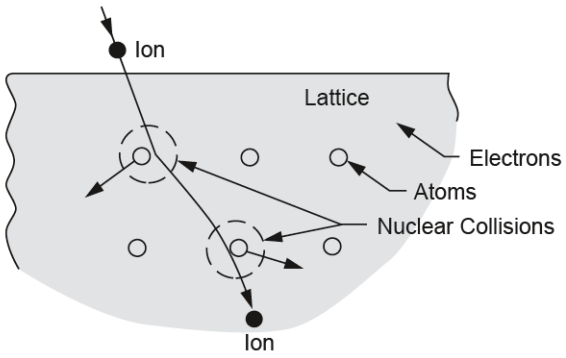

Figure 3.5: **A transient ion in a crystal lattice.** An ion interacts with a crystal lattice, and experience a deflection due to nuclear collision processes with the host atoms. The ion loses energy through collisions with the electrons [62].

The nuclear stopping process

The amount of energy that a moving particle loses as a result of elastic collisions per unit distance traveled in the target material is known as the nuclear stopping power. From the probability of a particle, with energy E, experiencing a collision and losing energy between T and $T + dT$ while traveling a distance dx, we get the following expression,

$$\frac{dP(E)}{dT} = N dx \frac{d\sigma(E)}{dT} dT. \tag{3.4}$$

The energy of the particle in motion is represented by E, while T represents the transferred or recoiled energy and $\sigma(E)$ is the differintial collision cross-section. In order to determine average energy lost by the ion in transit over a distance dx, multiply Eq. 3.4, by the transfer energy T and integrate over all possible values of T,

$$\langle dE \rangle = \int T \frac{dP(E)}{dT} dT = N \int_{T_{min}}^{T_M} T \frac{d\sigma(E)}{dT} dT dx \tag{3.5}$$

When considering a very small change in x (i.e., infinitesimal dx), we can remove the averaging sign on dE,

$$\left(\frac{dE}{dx}\right)_n = N \int_{T_{min}}^{T_M} T \frac{d\sigma(E)}{dT} dT, \tag{3.6}$$

where $(dE/dx)_n$ represents the nuclear stopping power and T_{min} represents the lowest amount of energy that can be transferred and does not necessarily have to be zero. The value utilized for T_{min} is the minimum energy required to displace an atom from its designated lattice site, which is estimated to be around 20–30 eV. T_M is the upper limit which is the highest amount of transfer energy possible, and is calculated using the formula $T_M = 4M_1M_2E/(M_1 + M_2)^2$. The nuclear stopping cross-section for an ion of energy E is given by,

$$S_n(E) = \frac{1}{N}\left(\frac{dE}{dx}\right)_n = \int_{T_{min}}^{T_M} T \frac{d\sigma(E)}{dT} dT. \tag{3.7}$$

$d\sigma(E)/dT$ represents the differential energy-transfer cross-section. By utilizing the power $d\sigma(E)/dT$, the nuclear stopping cross-section can be determined, provided,

$$\frac{d\sigma(E)}{dT} = \frac{C_m}{E^m T^{1+m}} \tag{3.8}$$

where the variable m depends on the reduced energy ϵ (**NB.** ϵ is proportional to the ion energy and $\epsilon^{1/2}$ is proportional to the ion velocity). C_m is a constant given by,

$$C_m = \frac{\pi}{2}\lambda_m a_{TF}^2 \left[\frac{2Z_1 Z_2 e^2}{a_{TF}}\right]^{2m} \left[\frac{M_1}{M_2}\right]^m, \tag{3.9}$$

where λ_m is an additional fitting variable and a_{TF}^2 is the Thomas-Fermi screening radius [62]. M_1 and M_2 are the masses of the the incident projectile and target particle, respectively. Taking T_{min}=0, the nuclear stopping cross-section based on the Thomas-Fermi atom becomes,

$$S_n(E) = \frac{C_m E^{1-2m}}{1-m}\left[\frac{4M_1M_2}{(M_1+M_2)^2}\right]^{1-m} \tag{3.10}$$

The nuclear stopping power, $S_n(E)$, is the dominant factor at low energy levels, as depicted in Fig. 3.6. This is the region where the most amount of damage often occurs, and the stopping power grows as the mass of the implanted ions increases. The combination of nuclear stopping power and nuclear displacement energy plays a crucial role in ion radiation damage processes occurring at extremely low energies.

The electronic stopping process

The electronic stopping process involves the interaction between the energetic incident ion and the host electrons. This is a process characterized by inelastic and rapid collisions, resulting in the ionization of the atoms in the target material. Electronic stopping is a significantly more intricate process than nuclear stopping and is commonly divided into numerous components by comparing the ion's velocity (v_1) to the Bohr velocity ($v_0 = e^2/\hbar$), where e and $\hbar$ denote the electronic charge and the Planck's constant, respectively [161].

As the velocity increases, the ion's charge state also increases and eventually reaches a point where it is loses all of its electrons at a velocity of $v_1 \geq v_0 Z_1^{2/3}$. At this stage, the ion is seen as a positively charged point with a charge of Z_1, moving at a velocity higher than the average electron velocity along the atomic orbitals in the shells of the host atoms. When the velocity of the projectile, v_1, is significantly higher than that of an electron in an orbital (in the case of fast collisions), the effect of the energetic ion on an atom can be considered as a sudden, minor external disturbance. This process is associated with Bohr's notion of stopping power. The impact results in an abrupt energy transfer between the incident ion and the host electrons. The energy dissipation resulting from the interaction between a high-speed particle and a stationary nucleus with orbiting electrons can be determined by analyzing the scattering in a central force field. The stopping cross-section diminishes as the velocity increases due to the reduced duration of the particle's presence near the atom. In this domain characterized by high energy and quick collisions, the values of electronic stopping exhibit a proportional relationship to the square of $(Z_1/v_1)^2$. In this scenario, the ion is an unshielded nucleus, and its interactions with the electrons of the host material may be precisely characterized using a purely Coulombic interaction potential,

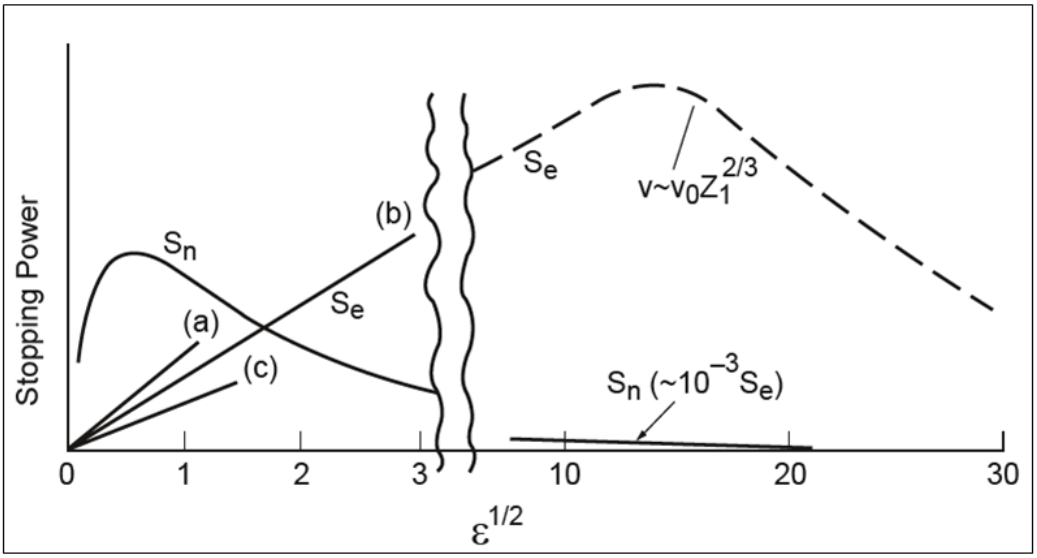

Figure 3.6: **Dependence of the reduced stopping power on the function $\epsilon^{1/2}$.** At low energy implants $(dE/dx)_n$ dominates in stopping the incident ion, while at higher energy implants $(dE/dx)_e$ dominates the stopping of the ion [62].

$$V(r) = \frac{Z_1 Z_2 e^2}{r}, \tag{3.11}$$

where r is the interatomic distance. Now, due to the heavy incident ion, the Coulomb force exerted on the electron undergoes continuous directional change. As the electron remains stationary while the ion passes by, then the impulse in the same direction as the path, represented by $\int F dt = 0$ due to symmetry. This is because for every position of the traversing energetic ion in the negative x direction, there is a corresponding positive position x direction that contributes an equal and opposite amount to the momentum's x component. Nevertheless, within the passage, there exists a force acting in the y direction, resulting in the transfer of momentum Δp to the electron. The electronic stopping energy is given by,

$$\left(\frac{dE}{dx}\right)_e = \frac{2\pi Z_1^2 e^4}{E} N Z_2 \left(\frac{M_1}{m_e}\right) \ln\left(\frac{2 m_e v_1^2}{I}\right), \tag{3.12}$$

where $I \cong 10 Z_2$ is the average excitation energy [62]. However, the description of this particular stopping power fails to account for the atomic shell structure and the changes in electron binding. Empirically, these effects manifest as small derivations, with an exception for the extremely light elements.

Figure 3.6, shows that the electronic stopping power $S_e(E)$ is the dominant factor at high energies and is ultimately determined by the ion's velocity. This is the point at which the high-energy ion comes into contact with clouds of electrons around the target atoms. This contact results in a direct transfer of kinetic energy from the ion to the electrons, creating a force that slows down the ion. Eventually, the nuclear stopping process takes over and begins to dominate the stopping process. As a result of the high energy of the injected ions, the transient ion has reduced interactions with the target atom-nuclei, leading to limited displacements of the target atom caused by electronic stopping. Lindhard and Scharff [160], established a correlation

between the electronic stopping power and the energy of the incoming ion in the following expression,

$$S_e(E) = \frac{8\pi e^2 a_0}{\epsilon_0} \frac{Z_1 Z_2}{\left(Z_1^{\frac{2}{3}} + Z_2^{\frac{2}{3}}\right)^{\frac{3}{2}}} \left(\frac{E}{E_0}\right)^{\frac{1}{2}} \tag{3.13}$$

where a_0 is the Bohr radius, E is the energy of the incident ion, E_0 is the Bohr energy, and ϵ_0 is the permittivity of free space. With this model, the electrons in the target material are viewed as an free electron gas interacting with a positive charge of the projectile. Also, there is proportional relation between the electronic stopping power and the ion velocity (i.e., $S_e(E) \propto \epsilon^{1/2}$) and does not allow any deviation in the projectile trajectory. The energy regions for the electronic stopping regime ranges from around 100 keV – 10 MeV. In this work we report on low keV energy regions, where the nuclear stopping power is more likely to dominate.

3.2.5 Ion range and distribution

The implanted ion dissipates energy by interacting with the host atoms via nuclear and electronic processes. The nuclear process involves discrete elastic collisions between the ion and the nuclei of the host atom, while the electronic counterpart involves a continuous viscous drag interaction between the incident ion and the surrounding cloud of electrons orbiting around the nucleus of the host atom. The energy levels often employed in low energy implantation ($\sim$ keV), the nuclear related processes usually dominate as mentioned before. This is evident in the specific paths followed by the ion as it slows down and ultimately stops within the solid material.

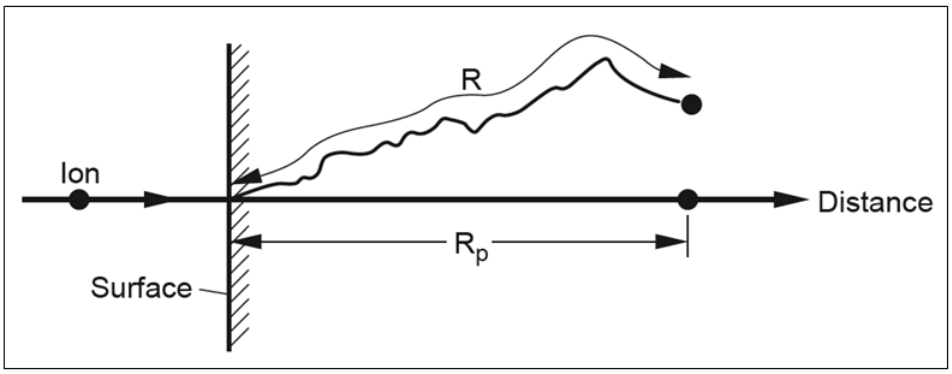

Figure 3.7: **Schematic showing the project range (R_p) of an incident ion.** An ion that impacts a semiconductor penetrates it with a total path length, denoted as R. This path length results in a projected range, denoted as R_p, in the same direction as the incident ion [62].

Figure 3.7, displays a two-dimensional diagram illustrating the trajectory of an ion during an ion implantation process until it reaches a state of rest within a material. when depicted in this diagram, the ion deviates from a linear trajectory when it encounters collisions with target atoms, preventing it from reaching its final destination in a direct path. The precise measurement of the ion's total distance traveled is referred to as the range R. The projected range of the ion, R_p, refers to its net distribution distance into the substrate along the incident direction, which is perpendicular to the surface.

Range distribution

Since the injected ion collides possibly with multiple target atoms, directing it into multiple directions, the traversing ion does not reach its position of rest in a straight line. And hence, the distance traveled is integrated into a range R. The net distribution distance of the ion into the host substrate, measured along the trajectory of the incident ion is known as the projected range R_p. The projected ion range is integral in estimating the damage within the crystal lattice, and is obtained by integrating over Eq. 3.1,

$$R_p = \int_{E_0}^{0} \frac{dE}{\left(\frac{dE}{dx}\right)_n + \left(\frac{dE}{dx}\right)_e}, \tag{3.14}$$

where the integration limits are from the initial ion energy to zero. Determining the projected ion range from the ion fluence $(\Omega_f) > 10^{10}$ ions/cm^2 is through a statistical process, where the ion concentration is given by,

$$N(x) = N_p \exp\left[\frac{-(x - R_p)^2}{2\Delta R_p^2}\right], \tag{3.15}$$

where the projected range R_p accounts for the mean penetration depth of the ion and ΔR_p represents the standard deviation for the distribution, which is essentially the longitudinal ion range straggling. The range straggling is the average fluctuation in the projected range, due to the uncertainty of the process, where the ions scatter and come to rest at distances less or greater than the projected range.

The peak concentration N_p at the center of a Gaussian shape distribution, depicted in Fig. 3.8, relates the ion fluence with ion depth distribution measured along the direction of the beam x. The peak concentration is given by,

$$N_p = \frac{\Omega_f}{\sqrt{2\pi}\Delta R_p}, \tag{3.16}$$

where $\Omega_f = \int_{-\infty}^{\infty} N(x)dx$, is the ion fluence. At low ion concentration in the absence of channeling effects, the probability function is approximated by a Gaussian profile, whereas for high ion concentration in the presence of channeling effects, the probability function deviates from the Gaussian profile.

Range straggling

The ion implantation process is characterized as being stochastic, meaning it is random in nature. The mean predicted range indicates the most likely position for an ion to stop moving. The inherent variability in the scattering process, occurring as the ion traverses the target, results in ions coming to a stop at distances less or greater than the estimated range. The variability in the projected range, measured by the standard deviation from the mean, is known as the range straggling, denoted as ΔR_p. Now, the influence of the ion mass, M_1, and the target mass, M_2, on the range straggling is depicted in a schematic manner in Fig. 3.9. It is evident that the paths followed by lighter particles within a denser material show greater deviations from their intended destination.

This behavior is governed by the principles of conservation of energy and momentum, which also applies to the scattering of large macroscopic spheres. The variations in elastic nuclear scattering characteristics will impact the boundaries of

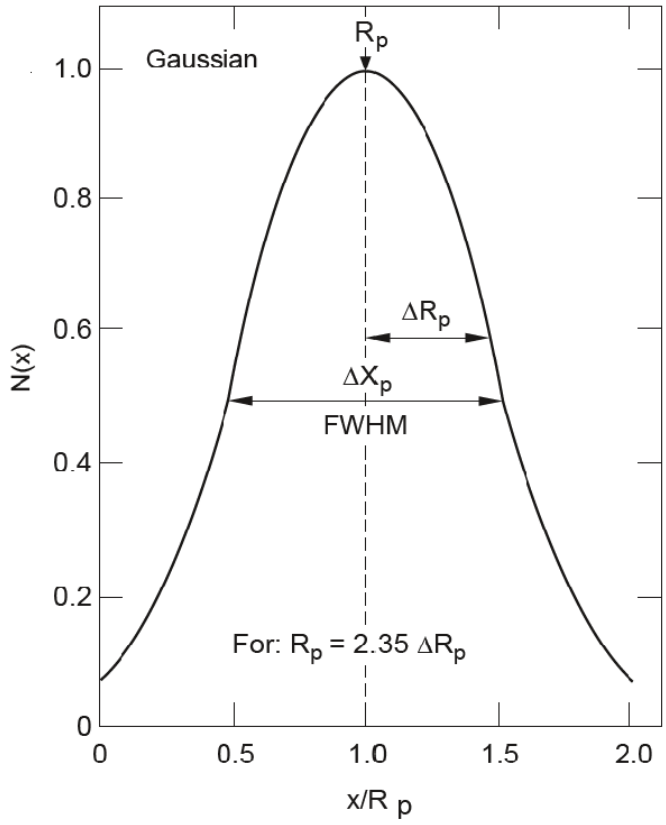

Figure 3.8: **Gaussian range distribution of implanted ion.** The projected range of the implanted ion with $R_p = 2.25\Delta R_p$ and FWHM of ΔX_p is described by Gaussian distribution [62].

halting positions and the breadth of the ion distribution within the solid. Due to similar physical factors, it is anticipated that the depth distribution for $M_1 < M_2$ will be broader compared to the depth distribution for $M_1 > M_2$. The range straggling can be determined by applying the approach by Lindhard et al. [162], specifically in cases when nuclear stopping is the dominant factor, using the following expression,

$$\Delta R_p \cong R_p/2.5 \tag{3.17}$$

3.2.6 Channeling effects

Thus far, the theory based on projected ranges of energetic ions for ion irradiation is limited to amorphous materials with disordered atomic structures. In these materials, the ions and target atoms move in a chaotic manner in relation to each other. The distribution of impact parameters is primarily influenced by the ion's energy E and the atomic numbers of the incident ion Z_1 and the target atom Z_2. In the context of a single crystal (monocrystalline) that has a regularly arranged and flawlessly ordered atomic structure, the alignment of the target material in relation to a probing beam also becomes a significant factor. When a beam of particles approaches a single crystal target in a direction parallel to a closely arranged row of atoms, the path of the beam is guided through the empty spaces between the rows of atoms due to the attractive forces exerted by the positively charged atomic potentials. Therefore, the reliance on the alignment of the crystal orientation in relation to the injected ion is

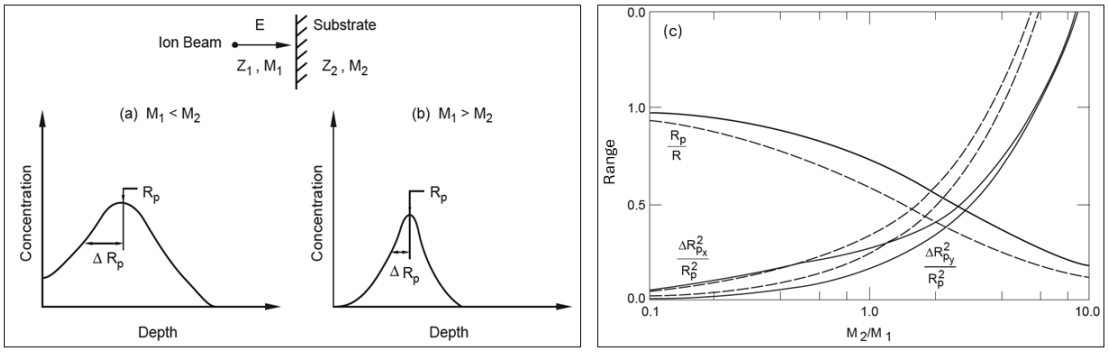

Figure 3.9: **Depth distribution of implanted ion and range straggling.** (a) The mass of ion is less than the mass of the host atoms, and (b) The ion mass is more than the mass of the host atoms. The average depth, R_p, can be roughly estimated based on M_1 and the incidence energy, E. On the other hand, the relative width, $\Delta R_p/R_p$, of the distribution is principally influenced by the ratio M_2/M_1. (c) The relationship between the range, R, the projected range, R_p, and the range straggling, ΔR_p, can be described as functions of the mass ratio, M_2/M_1. ΔR_{px}, occurs parallel to the incident ion, while ΔR_{py} occurs perpendicular to the incidence ion [62].

known as channeling.

As the ion channels through the material, it is able to penetrate to a greater depth within the target material. During this process, the ion collides with the atomic rows at small angles, resulting in a decrease in the scattering yield in the substrate. Figure 3.10, illustrates the range of an incident ion that is channeled down the (100)-axis, represented by a solid line. This range is compared to a Gaussian range distribution, represented by a dashed line, which shows the range of an incident ion that does not experience any channeling effects. The depth distribution of the channeled ion is greatly decreased, while the predicted range R_p along x is dramatically increased, as a result of the decreased scattering yield within the target material. In order for channeling to occur, the incident ion must be injected at an angle ($\psi_c < 5°$) that is less than 5 degrees in relation to the crystal axes. To prevent this effect, it is typically recommended to inject ions at an angle of around 7° relative to the crystal axes of the target. Numerous scholarly articles have been written on the interaction between a forcefully injected ion and a solid material. For more comprehensive understanding on this topic, interested readers might refer to the works of Nastasi and Mayer [62], Dresselhaus and Kalish [156] and Kalish [163].

3.3 Ion distribution and calculated damage

Ion irradiation on a crystal substrate like diamond can be simulated using the Stopping and Range of Ions in Matter (SRIM) program. SRIM is a Monte-Carlo simulation program that utilizes the Binary Collision Approximation (BCA) coupled with its integrated calculation tool TRIM (Transport of Ions in Matter) to predict the structural impact of a high-energy ion penetrating a solid material. It was first introduced in the 1980s by Ziegler and Biersack [159]. Their work extensively reviews the theoretical foundation of ion implantation to aid in operating the simulation program. The program is commonly cited in literature and renowned for its precision in simulating ion radiation damage in crystals. The program has been consistently revised every five years since its inception to stay current with new

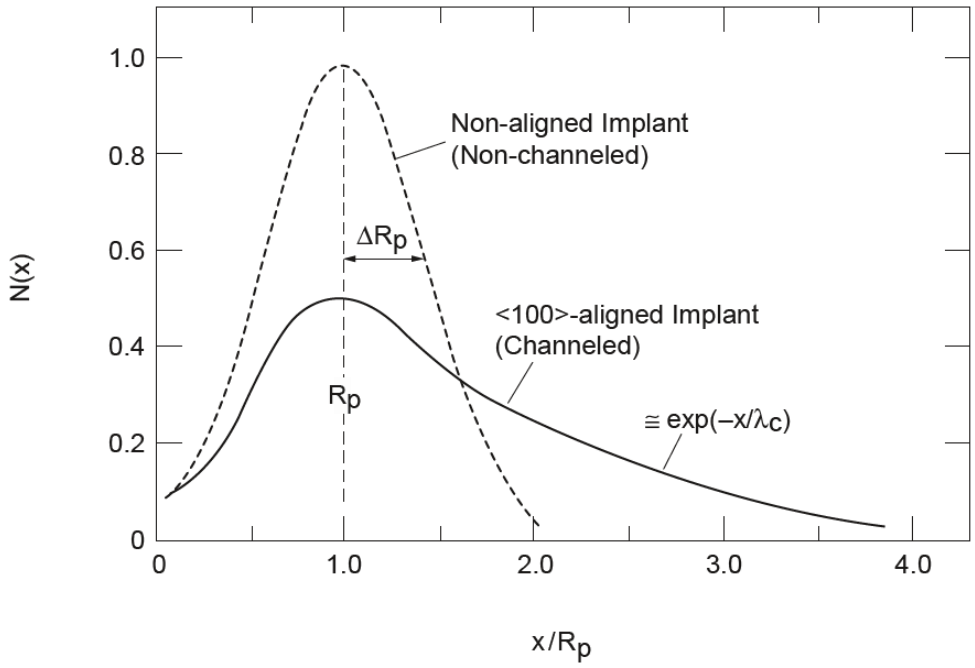

Figure 3.10: **Range distribution for an ion channeled along (100) axis.** The solid line shows the range distribution for a channeled ion in comparison with a Gaussian distribution (dashed line) for an ion undergoing no channeling effects [62].

scientific advancements.

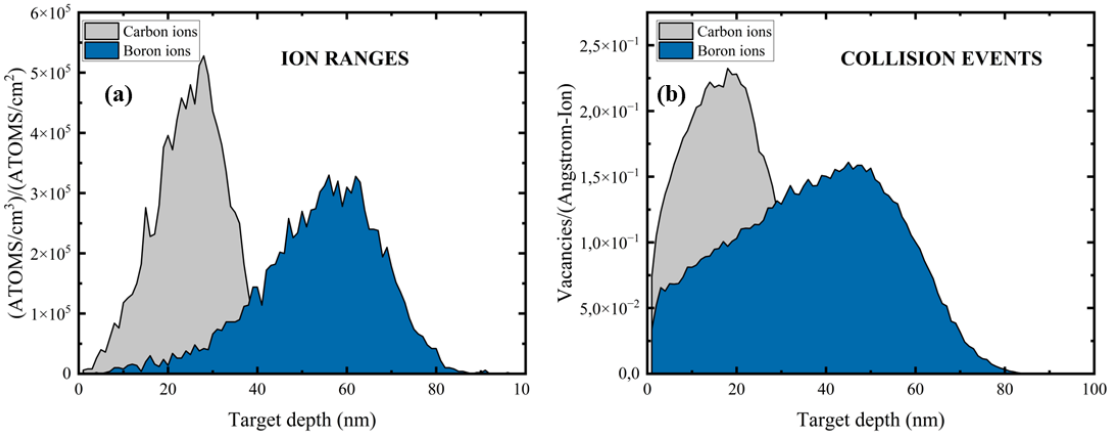

Figure 3.11: ***SRIM* calculations for** 15 keV **carbon and** 30 keV **boron beam incident on a diamond crystal with a** $\sim$ 50 eV **displacement energy.** Details from calculations with full damage cascades. (a) Depth profile of the carbon and boron ions. (b) Vacancy distribution due to cascading of carbon and boron atoms.

This study utilizes the SRIM-2008.03 version to calculate the damage and penetration depth caused in diamond by the forceful injection of extrinsic boron ions. SRIM employs a statistical technique in which an ion is introduced into a target substance. The ion travels in a straight line through the material until it hits a target atom, at which point an impact parameter is chosen randomly. TRIM calculates the kinematics of the impact and tracks the trajectory of the recoiling target atom, which undergoes collisions with additional target atoms, leading to the formation of

a group of recoiling target atoms. After all the recoiling target atoms reach energies lower than the cutoff energy (E_{co}), the program resumes and tracks the movement of the initial implanted ion. The ion continues its movement with a different energy and direction until it undergoes another collision, resulting in the creation of more recoils. The process continues until the ion's energy drops below the displacement energy (E_d), preventing it from dislodging more target atoms and eventually stopping. The program records all collision occurrences between the primary ion and target atoms and then tracks a newly injected ion.

The study simulated the implantation of carbon and/or boron ions into diamond at low energies ($\sim$ keV), to determine and ascertain the desired projected range and ion distribution caused by the ion implants in the diamond (i.e., a preliminary test conducted prior to the actual experiment). This describes the interactions that occur when a single incident boron ion moves through the diamond matrix and affects the stationary target carbon atoms. The simulated outcomes depend on input factors including ion type, ion energy, angle of incidence, target material, target atoms, displacement energy of the target atoms, and their density. A simulation was conducted to do precise calculations involving complete damage cascades caused by, not limited to, $\sim$ 15 keV carbon ions and/or $\sim$ 30 keV boron ions, independently. The process was carried out for the implanted ions into diamond with a specified diamond layer width of approximately 1000 Å. The diamond has a density of about $\sim$ 3.52 g/cm^3 and a displacement energy E_d set at around $\sim$ 50 eV for diamond carbon atoms. The simulation involved approximately 5000 ions, providing adequate statistical data to forecast the stopping depth of the majority of ions and the distribution of damage, namely the vacancies formed.

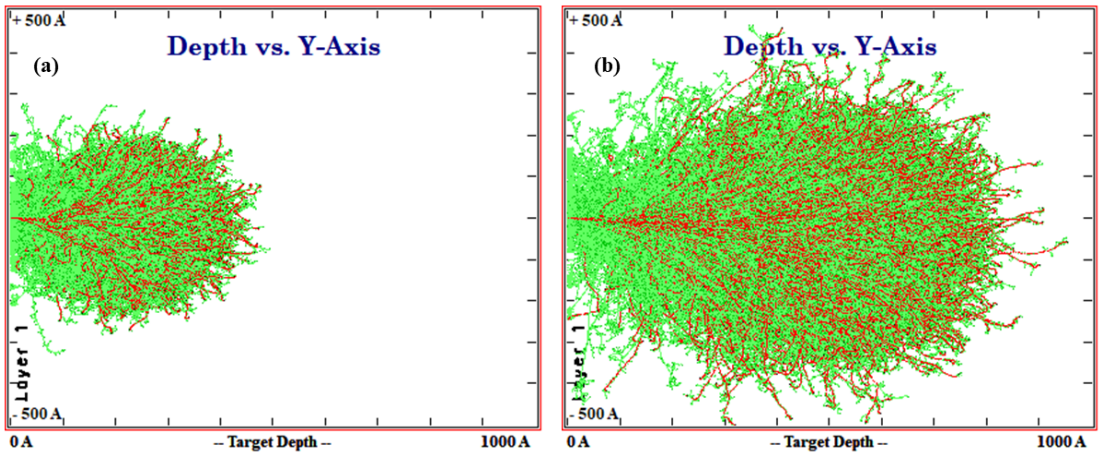

Figure 3.12: ***SRIM* calculations for** 15 keV **carbon and** 30 keV **boron beam incident on a diamond crystal.** Ion distribution in red with collision cascades of the carbon recoils in green in the Y transverse coordinate – (a) due to incident carbon ions – (b) due to incident boron ions.

The model calculations provide a reliable estimate of the ion depth and scattering of target atoms, but they do not consider ion channeling or potential phase alterations that may occur during ion implantation. Figures 3.11 and 3.12 show direct SRIM output illustrations. Figures 3.11, shows distinct SRIM simulated plots for the ion range or depth profile of the implanted ions and the vacancy distribution of the target atoms when $\sim$ 30 keV boron ions are implanted into a diamond sample. By analyzing

collision events represented as the number of vacancies per angstrom ion versus depth, one can calculate the estimated damage in the material. This is achieved by dividing the plot by 10^{-8} and then multiplying it by the ion fluence (ions/cm^2) used in the experiment to determine the vacancy density (vac/cm^3). Figure 3.12, illustrates the distribution of carbon and boron incident ions in Y transverse coordinates. The red trails show the dispersion of boron ions in the diamond matrix, while the green paths depict carbon recoils. The dark areas indicate where the main ions stopped after being injected at an incidence angle of 5° to the surface. The radiation damage and range dispersion of the implanted ions is expected to occur inside a depth of 50 nm for carbon ions and 90 nm for boron ions starting from the surface of the diamond. Additional information regarding the outcomes derived by SRIM will be provided in Chapter 5.

3.3.1 Diffusion mechanisms

Following the process of ion implantation, annealing processes at elevated temperatures are employed, assisting the implanted ions to diffuse into the host materials. Atoms move from an area of high atomic concentration to areas with a low concentration in a solid [62]. The atomic flux is represented by the first law of diffusion (Fick's law),

$$F = -D\frac{\partial C}{\partial x}, \tag{3.18}$$

where the concentration gradient is denoted by $\partial C/\partial x$ and D represents the difussion coefficient. Since $\partial C/\partial x$ is negative when the concentration decreases with depth, then the flux into the sample is positive because of the negative in Eq. 3.18. The flux equation describes the movement of atoms from areas of high atomic concentration to areas of low atomic concentration.

Consider a volume with unequal rates of atom influx and efflux. The concentration of diffusing atoms in a volume changes over time based on the flux gradient. This can be stated as,

$$\frac{\delta C}{\delta t} = \frac{\delta}{\delta x}\left(D\frac{\delta C}{\delta x}\right) \tag{3.19}$$

The above expression is referred to as Fick's second law of diffusion, otherwise known as the continuity equation, where the concentration C is the function of position and time. When D is constant, Eq. 3.19 becomes,

$$\frac{\delta C(x,t)}{\delta t} = D\frac{\delta^2 C}{\delta x^2} \tag{3.20}$$

The diffusion coefficient is highly dependent on temperature. The temperature dependency occurs due to the energy needed for an atom to transition between atomic positions, usually a few electron volts (eV). This energy is commonly referred to as the activation energy, E_A. Now, the diffusion coefficient can be expressed as follows,

$$D = D_0 \exp\left(-\frac{E_A}{kT}\right), \tag{3.21}$$

where D_0 is the pre-exponential parameter.

Substitutional vs Interstitialcy mechanisms

Diffusion in materials occurs by vacancies, interstitial, or interstitialcy processes [62]. The prevalent mechanism among these is the substitutional or vacancy mechanism. Three conditions are necessary for the rate of diffusion: a vacancy that is adjacent to a lattice site, jumping energy and the duration of time the vacancy remains near the energetic atom. The likelihood of a vacancy occurring is determined by $\exp(-E_f/k_BT)$. E_f is a vacancy's formation energy in the lattice. This results in the breaking of existing bonds and the formation of new bonds during the transition.

Now, an atom cannot occupy the vacant site when it lacks the necessary energy for it to jump, causing it to oscillates around its equilibrium position. The frequency of jumps is determined by the time the vacancy stays near the atom. If any of these characteristics are missing, an atom cannot jump into the vacant site. Interstitials are common for atoms with a relatively small radii compared to the host material. Small atoms cause less lattice distortion during the diffusion process, i.e., they diffuse easily compared to much larger atoms. Larger atoms often struggle to fit into the interstitial sites or move from one site to another without effectively displacing the surrounding atoms. When the diffusing interstitial atoms are bigger or similar in size to the lattice atoms, the interstitialcy diffusion mechanism occurs. In this scenario, the interstitial impurity atom displaces a host atom from its lattice site. The mechanism repeats when a self-interstitial displaces an impurity atom that is occupying a host lattice site into an interstitial location.

Since boron ions have a relatively larger radius compared to the carbon host atoms in the diamond matrix (refer to text in subsection 2.3.2), it is most likely that the substitutional or interstitialcy mechanism occur during annealing processes.

Diffusion by irradiation

Ion irradiation is quite effective in creating pairs of vacancy-interstitials. Energetic recoiling atoms can cause extremely concentrated atomic displacements in localized regions with high concentrations of defects beyond the equilibrium value. Temperature dependent mobility of defects that can partially anneal out, result in a continuous excess concentration of the defects due to the balance between formation and annihilation rates. An increased concentration of defects results in a higher atomic diffusivity, hence enhancing the diffusion process. For enhanced diffusion due to an irradiation process, the diffusion coefficient is written as,

$$D = \Gamma d^2/6, \tag{3.22}$$

where Γ and d represent the atomic jump frequency and the atomic jump distance, respectively. From the mechanism of a vacancy related diffusion, Γ is represented by,

$$\Gamma = f_v C_v \Gamma_v, \tag{3.23}$$

where C_v represents the vacancy concentration, Γ_v is the vacancy jump frequency proportional to $\exp(-E_m^v/k_BT)$, where E_m^v is the vacancy migration energy and f_v is the correlation factor ~ 1.

The vacancy diffusion coefficient can be defined similarly to the atomic diffusion coefficient,

$$D_v = \Gamma_v d^2/6. \tag{3.24}$$

From the above equations, the vacancy–atomic diffusion coefficient can now be expressed as,

$$D = f_v C_v D_v \tag{3.25}$$

This clearly shows that there is a directly proportional relationship between the enhancement in the vacancy concentration and enhancement in the atomic diffusivity.

Diffusion under irradiation can be accelerated not just by vacancies but also by the creation and movement of additional types of defects such as self-interstitials, divacancies, and defect clusters, which do not exist under normal conditions. The diffusion atomic coefficient can be expressed in relation to different point defects as follows,

$$D = f_v C_v D_v + f_i C_i D_i + f_{2v} C_{2v} D_{2v} + \ldots, \tag{3.26}$$

where C_i is the concentration of the interstitials, C_{2v} is the concentrations of the divacancies, and D_i and D_{2v} are the respective diffusion coefficients. This means that an increase in the concentration of vacancies, interstitials, or divacancies caused by irradiation will lead to a higher diffusion coefficient, D.

3.3.2 Damage recovery with thermal annealing

The ion implantation process involves the transfer of energy between the implanted ions and the target atoms of a solid material, as discussed in the following sections [159, 161]. Varying the energy exchange can be achieved by regulating both the ion dosage and ion energy levels during implants. Contrary to other semiconducting materials or covalently bonded solids such as silicon, which typically returns to an amorphous state when exposed to high ion doses (i.e., a non-crystalline version of silicon without the large-scale structural repeat of the silicon crystalline structure) [129]. The high dosages of ion implantation cause structural damage to the diamond crystal, resulting in a graphite-like condition that negatively impacts the electrical characteristics necessary for semiconducting diamond. Ion impact causes the strong sp^3 bonds in diamond to shatter, leading to a rearrangement into the more stable sp^2 bonds seen in graphite. There is a higher level of intricacy in irradiation damage in diamond compared to other materials [129]. The transformation of diamond into graphite due to excessive damage density during implantation is referred to as graphitization of diamond [146, 164]. The damage density threshold is approximately $\sim 1 \times 10^{22}\,\mathrm{vac/cm^3}$, as reported by Prawer and Kalish [129] and Uzan-Saguy et al. [164]. It is known as the graphitization threshold or amorphization threshold for diamond in literature. Ion-doping investigations suggest that defects created during ion implantation are mostly vacancies/unoccupied lattice sites and interstitials caused by foreign atoms [62, 149, 152]. Therefore, it is proposed that the damage buildup results from interactions between vacancies and interstitials, maybe by recombination of the two defects [149, 152]. Other scientists have suggested that recombination is influenced by the temperature of the substrate. Around T $\approx$ 50°C, the movement of the interstitials is restricted, whilst the vacancies show almost little mobility. Between 50°C and 500°C, the interstitial atoms become mobile and interact with the vacancies, leading to their final annihilation. At temperatures beyond $>$ 500°C, both vacancies and interstitials are able to move and spread across the substrate, potentially combining to create larger flaws or recover the crystalline state.

Thermal annealing of boron implanted diamond

Heat treatment of a semiconducting material implanted below the amorphisation threshold can repair structural damage caused during the implantation procedure and create to a degree the desired defects [94, 165]. Several investigations have been conducted on the impact of annealing after ion implantation of diamond substrates above and below the graphitization limit [166]. The majority of the research is focused on analyzing the variations in electrical conductivity observed during specific annealing procedures, in relation to temperature and duration, as the substrate transforms into graphite or reverts back to diamond [157, 167]. These investigations have shown that graphite has a higher electrical conductivity compared to diamond. Nitrogen is an extensive impurity in diamond that is also used to scale the content of vacancies after ion implantation by utilizing photoluminescence spectroscopy. That is, ion implantation induces the formation of NV^0 and NV^-. During this process below the graphitization limit, substitutional nitrogen N_s and vacancies are generated together with other defects [94, 166]. Several scientists have proposed and demonstrated that vacancies are capable of movement at temperatures between 500°C and 600°C [41, 165, 166]. The N_s defect is persistent with an activation energy of around $\sim 5\,\text{eV}$, observed at temperatures over ~ 1700°C. This high energy barrier influences the creation of defects associated with the interaction between N_s and vacancies, which is dependent on the vacancies' mobility [168, 169]. Mobile vacancies are typically captured by substitutional N_s, leading to the creation of NV center species, specifically NV^0 and NV^- [169]. For boron implanted samples, the presence of some of these impurities limits the desired doping efficiencies and carrier mobilities associated with boron [92]. With the pursuit of superconducting phases via ion implantation techniques, scientists have recently shown that the diamond structure of substrates implanted with high fluences of boron close to $1 \times 10^{17}\,\text{B/cm}^2$, can be adversely affected but recovered when annealed at high thermal temperatures (>1000°C) [39, 92]. The samples also underwent dynamic annealing at temperatures >600°C during the implantation process to limit graphitization. Postannealing at temperatures between 1150°C and 1300°C has been reported to electrically activate the acceptor boron even after implanting at room temperature (RT) [170].

Chapter 4

Experimental considerations: instrumentation and sample preparation

This chapter covers the experimental techniques used to induce p-type type behavior and fabricate MIT layers in type IIa diamond samples. Discussions will focus on the equipment used for ion implantation and heat treatment methods to achieve a specific level of ion-induced damage on the diamond sample used in the project, as well as the equipment used for electronic conduction measurements. The chapter also provides a detailed explanation of the spectral analysis used to confirm the creation of specific defects during ion implantation with dynamic and thermal annealing. The chapter provides sufficient information on the preparation processes for the diamond sample utilized in this study.

4.1 Raman and Luminescence spectral analysis

Photoluminescence spectroscopy

I first consider the Raman and Photoluminescence spectral unit, and give a concise discussion on the photo–mechanisms of both techniques.

Essentially, Photoluminescence is a luminescence phenomenon characterized by a spontaneous radiative energy transition process that includes photon absorption and emission from any form of matter [171, 172]. It is classified into two photon emission mechanisms: fluorescence and phosphorescence. These processes are differentiated by their excitation lifetimes (τ). Fluorescence decreases rapidly after being excited, having a duration of approximately $\sim 10\,\text{ms}$, whereas phosphorescence decreases considerably more slowly with a lifetime of around $0.1\,\text{s}$ [173]. This study utilized an Argon (Ar) laser with a wavelength of 514.5nm to confirm the presence of NV center defects in diamond that exhibit a rapid emission rate of over $>10\,\text{ns}$. We utilize photoluminescence (PL) spectroscopy to study the optical characteristics of NV centers in diamond material in order to scale the formation of vacancies in diamond.

When semiconducting materials are photo-excited with energy matching the band gap of the material (i.e., $E_i = hv_1 = E_g$), it generates an abundance of electron-hole recombination couples [174, 175]. When the excitation energy exceeds the band gap energy, it might stimulate defect levels within the band gap of the substance. The laser source with an energy of $2.41\,\text{eV}$ ($514.5\,\text{nm}$) is absorbed

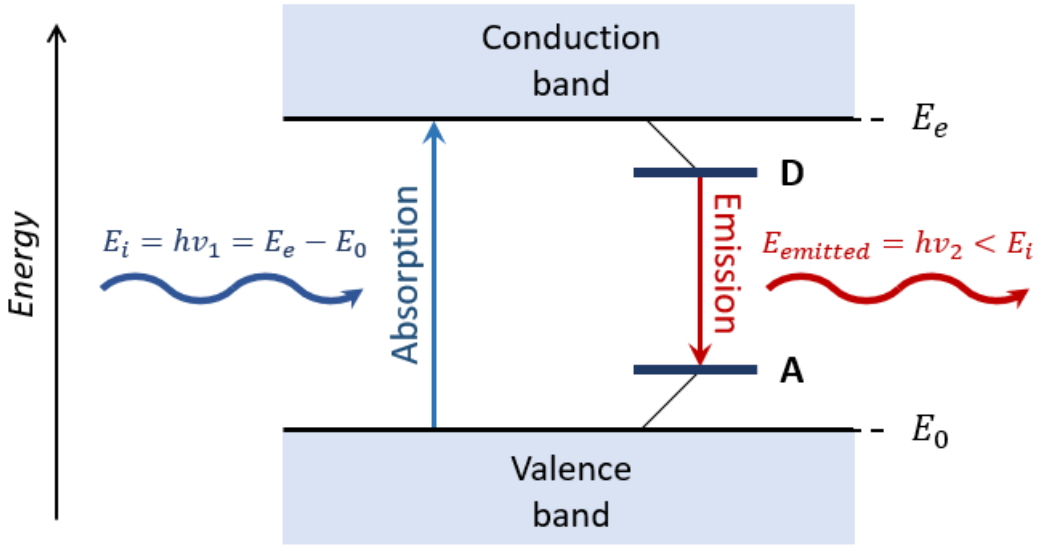

Figure 4.1: **Schematic for band-to-band excitation process.** A photon with incident energy (E_i) excites an electron from its ground state energy (E_0) to an excited state (E_e). For $E_i \geq E_g$, photoluminescence generation takes place, with electron and hole donor-acceptor (D⟶A) emission pair, and emits a photon.

by the NV centers, causing the ground state defect electrons to move to higher energy levels inside the energy gap. During the process, photons are emitted with energies of 1.945 eV and 2.156 eV for NV^- and NV^0 centers, respectively. This refers to the band gap between the conduction and valence bands' electronic states. When semiconductors are photo-excited, the electrons and holes undergo radiative recombination, leading to photo-induced luminescence. This process involves the emission of photons with less energy than the incident photons ($E_{emitted} = hv_2 < E_i$) between the donor and acceptor energy levels (D→A), as shown in Fig. 4.1 [173]. Thus, Photoluminescence spectroscopy involves measuring the emission of photons from a material, often caused by an excited electron returning to its ground state after being stimulated by photons. The technique yields useful insights into the electrical structures, emission mechanisms, and defect makeup of the material. Contemporary devices may now provide spectra showing the relationship between intensity and wavelength by analyzing the scattered optical signal in photoluminescence studies. Photoluminescence studies of diamond have been commonly used to analyze the different flaws present inside the diamond structure. The spectra of NV centers exhibit zero-phonon lines (ZPLs) at 637 nm and 575 nm for NV^- and NV^0, respectively, when irradiated with a green laser source with a wavelength between 514 nm and 570 nm. The zero-phonon lines (ZPLs) for both charged states of the center align with the indicated emitted photon energies. The sample analyzed in this experiment underwent PL intensity analysis to identify the existence of NV center defects both before and after the ion implantation procedure.

Raman spectroscopy

When beam of light shines on a sample, photoluminescence caused by the ionization of atomic electrons is not the sole phenomenon that occurs. Raman scattering process also occurs during the illumination process where a very small fraction of the incident photons are scattered, and a change of energy is observed associated with Stokes

and anti-Stokes transitions in conjuction with Rayleigh scattering (refer to Fig. 4.2). Rayleigh scattering is the most common transition because it does not need a change in the vibrational state of the molecule. The anti-Stokes transition is less frequent since it necessitates the molecule to be in a vibrationally excited state prior to the photon's impact. Typically, Raman measurements utilize only Stokes scattering due to the weak anti-Stokes signal intensity and the need for filtering out photons with greater incoming energy.. The process entails a photon interacting inelastically with a molecule, resulting in the photon losing energy and causing the molecule to vibrate. Raman scattering produces a Raman effect in which the scattered photon has lower energy. The light that is linked to it shows a change in frequency or wavenumber (cm^{-1}). Different chemical vibrations cause frequency shifts that create a unique spectrum for each substance.

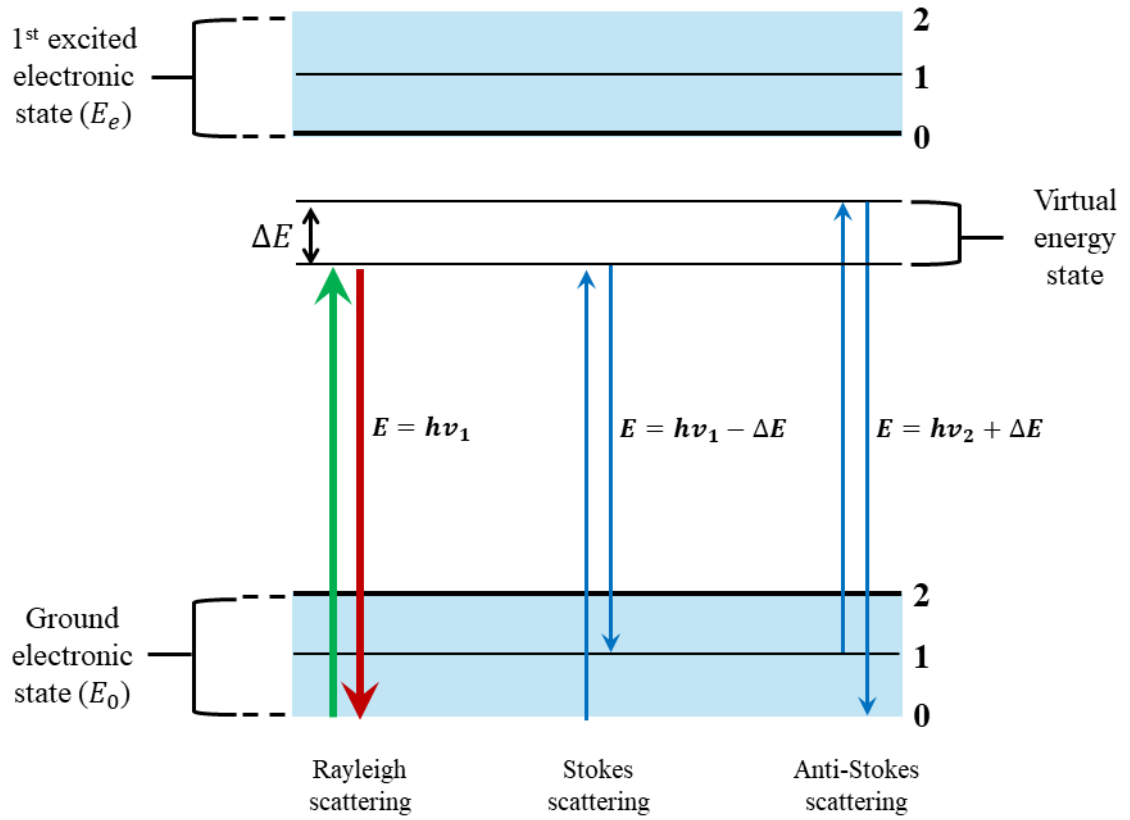

Figure 4.2: **Raman scattering of light.** Three types of Raman scattering induced in a molecule by a photon energy with $E = hv$.

Sir Chandrasekhara V. Raman is recognized as the first individual to showcase this phenomenon in 1928 by utilizing sunlight filtered via a prism and toluene as the scattering medium. Raman analysis is not included in this dissertation as the focus is mostly on photoluminescence effects. We utilize a Raman spectroscopy equipment for material analysis because of its excellent spectral resolution [176]. For a thorough grasp of Raman spectroscopy, consult the following texts: Karr [177] and Brüesch [178].

4.1.1 Raman & PL experimental system

The Horiba Jobin-Yvon LabRam HR800 spectrometer was employed for spectral analysis of the pristine diamond substrate before and after ion implantation. It is

located at the Raman and Luminescence laboratory, School of Physics and Microscopy and Microanalysis unit, University of the Witwatersrand, as depicted in Fig. 4.3. Each unit of the setup comprises four main components: two lasers (Argon Ion laser for 514.5 nm and 457.9 nm excitation), an optical microscope system, a spectrometer, and an optical detecting system. The equipment also has a motorized micrometer movement (x,y) stage to enable precise examination of samples of different sizes at small position intervals. The LabSpec software is pre-programmed to automate the stage motions during PL intensity mapping measurements, with a step-size resolution that may be adjusted to as tiny as 0.1 µm.

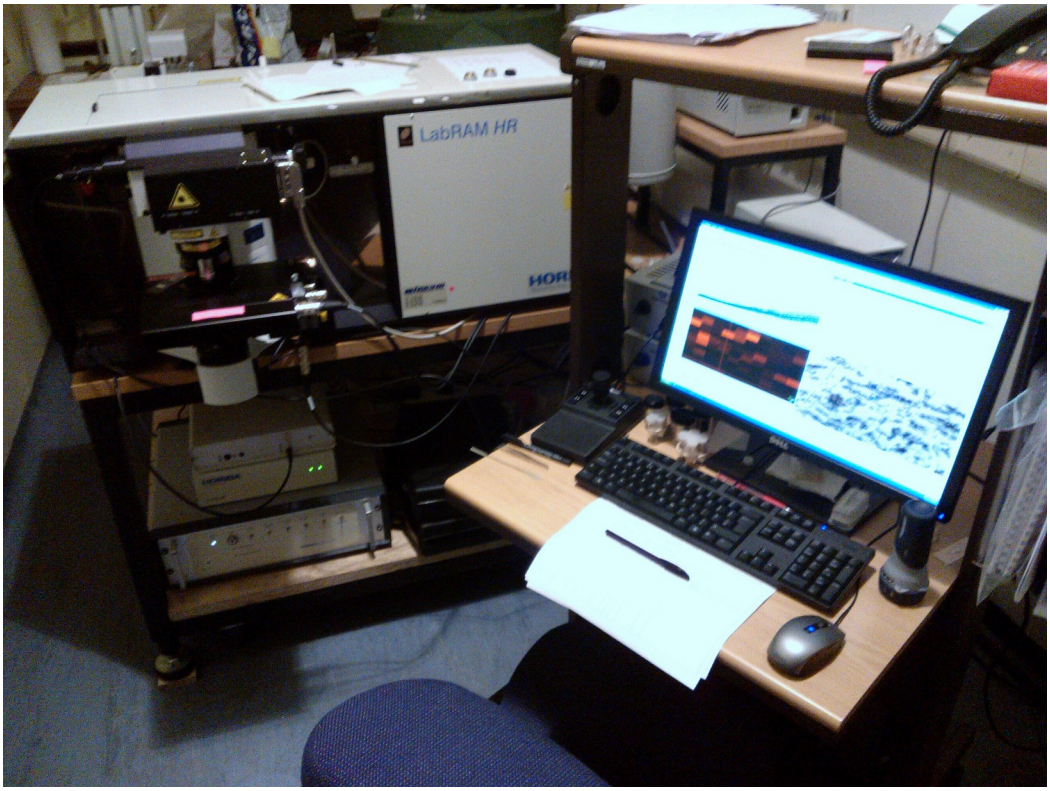

Figure 4.3: **The Horiba Jobin Yvon LabRam HR800 spectrometer.** A photograph of an operational Raman/PL spectrometer hardware taking measurements.

Figure 4.4 depicts the design of the system while operating with either laser 1 (He-Ne) or laser 2 (Argon) entering the spectrometer. Plasma line filters are installed at every laser input point to eliminate any laser plasma emission lines. The laser beam passes via an Optical Density (OD) wheel to adjust its wavelength strength, then is fully reflected by an edge filter and directed towards a sample on a computer-controlled (x,y) stage. The stage is located beneath an Olympus system microscope type BX40, which is equipped with various objectives using variable numerical apertures (NA). The laser beam is focused through one of the objectives onto the sample, and the scattered light is collected in a backscattering arrangement by the same objective. The edge filter allows the passage of PL and Raman scattered photons from the sample while reflecting any backscattered laser light. The polarized light scatters and is concentrated by a converging lens through a pinhole to create a picture of the sample.

The light is collimated and sent into a diffraction grating to scatter it according on

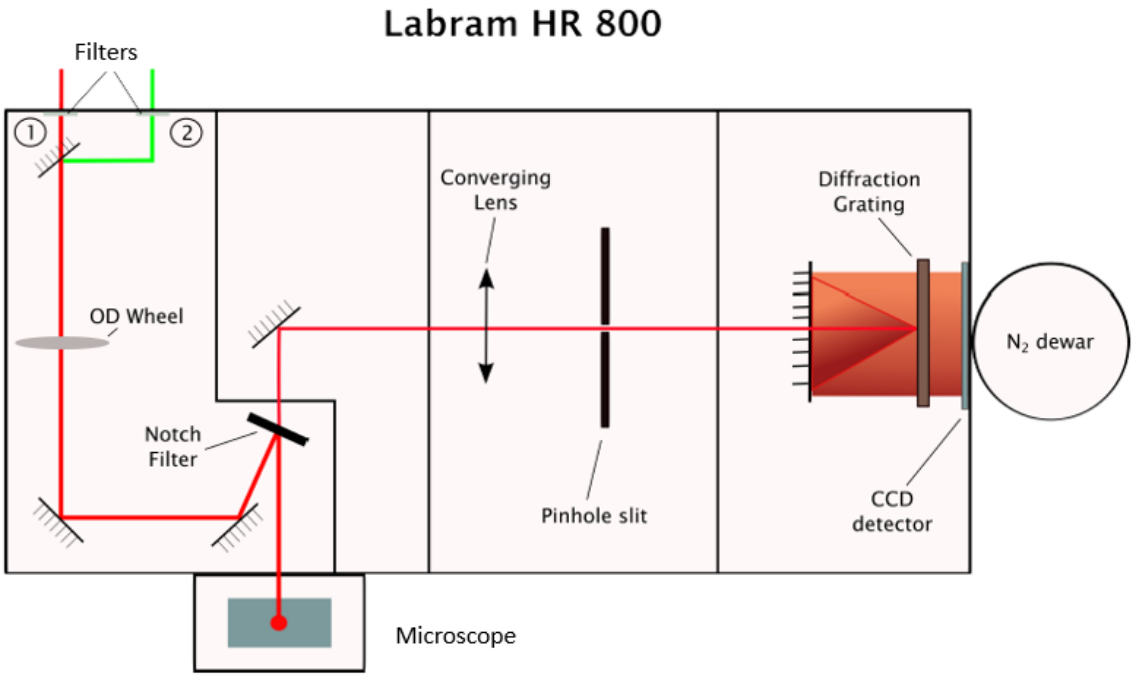

Figure 4.4: **Schematic of a Raman spectrometer.** Laser light is directed into a specimen by optical components. The resulting fluorescence is dispersed and directed to a CCD detection system for imaging.

its wavelength. It then reaches a Symphony charge-coupled device (CCD) detecting system, which is chilled with nitrogen to enhance signal detection. A TV display is connected to the CCD detection camera to observe the sample or laser on the sample.

4.2 Ion Implantation system

Throughout this research I utilized ion implantation as the primary method to introduce foreign ions into diamond samples in a consistent and controlled manner. The instrument used was the Varian-Extrion 200–20A2F ion implanter located at iThemba LABS ,Gauteng, South Africa. Figure 4.5, depicts an image of the ion implanter system that was used. The ion implanter is designed for introducing dopants into semiconducting materials by using electrostatic beam scanning on target wafers, primarily for producing commercial semiconductor devices. The apparatus was modified for research purposes.

This ion implanter, like many others utilized in current research, consists of five main components that work together effectively to move ions from a source to a target specimen through a processing chamber [179–181]. Figure 4.6, is a schematic of a standard ion implanter, highlighting the five main components: the ion source, magnetic particle filter, electrostatic accelerator, beam manipulating system and an end station which has been modified for research applications and does not include the typical wafer processing assembly found in production type semiconductor wafer processing ion implanters. Every part is essential in the ion implantation process, where high-energy beams are used to insert specific dopant species into a chosen target material, typically a semiconductor. The dopant species vary from solid to gaseous compounds produced from suitable sources [180, 182].

Figure 4.5: **Photograph of the ion implanter at iThemba LABS.** A Varian-Extrion model 200-20A2F.

The ion source produces plasma containing the necessary ion species for implantation. An electrostatic field created by a 23 keV energy supply extracts the hot ionized beam from a hot cathode arc discharge ion source. The 2 keV from the electrodes guide the charged ions towards a 90° magnetic particle filter, where the magnetic field can be adjusted to selectively filter ions of a given atomic weight. Undesired ions are captured by the magnetic walls of the analyzing magnet chamber, while a beam of the required ions is sent via an adjustable slit, which also regulates the intensity of the beam by opening and closing. After being resolved, the ion beam is directed into an accelerating tube to supply the necessary energy for effective ion implantation.

The acceleration tube can be adjusted in three modes: drift mode, post-acceleration, and post-deceleration modes, based on the desired implantation energy. Drift mode is when the beam energy stays constant. The source energy provides the initial energy, while the post-acceleration and post-deceleration modes include adjusting the ion beam energy within the ranges of 25 keV – 180 keV and 0 keV – 7 keV, respectively [183]. The acceleration is generated via a high-frequency Cockcroft-Walton power source that is built into the accelerating tube, as shown in Fig. 4.6. The 25 kV boron ion beam from the source was accelerated to 30 kV in the acceleration tube, while a carbon beam with the same voltage was decelerated to 15 kV during the implantation process. Upon entering the manipulating system, the ion beam encounters a series of electrostatic quadrupole lenses that realign the beam towards the horizontal (X) and vertical (Y) electrostatic beam deflecting plates. The plates alter the direction of the beam in both vertical and horizontal planes, allowing

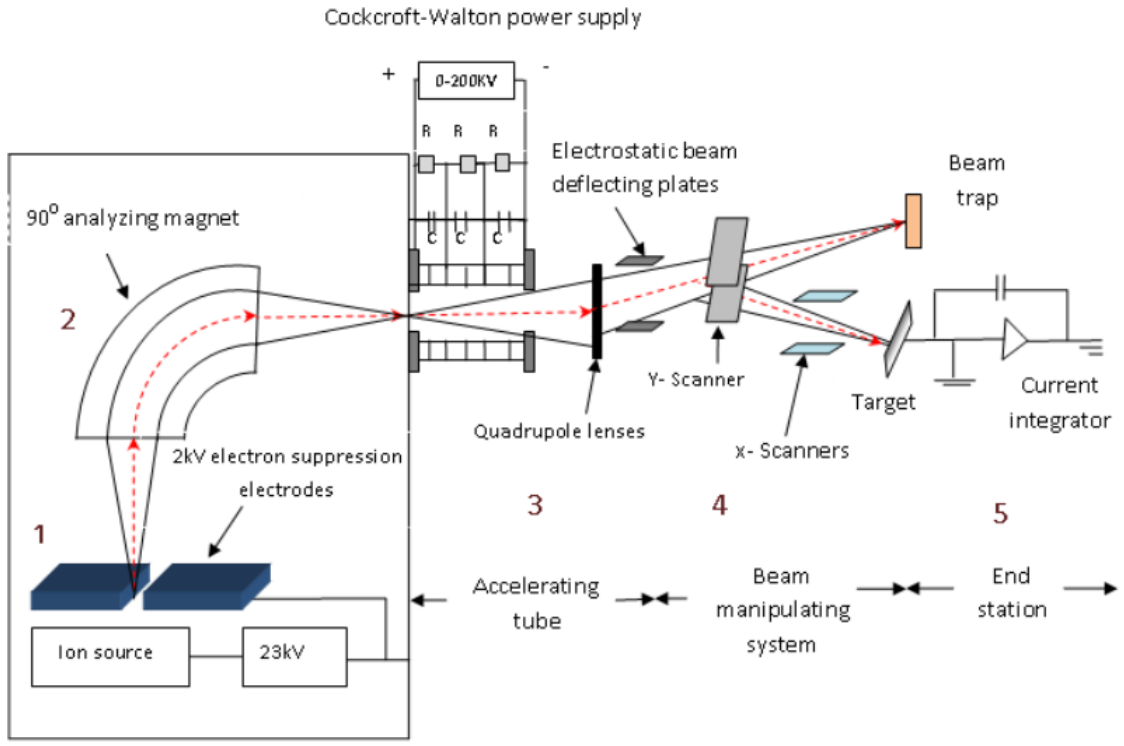

Figure 4.6: **Schematic of an ion implantation process.** A schematic of the ion implanter made up of 5 components: ion source, magnetic particle filter, electrostatic accelerator, beam manipulating system and the end station [183].

it to scan across the surface of the wafer in a raster pattern to evenly cover the area being scanned. The substance being targeted is typically placed in a clean target chamber. The ion beam is analyzed by a Faraday cup assembly positioned at the end station of the system to determine the implanted ion fluence. The ion fluence can be determined by measuring the integrated current at four corner Faraday cups positioned in the end station assembly of the ion implanter. A current integrator monitors the ion fluence being implanted into the sample and redirects the beam once the necessary ion fluence is achieved.

4.3 Thermal Tube furnace

As discussed in the preceding, heat treatment is necessary after implantation to repair the integrity of the sample and influence the concentration of the desired defects. A commercial Carbolite (Gero type) Wire Wound Tube Furnace was used for this project. CFT 17/300, shown in Fig. 4.7, was utilized to activate the mobility energy for vacancies produced. The equipment is a 1700°C horizontal tube furnace with a 9 cm accessory tube for gas flow, computer control, and full data logging capabilities. The facility is situated at the Wits University campus, namely at the School of Physics, University of the Witwatersrand in Johannesburg.

The design features high temperature recrystallized alumina (RCA) worktubes to ensure thermal homogeneity, specifically tailored for high temperature applications, as illustrated in Fig. 4.8. The sample is placed in a quartz boat crucible and inserted into a quartz worktube with dimensions of 9 cm in diameter and 75 cm in length during operation. The boat is positioned near the center of the furnace tube to

Figure 4.7: **A photograph of a Carbolite high temperature horizontal thermal tube furnace.** A wire wound tube furnace (CTF 17/300) with a 0°C – 1700°C temperature range.

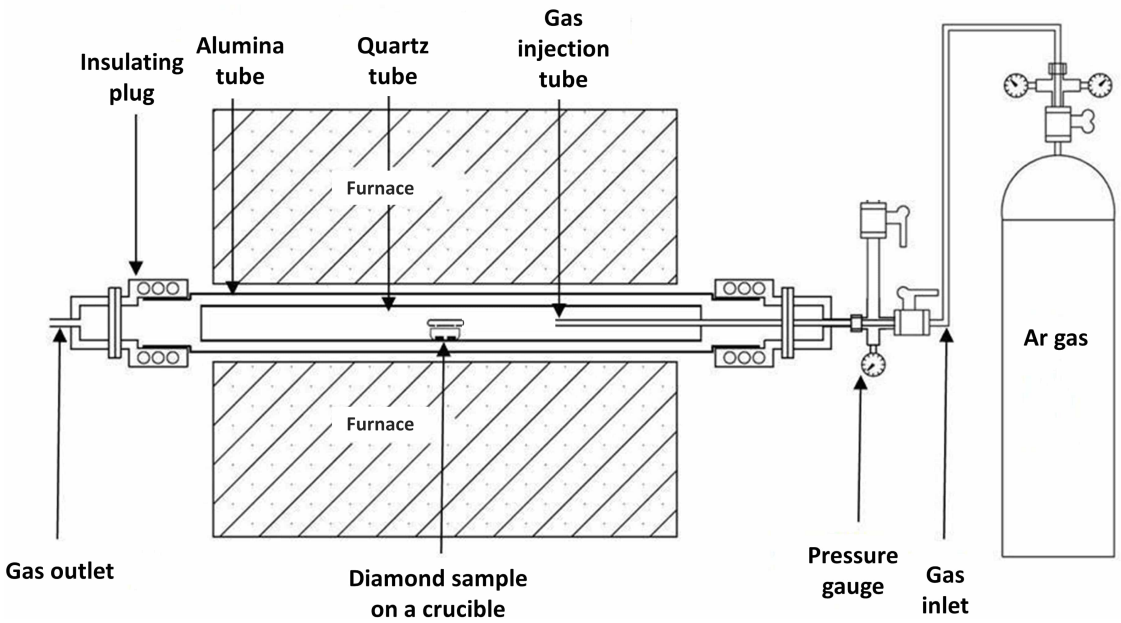

Figure 4.8: **Schematic of a typical horizontal furnace tube.** A diamond sample is annealed in a presence of Ar gas enclosed by an RCA high temperature tube [184].

ensure even temperature distribution. The tube is tightly sealed using cylindrical end guards at both ends, which are equipped with seal rings and connected to insulating plugs to provide consistent temperature distribution. High-purity argon gas is continuously flowed into the quartz tube through a gas nozzle at the end guards to prevent graphitization by avoiding an oxidizing environment during annealing. Each of the main diamonds used in this research underwent 3 separate annealing processes for a period 30-minutes at a temperatures of 650°C, 850°C and 1000°C.

Finally, to eliminate any contamination and prevent the production of graphite on the sample surface, the annealed substrates were immersed in an oxidizing acid solution and boiled for a specified duration [156, 185].

4.4 Metal evaporation system

The technological advancement of electronic and sensing devices based on super-hard materials such as diamond has been prevalent in recent times [186]. Nearly all of this devices rely on the fabrication of at least one low-resistivity Ohmic contact [187], i.e., non-rectifying metal contact pads that act as junctions for conducting materials, having a characteristic linear I–V curve. High-resistivity Ohmic contacts have been shown to significantly modify the electric characteristics of the measured device [188]. Although, the performance of the contacts mainly depend on the dopant concentration within the material involved, the annealing temperatures as well as the surface pre-treatment of the material [187, 188]. Scientist have demonstrated over the years that heat treatment of metal diamond contacts results in the formation of carbides which reduces the electric resistivity of the contacts [188]. To date, numerous studies based on diamond contact resistivity and annealing have been conducted. And, conventionally a bilayer of titanium (Ti) and gold (Au), Ti–Au metallization scheme is largely utilized due to the reduction of contact resistivity imposed by Ti induced carbide [187]. This follows the deposition of thin Ti adhesion layer and a Au interconnect metal layer on top of a diamond substrate.

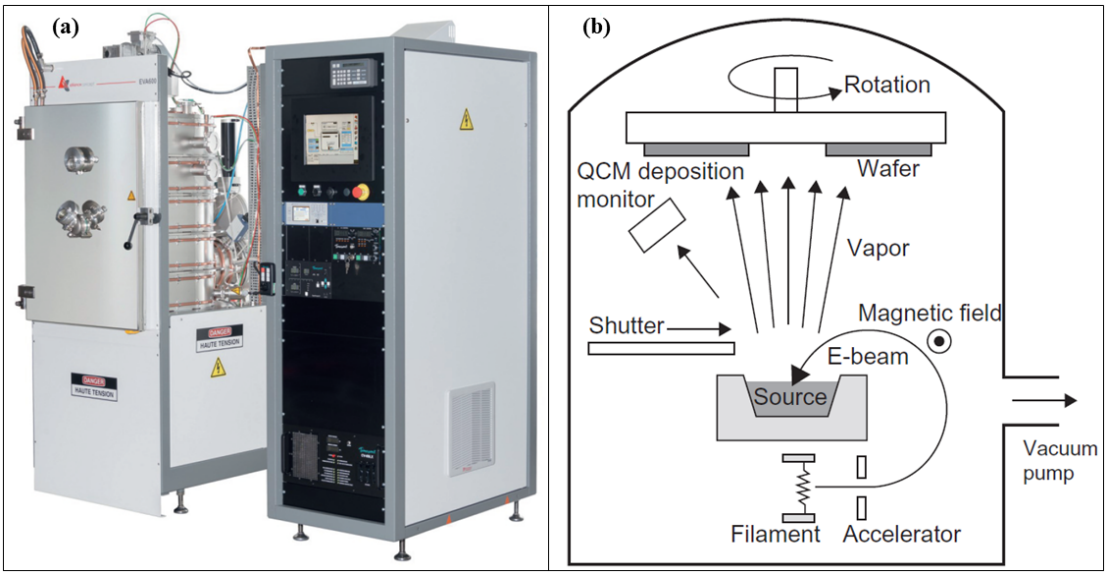

Figure 4.9: **PVD system for thin film coating by evaporation and schematic of an e-beam system.** (a) This is the EVA600 e-beam system that allows metal film deposition of various metal concurrently without breaking vacuum. (b) A filament generated e-beam is accelerated and magnetically directed towards a source material which evaporates inside a vacuum chamber [189].

Figure 4.9 (a), depicts the Physical Vapor Deposition (PVD) for e-beam evaporation system that was used to fabricate thin films of Ohmic contacts in a 4-point Van der Pauw configuration in order to effectively study both Hall effect and electronic transport properties in boron doped diamond. The system used is located at the Claude Bernard Lyon 1 University, Lyon, France. Figure 4.9 (b), shows

the schematic for the process of metal deposition. E-beam evaporation utilizes the thermal emission of electrons from a filament to heat a metal source [190]. Usually, operation is under high vacuum($\sim 10^{-7}$ Torr), to reduce contamination on the surface of the substrate. A magnetic field is utilized to deflect the electron beam by an angle of 270° in order to prevent direct contamination from the filament (see Fig. 4.9 (b)). While heating a metal source, a shutter is used to prevent any unnecessary contaminants landing directly onto the substrate surface during the melting or sublimation process of the metal. A Quartz crystal microbalance (QCM) is used to monitor the deposition rate and thickness of the deposited film by detecting changes in resonance frequency caused by variations in mass on the chip surface of the device. Electron beams are suitable for materials that necessitate elevated temperatures for evaporation. Also, e-beam is appropriately utilized for deposition on a larger set of samples.

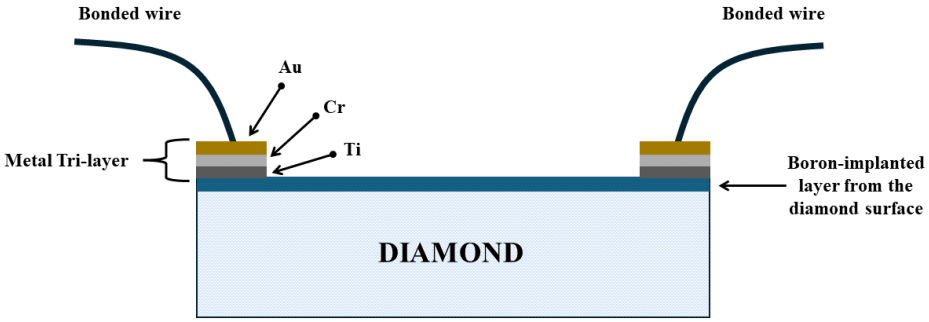

Figure 4.10: **Schematic of diamond with a metal tri-layer.** Wire-bonded metal tri-layer of Ti, Cr and Au deposited onto the diamond surface.

In this study a layer stacking of metals Ti–Cr–Au were deposited sequentially on several boron-doped diamond acid cleaned surfaces without breaking vacuum and the pressure never went above $>10^{-4}$ Torr (see the metal stacking schematic in Fig. 4.10). Cr is essentially a barrier that prevents diffusion between Ti and Au [191]. The diamond was masked with two foil strips in a cross-shape to expose only the corners of the sample. The metal stacking was 350 nm–Ti, 100 nm–Cr and 150 nm–Au, all with a deposition rate of 4 Å/s. After deposition, the metal deposited diamonds are transferred into an ultra-high vacuum (UHV) chamber (located at ILM, Lyon, France), for annealing at 450° for the formation of titanium carbide (TiC) [192]. The thremally annealed samples are then wire-bonded to suitable Lead-less chip carrier (LCC) or a PPMS puck for Hall effect and electronic transport measurements.

4.5 Low-temperature measurement system

The electrical properties of materials are crucial in determining the performance of solid-state devices and, consequently, their suitability for various applications [193]. As stated thus far during the course of this thesis, hall effect and electronic transport properties of boron-doped diamonds have been vastly studied, more so in the last few years due to the superconducting behavior of such materials. Interest being the "*holy grail*" of condensed matter Physics, i.e., to experimentally achieve the theoretically predicted critical temperature (T_c) close to room temperature. The Van der Pauw 4–point probe configuration (see Fig. 4.11), is commonly used to test the electrical properties of semiconductors, including conductivity, carrier density, and

mobility [193, 194]. This method can test samples of any shape, although, specific sample conditions must be met to get precise measurements [195]. The most crucial factors include uniformity of the sample, consistent sample thickness, and ideally, small point contacts positioned at the sample edges. Furthermore, it is essential to ensure that the contact quality exhibit good ohmic behavior.

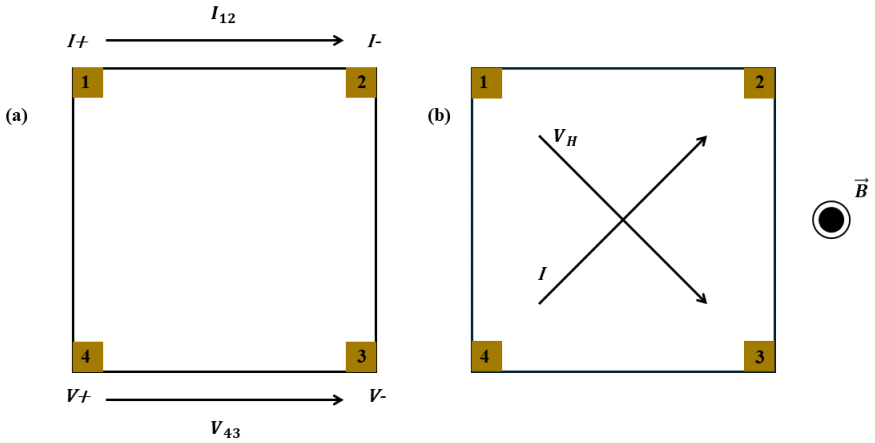

Figure 4.11: **The 4-point contact configuration.** Van der Pauw configuration for the electrical properties of square boron-doped diamonds with magnetic field $\vec{B}$.

The Van der Pauw method for measuring resistivity utilizes a constant-current approach (refer to 4.11 (a)). This is very beneficial for measuring small samples as the sample size and contact space are insignificant. This method involves utilizing four separate contacts located on the edge of a flat sample of any shape. Eight measurements are taken around the sample [196]. At zero magnetic fields, two values of resistivity ρ_A and ρ_B are computed as follows,

$$\rho_A = \frac{\pi}{ln2} f_A t_s \frac{V_{34} - V_{43} + V_{41} - V_{14}}{4I} \tag{4.1}$$

and

$$\rho_B = \frac{\pi}{ln2} f_B t_s \frac{V_{21} - V_{12} + V_{32} - V_{23}}{4I}, \tag{4.2}$$

where t_s thickness of the conduction layer in cm, f_A and f_B are the geometrical correction factors. A constant current I is passed through adjacent contact pairs while the voltages V_{xy} are measured between the corresponding adjacent contact pairs (where $x, y = 1, \ldots, 4$). The two resistivities should agree to within $\pm 10\%$. If not, the sample maybe overly inhomogeneous or anisotropic. The geometrical factors f_A and f_B are based on sample symmetry and are related to voltage ratios Q_A and Q_B, expressed as follows,

$$Q_A = \frac{V_{34} - V_{43}}{V_{41} - V_{14}} \tag{4.3}$$

and

$$Q_B = \frac{V_{21} - V_{12}}{V_{32} - V_{23}} \tag{4.4}$$

The relationship between f and Q is given by the following transcendetal expression,

$$\frac{Q-1}{Q+1} = \frac{f}{ln2} cosh^{-1}\left\{\frac{1}{2}\left[\exp\frac{ln2}{f}\right]\right\} \tag{4.5}$$

For perfect contact symmetry $f_A = f_B = 1$ [196].

Correction factors are necessary when the sample is much smaller than the probe separation in any of its dimensions. Essentially, resistivity measurements are influenced by the geometry and are very responsive to boundary conditions. Therefore, correction factors have to be computed. Special restrictions are often enforced, especially in the instance of a small irregular region. Hence, the 4–point probe has been the most convenient method for measuring resistivity, leading to the development of various corrections. The probe array does not always have to be linear. The square design is the most frequently utilized, with different configurations offering advantages for specific applications or sample shapes.

During Hall measurements in the presence of a magnetic field ($\vec{B}$), the same 4-point configuration is used where the current and voltage are oriented perpendicular to each other, as depicted in Fig. 4.11 (b). Two resistivity measurement configurations are computed: $R_{13/42}$ or $R_{42/13}$. Now, from the Hall voltage (V_H) that is measured (refer to Fig. 4.11 (b)), it is possible to determine the Hall coefficient (R_H),

$$R_H = \frac{V_H t_s}{I\vec{B}} \tag{4.6}$$

and subsequently the carrier concentration (n),

$$n = \frac{1}{R_H q}, \tag{4.7}$$

where q is the elementary charge. From the Hall coefficient and resistivity, it is possible to determine the Hall mobility (μ), by using the following expression,

$$\mu = \frac{R_H}{\rho} \tag{4.8}$$

The Lake Shore cryogenic system

Now, amongst other similar operational systems that were used in this project, Fig. 4.12, shows the Lake Shore Hall effect/electronic transport measurement system (HMS) used for the electrical properties of certain samples investigated in this project. The experimental setup is located at the Nano Electronics Research Laboratory, Department of Physics, University of Cape Town, Rondebosch, Cape Town, South Africa. The system comprises capable, integrated hardware and software that are available commercially. That is, single-field measurements for bulk semiconductors and variable-field measurements for complex compound semiconductor characterization at temperatures ranging from 2 K to 800 K. The system comes with a standard measurement instrument configuration that includes: Lake Shore Model 776 Hall matrix card, Lake Shore Model 475 DSP gaussmeter, Keithley Model 6220 current source, Keithley Model 6485 picoammeter and a Keithley 2182A nanovolmeter. Notwithstanding, a sample module that is the physical interface between the sample and the measurement instrumentation.

Figure 4.12: **A Lake Shore transport measurement system.** The system is capable of measuring the electronic transport characteristics of electrically conductive materials.

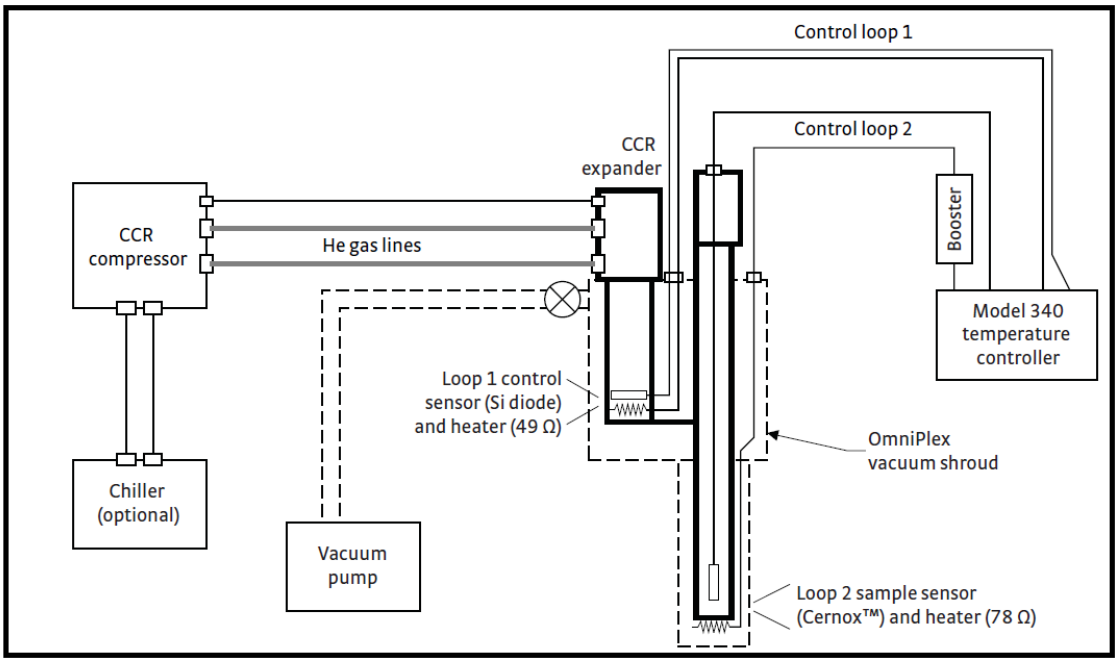

Figure 4.13: **Operation schematic of a the HMS Lake Shore system.** A sample with ohmic contacts in a 2- or 4-point configuration is attached to the sample sensor for measurements at liquid helium temperatures.

Figure 4.13, shows the operation schematic for the HMS. The setup consists of a gas supply line for the refrigerant, in this case helium. This enables the cooling capacity of the system which is achieved by the closed cycle refrigerator (CCR) by providing a variable temperature environment through the cooling helium exchange gas. The temperature range is balanced by two heater circuits controlled by a temperature controller. The vacuum pump evacuates the Omniplex vacuum shroud

by pumping to the lowest pressure ($<10^{-2}$ torr). A sample with ohmic contacts is soldered or connected to a suitable sample card on the closed cycle refrigerator sample module (CCRSM). Which in turn is slotted into the Omniplex vacuum shroud where the sample is located at the tail of the vacuum chamber, i.e., close to loop 2 sample sensor. The cooldown to $\sim 10\,\mathrm{K}$ takes about $1-2\,\mathrm{h}$. Measurements can be taken as the system cools down from or ramps up to room temperature.

Temperature-dependent I–V plots

By utilizing the low-temperature measurement system it was possible to generate temperature–dependent I–V plots in order to study the carrier transport mechanisms of the samples. A linear current sweep for the I–V curves was employed to examine the Ohmic behavior of the boron implanted samples. That is, current is varied linearly over time, while the corresponding voltage is measured at each temperature set-point from $10\,\mathrm{K} \longleftrightarrow$ RT. The temperature set-points can be attained while ramping up or down at specified intervals for consistent measurements, i.e., 5 K or 10 K.

The current applied to the Ohmic contact pads was swept with a current range between $0\,\mu\mathrm{A} - 1\,\mu\mathrm{A}$ at $0.1\,\mu\mathrm{A}$ intervals for the *relatively* more restive samples (**NB.** the current range depends on the electronic response of the sample). The voltage is measured continuously and plotted as a function of the applied current to generate the I–V curves $\Longrightarrow$ the investigation of the samples' resistance using Ohm's law. The I–V curves provide the necessary information pertaining to the sample's behavior under different current levels. This is a pivotal process to determine the electronic characteristics of the boron implanted regions of the samples such as the threshold voltage, breakdown voltage, and regions of Ohmic and non-Ohmic behavior.

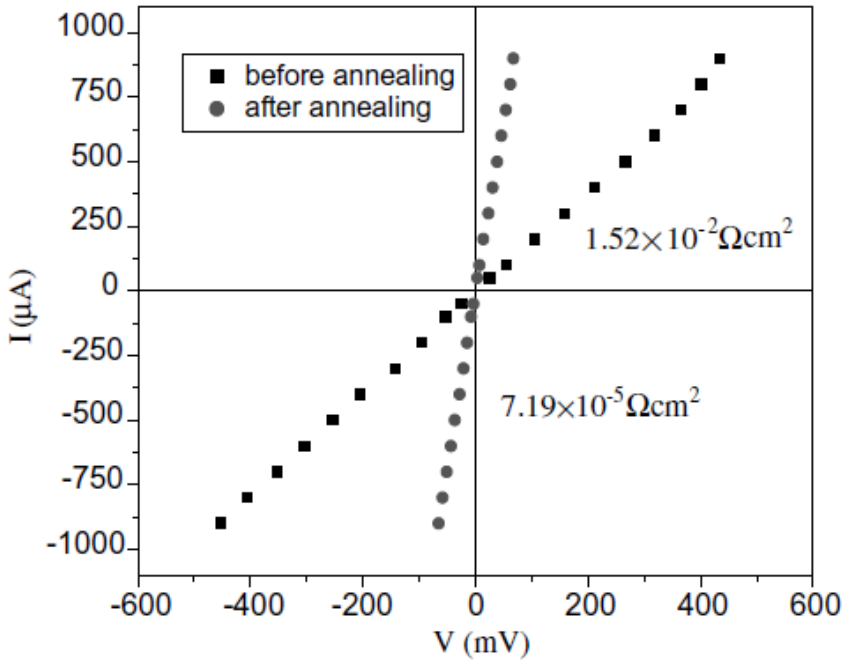

Figure 4.14: **Ohmic behavior of boron implanted diamond.** The I–V curves of a boron implanted sample determined using Ta–Au Ohmic contact pads. The Ohmic characteristics improve with thermal annealing at 500° [197].

For a semiconducting material such as diamond with a wide band-gap the

conducting properties can be altered by extrinsic factors such as the fluence used in ion implantation, annealing [198–200] and types of Ohmic contact pads [188, 201]. Regarding Ohmic contacts, Zhen et al. [197], showed the effect of thermally induced carbide formation (TaC) on the I–V characteristics of a boron implanted diamond (see Fig. 4.14). Clearly, after annealing there is a significant increase of the gradient of the linear I–V profiles, implying a decrease in the resistivity.

Space charge limited current in diamond (SCLC)

Furthermore, the electrical conduction in diamond can also be negatively influenced by the *space charge limited current* phenomena rather than the intrinsic properties of the material such as resistance [67, 202, 203]. That is, the accumulation of localized charge carriers (electrons or holes) such that the resultant electric field affects the mobility of additional charges. Consequently, the current does not increase linearly with applied voltage consistent with Ohmic behavior. In contrast, the current follows a power law dependence to the applied voltage: $I \propto V^2$.

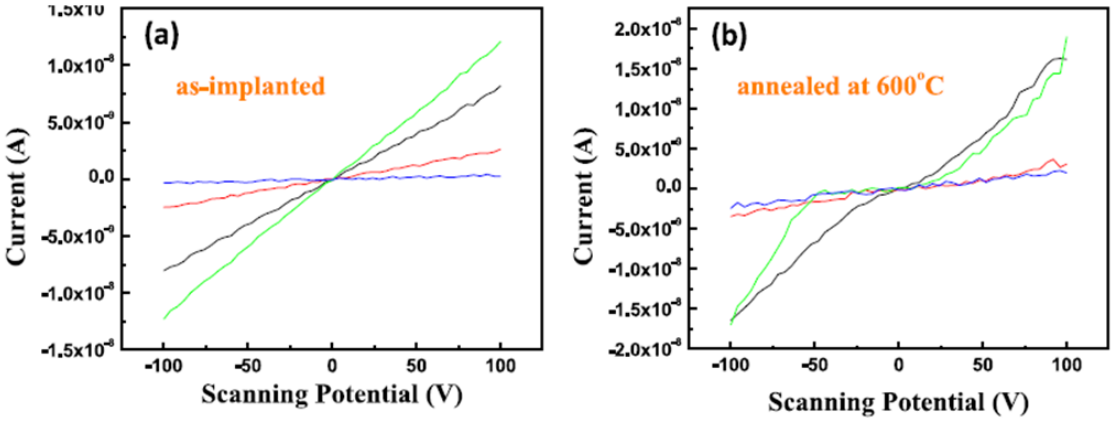

Figure 4.15: **I–V plots with SCLC characteristics for carbon-implanted diamond.** The measured I–V curves of carbon-implanted diamond (a) before annealing and (b) after annealing at 600 °C. The carbon fluence is $1 \times 10^{14}\,\mathrm{cm}^{-2}$ (blue line), $1 \times 10^{15}\,\mathrm{cm}^{-2}$ (red line), $2 \times 10^{15}\,\mathrm{cm}^{-2}$ (black line) and $5 \times 10^{15}\,\mathrm{cm}^{-2}$ (green line) [203].

Wang et al. [203], has recently characterized the (SCLC) on surfaces of carbon-implanted diamonds. Figure 4.15, demonstrate the carbon ion fluence threshold ($\sim 1 \times 10^{15}\,\mathrm{cm}^{-2}$) that induces the SCLC effects after annealing at 600 °C. It has been suggested that the vacancies created by the carbon transient ions likely result in the creation of a band for the localization and transport of free carriers, whereas the resulting interstitials in the shallow surface layers may produce a localized field that opposes the drift current. As a result, the interaction between the external and localized fields can cause a trapped space charge to form near the anode, ultimately restricting the electrical current flow through the diamond layers.

4.6 Sample preparation

The low temperature properties of Boron implanted diamond is an ongoing research odyssey within the science community. In this particular study, seven similar commercial diamond samples have been uniquely prepared to study the effect of Boron ion implantation with subsequent annealing. The commercially available

single crystal CVD diamond samples having dimensions $2.6 \times 2.6 \times 0.25\,\mathrm{mm}^3$ with (100) crystallographic orientation were used for boron ion implantation, annealing and analysis. The impurity concentration of this samples is given as less than 1 parts per million and less than 0.05 parts per million for nitrogen and boron respectively (i.e., N<1 ppm and B<0.05 ppm). All diamond samples are courtesy of Element Six.

4.6.1 Fabrication of boron p-type layers

Implantation process

Raman and PL measurements were performed to study the structural integrity of all the samples before the ion implantation and annealing processes (i.e., a pristine structure). The samples showed little to no Raman or PL activity apart from the 1st order Raman peak (to be discussed in detail in Chap. 6). This was followed by SRIM simulations as discussed in Chap. 3 (C), which was conducted before the ion implantation process for 5000 carbon and/or boron ions injected in a diamond material for various ion energies as specified in Tab. 4.1. The simulations gave a good indication of the expected depth and ion damage distribution.

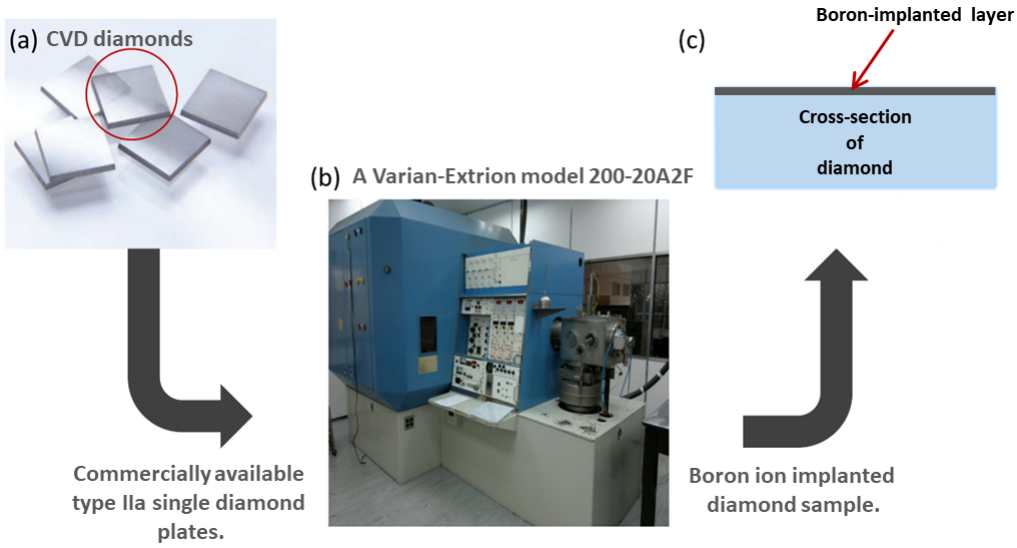

Figure 4.16: **Ion implantation process.** (a) A single commercially available diamond plate undergoes ion implantation process. (b) A Varian-Extrion model 200-20A2F. (c) Ion implanted diamond plate with a keV boron-implanted layer in proximity to the diamond surface.

Boron triflouride (BF_3) and carbon monoxide (CO) gases were used to produce the ions required for boron and carbon implants, respectively. The implantation parameters for the seven implanted samples are depicted in Tab. 4.1. Figure 4.16, depicts the schematic for the process of ion implantation. Samples A–B and D, have been implanted with carbon and boron ions with a consistent low temperature dynamic annealing at 200 °C and 400 °C for carbon and boron ions, respectively. The low energy 15 keV carbon ions ascertain lattice vacancies close to the diamond surface (~ 40 nm) where the deeper (~ 80 nm) implanted low energy 30 keV boron ions should "expectantly" diffuse and occupy the vacant lattice sites (see Fig. 3.12). The difference in fluence falls within the MIT range ($2 \times 10^{20} - 3 \times 10^{21}\,\mathrm{cm}^3$) and is used to investigate the damage profile of the diamond samples. Sample C was

Table 4.1: Sample parameters before and after ion implantation and annealing.

Sample	**Ion Energy** (keV)	**Fluence (ions/cm^2)**	**Dynamic Annealing (°C)**	**Thermal Annealing (°C)**	**Impl. – Cycle**	**R – range**
A	C^+ 15 keV, B^+ 30 keV	C^+ 1×10^{15}, B^+ 4×10^{15}	C^+ 200°C, B^+ 400°C	650°C, 800°C, 1000°C	x1	$\sim$ MΩ, $\sim$ kΩ, $\sim$ kΩ
B	C^+ 15 keV, B^+ 30 keV	C^+ 1×10^{15}, B^+ 1×10^{16}	C^+ 200°C, B^+ 400°C	650°C, 800°C, 1000°C	x1	$\sim$ MΩ, $\sim$ kΩ, $\sim$ kΩ
C	C^+ 15 keV, C^+ 30 keV	C^+ 1×10^{15}, C^+ 1×10^{16}	C^+ 200°C, C^+ 400°C	650°C, 800°C	x1	$\gg$ MΩ
D	C^+ 15 keV, B^+ 30 keV	C^+ 1×10^{15}, B^+ 1×10^{16}	C^+ 200°C, B^+ 400°C	650°C	x1	$\sim$ MΩ
SE	B^+ 15 keV	B^+ 1×10^{16}	B^+ 400°C	650°C	x2	$\sim$ kΩ
ME	B^+ 10 keV	B^+ 1×10^{15}	RT	650°C	x9	$\sim$ MΩ
BE	B^+ 30–155 keV	B^+ 1×10^{16}	RT	650°C	x1	$\sim$ Ω

implanted similarly to samples A–B and D, albeit, with only carbon ions to highlight the difference in the structural impact ascribed to both incident carbon and boron ions. Sample SE underwent 2–cycles of 15 keV boron implantation with dynamic annealing at 400 °C, while sample ME was implanted in 6–cycles of 10 keV boron ions at room temperature (RT). The BE sample was boron implanted at room temperature with six different energies (35 keV, 55 keV, 80 keV, 105 keV, 155 keV) to create a "box profile" with a depth of about 250 nm from the surface. The fluence for all the samples was relatively consistent and ranged between $1 \times 10^{15} - 1 \times 10^{16}$ cm^3. The conductive nature of the samples was confirmed by using a Digital Fluke. All the samples apart from carbon-only implanted sample C, showcased a decrease in resistance with each process of implantation and annealing (i.e., MΩ $\rightarrow$ kΩ).

PL intensity analysis after implantation and annealing

Following the implantation process, a Raman and PL intensity analysis was conducted to investigate the creation of defects and any structural changes resulting from the implantation. A coherent argon ion laser was utilized for laser excitation (with 514.5 nm and 457.9 nm excitation wavelengths). A visible long working distance 50× microscope objective with a numerical aperture of 0.50 and a working distance of 10.6 mm was used to concentrate light onto the sample, with a spot size of 2 µm on the sample's surface. The microscope objective lens collected the backscattered light, which consisted of scattered Rayleigh light, the scattered Raman signal and the PL signal from the boron-implanted diamond substrates.An edge filter was employed to allow the backscattering Rayleigh light to pass through while transferring both the Raman and PL signals to the spectrometer for additional processing. The

photoluminescence signal at room temperature, produced by the dispersed light, was examined using a spectrograph equipped with a 600 lines/mm grating and a CCD detection device that was cooled using liquid nitrogen to enhance sensitivity. The mappings were conducted across a 2600 µm × 2600 µm square area, consisting of 31 × 31 grid points covering the entire sample. A 150 lines/mm grating provided a superior spectral range compared to the 600 lines/mm grating. This was primarily employed to decrease the data acquisition time caused by the significantly larger ∼ 220 mm spectral range of the 150 lines/mm grating. The spectrum characteristics associated with carbon created vacancies and the subsequent boron implantation are distinctly observable in the diamond samples under investigation, even prior to annealing. Please see Chap. 6 for more details.

Annealing

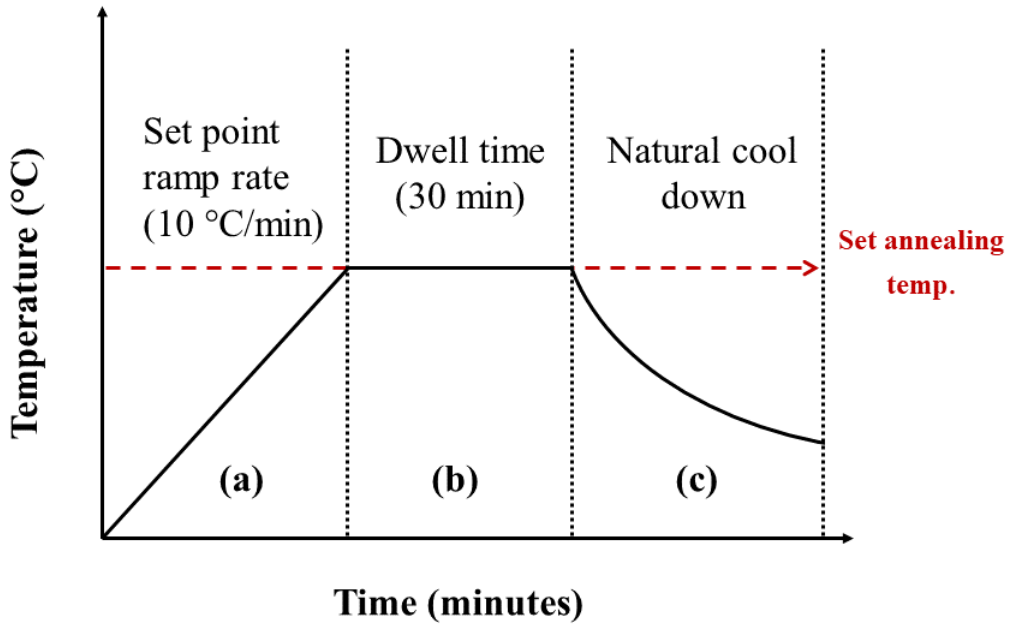

Figure 4.17: **Summary of the annealing process.** (a) The ramping rate. (b) The annealing dwell time. (d) Natural cooling.

Each one of the samples were placed within a horizontal quartz tube and subjected to heat treatment where the tube furnace was isochronally thermally heated in an argon atmosphere to a set temperature of 650 °C for all the treated samples, at a ramping rate of 10 °C/minute. Other samples within the batch were subject to annealing at higher temperatures (i.e., 800 °C and 1000 °C), in order to further activate the implanted boron ions. The annealing duration was set at 30 minutes once the appropriate temperature had been reached. After the set time had elapsed the temperature in the tube furnace was slowly cooled down to room temperature in order to prevent the diamond surface from graphitizing (see Fig. 4.17 for summary of the annealing process). Immediately after the annealing process, the samples were boiled in an oxidizing acid solution composed of nitric, sulfuric, and perchloric acids in a ratio of 1:3:4 for 30 minutes to eliminate any potential contamination introduced during annealing. Afterward, the diamond surfaces were cleaned using ultrasonic baths in an alcohol solution and then rinsed with deionized water to eliminate any visible inorganic or organic contaminants.

4.6.2 Ohmic contacts

The metal fabrication recipe used in this study is reported in recently published work by Salami et al. [204]. In this work we studied the thermo-electronic properties of a helium-implanted diamond sample; of which the properties studied are partly the basis of this current work involving electron-phonon interactions at low temperatures in implanted diamond, i.e., in this current study the focus is mainly the electronic transport properties in boron-implanted diamonds.

Tri-layer metal stacking

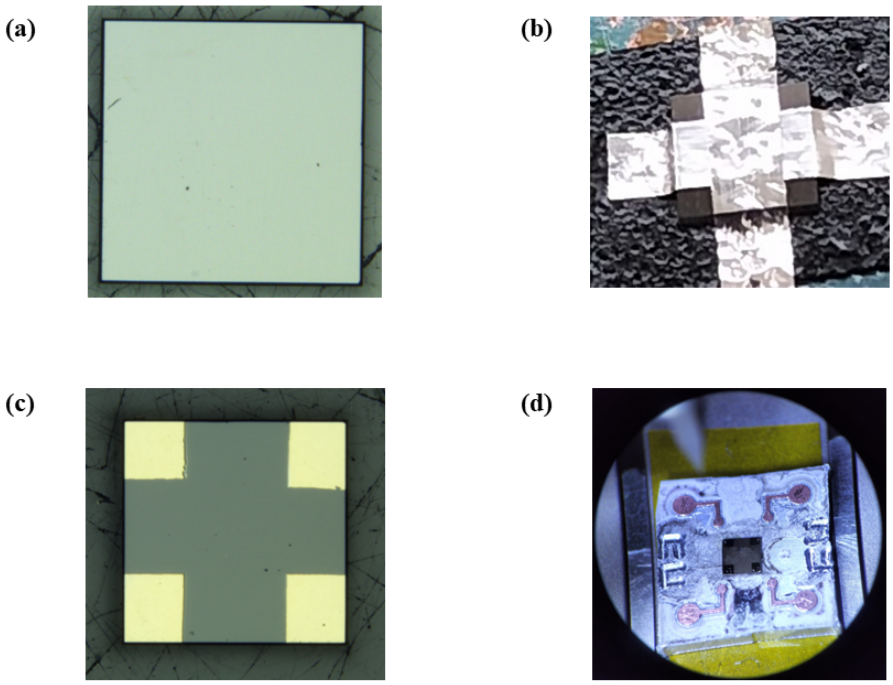

Figure 4.18: **Diamond preparation for electronic measurements.** Optical images of: (a) Acid cleaned boron-implanted diamond. (b) A Greek cross mask placed on top of the diamond. (c) Square Ohmic contacts at the corners of the diamond. (d) The diamond is wire-bonded to a PCB for measurements.

After the successful fabrication of boron p-type conduction layers within the various diamond samples, the samples underwent a metal evaporation process. Before entering the chamber the samples were dipped in an HCl and H_2O solution with a 1:10 ratio to remove any surface contaminants. Two thin strips of aluminium foil were placed ontop of each sample in a Greek cross format in order to create a mask that exposes the four corners of the square-shaped samples for Van der Pauw measurements, as shown in Fig. 4.18 (b). Metals Ti, Cr, and Au and gold were placed in separate suitable e-beam crucibles. The crucibles were slotted into a 'rotary pocket e-beam source' with multiple pockets that can be indexed into position for evaporation. The evaporation chamber was pumped overnight to a vacuum pressure of about $\sim 10^{-7}$ Torr. The metals were evaporated sequentially to create a thin trilayer metal stacking on the exposed diamond surface. The deposition rate was 4 Å/s for 350 nm Ti, 50 nm Cr and 150 nm Au. During evaporation the vacuum chamber pressure never went above $\sim 10^{-4}$ Torr. After the evaporation process the

vacuum chamber was left to cool down to room temperature before the samples were taken out.

UHV annealing

UHV thermal annealing with a ramping rate of 10 °C/minute to 450 °C for 30 minutes was employed immediately after taking the samples out of the metal evaporation chamber. The vacuum pressure was $>10^{-7}$ Torr. This process aid in the adhesion of Ti to the diamond surface as it induces the formation of TiC for quality low resistance ohmic contacts. Due to the system temperature overshooting at lower temperatures, an initial temperature set point of 150 °C was set and allowed to dwell and settle for 15 minutes before ramping up again to 450 °C. The system cooled down under vacuum under the cooling rate of the environment. After UHV annealing the samples were wire-bonded to suitable printed circuit boards (PCBs) for electronic measurements (please refer to Fig. 4.18).

Chapter 5

SRIM Simulations for boron ion implantation

As underlined in most of Chap. 3, SRIM simulations were conducted before experimentally processing the diamond samples. This is a necessary undertaking before such processes in order to predict, with good accuracy, the boron ion distribution and damage profile within the investigated samples. Low ion implantation energies were utilized intentionally in all the samples to guarantee a good volume of vacancies concentrated near the diamond surface. The relatively low and moderate boron and carbon ion fluences were utilized to reduce any possibility of irreversible damage to the diamond matrix structure. The distribution of vacancies increases the likelihood of substitutional boron, which is crucial for p-type conduction studies. The SRIM simulation computes the ion and target vacancy production, yielding the average number of vacancies generated by each ion per angstrom. The average number is multiplied by the fluence for implantation to calculate the damage density, denoted as ρ_v in vacancies/cm^3, using the equation [161],

$$\rho_v = \text{Mean number of vacancies} \times \text{Ion fluence}, \tag{5.1}$$

where the units of ρ_v can be worked out as follows,

$$\begin{aligned} \rho_v(\text{units}) &= (\text{vacancies/ion}/10^{-8}\text{cm}) \times (\text{ions/cm}^2) \\ &= (\text{vacancies/cm}^3). \end{aligned} \tag{5.2}$$

Below, I present the simulated data for all the samples that were implanted and studied (refer to Tab. 4.1). It is worth noting that the simulations do not account for any dynamic or thermal annealing processes which are mainly used in this case to induce substitutional defect formation and to preserve and restore the diamond matrix after implantation. In reality, the radiation damage that occurs is influenced by the implantation conditions, target material qualities, ion species used, and interactions between defects throughout the process and subsequent annealing. The damage density threshold in diamond limits the amount of foreign atoms introduced into the diamond lattice. As discussed in Sec. 3.3.2, studies over the years have shown that the damage density produced by ion irradiation in diamond exceeding values of $\sim 10^{22}$ vac/cm^3 result in irreversible graphitization of the damaged region upon annealing.

5.1 Atomic density and concentration

The simulated range distribution of ion species implanted into the diamond matrix affords us the opportunity to predict the atomic density and concentration of that particular ion. In Chap. 3, I specified the relationship between the peak atomic density N_p and projected range R_p, determined from a Gaussian distribution curve with a standard deviation ΔR_p – the projected range straggle. Evidently, from the plots presented below, the distribution of boron ions shows typical features, displaying a higher degree of symmetry and can be fitted with a Gaussian curve. Now, in order to determine the atomic concentration C_p resulting from N_p of the implanted ions, it is necessary to have knowledge of N, which represents the atomic density of the substrate. The concentration of the implanted species at the peak of the dispersion can be described by the following relation,

$$C_p = \frac{N_p}{N_p + N}, \tag{5.3}$$

where the atomic density N of diamond is 1.76×10^{23} atoms/cm^3.

For sample SE with 2–cycles of 15 keV boron implantation as seen in Fig. 5.1, the projected range is 29.94 nm with range straggling of about 9.1 nm. From an ion fluence of 2×10^{16} atoms/cm^2, this gives a boron atomic density of 8.8×10^{21} atoms/cm^3 resulting in ~ 4.84 at.% boron concentration implanted within a shallow ~ 44 nm buried channel below the diamond surface.

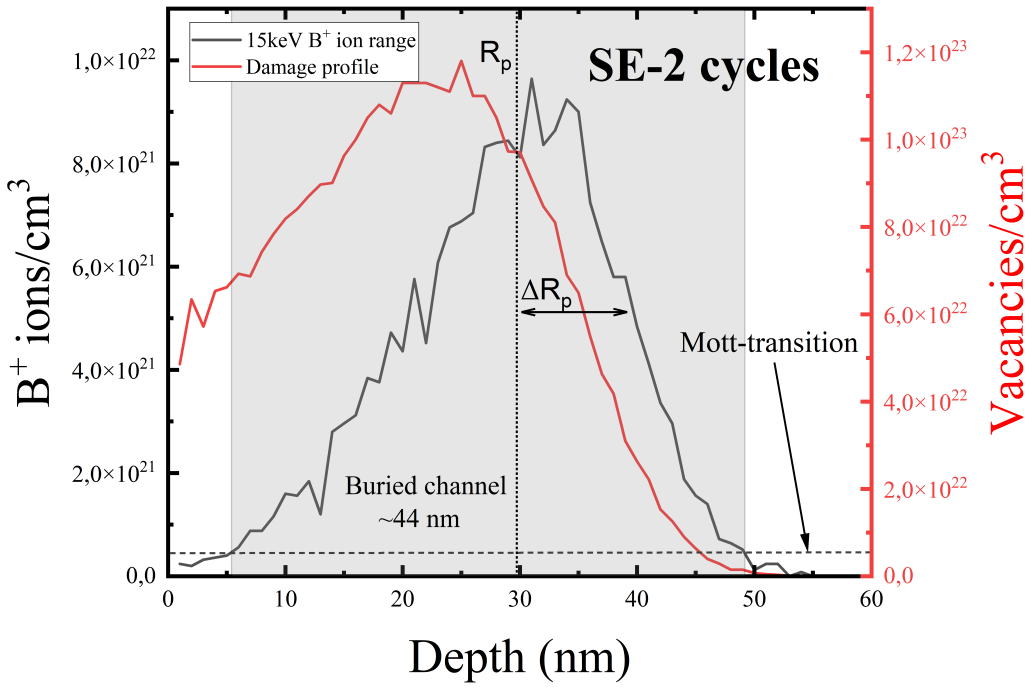

Figure 5.1: **SRIM simulation for the damage and ion depth profiles.** The predicted damage for sample SE caused by boron ions with incident implant energy of 15 keV. The depth profile of the damage stretches ~ 50 nm into the material with a damage peak at ~ 25 nm from the surface. The projected range R_p of the boron ions is about ~ 29.94 nm deep from the surface within a boron buried channel with a width of ~ 44 nm determined from the Mott-transition level.

In Fig. 5.2, the simulation of 10 keV boron ions implanted in 9–cycles for

sample ME each with a boron fluence of 1×10^{15} atoms/cm^2 yields a projected range of 20.51 nm with range straggling of about 7 nm resulting in a relatively high boron atomic density of 5.15×10^{21} atoms/cm^3 and ~ 2.9 at.% boron concentration implanted in a very thin ~ 31 nm buried channel that begins 5 nm below the diamond surface.

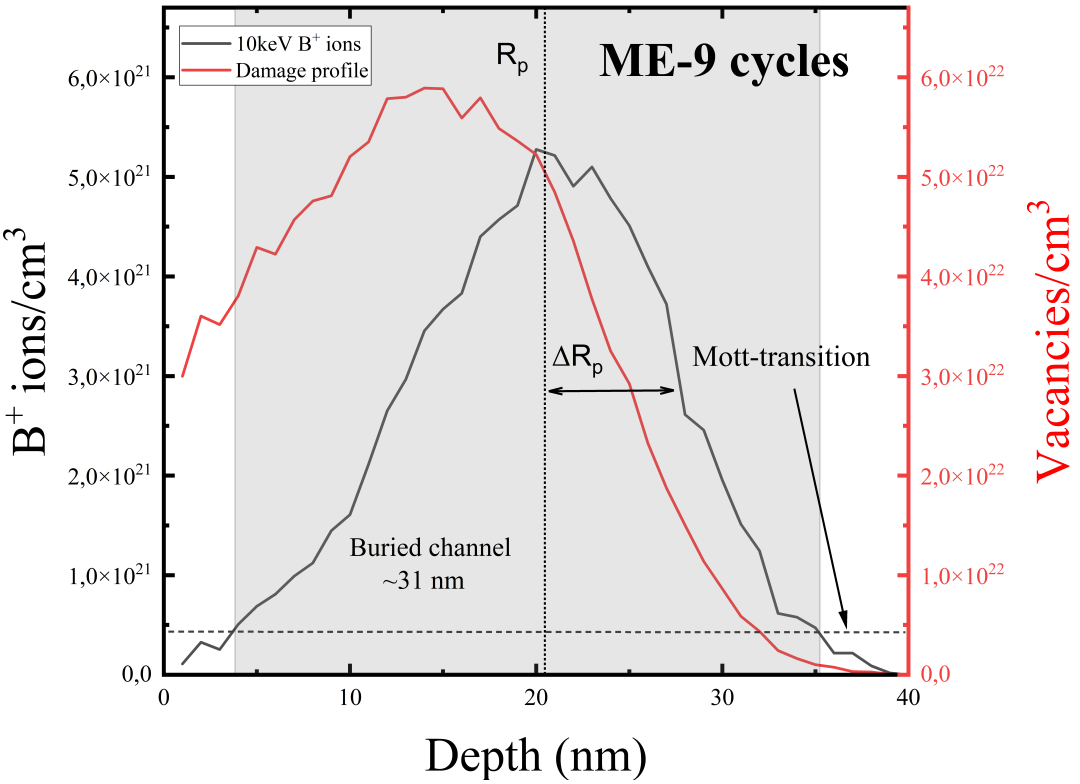

Figure 5.2: **SRIM simulation for the damage and ion depth profiles.** The predicted damage for sample ME caused by boron ions with incident implant energy of 15 keV. The depth profile of the damage stretches ~ 35 nm into the material with a damage peak at ~ 15 nm from the surface. The projected range R_p of the boron ions is about ~ 20.51 nm deep from the surface within a boron buried channel with a width of ~ 31 nm determined from the Mott-transition level.

Figure 5.3, depicts the effect of multiple energy boron implantation resulting in a '*box profile*' atomic distribution (i.e., 30 keV, 55 keV, 80 keV, 105 keV, 130 keV, 155 keV) with the same fluence, 1×10^{16} atoms/cm^2. The simulation provides the projected range for each ion energy in order to determine the average peak atomic density across a 221 nm buried channel ~ 25 nm deep below the diamond surface. The average boron atomic density is predicted to be $\sim 1.84 \times 10^{21}$ atoms/cm^3 which yields an average boron concentration of about ~ 1.05 at.%. R_{p30} and ΔR_{p30} represents the projected range and straggling, respectively, for 30 keV ion energy.

Figures 5.4 and 5.5 represents the carbon and boron implantation in diamond with energies 15 keV and 30 keV, respectively. As suggested before, this is mainly for boron diffusion purposes. The same energy, the projected range for both samples is predicted to be 56.17 nm while the projected straggling is 12.27 nm. Due to the difference in boron fluence, the boron concentration for sample A is ~ 0.75 at.% from a peak atomic density of about 1.3×10^{21} atoms/cm^3 within a thin ~ 38 nm boron layer buried ~ 36 nm below the diamond surface. The higher fluence of sample

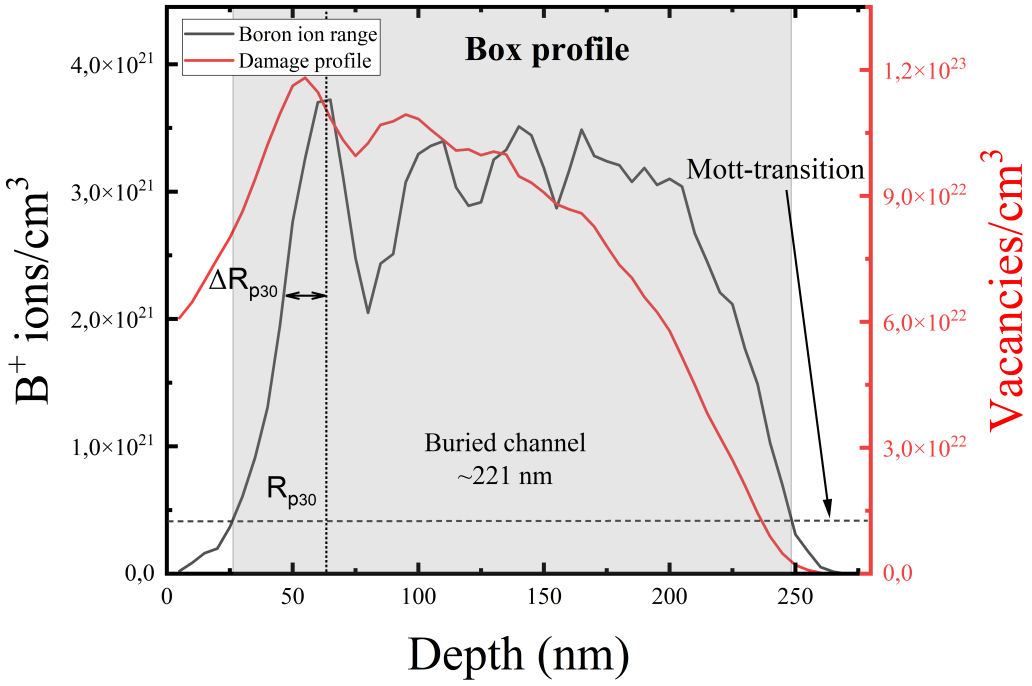

Figure 5.3: **SRIM simulation for the damage and ion depth profiles.** The predicted damage for sample BE caused by boron ions with multiple incident implant energies of $30 - 155$ keV. The depth profile of the damage stretches ~ 250 nm into the material. The projected range R_{p30} of the boron ions with energy 30 keV is about ~ 63 nm deep from the surface. The projected ranges for all the ion energies are averaged within a boron buried channel with a width of ~ 221 nm determined from the Mott-transition level.

B yields a higher boron concentration of ~ 1.85 at.% from a peak atomic density of $\sim 3.26 \times 10^{21}$ atoms/cm^3 embedded in a ~ 51 nm channel buried ~ 29 nm below the surface of the diamond. Evidently, the projected range and straggling increases with ion energy for the same ion type. For all the boron implanted samples the Mott–transition (i.e, $\sim 4 \times 10^{20}$ atoms/cm^3) is used to estimate the position and width of the boron layer buried beneath the diamond surface. The Mott-transition is known as the onset of superconducting properties and/or metallic-like behavior of diamond due to boron.

5.2 Damage profile

Before any subsequent thermal annealing, the ions can cause several types of damage, including intrinsic point defects such as vacancies and interstitials, localized amorphous zones in the case of particularly heavy ions, and total amorphization when the critical ion dosage is surpassed. Ions with a similar mass to carbon atoms in diamond are of interest for doping in this study. The radiation damage caused by these ions is primarily determined by the intrinsic point defects that are produced during collision cascades.

The vacancies created are of important interest in this study as they offer the implanted boron ions in close proximity the potential to jump and diffuse into the vacant lattice sites. It is apparent that the vacancy distribution is less symmetric and peaks slightly above the atomic boron distribution with respect to depth. A deeper

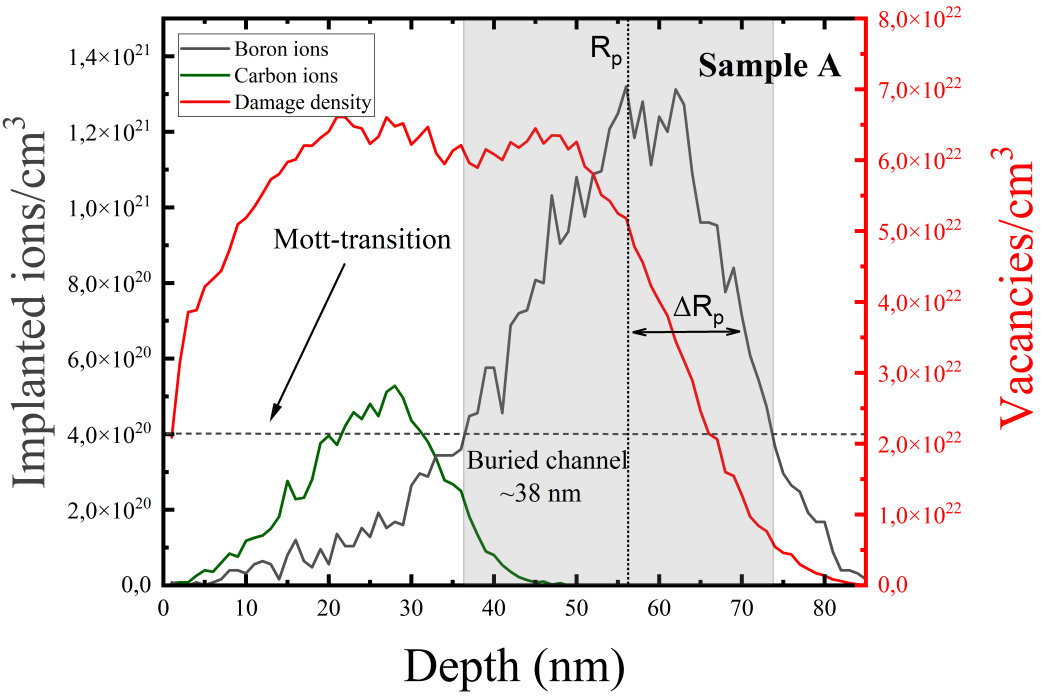

Figure 5.4: **SRIM simulation for the damage and ion depth profiles.** The predicted damage for sample A caused by carbon and boron ions with incident implant energies of 15 keV and 30 keV, respectively. The depth profile of the damage stretches $\sim$ 85 nm into the material. The projected range R_p of the boron ions is about $\sim$ 56.17 nm deep from the surface within a boron buried channel with a width of $\sim$ 38 nm determined from the Mott-transition level.

atomic peak is proportional to the ion's inability to remove lattice atoms once its energy has dropped below the displacement energy $E_d \approx 50$ keV. At the beginning of this region, one can also anticipate replacement collisions, in which a boron ion has sufficient energy to displace a carbon lattice atom and occupy its position. Hence, it is anticipated that within the buried boron channel there is relatively high concentration of substitutional boron where the diffusion coefficient is proportional to temperature. That is, the rate of diffusion within this region should be high for boron ions implanted with dynamic annealing. Moreover, within the damage profile which is mainly made up of vacancies and interstials (i.e., mainly of carbon, nitrogen, boron atoms), interactions within this region between the defects is expected during the implantation process or the thermal annealing process. Consequently, the rate of diffusion of such ions should be proportional to the concentration of vacant sites. The formation of substitutional boron via ion implantation follows a complex mechanism that involves the interactions of defects due to both dynamic and thermal annealing.

The damage density for all the samples is close to the critical limit for irreversible graphitization. Thus, the diamond matrix for all samples is expected to retain its structural integrity after ion implantation and annealing. Figures 5.6 and 5.7, depicts the simulated atomic density against the vacancy density. The damage density for samples A and B accounts for both carbon and boron ions. All the plots have been normalized to the damage threshold – 10^{22} vac/cm^3. Clearly, the boron atomic distribution peak of sample SE is 2× higher than all the other samples coinciding with the highest atomic concentration, as reported above. Samples ME, BE and

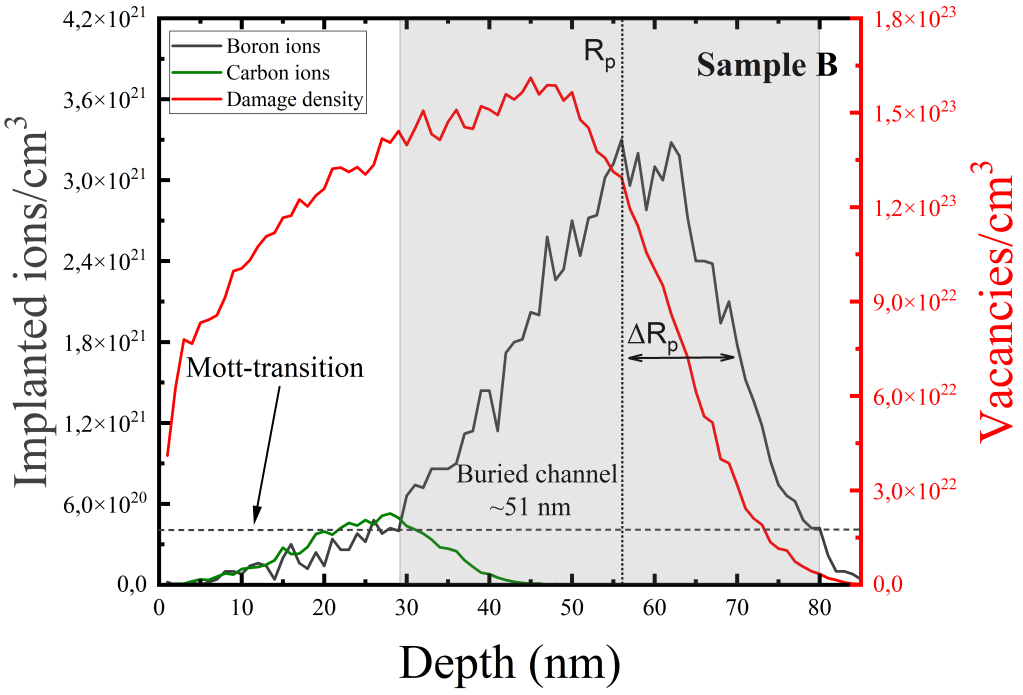

Figure 5.5: **SRIM simulation for the damage and ion depth profiles.** The predicted damage for sample A caused by carbon and boron ions with incident implant energies of 15 keV and 30 keV, respectively. The depth profile of the damage stretches $\sim$ 85 nm into the material. The projected range R_p of the boron ions is about $\sim$ 56.17 nm deep from the surface within a boron buried channel with a width of $\sim$ 51 nm determined from the Mott-transition level.

B have relatively similar peak thresholds while sample A is nearly 2× less than the other 3 samples. However, sample A has a much larger boron concentration compared to sample ME. This is reasonable considering the width of the buried layers. Moreover, at each of the six energy peak points for Sample BE the average atomic density is 2× less than sample SE. However, taking into account the much larger boron channel of the box profile the total boron concentration is 6× more than that of sample SE. Expectantly, sample BE should have much better conduction than all the other samples. **NB.** the buried channel represents the boron conduction thickness t_s as discussed in Chap. 4.

A high volume of vacancies in comparison to the boron atomic density and distribution due to implantation may likely induce localized substitutional boron states that are associated with hopping mechanisms. Hence, the necessity of subsequent boron implantation and annealing processes in these trailing regions just below the diamond surface. Please note, that since the implantation parameters for samples B and D are the same, the simulation for sample D is exactly the same as that of sample B. The only difference between the two samples is the thermal annealing process which has no effect in any of the simulations.

5.3 Carbon ion simulation

Figure 5.8, represents the simulation for sample C with only carbon ion implantation. Sample C is used as a reference to ascertain the effect of boron related defects induced within the diamond matrix due to ion implantation. Apart from the difference in

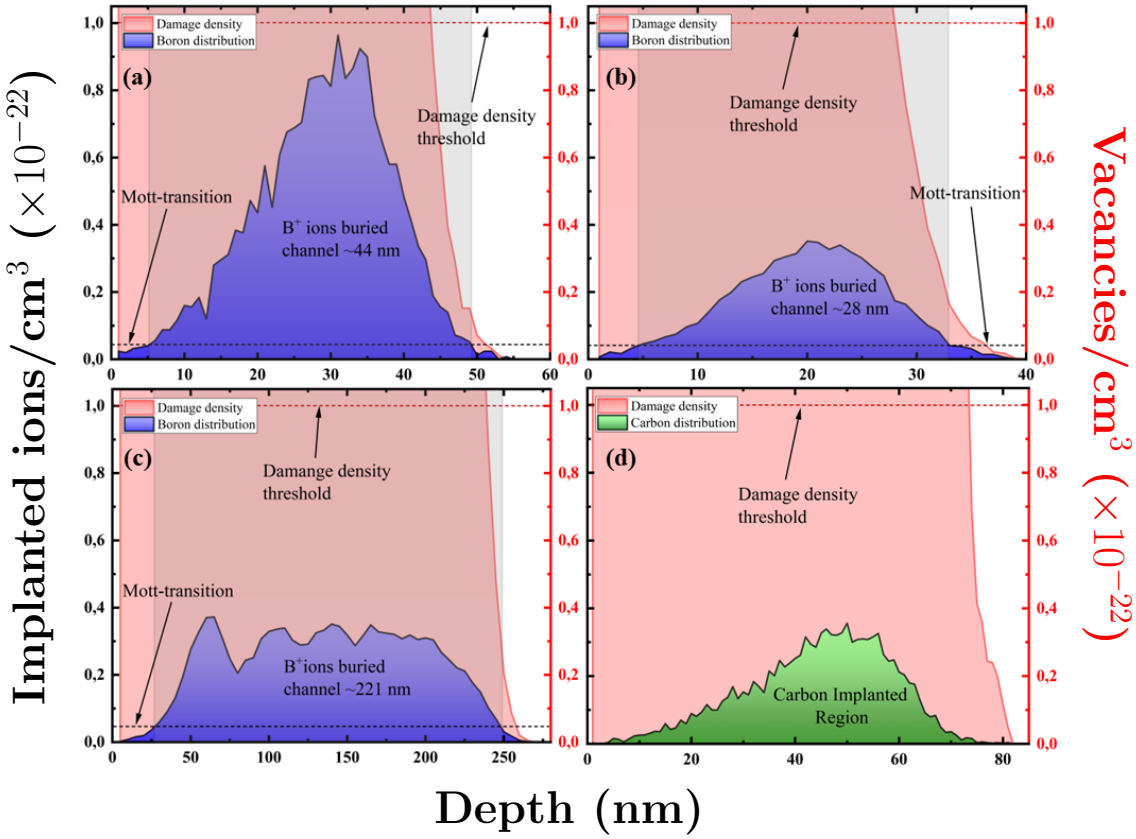

Figure 5.6: **SRIM simulation for the damage density and ion distribution.** The predicted damage density and ion distribution normalized to the critical damage $\sim 10^{22}$ vac/cm^3 for samples (a) SE, (b) ME, (c) BE and (d) C.

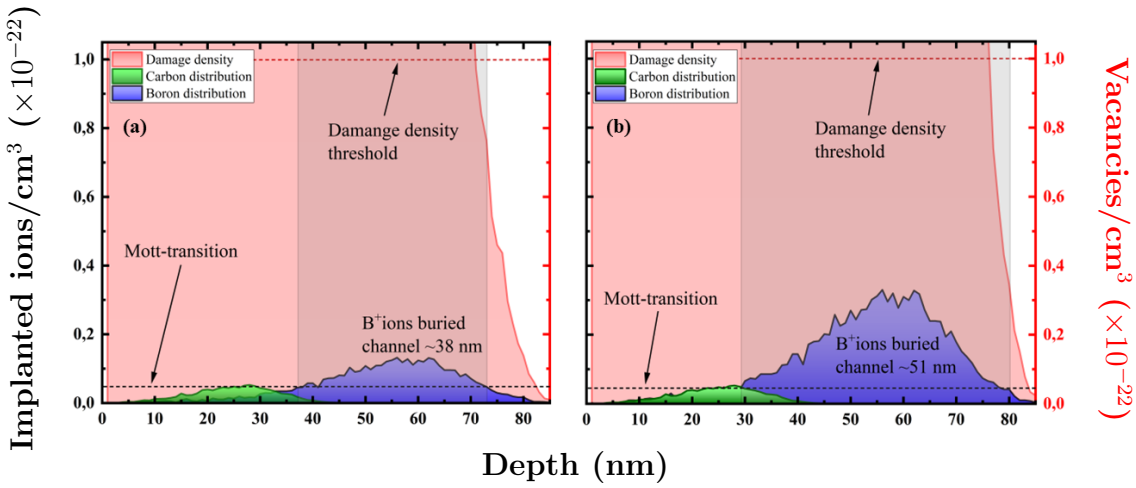

Figure 5.7: **SRIM simulation for the damage density and ion distribution.** The predicted damage density and ion distribution normalized to the critical damage $\sim 10^{22}$ vac/cm^3 for samples (a) A and (b) B.

implantation ion species, the implantation parameters for sample C are the same as that of sample B. The minute difference in size between carbon and boron yields mildly contrasting damage and distribution results. Incident boron ions are expected to have a slightly broader depth distribution due to a relatively smaller mass as

compared to the target diamond substrate (i.e., 10.5% difference between M_1 and M_2). Moreover, the damage density caused by the incident carbon ions is one order of magnitude more than the damage density due to boron ions. That is, carbon ions produces more vacancies and interstitials than boron. Hence, the use of carbon ions to create trailing vacant sites just above the buried channels for samples A, B and D.

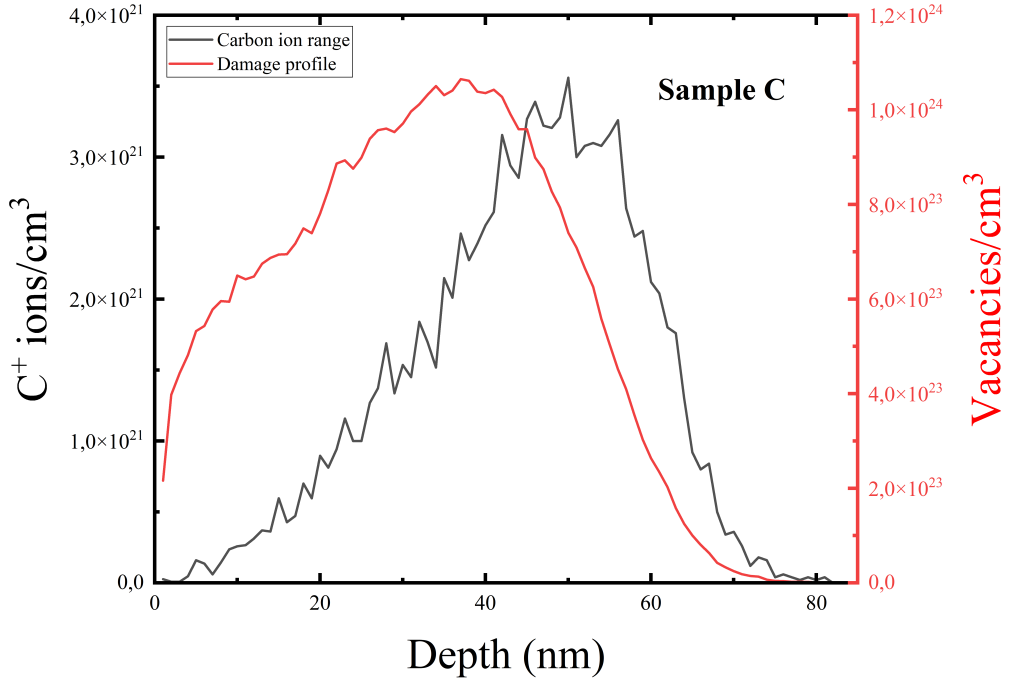

Figure 5.8: **SRIM simulation for the damage and ion depth profiles.** The predicted damage for sample C caused by carbon ions with incident implant energies of 15 keV and 30 keV, respectively. The depth profile of the damage stretches $\sim$ 75 nm into the material with a damage peak at $\sim$ 38 nm from the surface while the ion depth profile is about $\sim$ 80 nm in the width from the surface with an ion distribution peak at $\sim$ 50 nm.

5.4 Discussion

The simulated data clearly indicates that with the parameters chosen for investigation, boron ions implanted into the diamond substrates are embedded into the diamond matrix close to the diamond surface with nanoscale layers within a reversible damage density range. The expected and prevailing defects for the implanted samples should be carbon vacancies, boron and carbon interstitials, localized clusters of boron, substitutional boron and NV centers due to an ever-present low concentration of nitrogen in the type IIa samples used in this project. Moreover, the heavily implanted samples with no dynamic annealing should incur reasonable damage that may lead to sp^2 and sp^3 localized amorphous zones. Of course, the defects that are of interest for this particular study are boron related with degenerate diamond ZCP lines and minimum amorphous phases associated with superconducting boron-doped diamond structures. Hence, dynamic and thermal annealing is employed to not only heal the diamond matrix during and after implantation but also to afford the opportunity for the formation of boron structures; mainly boron interstitials jumping and diffusing into carbon vacant sites. In the succeeding chapters, spectral and electronic analysis

for all samples is used to determine the structural effects and changes due to the various implantation and annealing processes.

Chapter 6

Spectral analysis of BDD

This chapter consolidates all the spectal results related to boron implanted diamond samples that have been meticulously prepared in accordance to the process parameters detailed in chapters 4 and 5. The first section provides a photoluminescence (PL) and Raman analysis of a pristine sample for reference, against the first implantation process for samples ME and SE. **NB.** All the investigated CVD grade diamonds are cut from the same single crystal (SC) plate. The second section provides a similar study as the first, albeit, focusing on the structural changes of all the implanted samples due to ion implantation and annealing (i..e., the relation of the diamond peaks due boron implantation). Additionally, apart from the boron related changes to the diamond matrix, the PL measurements primarily investigates the occurrence of both charge states of the NV center defects to ascertain the production and annihilation of vacancies with respect to each succeeding fabrication process. Furthermore, the Raman spectrum of samples A and B is fitted with a Fano line shape to investigate the appearance of the asymmetrical bands associated with the maximum phonon density of states (PDoS) and degeneracy of the diamond zero center phonon (ZCP) line in correlation with boron and vacancy concentrations.

6.1 Raman and PL spectra analysis of pristine diamond

This section presents the Raman and PL intensity results for the diamonds under investigation, i.e., a pristine sample, samples SE and ME after boron ion implantation. An excitation scan using a laser was performed on the diamond substrates with area measuring 2000 µm × 2000 µm. In accordance with Section 4.3, the laser was concentrated on the diamond surface, resulting in a spot size of approximately 2 µm. The laser was then scanned over a grid consisting of 31 × 31 points. The same system configuration was utilized for performing PL and Raman measurements on all diamond substrates investigated in this project.

Figure 6.1, displays the Raman spectra obtained from a randomly chosen location on the unimplanted diamond at room temperature. A laser utilizing Argon (Ar) gas with a specific wavelength of 514.5 nm was used for the purpose of excitation. The obtained spectra exhibited typical characteristics of a relatively unperturbed type IIa diamond structure. The features pertain to the 1st order Raman scattering of diamond. The Raman sharp 1st order peak observed in diamond, resulting from the Raman effect, was initially investigated by Ramaswamy [205]. He documented the presence of distinct and highly intense Raman line that corresponded to a frequency

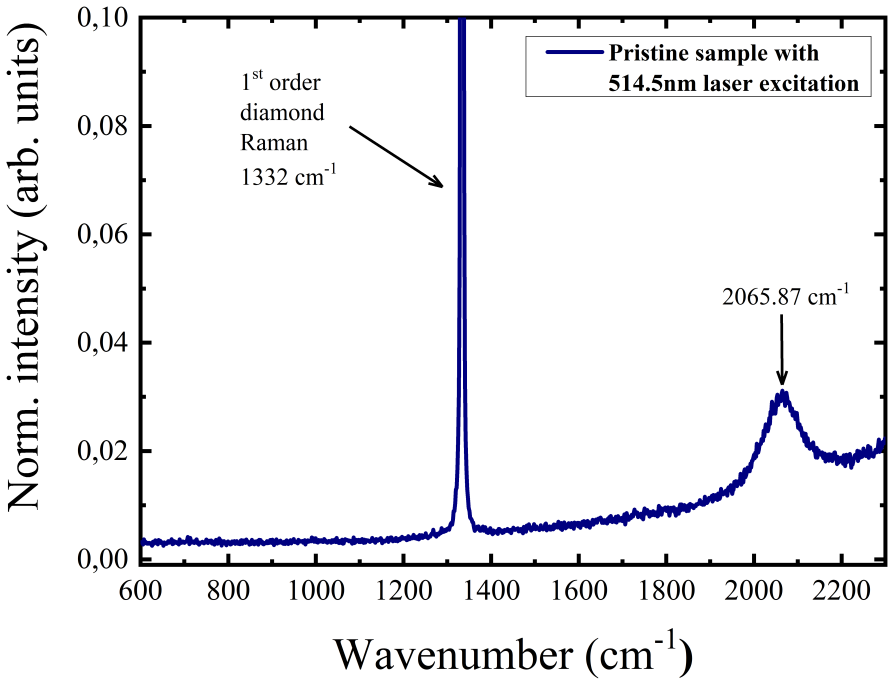

Figure 6.1: **Raman spectra of a pristine SC Plate CVD.** A Raman spectra of an unimplanted diamond sample with a 1st order diamond Raman at 1332 cm^{-1} and a peak at 2065.87 cm^{-1} from a laser excitation wavelength of 514.5 nm at room temperature.

shift of 1332 cm^{-1}. Subsequently, numerous additional scientists corroborated the findings through studies of their own, which focused on different diamond types with unique optical properties. These studies revealed relatively minor differences in the Raman frequency shift, measured in cm^{-1} [206]. The Raman shift in wave numbers can be determined by using the equation that relates the excitation laser photons (λ_{ex}) and the scattered photons from the diamond (λ_{sca}) as follows,

$$\nu[\mathrm{cm}^{-1}] = \frac{10^7}{\lambda_{ex}[\mathrm{nm}]} - \frac{10^7}{\lambda_{sca}[\mathrm{nm}]}. \tag{6.1}$$

Therefore, by understanding the Raman sharp peak for diamond, we can determine the exact wavelength of the scattered photons from the diamond using the same equation.

Figure 6.2, displays a PL spectrum of a pristine sample, samples SE and ME. The 1st order Raman peak at a wavelength of 551.75 nm, resulting from laser excitation at a wavelength of 514.5 nm, is easily observable. In addition to the primary Raman peak of the first order, there are two distinguishable peaks at 575.7 nm (2065.87 cm^{-1}) and 638 nm (3754.73 cm^{-1}) associated with NV^0 and NV^- centers, respectively [93–95]. For Fig. 6.1 and 6.2, the spectra are normalized to the 1st order Raman of the pristine diamond structure.

Spectral features related to implantation

Raman Spectroscopy was used to study the effects of ion implantation with subsequent annealing. Samples SE and ME were designated to investigate the damage profile incurred from the diamond matrix after Boron ion implantation.

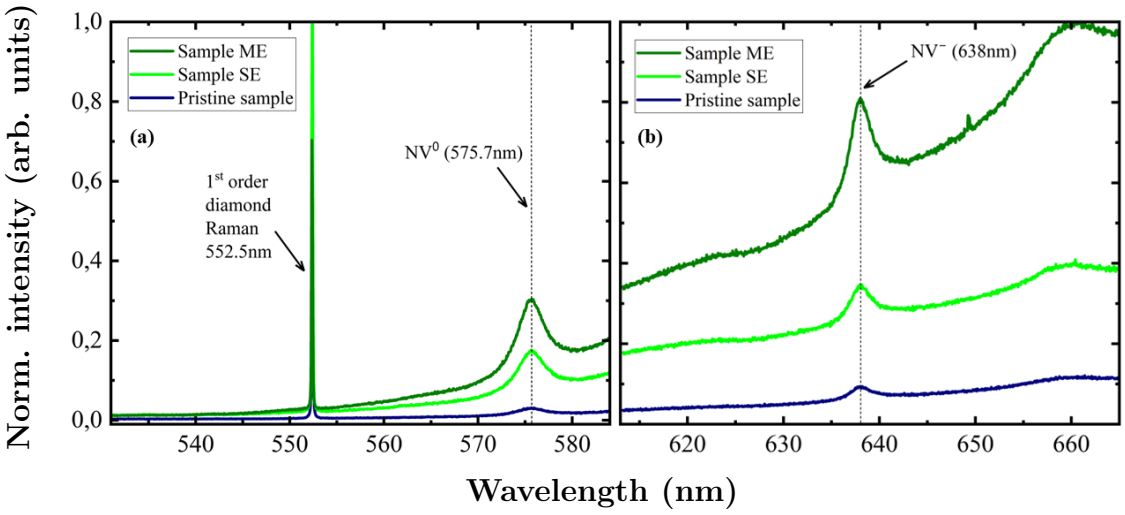

Figure 6.2: **PL intensity spectra.** (a) A typical PL spectra of an unimplanted sample, samples SE and ME with a Raman peak at 551.75 nm and NV^0 center at 575.7 nm from a laser excitation wavelength of 514.5 nm (b) NV^- center at 638 nm.

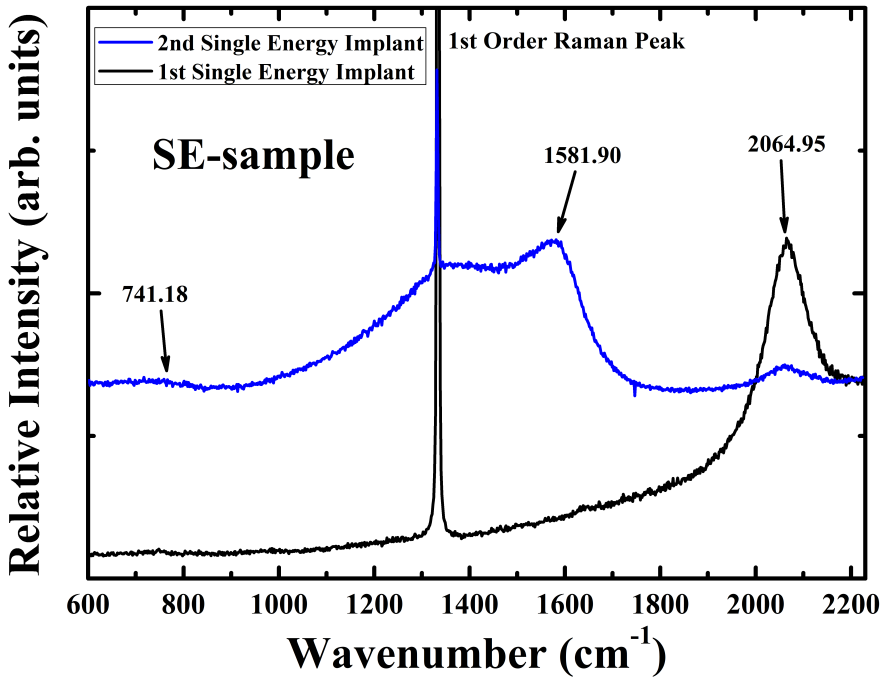

Figure 6.3: **Raman spectra of the SE sample.** The first cycle of Boron ion implantation process (black) vs the second cycle process (blue). Dynamic annealing was preferred during implantation and thermal annealing after implantation.

The Raman spectra of the SE sample after one cycle of Boron implantation ($1 \times 10^{16}\,cm^{-2}$, 15 keV at 400°C–dynamic annealing), did not show any distinct features except for a peak at $2064.95\,cm^{-1}$, consistent with the spectra of a pristine sample (see Fig. 6.1). The second cycle of Boron implantation of the SE sample yielded two more distinct peaks at $741.18\,cm^{-1}$ and $1581.90\,cm^{-1}$ (amorphous graphitic

regions, consistent with the graphitization of the diamond matrix). A reduction of the 2065.87 cm^{-1} peak is also observed.

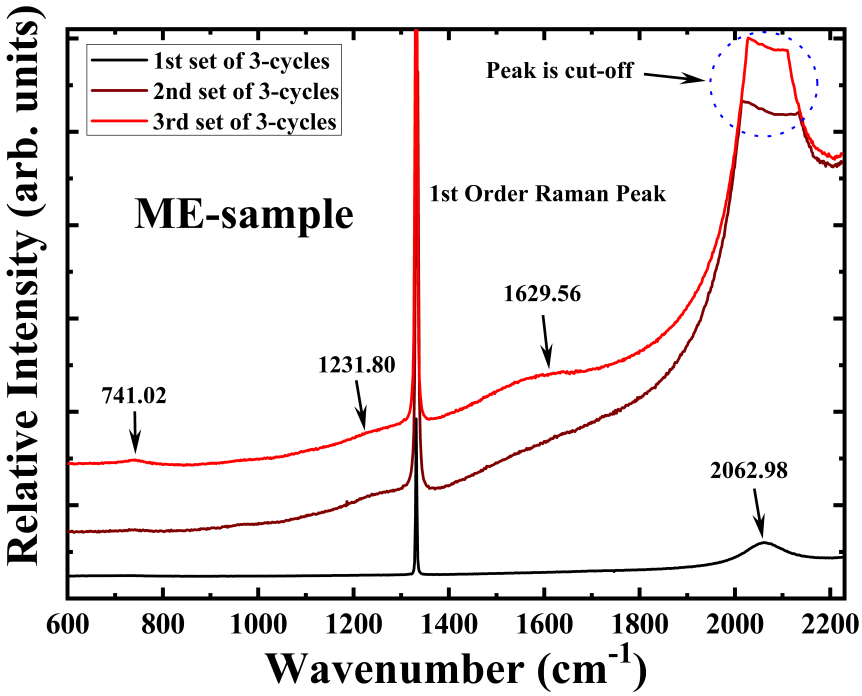

Figure 6.4: **Raman spectra of the ME sample.** Three sets three cycles of Boron ion implantation and subsequent annealing. All cycles were processed under room temperature.

The ME sample underwent three sets of multi(3)–boron ion implantation cycles, with a fluence of $1 \times 10^{15}\,cm^{-2}$ and ion energy of 10 keV at room temperature. The total fluence at the buried region is $9 \times 10^{15}\,cm^{-2}$. Similarly to sample SE, the spectra of the ME sample after the first 3–cycles of boron implantation is consistent with that of the pristine sample, with only a peak at 2062.98 cm^{-1}. Evidently, after the second set faint peaks appear at 741.02 cm^{-1}, 1231.80 cm^{-1} and 1629.56 cm^{-1}. Moreover, after the third set of boron implantation the peaks become slightly more defined. The intensity of the peak at 2062.98 cm^{-1} increases significantly after the 2nd and 3rd set of boron implantation cycles. It is worth noting that the peak does not dissociate into two peaks but rather it is cut-off due to saturation experienced by the detection system when using a longer acquisition time (60 s).

Figure 6.5, represents the Raman spectra for sample BE. Six different ion energies (i.e., 30 keV, 55 keV, 80 keV, 105 keV, 130 keV, 155 keV), were used to fabricate a boron box profile with the same fluence of $1 \times 10^{16}\,cm^{-2}$ at room temperature. The spectra shows a highly amorphized diamond structure centered around the 1518.6 cm^{-1} with a faint red-shifted 1st order Raman peak at 1313.2 cm^{-1}, consistent with previous work on heavily BDDs [33, 34]. There are also clear peaks at 423.6 cm^{-1}, 706.6 cm^{-1} and 862.2 cm^{-1} associated with lattice disorder induced by the irradiation of boron ions.

The PL intensity spectra for the box profile in Fig. 6.6, shows a highly disordered diamond structure with a broadening around the 558.53 nm (2.22 eV) with a narrow 553.1 nm (2.24 eV) emission near the 1st order diamond Raman $\sim$ 552 nm (2.25 eV). The broadband PL is likely influenced by optical transitions of in-gap states attributed

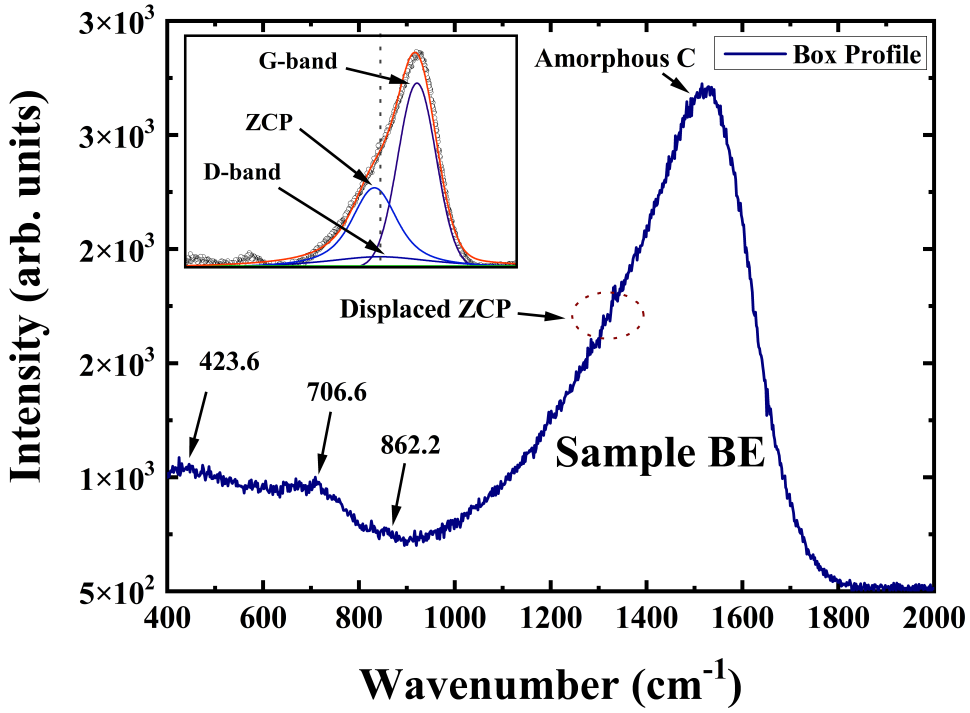

Figure 6.5: **Raman spectra of the BE sample.** Boron ion implantation with six different ion energies. All cycles were processed under room temperature. The insert shows the deconvolution of the peaks with clear contribution from the D- and G-bands. The ZCP is red-shifted to 1313.2 cm^{-1} peak position. The dotted line is the ZCP peak position for pristine diamond $\sim$ 1332 cm^{-1}.

to the amorphization of the diamond lattice and disordered sp^3-hybridized states of carbon due to heavy ion doping [207, 208], this related to the Raman transitions centered around the 1518.6 cm^{-1} peak as seen in Fig. 6.5. Moreover, no NV centers are present in this particular spectrum. An increase in the boron concentration with annealing is known to decrease the PL intensities of NV centers [92, 209], likely due to the boron occupation of the diamond carbon vacancies. There are broad peaks located at 527.33 nm (2.35 eV) and 604.42 nm (2.05 eV) which are prevalent in other reported ion implanted and annealed samples [210]. Additionally, the 527.33 nm is said to be observed after the irradiation of nitrogen containing diamonds and it is likely due to nitrogen bonded to a carbon in an interstitial position [211]. The PL center located at 604.42 nm is typically detected in brown natural diamonds with nitrogen defects is also likely associated with nitrogen-vacancy complexes, albeit, with a strong electron-phonon coupling [211–213]. The spectral structure of sample BE is fairly distinct and hence requires further investigation to ascertain the role of heavy boron ion implantation.

The Raman spectra of samples A–D were used to study the structural effects of diamond after implanting two distinct ion species, i.e., carbon and boron. The results shown are for two separate subsequent cycles of carbon and boron ion implantation with dynamic annealing (at 200°C and 400°C, respectively) with thermal annealing for samples A–C after each cycle, while sample D only underwent thermal annealing after Boron ion implantation.

Now, the implantation parameters of all the samples, including sample A are shown in Tab. 4.1. The spectra of sample A shows little degradation of the sample's

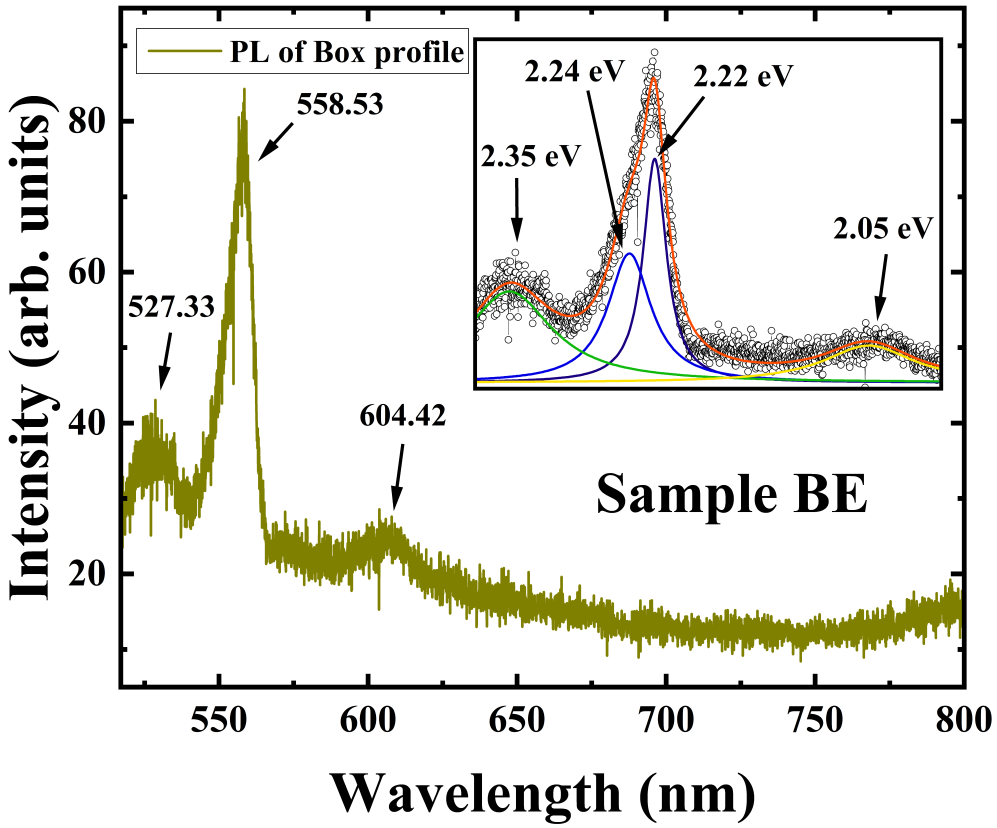

Figure 6.6: **PL spectra of BE.** The PL spectra from 514.5 nm laser excitation at RT. A faint disordered diamond peak centered around 553.1 nm (2.24 eV) is observed. No visible NV color centers. The insert shows the dominant peaks of the broadband energy spectrum ($2 - 2.38$ eV).

structural integrity after carbon is implanted into the diamond (see Fig. 6.7). However, peaks at 742.42 cm^{-1}, 1499.71 cm^{-1} and 1646.65 cm^{-1} are considerably clear after thermal annealing. After boron ion implantation and annealing, the aforementioned peaks become more prevalent while other peaks also appear at 495.91 cm^{-1}, 971.90 cm^{-1}, 1118.84 cm^{-1} and 1244.32 cm^{-1}. The 1499.71 cm^{-1} peak not present after boron ion implantation and annealing.

The PL spectra of Sample A is shown in Fig. 6.8. The zero phonon lines (ZPLs) of both charge states of the NV color centers are clearly visible (i.e., NV^0 and NV^-). These photo-induced centers are known to couple with vibrational modes (phonons), resulting in additional spectral features that are typically broad alongside the ZPLs at longer wavelengths (lower energies) known as phonon sidebands (PSBs) with a wide bandwidth between $560 - 800$ nm [95, 96], as seen in Fig. 6.8. The spectral intensity of the aforementioned peaks after carbon ion implantation and annealing is more prominent than the spectra obtained after boron ion implantation and annealing. Interestingly, the insert exhibits the impact of dynamically implanting boron ions at 400°C with subsequent thermal annealing at 650°C; showcasing a center located at 549.9 nm that relates to dislocations within the diamond structure [211]. The center is more distinct in boron implanted samples with a higher boron fluence (refer to Fig. 6.17). The centers at shorter wavelengths are closely related to nitrogen complexes and induced vacancies due to ion irradiation (i.e., 525.6 nm, 534.8 nm and 541.7 nm) [211].

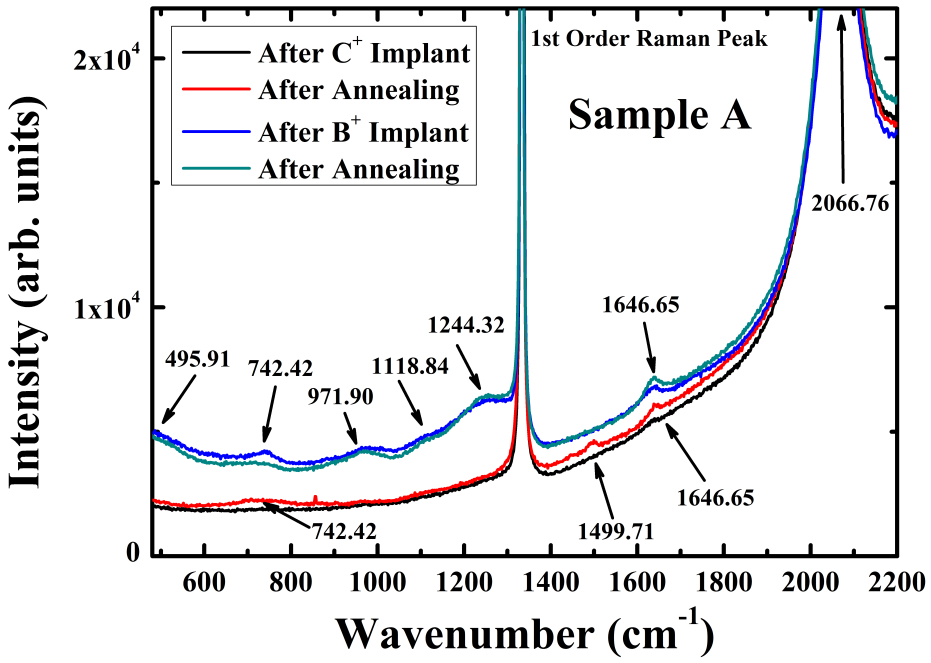

Figure 6.7: **Raman spectra of sample A.** The Raman spectra of sample A after 15 keV carbon and 30 keV boron ion implantation with two subsequent annealing at 650°C after each implantation process.

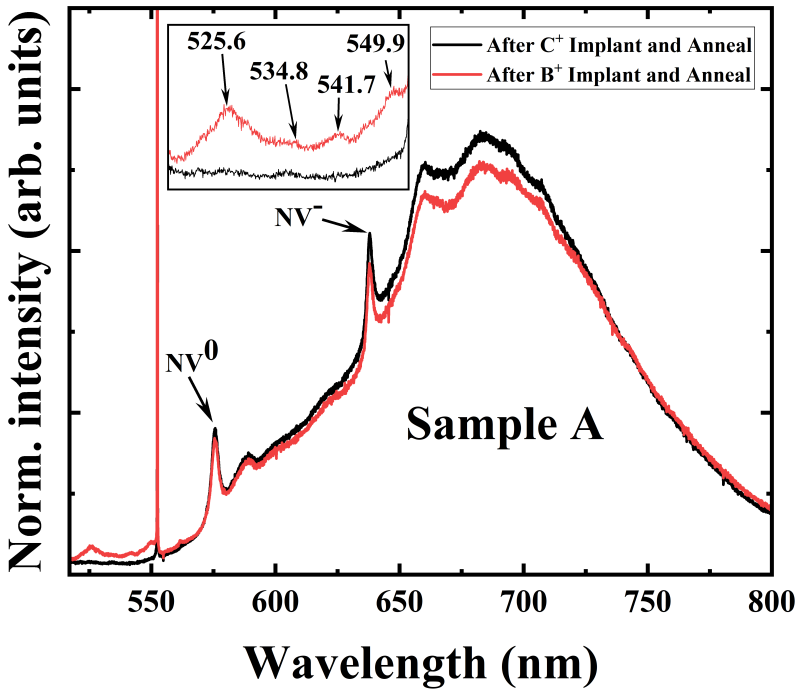

Figure 6.8: **PL spectra of sample A.** The PL spectra with a distinct phonon side band and both charge states of the NV centers. The insert shows a zoomed PL spectra of sample A, ranging between $517 - 552$ nm.

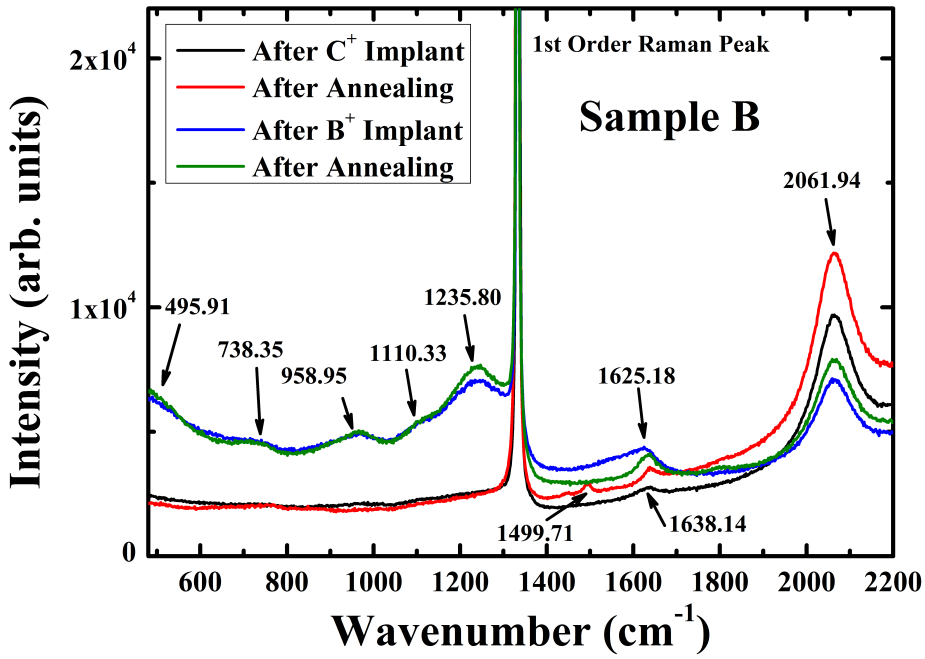

Figure 6.9: **Raman spectra of sample B.** The Raman spectra of sample B after 15 keV carbon and 30 keV boron ion implantation with two subsequent annealing at 650°C after each implantation process.

The ion implantation effects of carbon and boron on the Raman spectra of sample B as shown in Fig. 6.9 is very similar to that of sample A. However, the Raman spectral peaks for sample B are much more prominent after implanting boron ion species with a higher fluence (see Fig. 6.15). Notwithstanding, the fluence of boron ions for sample B ($1 \times 10^{16}\,\mathrm{cm}^{-2}$) is much higher than that of sample A ($4 \times 10^{15}\,\mathrm{cm}^{-2}$).

The PL spectra of sample B after carbon and boron ion implantation, as shown in Fig. 6.10, also has similar attributes to that of sample A. Howbeit, the PL spectral intensities of the NV center peaks from sample B are significantly reduced compared to that of sample A, which may indicate an increase in substitutional boron within the diamond matrix. Again, the difference in intensity of the PL spectra between the 1st cycle of implantation (carbon implantation and annealing) and the 2nd cycle with boron ions is clearly more defined as compared to sample A. The PSBs appearing in the PL spectra of sample B is less intense for all cycles.

Sample C followed the same ion implantation procedure as samples A and B, albeit, with only carbon ions for both cycle. This was done to mainly establish whether the distinct peaks from the Raman spectra of samples A and B are due to the structural damage incurred in diamond, specifically by boron ions. Though the Raman spectra of sample C (see Fig. 6.11), is similar to that of samples A and B the intensity of peaks at wavenumbers lower than the 1st order Raman peak is very faint in comparison. Moreover, there is no significant change of the spectra after each cycle of implantation and annealing. Also, the peak at $\sim$1230 cm^{-1} close to the diamond Raman peak is absent for all the cycles as compared to the boron

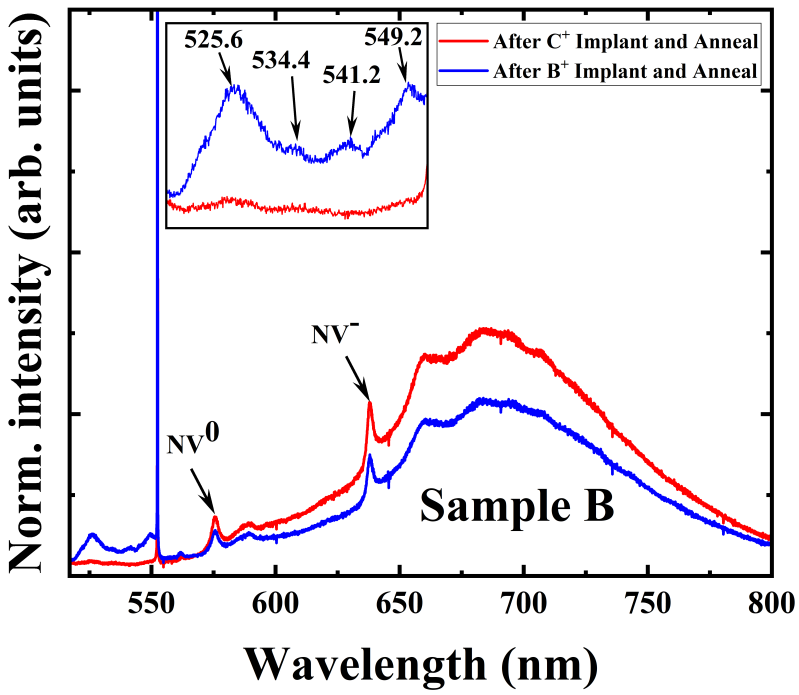

Figure 6.10: **PL spectra of sample B.** The PL spectra with a distinct phonon side band and both charge states of the NV defect. The insert shows a zoomed PL spectra of sample B, ranging between $517 - 552\,\text{nm}$.

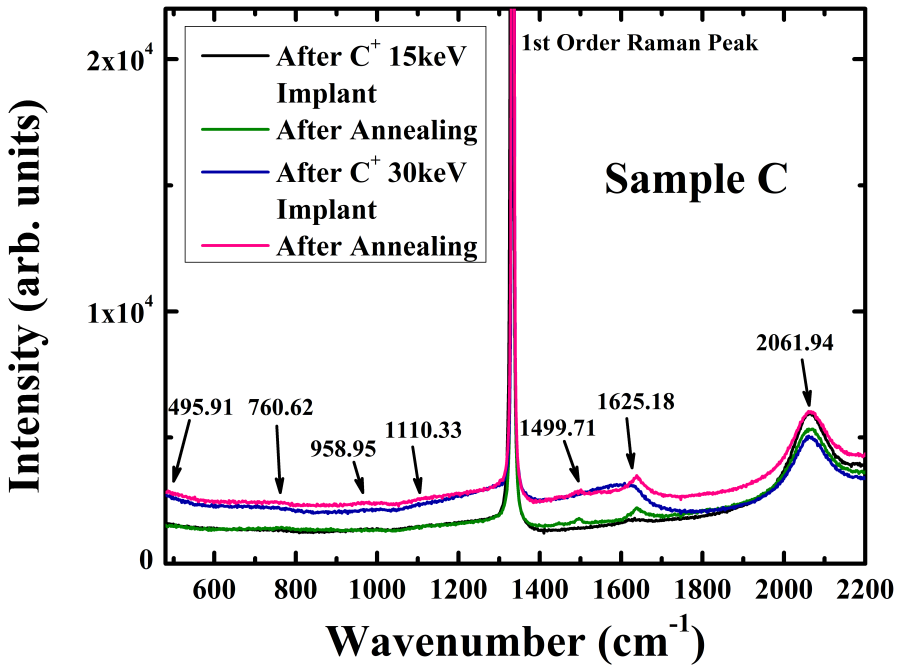

Figure 6.11: **Raman spectra of sample C.** The Raman spectra of sample C after 15 keV carbon and 30 keV carbon ion implantation with two subsequent annealing at 650°C after each implantation process.

implanted samples while the ∼1499.71 cm^{-1} peak remains even after the second cycle of implantation and annealing.

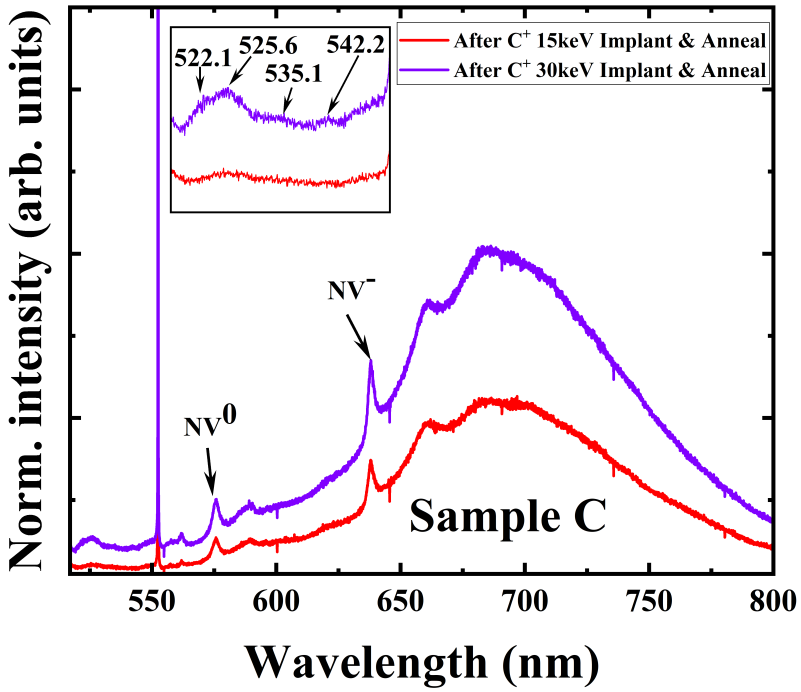

Figure 6.12: **PL spectra of sample C.** The PL spectra with a distinct phonon side band and both charge states of the NV defect. The insert shows a zoomed PL spectra of sample C, ranging between 517 − 552 nm.

The structure of the PL spectra for sample C (presented in Fig. 6.12), is also very similar to that of samples A and B (refer to Fig. 6.17), apart from the PL center associated with lattice dislocations (∼ 549 nm). That is, the dislocations near the 1st order Raman are mainly due to the implanted boron ion species. In addition, the spectral intensity is very similar to that of sample B, with a reasonably less established PSBs as compared to the PL spectra of sample A. This implies that low fluence ion implantation with dynamic annealing induces more NV center defects that leads to significant interactions between the emitted photons due to laser excitation and the lattice phonons resulting in additional spectral features at longer wavelengths (lower energies). Intriguingly, the intensity and sharpness of the spectral peaks increases after the 2nd cycle which suggests more vacancies are being created and remain unoccupied by diffusing ions even after annealing. Consequently, this suggests that the boron ion species with a larger atomic radius than carbon is likely to diffuse more into the carbon lattice sites for samples A and B, resulting in dislocations near ZCP line which has positive implications to the boron induced conduction studies in diamond.

For sample D, the carbon and boron ion species were implanted in one cycle with a single subsequent thermal annealing process instead of two, relative to samples A–C, and hence contains only one spectrum. The intensity and sharpness of the spectrum (as seen in Fig. 6.13), closely resembles that of sample B, of which the implantation parameters are 1×10^{15} cm^{-2}, 15 keV at 200°C–dynamic annealing for carbon ions and 1×10^{16} cm^{-2}, 30 keV at 400°C–dynamic annealing for boron ions, as indicated in Tab. 4.1. Thermal annealing is likely the reason for the difference in

intensities of the spectra between samples B and D since samples A–C were annealed twice at 650°C after the implantation of each ion species into the diamond matrix.

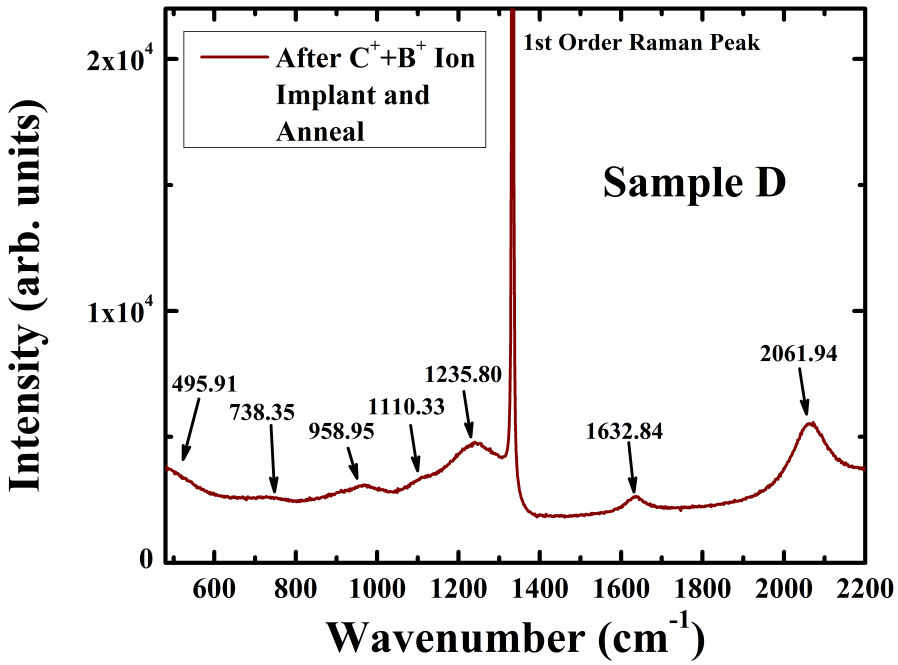

Figure 6.13: **Raman spectra of sample D.** The Raman spectra of sample D after one 15 keV cycle of carbon and 30 keV boron ion implantation with a single subsequent annealing at 650°C.

The PL spectra of sample D (see Fig. 6.14) is also very similar to that of samples B and C after ion implantation and annealing, with relative sharp features for the ZPL of both charged states of the NV color centers. The spectral intensity of the PSBs is also evidently lower than that of sample A. A comparisons between all the spectral lines is shown in Figs. 6.15, 6.16 and 6.17.

The Raman spectral comparison for samples A–D, is displayed in figures 6.15 and 6.16 relative to 514.5 nm (2.41 eV) and 457.9 nm (2.54 eV) laser excitation wavelengths, respectively. There are clear similarities with the background structure of the boron doped samples. That is, all spectra have Raman bands centered around identical positions for both excitation wavelengths. However, some of the band positions seemingly undergo slight frequency shifts or broadening likely due to resonant effects related to the different excitation energies. At high excitation energies the Raman bands centered around $\sim$1200 cm^{-1} and $\sim$1620 cm^{-1} broaden for the boron implanted samples. Moreover, there is a blue-shift of the asymmetric center $\sim$1200 cm^{-1} with a decrease in intensity relative to the longer excitation wavelength. Furthermore, the bands are less prominent for the shorter excitation wavelength, likely due to low boron concentration as reported by other scientists [33]. Albeit, the spectra due to the 514.5 nm excitation wavelength presented in this work show distinct band contributions between 1000 cm^{-1} and 1200 cm^{-1} that appear to be prevalent in boron irradiated samples. For sample C, the peaks on the left side of the diamond Raman peak ($\sim$1332 cm^{-1}) are hardly visible in comparison to the

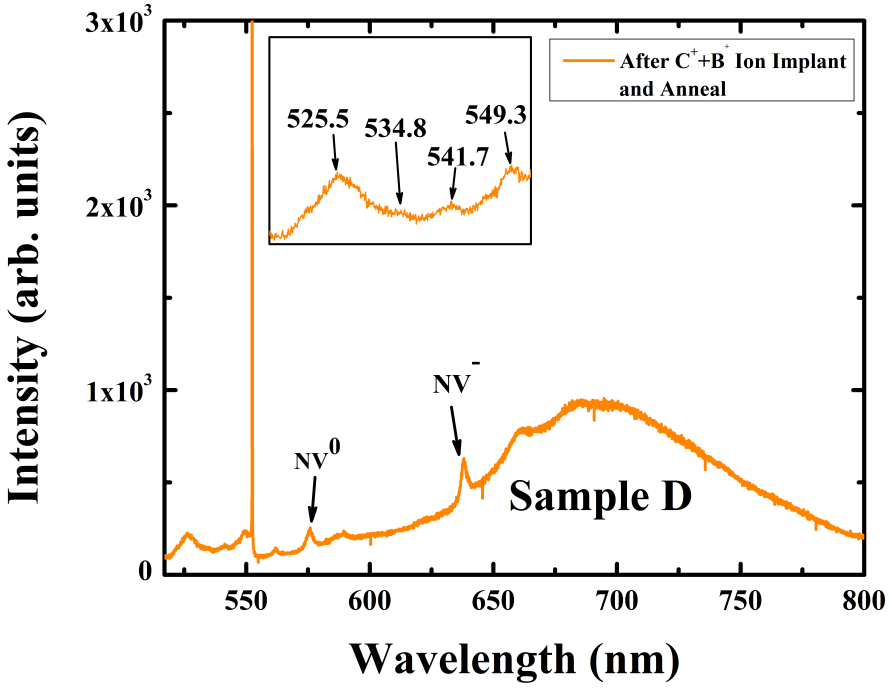

Figure 6.14: **PL spectra of sample D.** The PL spectra with a distinct phonon side band and both charge states of the NV defect. The insert shows a zoomed PL spectra of sample D, ranging between $517 - 552\,\text{nm}$.

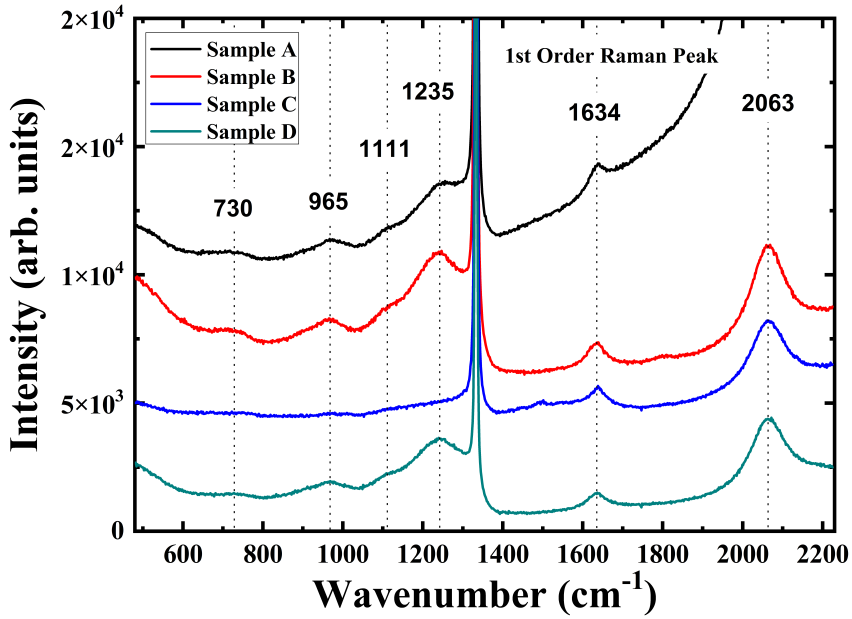

Figure 6.15: **Raman spectra of samples A–D.** A comparison of samples A–D after carbon and boron ion implantation with subsequent annealing using a 514.5 nm excitation laser.

other samples. The visible peaks on the right side of the diamond Raman peak are mainly related to the structural changes within the diamond matrix induced by implanted ions (i.e., Amorphous carbon sp^2 appearing between $1500 - 1600\,\text{cm}^{-1}$ and

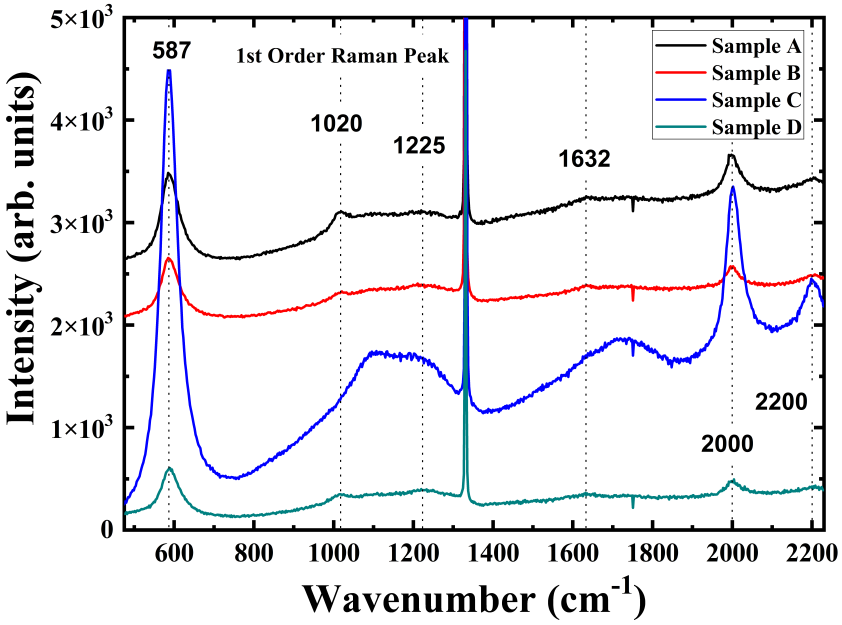

Figure 6.16: **Raman spectra of samples A–D.** A comparison of samples A–D after carbon and boron ion implantation with subsequent annealing using a 457.9 nm excitation laser.

the diamond split-interstitials at $\sim$1620 cm^{-1}). Moreover, the small G-band due to carbon implantation and annealing vanishes after boron implantation and annealing for samples A, B & D whilst it remains detectable for the carbon implanted sample C. Seemingly, there are features that are unique to the carbon implanted sample C when excited with the shorter wavelength (i.e., high excitation energies induces minimal spectral response along the PDoS and ZCP lines for the boron implanted samples with relatively low boron content). However, a red-shifted anti-resonance dip of the Fano-shaped ZCP line is noticeable. According to Mortet et al. [33], this is characteristic of a quantum interference with the continuum electronic states. Moreover, a sharp peak located at 587 cm^{-1} that decreases in intensity with an increase in boron concentration.

The PL spectra presented in fig. 6.17, shows the familiar NV color centers that seem to decrease in intensity with an increase in ion fluence. That is, the NV color centers are more prominent in sample A with lower ion fluence compared to the other samples. The color centers are not as prominent for sample D which was annealed once at 650°C.

Spectral features related to annealing

Figure 6.18 (a) and (b), displays the effect of annealing on the Raman and PL spectra of boron implanted samples A and B. From 650°C to 800°C, the PDoS peak ($\sim$1200 cm^{-1}) associated with substitutional boron becomes more prominent while the self-interstitials peak ($\sim$1600 cm^{-1}) is significantly reduced. The diamond structure completely recovers and the aforementioned peaks disappear after annealing at 1000°C for both samples. Moreover, the PL intensity spectra with NV color centers appear to be stronger after annealing at 800°C and weakens considerably after annealing at 1000°C for sample A while for sample B the intensity remains relatively higher than the PL spectra after annealing at 650°C. Figures 6.18 (c) and (d) presents

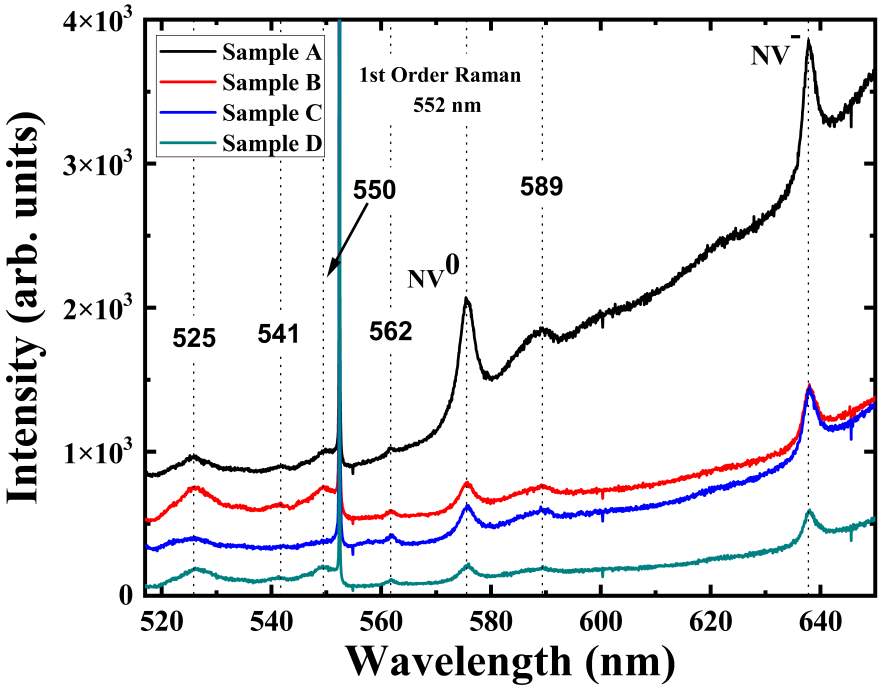

Figure 6.17: **Photoluminescence spectra of samples A–D.** A comparison of samples A–D after Carbon and Boron ion implantation with subsequent annealing.

the Fano function fit for the Raman spectra of both samples A and B after annealing at 800°C. The parameters for the Fano line profile are listed in Tab. 6.1. The subscripts 1 and 2 represent the composition parameters for the PDoS and ZCP, respectively. The intensities of both the PDoS and ZCP lines are modeled into the Raman scattering ($I(\omega)$) in Eq. 2.3. The absolute value of the asymmetric parameter $q_1 \to 1$ for both samples indicate a similar probability of the Raman scattering of the PDoS maximum with the lattice disorder induced by the substitutional boron atoms. The absolute value of the q_2 which characterizes the Raman scattering probability of the ZCPs with the lattice disorder is significantly large for sample B with a higher boron concentration. This suggests an unusual increase in the scattering intensity with increasing boron concentration. Similar to Fig. 6.4, the intensity Raman peak is cut-off at 5.5×10^4 (arb. unit), which is likely the reason for the unusual discrepancy. Hence, the value of the asymmetric parameter q_2 for the ZCP is not reliable.

Table 6.1: Line profile parameters for the Fano function fit after annealing at 800°C.

Sample	$\omega_1(\mathrm{cm}^{-1})$	$\Gamma_1(\mathrm{cm}^{-1})$	q_1	$\omega_2(\mathrm{cm}^{-1})$	$\Gamma_2(\mathrm{cm}^{-1})$	q_2
A	1245	74	-1	1330	4.1	-7.36
B	1242	73.3	-0.92	1329	4.67	-1000

Both spectra indicate an asymmetric line shape of the ZCP line that is red-shifted and centered below $\sim$1330 cm^{-1} and a Lorentzian-like PDoS at $\sim$1245 cm^{-1} for sample A and $\sim$1242 cm^{-1} for sample B. These spectral features are more prominent in sample B with nearly twice as much boron fluence. The increase in the annealing temperature for these samples seemingly affects the anti-resonance dip from the left shoulder of the ZCP line while increasing the intensity of the Raman scattering

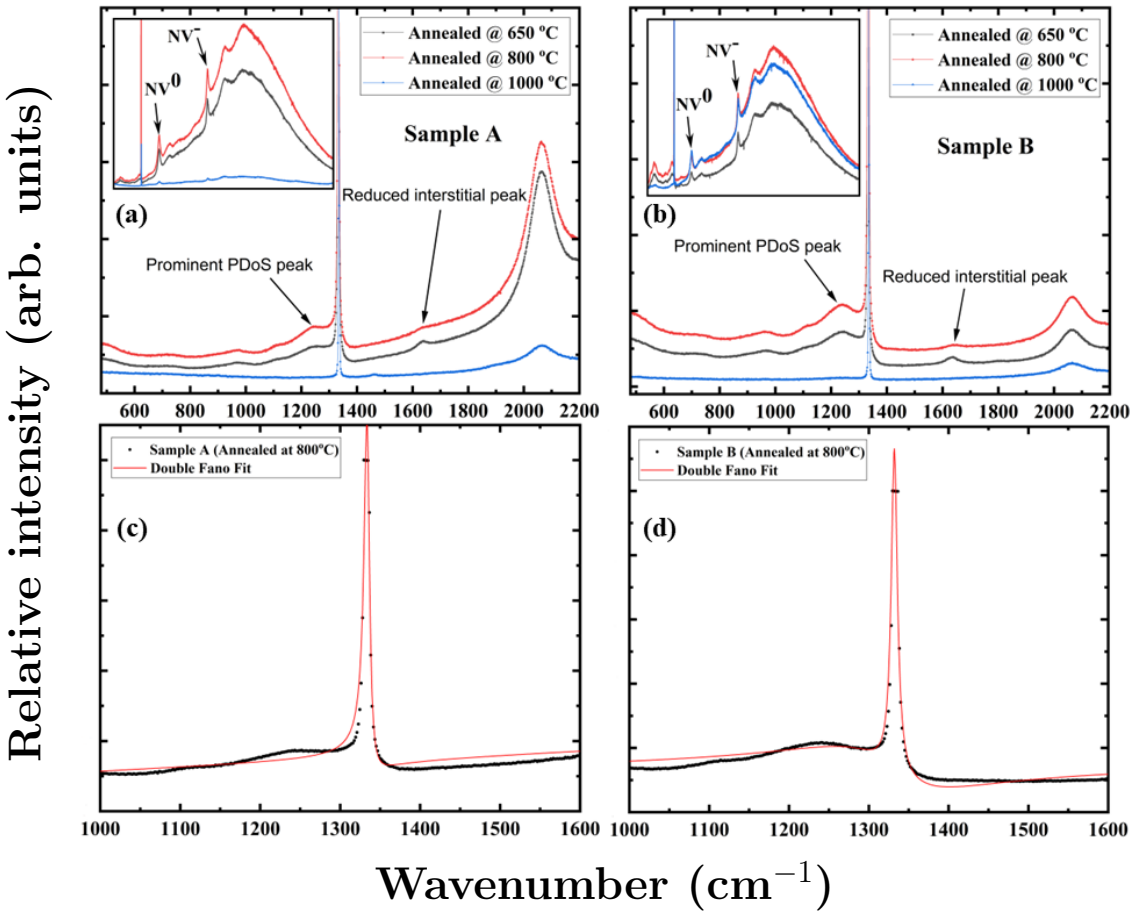

Figure 6.18: **The effect of annealing on the spectral features of boron implanted diamond.** (a) Raman spectra with a PL insert for sample A annealed at temperatures 650°C, 800°C and 1000°C. (b) Raman spectra with a PL insert for sample B annealed at temperatures 650°C, 800°C and 1000°C. A Fano function fit for the Raman spectra of (c) sample A and (d) sample B.

continuum. Evidently, sample B with a higher boron content experiences these effects more. Moreover, according to literature the degeneracy of the diamond Raman with a Fano line shape indicates the existence of charge carriers which are supposedly responsible for the quantum interference between the vibrational modes and the electronic states of the continuum.

6.2 Discussion

The effect of boron implantation has been observed with various results for different implantation and annealing processes. The samples that included the enhancement of vacant lattice sites with carbon ions close to the diamond surface clearly show a correlation between the vacancies produced in proximity to a deeper boron channel to the degeneracy of the diamond ZCP line and the boron-carbon complex structures associated with the maximum PDoS line around $\sim$1200 cm^{-1}. These structures appear after subsequent boron implantation with dynamic annealing and they become more prominent after thermal annealing. These Raman structural changes appear to be consistent with good conduction properties that can potentially lead to a superconducting state. Hence, the need to conduct electronic measurements of the

boron implanted samples (discussed in chapter 7).

Moreover, the implantation of carbon ion species with thermal annealing enhances the formation of NV color centers. A subsequent implantation and annealing process in the case of sample C has little to no effect to the aforementioned centers. However, with regard to the subsequent boron implantation and annealing in the case of samples A and B, the resulting concentration of NV centers is adversely affected. This is an indication that the scattered boron ions may very well diffuse into the vacant lattice sites through dynamic and thermal annealing processes. The diffusion of boron into these lattice sites is thought to be related to the hole state H induced below the valence band – which increases with boron concentration while the in-gap state I (related to boron interstitials) remains relatively constant with respect to boron-doped non-superconducting diamond. For future work, it is expedient to study the (B)-2p and C-2p states of these implanted samples using soft X-ray absorption (XAS) spectroscopy. This will assist in understanding the impact of boron ion implantation to the fermi-energy level.

Although, the asymmetric variations are minimal due to instrument limitations; the line widths (Γ_1 and Γ_2) of both center lines vary expectantly with respect to the boron fluence. That is, the ZCP line broadens with an increase in boron concentration while the normally Raman inactive PDoS center line becomes narrower. Notwithstanding, the line positions (ω_1 and ω_2) are red-shifted further with increasing boron content. This is consistent with the recent work by Mortet et al. [33]. Now, pending further investigation, the main objective of fabricating boron implanted layers with Fano-shape spectral features that are prevalent in superconducting states via boron keV–**implantation** and annealing has produced interesting and positive results. The enhancement of such features while maintaining the diamond structure is a necessary endeavor with the possibility of transitioning into a superconducting state. Regrettably, heavy ion implantation within a thick buried boron channel (221 nm) without any dynamic annealing leads to amorphization of the diamond structure as in the case of sample BE. Furthermore, heavy boron implantation within a thin buried boron channel (44 nm) leads to amorphous structures even with dynamic annealing as in the case of sample SE. Sample ME without dynamic annealing has potential to develop similar structural features to samples A and B within a very thin boron buried channel (31 nm). However, the self-interstial peak at $\sim$1600 cm^{-1} appears to broaden and overlaps with the amorphous-related peak at $\sim$1500 cm^{-1}. All these features in samples BE, ME and SE are known to have adverse effects to the conduction properties associated solely on p-type boron acceptor states.

Hence for future work, dynamic annealing with a scaling down of the boron fluence for subsequent implantation processes will be considered. In the next chapter, I examine the relationship between the electronic properties and the boron layer fabrication process with varying boron content for any correlations.

Chapter 7

Low-temperature measurements

The success of demonstrating the unique effects of distinct fabrication processes of keV p-type boron layers in diamond provides with the obligation to correlate the spectral results to the electronic response of the samples in a wide temperature range (i.e., 10 K $\longleftrightarrow$ 300 K). This chapter reports on the temperature-dependent electronic transport properties of the aforementioned boron implanted CVD synthetic samples. Observations from these measurements will assist in extracting important information pertaining to the temperature-dependent conduction mechanisms, as well as the charge densities and carrier mobilities associated with very thin implanted boron channels. Structurally, the first part of this chapter details the ohmic behavior of the samples as a function of temperature. This will then be extend to electrical conduction studies via two-terminal resistance versus temperature of five uniquely prepared low energy boron-implanted diamond samples. The third part of this chapter investigates the four-terminal Hall effect measurement of sample B for carrier concentration and mobility studies related to a confined boron layer buried just below the diamond surface.

7.1 Ohmic behavior

In all samples, current-voltage (I–V) measurements were taken from the diamond surface in order to extract electronic transport properties for the processed materials. A linear Ohmic behavior was determined for the boron implanted samples across a wide temperature range (10 K $\longleftrightarrow$ 300 K). Figure 7.1, shows the I–V curves for samples A and B. Sample B exhibit favorable carrier transport mechanism with Ohmic behavior from RT $\longleftrightarrow$ 122 K. A typical linear relationship between the current and the voltage for resistive semiconducting materials. Moreover, at the previously mentioned temperature range, the voltage increases with a decreasing temperature under a constant applied current (i.e., V $\propto$ R). However, a current threshold emerges from 0.8 µA corresponding to 1940 mV; displaying Ohmic and non-Ohmic regions between temperatures 182 K − 122 K, after which the Ohmic behavior ceases (refer to Fig. 7.1 (b) and (d)), suggesting a limitation of charge carrier transport mechanisms with decreasing temperature. Sample A also demonstrate Ohmic and non-Ohmic characteristics alongside a current threshold starting from 0.26 µA corresponding to 1426 mV between RT $\longleftrightarrow$ 170 K. Evidently, the current flow is significantly restricted within this temperature range compared to sample B as shown in Fig. 7.1 (a) and (c). Moreover, space charge limited current (SCLC) mechanisms [202, 203, 214], dominate from 0.026 µA − 340 mV starting from 165 K

as seen in Fig. 7.2. This behavior is likely due to the adverse effect of carbon implantation relative to the low boron fluence for sample A. At this point, sample A exhibit non-Ohmic behavior with a dependence $\longrightarrow I \propto V^2$.

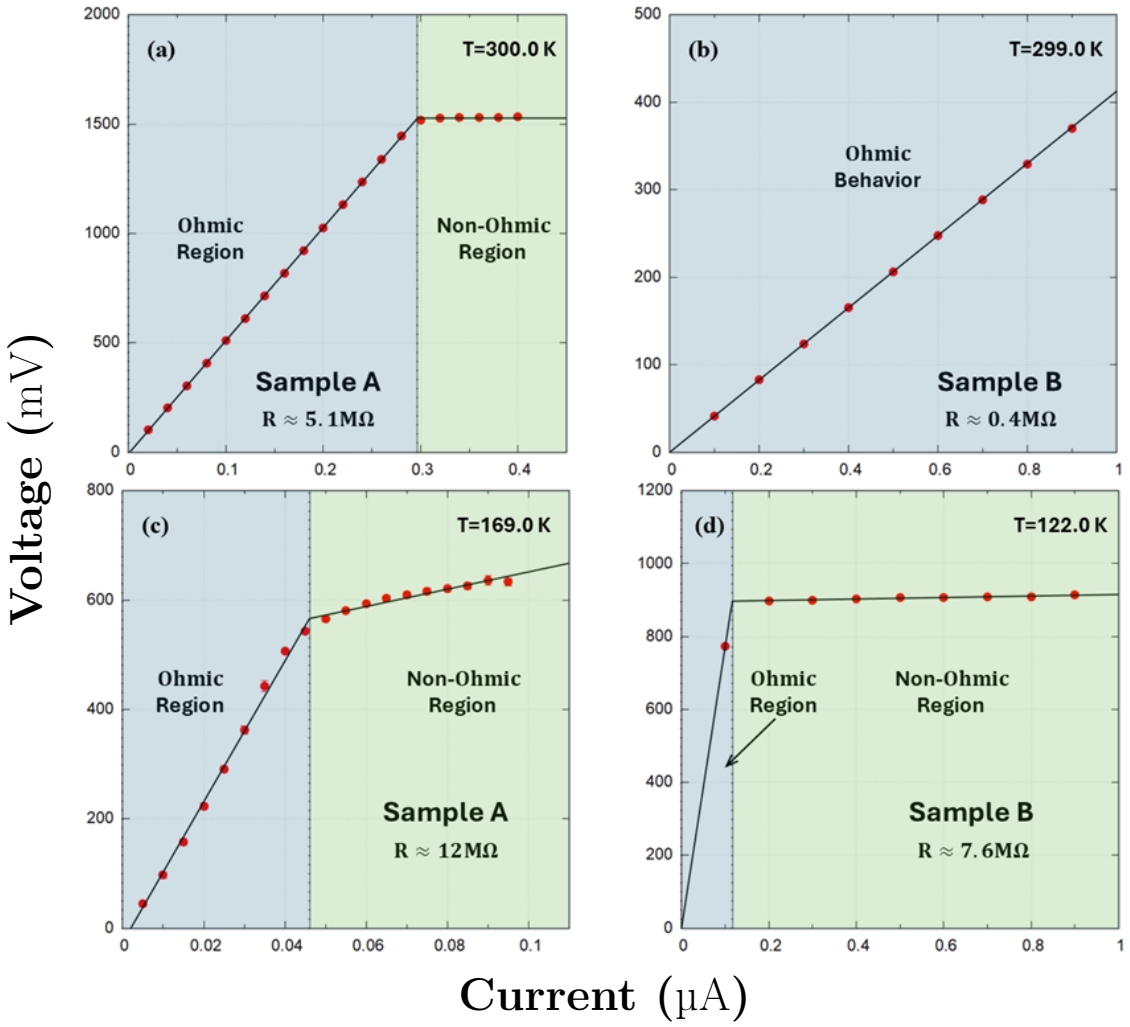

Figure 7.1: **Current–voltage measurements.** (a)–(b) A comparison of carrier transport mechanisms between sample A and B at RT, with a resistance of 5.1 MΩ and 0.4 MΩ, respectively. (c)–(d) A comparison of carrier transport mechanisms between sample A and B at low K temperatures, with a resistance of 12 MΩ and 7.6 MΩ, respectively.

The threshold values seem to have a direct correlation to the fluence of the boron ions injected into the shallow diamond regions. At first, both samples were implanted with carbon ions with a fluence of $1 \times 10^{15}\,\mathrm{cm}^{-2}$ very close to the surface (15 keV) and annealed at 650°C before implanting with varied boron concentrations. At such thermal annealing temperatures self interstitial–vacancy recombination processes are expected to occur due to the high mobility of the vacancies. These recombination processes in close proximity to the diamond surface may result in the delocalization of the trapped charged states, potentially having a positive influence on the conduction properties of the materials. Contrarily, the consequent low boron fluence with annealing for sample A appear to be inadequate to compensate this effect with evident SCLC mechanisms emerging at low temperatures. Similar behavior was

reported by other researchers at RT with high carbon implantation energies $\sim$ MeV [203, 214]. However, the increase in boron fluence (by 1 order of magnitude greater than the carbon fluence) with annealing clearly compensates such effects as evidenced by the comparison between sample A and B. This may well indicate that there is also a correlation between the concentration of boron and the diffusion of boron into the vacancies.

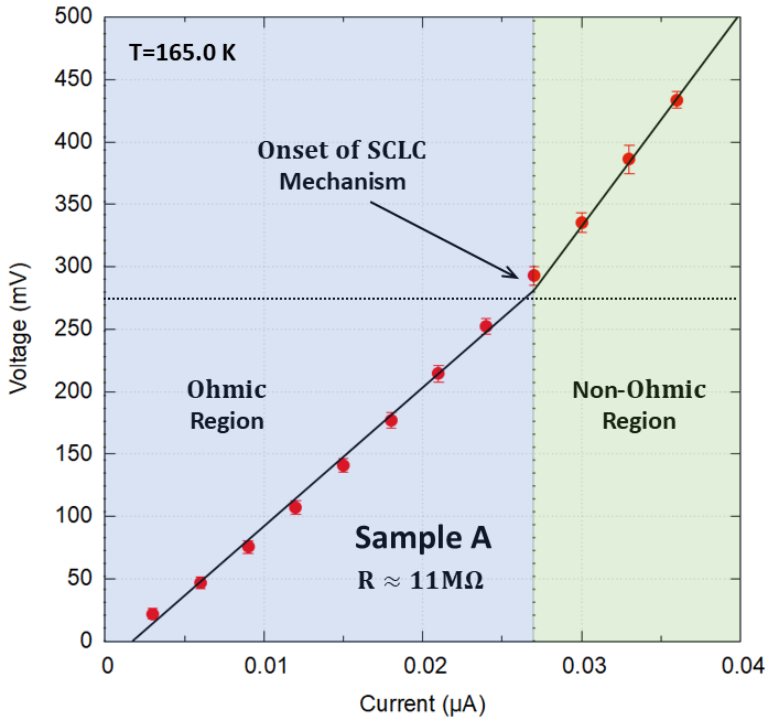

Figure 7.2: **SCLC Mechanism at low K temperatures for sample A.** Temperature-dependent SCLC behavior on sample A with onset at 165 K.

The slope of the I–V curves give the resistance of the materials. As expected for semiconducting materials, the resistance increases exponentially with decreasing temperature. The current threshold in Fig. 7.1, indicate constraints to the conduction properties of the boron implanted layer likely due to low activation of the boron ions such that the voltage reaches a saturation point at specific current values; influencing the electronic response of the samples. Interestingly, the current threshold values of sample B are much greater than that of sample A, which implies greater conduction properties for sample B. Furthermore, the current threshold of both samples A and B decreases exponentially with decreasing temperature as seen in Fig. 7.3, until the Ohmic behavior stops. Moreover, there is a clear dependence on the boron content for the onset of the current threshold. That is, the sweeping current range (μA) applied in order to measure the corresponding voltages (mV) used to investigate the conduction properties for sample A is only a fraction of that used for sample B which has a relatively higher boron concentration. This is a clear experimental observation of the exponential decrease of the conduction of electrons with decreasing temperature in boron induced p-type diamond.

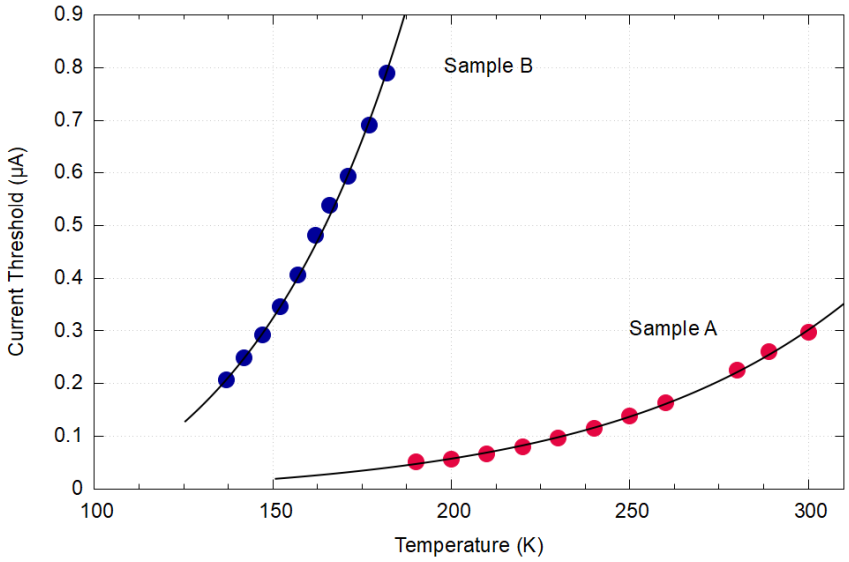

Figure 7.3: **Temperature-dependent current threshold.** The current threshold of samples A and B. The onset is due to boron content.

7.2 Two-terminal resistance measurements

Figure 7.4, shows the results for resistivity as a function of temperature for samples A, B, ME, SE and BE where the correction factor f was very close to ~ 1. Evidently, the resistivity seem to have an inverse relationship to the atomic concentration of p-type boron in diamond.

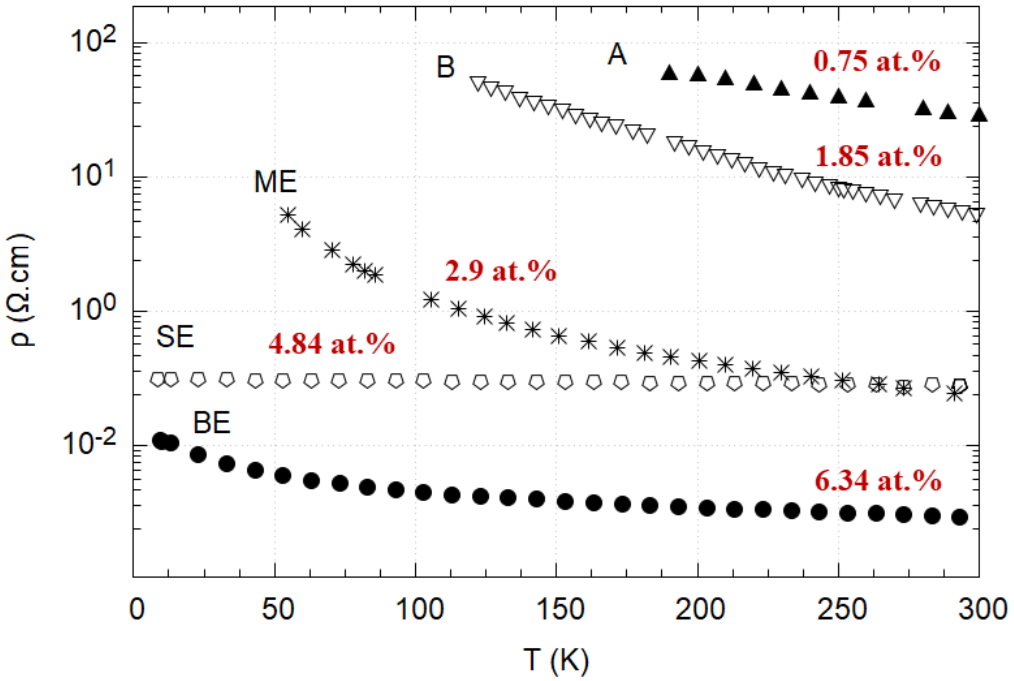

Figure 7.4: **Temperature-dependent resistivity measurements.** A comparison between boron implanted samples A, B, ME, SE and BE. The boron content are included in red.

The samples A and B implanted with carbon and boron reach a surface conduction

limit at relatively high temperatures ($\sim$ 100 K) with low-temperature resistivity that is 2–3 orders of magnitude more as compared to the multi boron-implanted samples. The annealing thermal temperature for boron activation is the same for all the samples, at 650°C. At this stage, it is not clear what fraction of the implanted boron is activated. The two-terminal electronic setup used was not configured for Hall effect measurements used to determine the carrier concentration. Only samples A and B underwent the aforementioned measurements using other systems. The boron activation is not expected to be very high due to the low thermal annealing temperature that was used.

However, the boron content variation within the buried channels associated with each sample should result in substantial differences in the activated boron concentrations inside the implanted layer. Nonetheless, from the conduction transitions the activation energies can be extracted to give good information regarding the transport properties within the boron implanted regions. **NB.** The physically destructive SIMS technique was intentionally avoided in order to preserve the structural integrity of the fabricated boron channels for further sample processing. A recent study by Willems van Beveren et al. [92], has shown a very close agreement between the SRIM simulated boron concentration and the experimentally determined SIMS boron concentration. Hence, the simulated atomic concentrations are fittingly considered in this study.

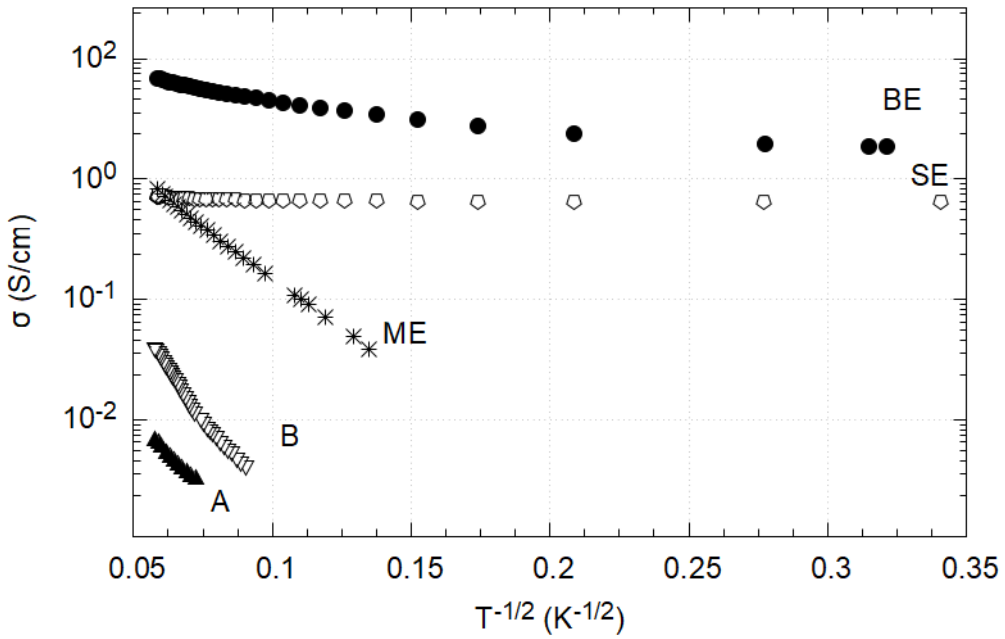

Figure 7.5: **Temperature-dependent conductivity measurements.** A comparison between boron implanted samples A, B, ME, SE and BE.

Figures 7.5, shows the low current ($\sim$ µA) DC conductivity σ as a function of $T^{-1/2}$. The more insulating samples (A, B and ME), exhibit linear regions as the temperature decreases which is consistent with Efros-Shklovskii (ES) hopping [38, 84, 110]. It is worth noting that at extremely low temperatures, while a material is in an insulating phase, the movement of charge carriers between different localized states in doped semiconductors is characterized by the conduction hopping law,

$$\sigma(T) = \sigma_m \exp(-[T_0/T]^m), \tag{7.1}$$

where σ_m is a temperature-independent factor, m is the hopping exponent determined from the reduced activation energy plots and T_0 represents the characteristic temperature that exhibits an inverse relationship with the localization length ξ_{loc}. As mentioned before, the variable-range hopping (VRH) depends on how the single-particle DoS behaves at the Fermi energy as the temperature decreases. Hence, T_0 can be classified as T_{Mott} with $m = 1/4$ for Mott VRH and T_{ES} with $m = 1/2$ for ES VRH. A high value of T_{Mott} suggests a reduced number of localized states at the Fermi level, while a high value of T_{ES} shows convergence in the dielectric response [38, 215]. From the conductivity plots (see Fig. 7.5 and 7.6), the characteristic temperature T_0 extrapolates to extremely low temperatures for the samples BE and SE which suggests large localization lengths ξ_{loc} over a long temperature range. Consequently, large ξ_{loc} imply very weak localization at the Fermi level, due to their high boron content confined within nm-sized regions (more extensively for sample SE with a boron-buried region of about $\sim 44\,\text{nm}$).

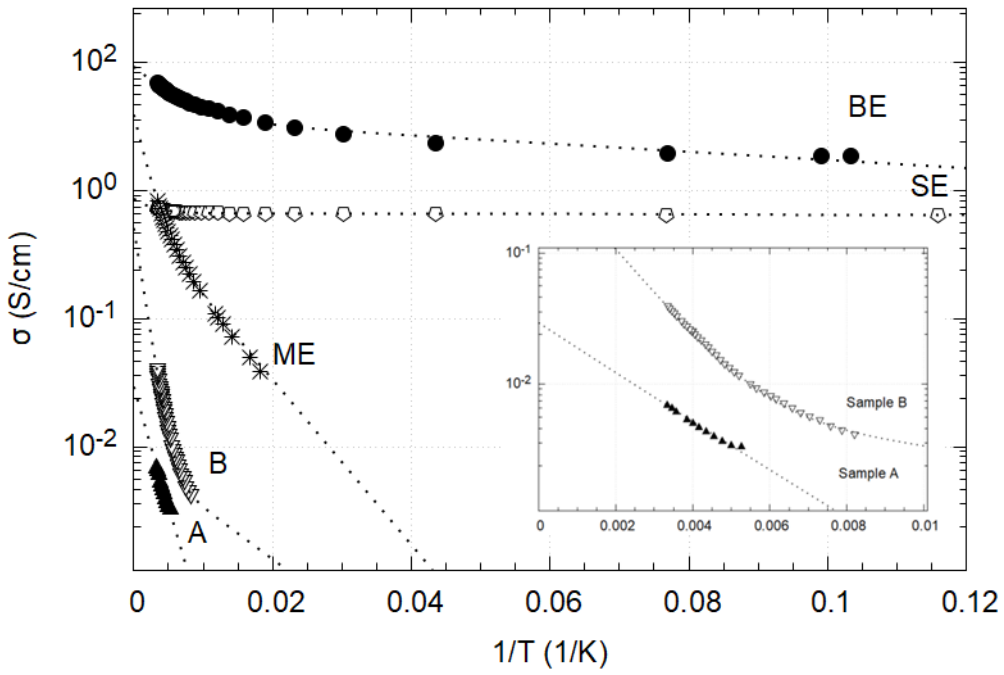

Figure 7.6: **Arrhenius plot of the conductivity.** A comparison between boron implanted samples A, B, ME, SE and B. The insert zooms into samples A and B.

Figure 7.6, shows the Arrhenius plot where activation energies can be extracted. From the slopes and intercepts, the VB conduction activation energies for all the samples is in the low $\sim$ meV level, i.e., 10 meV $\rightarrow$ BE, 6.8 meV $\rightarrow$ SE, 52 meV $\rightarrow$ ME, 82 meV $\rightarrow$ B and 43 meV $\rightarrow$ A. These are much lower than the 370 meV that has been extensively cited in literature for boron-doped diamonds with low doping concentrations ($\approx 10^{19}\,\text{cm}^{-3}$). For doping concentrations close to the Mott transition level ($\approx 4\times10^{20}\,\text{cm}^{-3}$), the activation energy E_{a1} significantly decreases and eventually vanishes. This suggests that all the investigated samples have surpassed the Mott transition.

Table 7.1: Activation energies of the conduction mechanisms.

Sample	E_{a1} (meV)	E_{a2} (meV)	E_{a3} (meV)	Boron/cm^{-3}	R_p(nm)	ΔR_p(nm)
A	43	–	–	1.3×10^{21}	56.1	12.3
B	82	35	24.4	3.5×10^{21}	56.1	12.3
SE	6.8	0.8	0.1	9.5×10^{21}	29.9	9.1
ME	52	26	15	5.2×10^{21}	20.5	7
BE	10	3	0.85	3.7×10^{21}	–	–

With an increase in impurity concentration, the wave functions of the excited levels of boron begin to overlap, resulting in the formation of an impurity band [200]. Consequently, the conduction mechanism shifts to variable hopping. Moreover, the activation energy E_{a3} for the hopping conduction between occupied and unoccupied acceptor sites observed at lower temperatures shows a significant increase with boron concentration between samples BE and SE. This is also the case for samples ME and B. The behavior is not consistent between the two batches likely due to the extended temperature range for samples BE and SE leading to a 1 order of magnitude disparity. E_{a3} is also related to the degree of compensation from donors such as neutral vacancies and nitrogen defects in CVD grown layers. However, the concentration of nitrogen donors commonly found in CVD produced layers vary from $10^{16}\,\mathrm{cm}^{-3}$ to $10^{18}\,\mathrm{cm}^{-3}$, resulting in enough number of ionized acceptor sites for boron concentrations close to the Mott density, i.e. $[N_A - N_D] > 10^{19}\,\mathrm{cm}^{-3}$.

The second term accounts for the hopping conduction due to thermal excitation of boron levels within the impurity band. This is where hole motion takes place in the presence of neutral acceptors and is activated by a thermal energy E_{a2}. From the results obtained, samples BE and SE requires minimum boron excitation energies as compared to samples ME, B and A. That is, close to the Mott density, the impurity band conduction dominates at high temperature regimes ($\geq$RT).

7.3 Hall effect measurements

There is minimum deviation of the temperature-dependent resistivity at different applied magnetic fields (see Fig. 7.7). This indicates minute increments in the localization of the wave functions of the embedded boron atoms with increasing magnetic fields for sample B [92]. That is, from mid-range temperatures ($\sim 100\,\mathrm{K} \rightarrow 0\,\mathrm{K}$) the resistivity increases slightly with the applied magnetic field. Which implies weak localization at temperature regimes where VRH dominates.

Figure 7.8 (a), shows the resistivity for sample B after thermal annealing at two different temperatures, 650°C and 800°C specifically for boron activation. Interestingly, there is a two orders of magnitude difference in resistivity after annealing at 800°C, where the resistivity level at room temperature is comparable to that of sample ME and SE. However, the conduction mechanisms between the same temperature range for sample B changes with the VB conduction activation energy $E_{a1} \approx 52\,\mathrm{meV}$ (see fig 7.8 (b)). At this stage, it is clear that the different fluences and

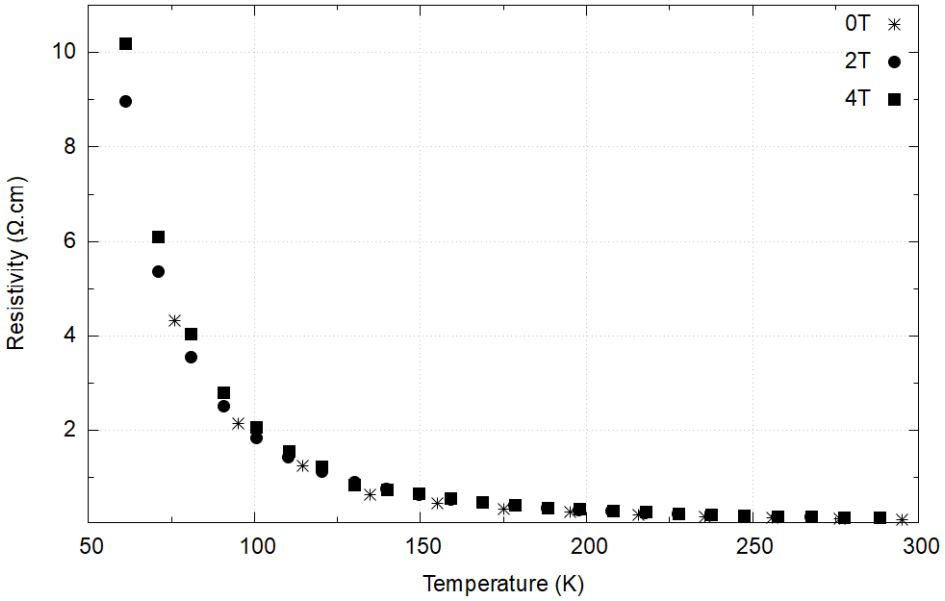

Figure 7.7: **Temperature-dependent resistivity measurements at different magnetic fields for sample B.** A minimum deviation of the resistivity between 0–4 T applied magnetic fields.

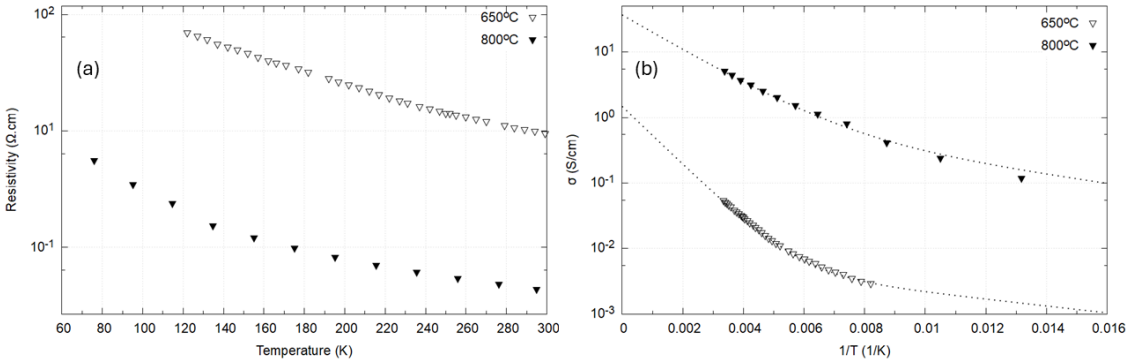

Figure 7.8: **Temperature-dependent resistivity and conductivity σ measurements for sample B.** A comparison between two different annealing temperatures, 650°C and 800°C of (a) Resistivity and (b) Conductivity with an Arrhenius fit.

annealing processes have distinct effects on the conduction mechanisms in diamond. Moreover, the temperature-dependent surface conduction limit was reduced by $\sim 60\,\mathrm{K}$ ($120\,\mathrm{K} \rightarrow 60\,\mathrm{K}$) which opens a gap to study the effect of annealing temperatures to conduction mechanisms at lower temperatures for highly compensated boron regions. Sample B was also annealed at 1000°C where the boron activation is expected to be much higher. As reported in the previous chapter, the diamond structure was fully recovered according to the spectral analysis. The low temperature measurements were unsuccessful mainly due to Ohmic contact issues. However, by using a fluke, the surface resistance was very similar for both annealing temperatures.

Figure 7.9, shows the carrier concentration measured at different applied magnetic fields (2 T and 4 T), for thermally annealed sample B. Clearly, the carrier concentration increases exponentially with temperature. The carrier concentration also increases with applied magnetic field, reaching maximums of $3.8 \times 10^{17}\,\mathrm{cm}^{-3}$ and

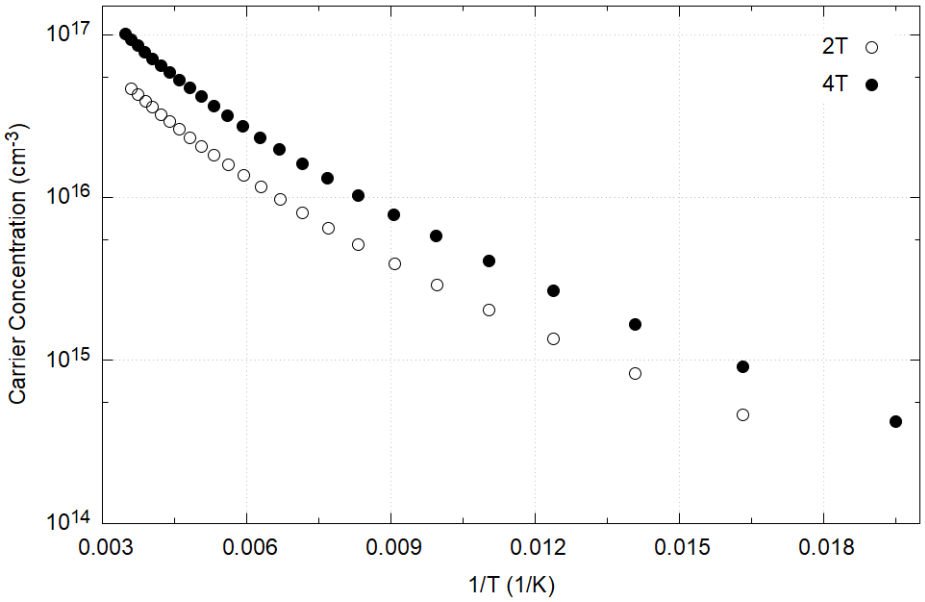

Figure 7.9: **Temperature-dependent carrier concentration measurements for sample B.** A comparison between two different magnetic fields, 2 T and 4 T.

$8.2 \times 10^{17}\,\mathrm{cm}^{-3}$ at 2 T and 4 T, respectively. This is comparable to the concentration of compensating nitrogen donors found in diamond. The carrier concentration converges to the same level of $4.4 \times 10^{15}\,\mathrm{cm}^{-3}$ close to the temperature-dependent surface conduction limit (i.e., the hall voltage v_H is the same around 60 K and 50 K for 2 T and 4 T, respectively). The active boron is much less than 1% of the predicted boron concentration in sample B. From the spectral features discussed in the previous chapter, this is likely due to the presence of compensation factors such as vacancies, self-interstitial and nitrogen defects within the buried region [216]. Nonetheless, this clearly indicates a relatively low thermal activation of boron ions in sample B even at RT. Similarly, the carrier mobility is also shown in fig. 7.10. The carrier mobility increases with a decrease in temperature, showcasing an inverse relationship between low carrier concentration and high carrier mobilities consistent with the VB conduction σ_1,

$$\sigma_1 = q p_1(T) \mu_1(T), \tag{7.2}$$

where q is the elementary charge, p_1 the concentration and μ_1 is the mobility of the charge carriers.

Recently, the carrier mobility of boron-implanted samples has been reported with values ranging between $1.77\,\mathrm{cm}^2/\mathrm{Vs} \rightarrow 3.9\,\mathrm{cm}^2/\mathrm{Vs}$ related to increasing boron concentration at RT [92] (similar range for superconducting diamond$\sim 10^1\,\mathrm{cm}^2/\mathrm{Vs}$ [217]). Consistent with results from BDDs investigated by other scientists detailing the adverse impact of scattering effects in the mobility of p^{++} samples [216, 217]. The relatively high mobility for sample B suggests minimum scattering effects within the $\sim$ 51 nm boron implanted layer; a reasonable inference due to the low boron concentration calculated from the RT hall data. Also, an increase in magnetic field adversely affects the carrier mobility. For the 2 T applied magnetic field, the mobility increases from $143\,\mathrm{cm}^2/\mathrm{Vs}$ at RT to $237\,\mathrm{cm}^2/\mathrm{Vs}$ at 60 K while for 4 T the mobility increases from $71.4\,\mathrm{cm}^2/\mathrm{Vs}$ at RT to $119\,\mathrm{cm}^2/\mathrm{Vs}$ at 60 K. The observed phenomenon

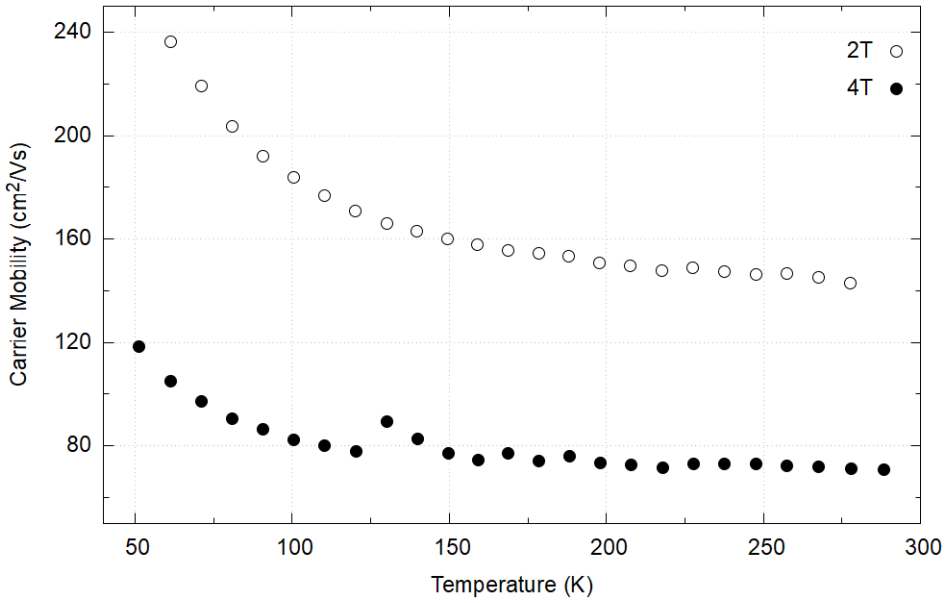

Figure 7.10: **Temperature-dependent Hall mobility measurements for sample B.** A comparison between two different magnetic fields, 2 T and 4 T.

can potentially be attributed to the reduced effective mobility of the carriers due to increased scattering in the presence of a magnetic field.

7.4 Seebeck coefficient

Seebeck measurements were conducted on the boron implanted diamond samples in conjunction with the study reported in [204]. However, the data was noisy and inconclusive for all the other boron implanted samples except for the highly boron-implanted sample BE. Likely, due to the amorphization of the diamond structure (please see Fig. 6.5).

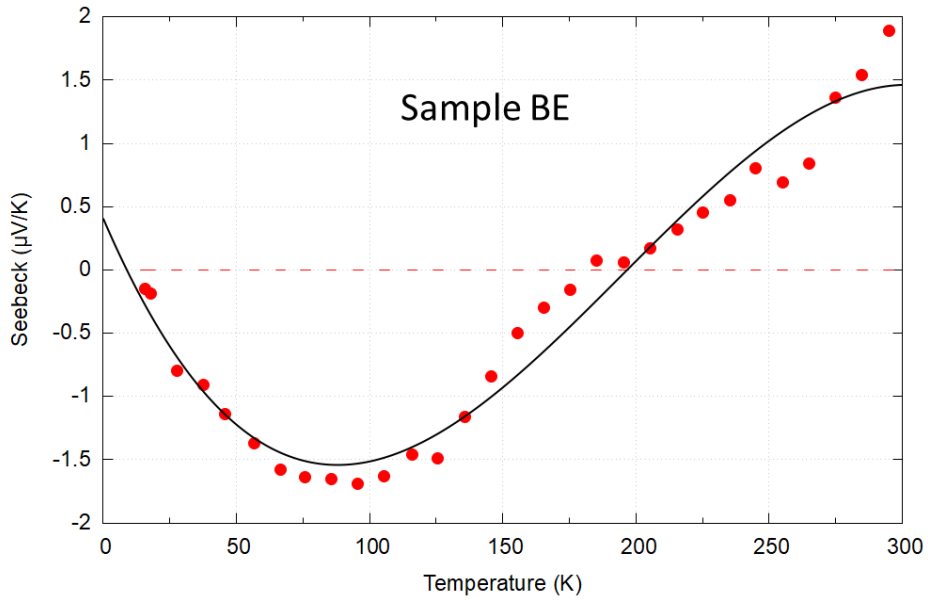

Figure 7.11: **Temperature-dependent Seebeck coefficient for sample BE.** A small dip at low temperatures signifying a phonon drag effect.

Figure 7.11, shows the temperature-dependent Seebeck coefficient for sample BE with a small phonon drag effect at low temperatures. Evidently, the behavior is both familiar and peculiar. The data exhibit a negative peak of about $-1.7\,\mu V\,K^{-1}$ at around 95 K and then tends to zero as the temperature approaches zero. However, beyond 95 K, the Seebeck coefficient constantly increase with temperature and reaches a positive value of $2\,\mu V\,K^{-1}$. The negative sign of the Seebeck at room temperature, where the phonon-drag contribution is assumed to be negligible, agrees with measurements reported in graphite. From galvanometric [218] and thermoelectric measurements [219–223], the negative sign of the Seebeck in graphite was interpreted as a higher mobility of electrons compared to holes. However, although the implanted region is highly graphitic, it is also highly implanted with p-type boron. This interesting behavior in boron-implanted diamond is still under investigation and discussions with respect to the contributing charge carriers. For further comprehension on the phonon drag effect in buried channels within diamond, refer to our recent published work [204].

7.5 Discussion

The electronic properties of the studied samples evidently show a clear dependence on boron concentration, thermal annealing temperatures and the implantation processes used. The highly boron-doped samples BE and SE exhibit good conduction properties across a wide temperature range 300 K $\rightarrow$ 10 K with high characteristic temperature T_0 for both Mott and ES VRH regions. This suggests week localized states near the Fermi energy level for both samples. The VB activation energy of these samples is very low $\sim$ 10 meV<370 meV, implying that the relationship between the inverse temperature and the ionization energy follows an exponential pattern, where higher temperatures lead to a decrease in ionization energy consistent with transitions even beyond Mott transition level. This leads to a high degree of boron ions activated at RT. Hence, the resistivity decreases significantly for the multi-implanted diamond samples BE, SE and ME.

There exists a proportional relationship between the boron fluence and the electronic conduction of the samples, irrespective of the fabrication processes used. The temperature-dependent surface conduction threshold at relatively high temperatures suggests a high degree of localized charge states in close proximity to unavoidable diamond defects due to ion irradiation; this adversely limits the conduction properties within the boron implanted layers. There is clearly compensating defects for samples fabricated with relatively low boron concentrations as well as with the vacancy inducing carbon ions close to the diamond surface for samples A and B. Overcoming such compensating factors is a necessary endeavor for the full activation of boron ion embedded diamond regions. The multi-implanted sample ME with a relatively small boron buried region $\sim$ 31 nm with a higher T_0 shows better conduction compared to samples A and B. This suggests that the careful overpopulation of boron ions within the same small buried region reduces the effect of the compensating defects that affect the conduction properties.

Moreover, annealing which is known to activate the boron ions in diamond also has a positive effect on the conduction of boron-implanted diamond. Sample B shows a conduction improvement by two orders of magnitude when the thermal annealing temperature is increased to 800°C. Many scientists have reported good activation of boron at even higher temperatures. Unfortunately, annealing at temperatures higher

than 1000°C anneals out the specific boron induced defects that are speculated to have a role in superconducting boron-doped diamonds,i.e., the red-shift of the ZCP and PDoS near the 1st order diamond Raman.

Regrettably, all the samples do not exhibit superconductive behavior. Furthermore, the samples that are highly implanted with boron (BE and SE), exhibit high conductivity with weak localization related to an overly disordered diamond lattice. This substantiates the sp^2 disorder features presented in Chap. 6, for the above mentioned samples. Samples A, B and ME that are relatively lightly boron implanted showcase low conductivity with significant localization of the wave functions. Moreover, the typical conduction properties are limited to high temperature ranges (i.e., $300 - 50\,\mathrm{K}$ for ME, $300 - 120\,\mathrm{K}$ for B and $300 - 180\,\mathrm{K}$ for A). Undoubtedly, there are conduction limiting factors associated with these samples as mentioned. Hence, a thorough investigation is needed in order to characterize all the limiting factors. Presently, sample B exhibits scattering effects in the presence of a magnetic field likely due to the ionization of the boron impurity ions and carrier-carrier scattering between the n-type and p-type defects. Furthermore, samples A demonstrate space charge limited currents (SCLC), likely due to the effects of the initial carbon implantation process relative to the boron fluence used. Notably, an increasing boron concentration with annealing processes seemingly has a positive impact on the conducting properties of these diamonds.

From the current data and discussion it is clear that in order to extend this study towards favorable results, an integration of the fabrication parameters is a necessity most likely with the utilization of EL SC CVD type IIa diamonds to limit scattering effects. That is, a meticulous low fluence multiple implantation of boron ions within a small buried channel close to the diamond surface with both dynamic annealing (~ 400°C) and thermal annealing (~ 800°C for an extended period of time for better boron activation) – presents the most probable route to avoiding amorphization of the diamond lattice whilst altering the positioning and intensities of ZCP and PDoS lines consistent with features that are associated with superconducting bulk diamonds.

Chapter 8

Conclusion and recommendations

8.1 Summary and Conclusion

From Raman spectral analysis, the fabrication of well-known boron-related features ($\sim 500\,\mathrm{cm}^{-1}$ and $\sim 1200\,\mathrm{cm}^{-1}$ with a red-shifting of the ZCP line) is confirmed after low energy ($\sim$ keV) boron ion implantation in thin shallow diamond layers uniquely for samples A and B. That is, diffusion by boron irradiation is established with an expected dependence on the boron fluence. This is achieved with no detectable graphitic characteristics emerging. Emphasizing on the favorable contribution of both dynamic annealing and subsequent thermal annealing as evidenced by the dissimilar structural evolution of sample ME, even though the total boron concentration is closely comparable; the Raman features due to boron mentioned above are barely detectable in sample ME. For sample BE and SE, there are dominant graphitic features post implantation and annealing, which contribute significantly to the electronic properties of the samples. The vacancy inducing carbon implantation process utilized for samples A and B also play a significant role such that the vacancy peak $\sim 1500\,\mathrm{cm}^{-1}$ appears readily after carbon implantation with annealing at 650°C. Interestingly, the peak vanishes completely after boron implantation and does not reappear after re-annealing at 650°C. Moreover, the split-interstitial peak at $\sim 1620\,\mathrm{cm}^{-1}$ also materializes after carbon implantation and increases in intensity with annealing and boron implantation. The aforementioned peak is reduced considerably and vanishes after annealing at 800°C and 1000°C, respectively. Regrettably, annealing at $\geq$1000°C also anneals out the boron-related peaks that are associated with superconducting properties in boron-doped diamond. This is a consistent trend also with high energy MeV boron implantation conducted by other scientists in recent years.

Based on the current electronic conductivity data of the samples, certain questions are addressed regarding low-energy boron ion implantation in diamond. Firstly, all the boron implanted samples confirm Ohmic behavior. However, the IV curves for samples A and B showcase current threshold characteristics above which the Space Charge Limited Currents (SCLCs) mechanisms is observed for sample A. The SCLCs have been demonstrated to be induced by the carbon implantation process, with annealing linked to the low fluence of the subsequently implanted boron ions. This is indicative of compensating defects such as interstitials and vacancies that likely generate localized fields that opposes the movement of charge carriers, resulting in localized trapped space charges which limit electrical conductivity through the boron

implanted channels. The evolution of such defects has been confirmed at the surface shallow layers by Raman spectral analysis (refer to chapter 6). Nevertheless, upon further processing and analysis of sample B, IV characterization show that the SCLC behavior can be circumvented by both increased boron fluence and likely thermal treatments of up to 800°C.

This is in agreement with the carbon induced defect-related conductivity model by Baskin et al. [202], where the activation energy E_{a2} is attributed to the vacancy concentration and annealing temperatures. According to the Arrhenius plot, the activation energies E_{a2} of the boron-only implanted samples with their corresponding vacancy concentration peaks are $0.8\,\mathrm{meV} - 1.8 \times 10^{23}\,\mathrm{cm}^{-3} \rightarrow$ SE, $3\,\mathrm{meV} - 1.7 \times 10^{23}\,\mathrm{cm}^{-3} \rightarrow$ BE and $26\,\mathrm{meV} - 3.9 \times 10^{22}\,\mathrm{cm}^{-3} \rightarrow$ ME. The carbon and boron implanted Sample B did not follow the same trend with an activation energy of $35\,\mathrm{meV}, 1.63 \times 10^{23}\,\mathrm{cm}^{-3} \rightarrow$ B, likely due to a high vacancy contribution due to the carbon implantation process. **NB.** Dynamic annealing at 200°C and 400°C comprehensibly eliminated the effect of graphitization. However, the carbon ion implantation process with annealing does not appear to achieve the desired effect of beneficially influencing the activation of boron's acceptor characteristics within the 1st cycle of boron implantation. Moreover, the conduction of the lower boron fluence implanted sample A is only attributed to the VB conduction activation energy E_{a1}. Initial Hall effect measurements after 650°C for sample B also confirm the suppression of hole carriers with contribution of n-type carriers that are ascribed to the "amphoteric" vacancy states. The electrical conductivity dependence to thermal annealing is also displayed after annealing at 800°C. The activation energies of boron sample B decreased slightly (E_{a1}=51 meV, E_{a2}=34 meV and E_{a3}=24 meV), with increasing annealing temperature while the carrier concentration increased by 1 order of magnitude.

Lastly, no superconducting states were found in all the samples. Also, sample SE displayed a peculiar metallic-like behavior of the highly implanted boron layer. From spectral analysis it is evident that there is a high degree of graphitic regions with a relatively low resistivity of $\sim 2 \times 10^{-1}\,\Omega\,\mathrm{cm}$ that extends across a wide temperature range. Although, the diamond structure is still intact as compared to sample BE which is mainly graphitized with a resitivity of $1 \times 10^{-2}\,\Omega\,\mathrm{cm}$ at RT that increases to $7 \times 10^{-2}\,\Omega\,\mathrm{cm}$ at $\sim 10\,\mathrm{K}$. Expectantly, a higher σ corresponds to the implanted layers characterized by higher $\mathrm{sp}^2/\mathrm{sp}^3$ ratios for these samples.

In conclusion, we have demonstrated a low energy boron implantation technique with dynamic annealing that transforms the diamond structure to exhibit boron related features that are ever present in superconducting boron-doped diamonds (i.e., the Lorentzian-like component $\sim 1200\,\mathrm{cm}^{-1}$ and the asymmetric line shape $\sim 1300\,\mathrm{cm}^{-1}$ in sample A and B). The emergence of these line shapes is an indication of the presence of free charge carriers thought to be heavily involved in the electron-phonon mechanism interpretation of superconductivity in diamond. These features are enhanced by an increase in boron fluence and thermal annealing up to 800°C. However, we have also shown experimentally the effect of boron dimers that arises due to the high density of vacancies and interstitials; adversely disrupting the flow of the free charge carriers within the diamond matrix. However, the positive impact of increasing the boron fluence and thermal annealing up to 800°C also proved to decrease the effect of these boron dimers. Moreover, the effect of low energy and low fluence multiple boron implantation with thermal

annealing was also demonstrated with similar features developing, albeit, with very low spectral intensities and a more robust impact on the diamond structure for sample ME. Furthermore, conventional heavy boron implantation in order to overpopulate nm–sized diamond channels with boron result in the formation of amorphous structures. Contingent upon further investigation of the samples with additional cycle implantation processes, the approach to positively influencing the conduction phases that lead to superconductivity in diamond primarily through the activation of boron is to optimize the boron-related characteristics while minimizing the compensating factors related to self-interstital and vacancy recombination processes, and n-type nitrogen defects, etc. Not a simple task. But effectively, there is a research gap to explore with multiple boron implantation processes via reasonably low fluences and annealing temperatures.

8.2 Future works & recommendations

First and foremost the completion of this research study came with its own fare share of unforeseen disrupting and delaying factors that adversely affected the progress of the study. The factors in question include the Covid-19 pandemic, severe electricity loadshedding in South Africa and the prolonged technical issues with the ion implanter at iThemba LABS, Johannesburg, South Africa. As a result, the collection of data was extremely challenging and chaotic at times. Consequently, there are other aspects of this study that are yet to be fully addressed due to time constraints; mainly the **multiple** boron implantation with annealing processes and analysis of sample B as well as the hall effect measurements of all the other samples. Reasonably, there has also been a reluctance to explore the more destructive depth and concentration profiling experimental techniques such as SIMS and XPS in order to conclusively confirm the simulated data.

Despite the setbacks, from the results obtained thus far, there is plenty of reason to be excited for new developments that will assist in fully realizing the effect of boron implantation in diamond. Less graphitic features in samples A and B implies that multiple boron implantation processes can be easily employed within the same implanted layers for additional evaluation of the diffusion and activation of intrinsic boron atoms in diamond. The improvement of the electronic properties due to increasing the boron concentration and annealing in nm-sized diamond layers proves to be a positive factor to pursue strongly correlated 2D boron layers in diamond. Further investigation of the carbon induced SCLC layers in proximity to the shallow boron implanted layers is an unintended outcome that can potentially lead to future developments that can circumvent compensating factors that suppress excellent boron induced conduction properties in diamond. And, eventually fabricate superconducting diamond structures with the theoretically predicted high temperature T_c via a non-equilibrium process such as ion implantation.

Finally, as per discussions with my supervisor and collaborators, plans are in progress to fully address every aspect of this study in the near future. The objective is to pursue the positive indicators that were established towards the end. Electron microscopy and diffraction characterization will also be considered. Hopefully, this will be possible with the implanters available in France. Moreover, a manuscript for publication in a peer reviewed journal is underway.

Appendices

Appendix A

Publication

- Rosales-Guzmán, C., Bhebhe, N., Mahonisi, N. and Forbes, A., 2017. Multiplexing 200 spatial modes with a single hologram. Journal of Optics, 19(11), p.113501.

- Salami, S., Pailhès, S., Adessi, C., Giordano, V.M., Mahonisi, N., Mthwesi, Z., Vignoli, S., Debord, R., Fulcrand, R., BLANCHARD, N. and Every, A., Phonon-Drag in a Graphite Channel Buried in Diamond. Available at SSRN 4658686.

- Mthwesi, Z., Salami, S., Mahonisi, N., Margueritat, J., Giordano, V.M., Debord, R., Adessi, Every, A., Pailhès, S. and Naidoo, S.R., Elastodynamic Properties of Embedded Amorphous Carbon Layer in Diamond Investigated by Surface Brillion Scattering.

Appendix B

Conferences attended and Presentations

- CoE-SM / AMSEN Annual Student Presentations: 28 April 2017, University of the Witwatersrand, Johannesburg, South Africa.

- South African Institute of Physics (**SAIP2017**) 62$^{\text{nd}}$ annual conference: 3-7 July 2017, Stellenbosch University, Cape Town, South Africa. **Poster** presentation: *Controlling the spatial distribution of multiplexed modes.*

- CoE-SM / AMSEN Annual Student Presentations Workshop: 04 April 2018, University of the Witwatersrand, Johannesburg, South Africa. **Poster** presentation: *Controlling the spatial distribution of multiplexed modes.*

- South African Institute of Physics (**SAIP2018**) 63$^{\text{rd}}$ annual conference: 25-29 June 2018, University of the Free State, Bloemfontein, South Africa. **Poster** presentation: *Single photon emission from NV defects in diamond.*

- Siegman International School of Lasers 63: 28 July-04 August 2018, Technical University of Denmark, Island Of Hven, Backafallsbyn, Sweden. **Poster** presentation: *Characterization of NV^- centers embedded in diamond.*

- CoE-SM / AMSEN Annual Student Presentations Workshop: 21 May 2019, University of the Witwatersrand, Johannesburg, South Africa. **Poster** presentation: *Characterization of NV^- centers embedded in diamond.* **Oral** presentation: *Fabrication of NV centers in diamond for quantum information processing.*

- South African Institute of Physics (**SAIP2019**) 64$^{\text{th}}$ annual conference: 08-12 July 2019, Protea Hotel Ranch Resort, Polokwane, South Africa. **Poster** presentation: *Fabrication of NV centers in diamond.* DPCMM award for best poster presentation.

- South African Institute of Physics (**SAIP2021**) 65$^{\text{th}}$ annual conference: 22-30 July 2021, Virtual conference, Hosted by North-West University, Potchefstroom, South Africa. **Poster** presentation: *Fabrication of MIT layers in Diamond.*

Appendix C

Simulated output for ion and target vacancy production

SRIM output data files with information regarding the simulation of the impact of injected boron ions inside a diamond matrix with energy 30 keV. The detailed information of the parameters involved in the simulation is shown in the TDATA.txt file. The damaged incurred inside the diamond because of the energetic ions interacting with the target vacancies is shown in the VACANCY.txt file. The distribution of the ion projectile is also provided in the RANGE.txt file along with the range straggling in the projected range. Both the VACANCY.txt and RANGE.txt files included tabulated data (not shown here) which were analyzed to provide suitable plots for analysis purposes.

TDATA.txt file

```
================== B (30) into Layer 1 ==================
                        SRIM-2008.04
=================================================
                  Data of TRIM Calculation
=================================================
Ion = B ( 5) Ion Mass= 011,0090
Energy = 3000000,E-05 keV
Ion Angle to Surface = 5 degrees
================= TARGET MATERIAL =================
Layer # 1- Layer 1
Layer # 1- Bottom Depth= 1,E+03 A
Layer # 1- Density = 17.64E22 atoms/cm3 = 3.52 g/cm3
Layer # 1- C = 100 Atomic Percent = 50 Mass Percent
=================================================
Target energies for target atom = C
Displacement = 50 eV, Binding = 3 eV, Surface = 7,41 eV
=================================================
Depth Range of Tabulated Data= 000000,E+00 - 100000,E-02 Angstroms
=================================================
Total Ions calculated = 005000
Average Range = 53340,E-02 Angstroms
Average Straggling = 13659,E-02 Angstroms
```

Average Vacancy/Ion = 77894,E-03
==========
Total Backscattered Ions= 1
Total Transmitted Ions = 0
==========

VACANCY.txt file

========== B (30) into Layer 1 ==========
SRIM-2008.04
==========
Ion and Target VACANCY production
See SRIM Outputs\TDATA.txt.txt for calc. details
==========
See file : SRIM Outputs\TDATA.txt.txt for calculation data
Ion = B Energy = 30 keV
========== TARGET MATERIAL ==========
Layer 1 : Layer 1
Layer Width = 1,E+03 A ;
Layer # 1- Density = 17.64E22 atoms/cm3 = 3.52 g/cm3
Layer # 1- C = 100 Atomic Percent = 100 Mass Percent
==========
Total Ions calculated =5000,00
Total Target Vacancies = 78 /Ion
Total Target Displacements = 81 /Ion
Total Target Replacement Collisions = 3 /Ion

!!!! NOTE : 2nd Column below is number of Primary Knock-Ons !!!! (PKO are number of Target Atoms Recoiling from the Ion.)
==========
Table Units are >>>> Vacancies/(Angstrom-Ion) <<<<
==========

RANGE.txt file

========== B (30) into Layer 1 ==========
SRIM-2008.04
==========
ION and final RECOIL ATOM Distributions
See SRIM Outputs\TDATA.txt.txt for calculation details
==========
See file : SRIM Outputs\TDATA.txt.txt for details of calculation
Ion = B Energy = 30 keV
========== TARGET MATERIAL ==========
Layer 1 : Layer 1
Layer Width = 1,E+03 A Layer # 1- Density = 17.64E22 atoms/cm3 = 3.52 g/cm3
Layer # 1- C = 100 Atomic Percent = 100 Mass Percent
==========
Total Ions calculated =5000,00

Ion Average Range = 533,4E+00 A Straggling = 136,6E+00 A
Ion Lateral Range = 116,3E+00 A Straggling = 144,8E+00 A
Ion Radial Range = 178,2E+00 A Straggling = 907,7E-01 A
==========
Transmitted Ions =; Backscattered Ions =1 (These are not included in Skewne- and Kurtosis below.)
Range Skewne- = -000,5862 &= [-(X-Rp)^3]/[N*Straggle^3]
Range Kurtosis = 003,3894 &= [-(X-Rp)^4]/[N*Straggle^4]
Statistical definitions above are those used in VLSI implant modelling.
==========
==========
Table Distribution Units are >>>> (Atoms/cm3) / (Atoms/cm2) <<<<
==========

Bibliography

[1] H Kamerlingh Onnes. Further experiments with liquid helium. c. on the change of electric resistance of pure metals at very low temperatures etc. iv. the resistance of pure mercury at helium temperatures. In *KNAW, Proceedings*, volume 13, pages 1910–1911, 1911.

[2] H Kamerlingh Onnes. The liquefaction of helium. *Koninklijke Nederlandse Akademie von Wetenschappen, Proceedings*, 11:1908–1909, 1908.

[3] Vladimir Z Kresin and Stuart A Wolf. *Fundamentals of superconductivity*. Springer Science & Business Media, 2013.

[4] Walther Meissner and Robert Ochsenfeld. A new effect when entering superconductivity. *natural sciences*, 21(44):787–788, 1933.

[5] Kristian Fossheim and Asle Sudbø. *Superconductivity: physics and applications*. John Wiley & Sons, 2005.

[6] John Bardeen, Leon N Cooper, and John Robert Schrieffer. Theory of superconductivity. *Physical review*, 108(5):1175, 1957.

[7] Emanuel Maxwell. Isotope effect in the superconductivity of mercury. *Physical Review*, 78(4):477, 1950.

[8] CA Reynolds, B Serin, and LB Nesbitt. The isotope effect in superconductivity. i. mercury. *Physical Review*, 84(4):691, 1951.

[9] Leon N Cooper. Bound electron pairs in a degenerate fermi gas. *Physical Review*, 104(4):1189, 1956.

[10] RE Glover III and Ms Tinkham. Conductivity of superconducting films for photon energies between 0.3 and 4 0 k t c. *Physical Review*, 108(2):243, 1957.

[11] Herbert Fröhlich. On the theory of superconductivity: The one-dimensional case. *Proceedings of the Royal Society of London. Series A. Mathematical and Physical Sciences*, 223(1154):296–305, 1954.

[12] J George Bednorz and K Alex Müller. Possible hight c superconductivity in the ba- la- cu- o system. *Zeitschrift für Physik B Condensed Matter*, 64(2): 189–193, 1986.

[13] AP Drozdov, PP Kong, VS Minkov, SP Besedin, MA Kuzovnikov, S Mozaffari, L Balicas, FF Balakirev, DE Graf, VB Prakapenka, et al. Superconductivity at 250 k in lanthanum hydride under high pressures. *Nature*, 569(7757):528–531, 2019.

[14] Marvin L Cohen. Superconductivity in many-valley semiconductors and in semimetals. *Physical Review*, 134(2A):A511, 1964.

[15] David Pines. Superconductivity in the periodic system. *Physical Review*, 109 (2):280, 1958.

[16] EA Ekimov, VA Sidorov, ED Bauer, NN Mel'Nik, NJ Curro, JD Thompson, and SM Stishov. Superconductivity in diamond. *nature*, 428(6982):542–545, 2004.

[17] Yoshihiko Takano, Masanori Nagao, Isao Sakaguchi, Minoru Tachiki, Takeshi Hatano, Kensaku Kobayashi, Hitoshi Umezawa, and Hiroshi Kawarada. Superconductivity in diamond thin films well above liquid helium temperature. *Applied physics letters*, 85(14):2851–2853, 2004.

[18] Etienne Bustarret, C Marcenat, P Achatz, J Kačmarčik, F Lévy, A Huxley, L Ortéga, E Bourgeois, X Blase, D Débarre, et al. Superconductivity in doped cubic silicon. *Nature*, 444(7118):465–468, 2006.

[19] Etienne Bustarret. Superconducting diamond: an introduction. *physica status solidi (a)*, 205(5):997–1008, 2008.

[20] Yoshihiko Takano. Superconductivity in cvd diamond films. *Journal of Physics: Condensed Matter*, 21(25):253201, 2009.

[21] Klaus Thonke. The boron acceptor in diamond. *Semiconductor science and technology*, 18(3):S20, 2003.

[22] Thierry Klein, Philipp Achatz, Josef Kacmarcik, Christophe Marcenat, Frederik Gustafsson, Jacques Marcus, Etienne Bustarret, Julien Pernot, Franck Omnès, Bo E Sernelius, et al. Metal-insulator transition and superconductivity in boron-doped diamond. *Physical Review B*, 75(16):165313, 2007.

[23] Karlheinz Seeger. *Semiconductor physics*. Springer Science & Business Media, 2013.

[24] R Kalish. Doping of diamond. *Carbon*, 37(5):781–785, 1999.

[25] Alan T Collins. The fermi level in diamond. *Journal of Physics: Condensed Matter*, 14(14):3743, 2002.

[26] JP Goss, PR Briddon, R Jones, and S Sque. Donor and acceptor states in diamond. *Diamond and related materials*, 13(4-8):684–690, 2004.

[27] Yoshihiko Takano, Masanori Nagao, Tomohiro Takenouchi, Hitoshi Umezawa, Isao Sakaguchi, Masashi Tachiki, and Hiroshi Kawarada. Superconductivity in polycrystalline diamond thin films. *Diamond and related materials*, 14(11-12): 1936–1938, 2005.

[28] John Walker. Optical absorption and luminescence in diamond. *Reports on progress in physics*, 42(10):1605, 1979.

[29] Y Takano, T Takenouchi, S Ishii, S Ueda, T Okutsu, I Sakaguchi, H Umezawa, H Kawarada, and M Tachiki. Superconducting properties of homoepitaxial cvd diamond. *Diamond and related materials*, 16(4-7):911–914, 2007.

[30] DL Creedon, Yi Jiang, Kumaravelu Ganesan, Alastair Stacey, Taisuke Kageura, Hiroshi Kawarada, JC McCallum, BC Johnson, Steven Prawer, and DN Jamieson. Irradiation-induced modification of the superconducting properties of heavily-boron-doped diamond. *Physical Review Applied*, 10(4): 044016, 2018.

[31] Dinesh Kumar, Maneesh Chandran, and Ramachandra Rao. Effect of boron doping on first-order raman scattering in superconducting boron doped diamond films. *Applied Physics Letters*, 110(19), 2017.

[32] V Mortet, A Taylor, Z Vlčková Živcová, D Machon, O Frank, P Hubík, David Trémouilles, and L Kavan. Analysis of heavily boron-doped diamond raman spectrum. *Diamond and Related Materials*, 88:163–166, 2018.

[33] V Mortet, Z Vlčková Živcová, A Taylor, M Davydová, O Frank, P Hubík, J Lorincik, and M Aleshin. Determination of atomic boron concentration in heavily boron-doped diamond by raman spectroscopy. *Diamond and Related Materials*, 93:54–58, 2019.

[34] Péter Szirmai, Thomas Pichler, Oliver A Williams, Soumen Mandal, Christopher Bäuerle, and Ferenc Simon. A detailed analysis of the raman spectra in superconducting boron doped nanocrystalline diamond. *physica status solidi (b)*, 249(12):2656–2659, 2012.

[35] VA Sidorov and EA Ekimov. Superconductivity in diamond. *Diamond and related materials*, 19(5-6):351–357, 2010.

[36] Milos Nesladek, Jiri J Mares, Dominique Tromson, Christine Mer, Philippe Bergonzo, Pavel Hubik, and Jozef Kristofik. Superconductivity and low temperature electrical transport in b-doped cvd nanocrystalline diamond. *Science and Technology of Advanced Materials*, 7:S41–S44, 2006.

[37] Jin Nakamura, Nobuyoshi Yamada, Kazuhiko Kuroki, Tamio Oguchi, Kozo Okada, Yoshihiko Takano, Masanori Nagao, Isao Sakaguchi, Tomohiro Takenouchi, Hiroshi Kawarada, et al. Holes in the valence band of superconducting boron-doped diamond film studied by soft x-ray absorption and emission spectroscopy. *journal of the physical society of japan*, 77(5): 054711–054711, 2008.

[38] T Tshepe, C Kasl, JF Prins, and MJR Hoch. Metal-insulator transition in boron-ion-implanted diamond. *Physical Review B*, 70(24):245107, 2004.

[39] V Heera, R Höhne, O Ignatchik, H Reuther, and P Esquinazi. Absence of superconductivity in boron-implanted diamond. *Diamond and related materials*, 17(3):383–389, 2008.

[40] Robert Robertson, JJ Fox, and AE Martin. Two types of diamond. *Philosophical Transactions of the Royal Society of London. Series A, Containing Papers of a Mathematical or Physical Character*, 232:463–535, 1934.

[41] W Kaiser and WL Bond. Nitrogen, a major impurity in common type i diamond. *Physical Review*, 115(4):857, 1959.

[42] John Walker. Optical absorption and luminescence in diamond. *Reports on progress in physics*, 42(10):1605, 1979.

[43] John Edwin Field and John Edwin Field. *The properties of diamond*. Academic Press, 1979.

[44] AM Zaitsev. Vibronic spectra of impurity-related optical centers in diamond. *Physical Review B*, 61(19):12909, 2000.

[45] Christopher M Breeding and James E Shigley. The "type" classification system of diamonds and its importance in gemology. *Gems Gemol*, 45(2):96–111, 2009.

[46] Sandra Veljković, Vojislav V Mitić, Vesna Paunović, Goran Lazović, Marcus Mohr, and Hans Fecht. Analyses of the surface parameters in polycrystalline diamonds. *Serbian Journal of Electrical Engineering*, 17(1):111–129, 2020.

[47] R Kalish. Ion implantation in diamond; damage, annealing and doping. *The Physics of Diamond (A. Paoletti and A. Tucciarone, eds.)*, pages 373–409, 1996.

[48] NW Ashcroft and ND Mermin. Solid state physics; thomson learning, inc. *Stamford, CT*, 1976.

[49] Charles Kittel, Paul McEuen, and Paul McEuen. *Introduction to solid state physics*, volume 8. Wiley New York, 1976.

[50] Lawrence S Pan and Don R Kania. *Diamond: electronic properties and applications*. Springer Science & Business Media, 2013.

[51] Simon M Sze, Yiming Li, and Kwok K Ng. *Physics of semiconductor devices*. John wiley & sons, 2021.

[52] GS Painter, Donald E Ellis, and AR Lubinsky. Ab initio calculation of the electronic structure and optical properties of diamond using the discrete variational method. *Physical Review B*, 4(10):3610, 1971.

[53] GBBM Sutherland, DE Blackwell, and WG Simeral. The problem of the two types of diamond. *Nature*, 174(4437):901, 1954.

[54] AR Lang, M Moore, APW Makepeace, W Wierzchowski, and CM Welbourn. On the dilatation of synthetic type ib diamond by substitutional nitrogen impurity. *Phil. Trans. R. Soc. Lond. A*, 337(1648):497–520, 1991.

[55] MF Thomaz et al. The decay time of n3 luminescence in natural diamond. *Proc. R. Soc. Lond. A*, 362(1710):405–419, 1978.

[56] HB Dyer, FA Raal, L Du Preez, and JHN Loubser. Optical absorption features associated with paramagnetic nitrogen in diamond. *Philosophical Magazine*, 11 (112):763–774, 1965.

[57] JFH Custers. Unusual phosphorescence of a diamond. *Physica*, 18(8-9):489–496, 1952.

[58] FP Bundy, H Tracy Hall, HM Strong, and RH Wentorf Jun. Man-made diamonds. *nature*, 176(4471):51, 1955.

[59] Seiichiro Matsumoto, Yoichiro Sato, Mutsukazu Kamo, and Nobuo Setaka. Vapor deposition of diamond particles from methane. *Japanese Journal of Applied Physics*, 21(4A):L183, 1982.

[60] Mutsukazu Kamo, Yoichiro Sato, Seiichiro Matsumoto, and Nobuo Setaka. Diamond synthesis from gas phase in microwave plasma. *Journal of Crystal Growth*, 62(3):642–644, 1983.

[61] W Zhu. Defects in diamond. In *Diamond: Electronic Properties and Applications*, pages 175–239. Springer, 1995.

[62] Michael Anthony Nastasi and James W Mayer. *Ion implantation and synthesis of materials*, volume 5. Springer, 2006.

[63] Jonathan E Moussa and Marvin L Cohen. Constraints on t c for superconductivity in heavily boron-doped diamond. *Physical Review B*, 77(6): 064518, 2008.

[64] Hiroyuki Okazaki, Takanori Wakita, Takayuki Muro, Tetsuya Nakamura, Yuji Muraoka, Takayoshi Yokoya, Shin-ichiro Kurihara, Hiroshi Kawarada, Tamio Oguchi, and Yoshihiko Takano. Signature of high t c above 25 k in high quality superconducting diamond. *Applied physics letters*, 106(5):052601, 2015.

[65] Jonathan E Moussa and Marvin L Cohen. Two bounds on the maximum phonon-mediated superconducting transition temperature. *Physical Review B*, 74(9):094520, 2006.

[66] Marvin L Cohen. Conceptual progress for explaining and predicting semiconductor properties. *Journal of Materials Research*, 26(22):2815, 2011.

[67] Yung-Hsin Chen, Chen-Ti Hu, and I-Nan Lin. Defect structure and electron field-emission properties of boron-doped diamond films. *Applied physics letters*, 75(18):2857–2859, 1999.

[68] JP Goss and PR Briddon. Theory of boron aggregates in diamond: First-principles calculations. *Physical Review B*, 73(8):085204, 2006.

[69] Yukako Kato, Fumihiko Matsui, Tatsuya Shimizu, Tomohiro Matsushita, Fang Zhun Guo, Takashi Tsuno, and Hiroshi Daimon. Stereophotographs of diamond and graphite. *Science and Technology of Advanced Materials*, 7 (S1):S45, 2006.

[70] Miwa Murakami, Tadashi Shimizu, Masataka Tansho, and Yoshihiko Takano. 11b nuclear magnetic resonance in boron-doped diamond. *Science and Technology of Advanced Materials*, 9(4):044103, 2009.

[71] AM Zaitsev. Vibronic spectra of impurity-related optical centers in diamond. *Physical Review B*, 61(19):12909, 2000.

[72] E Gheeraert, A Deneuville, and J Mambou. Boron-related infra-red absorption in homoepitaxial diamond films. *Diamond and related materials*, 7(10): 1509–1512, 1998.

[73] E Bustarret, F Pruvost, M Bernard, C Cytermann, and C Uzan-Saguy. Optical conductivity studies in heavily boron-doped diamond. *physica status solidi (a)*, 186(2):303–307, 2001.

[74] Yoshihiro Yokota, Takeshi Tachibana, Koichi Miyata, Kazushi Hayashi, Koji Kobashi, Akimitsu Hatta, Toshimichi Ito, Akio Hiraki, and Yoshihiro Shintani. Cathodoluminescence of boron-doped heteroepitaxial diamond films on platinum. *Diamond and related materials*, 8(8-9):1587–1591, 1999.

[75] C Baron, M Wade, A Deneuville, F Jomard, and J Chevallier. Cathodoluminescence of highly and heavily boron doped (100) homoepitaxial diamond films. *Diamond and related materials*, 15(4-8):597–601, 2006.

[76] C Tavares, F Omnes, J Pernot, and E Bustarret. Electronic properties of boron-doped {111}-oriented homoepitaxial diamond layers. *Diamond and related materials*, 15(4-8):582–585, 2006.

[77] H Sternschulte, J Horseling, T Albrecht, K Thonke, and R Sauer. Characterization of doped and undoped cvd-diamond films by cathodoluminescence. *Diamond and related materials*, 5(6-8):585–588, 1996.

[78] E Bustarret, E Gheeraert, and K Watanabe. Optical and electronic properties of heavily boron-doped homo-epitaxial diamond. *physica status solidi (a)*, 199 (1):9–18, 2003.

[79] Michele Ortolani, Stefano Lupi, Leonetta Baldassarre, U Schade, Paolo Calvani, Y Takano, M Nagao, T Takenouchi, and H Kawarada. Low-energy electrodynamics of superconducting diamond. *Physical review letters*, 97(9): 097002, 2006.

[80] Dan Wu, YC Ma, ZL Wang, Q Luo, CZ Gu, NL Wang, CY Li, XY Lu, and ZS Jin. Optical properties of boron-doped diamond. *Physical Review B*, 73(1): 012501, 2006.

[81] M Bernard, C Baron, and A Deneuville. About the origin of the low wave number structures of the raman spectra of heavily boron doped diamond films. *Diamond and Related Materials*, 13(4-8):896–899, 2004.

[82] S Ghodbane and A Deneuville. Specific features of 325 nm raman excitation of heavily boron doped polycrystalline diamond films. *Diamond and related materials*, 15(4-8):589–592, 2006.

[83] E Gheeraert, P Gonon, A Deneuville, L Abello, and G Lucazeau. Effect of boron incorporation on the"quality" of mpcvd diamond films. *Diamond and Related Materials*, 2(5-7):742–745, 1993.

[84] NF Mott. Conduction in glasses containing transition metal ions. *Journal of Non-Crystalline Solids*, 1(1):1–17, 1968.

[85] Koichi Ushizawa, Gamo Mikka N, Kenji Watanabe, Isao Sakaguchi, Yoichiro Sato, and Toshihiro Ando. Raman spectroscopic study on {100} facet of boron-doped chemical-vapour-deposited diamond crystals with fano line fitting. *Journal of Raman spectroscopy*, 30(10):957–961, 1999.

[86] Ugo Fano. Effects of configuration interaction on intensities and phase shifts. *Physical review*, 124(6):1866, 1961.

[87] Fernando Cerdeira, TA Fjeldly, and M Cardona. Effect of free carriers on zone-center vibrational modes in heavily doped p-type si. ii. optical modes. *Physical Review B*, 8(10):4734, 1973.

[88] S Prawer, KW Nugent, and DN Jamieson. The raman spectrum of amorphous diamond. *Diamond and Related Materials*, 7(1):106–110, 1998.

[89] JO Orwa, KW Nugent, DN Jamieson, and S Prawer. Raman investigation of damage caused by deep ion implantation in diamond. *Physical Review B*, 62 (9):5461, 2000.

[90] Lilia Boeri, Jens Kortus, and OK Andersen. Three-dimensional m g b 2-type superconductivity in hole-doped diamond. *Physical review letters*, 93(23): 237002, 2004.

[91] F Marsiglio and JP Carbotte. Electron-phonon superconductivity. In *Superconductivity: conventional and unconventional superconductors*, pages 73–162. Springer, 2008.

[92] LH Willems van Beveren, Rong Liu, Haydn Bowers, Kumaravelu Ganesan, Brett C Johnson, Jeffrey C McCallum, and S Prawer. Optical and electronic properties of sub-surface conducting layers in diamond created by mev b-implantation at elevated temperatures. *Journal of Applied Physics*, 119 (22):223902, 2016.

[93] Gordon Davies. The a nitrogen aggregate in diamond-its symmetry and possible structure. *Journal of Physics C: Solid State Physics*, 9(19):L537, 1976.

[94] Gordon Davies and MF Hamer. Optical studies of the 1.945 ev vibronic band in diamond. *Proc. R. Soc. Lond. A*, 348(1653):285–298, 1976.

[95] I Aharonovich, Stefania Castelletto, DA Simpson, Chun-Hsu Su, AD Greentree, and Steven Prawer. Diamond-based single-photon emitters. *Reports on progress in Physics*, 74(7):076501, 2011.

[96] CD Clark and CA Norris. Photoluminescence associated with the 1.673, 1.944 and 2.498 ev centres in diamond. *Journal of Physics C: Solid State Physics*, 4 (14):2223, 1971.

[97] Arthur Marshall Stoneham. *Theory of defects in solids: electronic structure of defects in insulators and semiconductors*. Oxford University Press, 2001.

[98] Yoshimi Mita. Change of absorption spectra in type-ib diamond with heavy neutron irradiation. *Physical Review B*, 53(17):11360, 1996.

[99] F Brunet, P Germi, M Pernet, A Deneuville, E Gheeraert, F Laugier, M Burdin, and G Rolland. Microstructure evolution of boron doped homoepitaxial diamond films. *Journal of applied physics*, 83(1):181–186, 1998.

[100] VV Brazhkin, EA Ekimov, AG Lyapin, SV Popova, AV Rakhmanina, SM Stishov, VM Lebedev, Y Katayama, and K Kato. Lattice parameters and thermal expansion of superconducting boron-doped diamonds. *Physical Review B*, 74(14):140502, 2006.

[101] J Kačmarčik, C Marcenat, C Cytermann, A Ferreira da Silva, L Ortega, F Gustafsson, J Marcus, T Klein, E Gheeraert, and Etienne Bustarret. Superconductivity in boron-doped homoepitaxial (001)-oriented diamond layers. *physica status solidi (a)*, 202(11):2160–2165, 2005.

[102] Takao Saotome, Kazutoshi Ohashi, Toshimaro Sato, Hiroshi Maeta, Katsuji Haruna, and Fumihisa Ono. Thermal expansion of a boron-doped diamond single crystal at low temperatures. *Journal of Physics: Condensed Matter*, 10 (6):1267, 1998.

[103] Moritz Hoesch, Tatsuo Fukuda, J Mizuki, T Takenouchi, H Kawarada, JP Sutter, S Tsutsui, AQR Baron, M Nagao, and Y Takano. Phonon softening in superconducting diamond. *Physical Review B*, 75(14):140508, 2007.

[104] Etienne Bustarret, J Kačmarčik, Christophe Marcenat, Etienne Gheeraert, Catherine Cytermann, Jacques Marcus, and Thierry Klein. Dependence of the superconducting transition temperature on the doping level in single-crystalline diamond films. *Physical review letters*, 93(23):237005, 2004.

[105] Katsuji Haruna, Hiroshi Maeta, Kazutoshi Ohashi Kazutoshi Ohashi, and Takuro Koike Takuro Koike. Thermal expansion coefficient of synthetic diamond single crystal at low temperatures. *Japanese journal of applied physics*, 31(8R): 2527, 1992.

[106] Gordon Davies et al. Properties and growth of diamond. *(No Title)*, 1994.

[107] THK Barron. Collins, jg and white, gk. *Themial Expansion of Solids at Low Tem perahires", A&. Php*, 29(1):980, 1980.

[108] Peter Phillip Edwards and Michell J Sienko. Universality aspects of the metal-nonmetal transition in condensed media. *Physical Review B*, 17(6):2575, 1978.

[109] K Winzer, D Bogdanov, and Ch Wild. Electronic properties of boron-doped diamond on the border between the normal and the superconducting state. *Physica C: Superconductivity and its applications*, 432(1-2):65–70, 2005.

[110] AL Efros. Coulomb gap in disordered systems. *Journal of Physics C: Solid State Physics*, 9(11):2021, 1976.

[111] Frédéric Fontaine. Calculation of the hole concentration in boron-doped diamond. *Journal of applied physics*, 85(3):1409–1422, 1999.

[112] J Serre and A Ghazali. From band tailing to impurity-band formation and discussion of localization in doped semiconductors: A multiple-scattering approach. *Physical Review B*, 28(8):4704, 1983.

[113] Toshimaro Sato, Kazutoshi Ohashi, Hiroyuki Sugai, Takashi Sumi, Katsuji Haruna, Hiroshi Maeta, Norimasa Matsumoto, and Hideo Otsuka. Transport of heavily boron-doped synthetic semiconductor diamond in the hopping regime. *Physical Review B*, 61(19):12970, 2000.

[114] JJ Mareš, P Hubík, M Nesládek, D Kindl, and J Krištofik. Weak localization-precursor of unconventional superconductivity in nanocrystalline boron-doped diamond. *Diamond and related materials*, 15(11-12):1863–1867, 2006.

[115] WL McMillan. Scaling theory of the metal-insulator transition in amorphous materials. *Physical Review B*, 24(5):2739, 1981.

[116] TG Castner. Einstein relations near the metal-insulator transition. *Physical Review B*, 55(7):4003, 1997.

[117] TH Borst and O Weis. Boron-doped homoepitaxial diamond layers: Fabrication, characterization, and electronic applications. *physica status solidi (a)*, 154(1): 423–444, 1996.

[118] Gk L Pearson and J Bardeen. Electrical properties of pure silicon and silicon alloys containing boron and phosphorus. *Physical Review*, 75(5):865, 1949.

[119] Allen Miller and Elihu Abrahams. Impurity conduction at low concentrations. *Physical Review*, 120(3):745, 1960.

[120] Boris Isaakovich Shklovskii and Alex L Efros. *Electronic properties of doped semiconductors*, volume 45. Springer Science & Business Media, 2013.

[121] Terukazu Nishizaki, Yoshihiko Takano, Masanori Nagao, Tomohiro Takenouchi, Hiroshi Kawarada, and Norio Kobayashi. Scanning tunneling microscopy and spectroscopy studies of superconducting boron-doped diamond films. *Science and Technology of Advanced Materials*, 7(sup1):S22–S26, 2006.

[122] B Sacépé, C Chapelier, C Marcenat, J Kačmarčik, T Klein, F Omnès, and E Bustarret. Experimental indications of a bcs behaviour in superconducting diamond. *physica status solidi (a)*, 203(13):3315–3323, 2006.

[123] P Townsend and J Sutton. Investigation by electron tunneling of the superconducting energy gaps in nb, ta, sn, and pb. *Physical Review*, 128 (2):591, 1962.

[124] F Giubileo, Dimitri Roditchev, William Sacks, Ronan Lamy, DX Thanh, Jean Klein, S Miraglia, Daniel Fruchart, J Marcus, and Ph Monod. Two-gap state density in mgb 2: a true bulk property or a proximity effect? *Physical review letters*, 87(17):177008, 2001.

[125] RC Dynes, JP Garno, GB Hertel, and TP Orlando. Tunneling study of superconductivity near the metal-insulator transition. *Physical Review Letters*, 53(25):2437, 1984.

[126] Hitoshi Umezawa, Tomohiro Takenouchi, Yoshihiko Takano, Kensaku Kobayashi, Masanori Nagao, Isao Sakaguchi, Minoru Tachiki, Takeshi Hatano, Guofang Zhong, Masashi Tachiki, et al. Advantage on superconductivity of heavily boron-doped (111) diamond films. *arXiv preprint cond-mat/0503303*, 2005.

[127] VA Sidorov, EA Ekimov, SM Stishov, ED Bauer, and JD Thompson. Superconducting and normal-state properties of heavily hole-doped diamond. *Physical Review B*, 71(6):060502, 2005.

[128] Jin Nakamura, Eiki Kabasawa, Nobuyoshi Yamada, Yasuaki Einaga, Daisuke Saito, Hideo Isshiki, Shigemi Yugo, and Rupert CC Perera. Electronic structures of b 2 p and c 2 p levels in boron-doped diamond films studied using soft x-ray absorption and emission spectroscopy. *Physical Review B*, 70(24):245111, 2004.

[129] S Prawer and R Kalish. Ion-beam-induced transformation of diamond. *Physical Review B*, 51(22):15711, 1995.

[130] R Höhne, P Esquinazi, V Heera, and H Weishart. Magnetic properties of ion-implanted diamond. *Diamond and related materials*, 16(8):1589–1596, 2007.

[131] Anna Dychalska, Piotr Popielarski, Wojciech Franków, Kazimierz Fabisiak, Kazimierz Paprocki, and Mirosław Szybowicz. Study of cvd diamond layers with amorphous carbon admixture by raman scattering spectroscopy. *Mater. Sci.-Pol*, 33(4):799–805, 2015.

[132] Anagh Bhaumik, Ritesh Sachan, and Jagdish Narayan. High-temperature superconductivity in boron-doped q-carbon. *ACS nano*, 11(6):5351–5357, 2017.

[133] G Baskaran. Strongly correlated impurity band superconductivity in diamond: X-ray spectroscopic evidence. *Science and Technology of Advanced Materials*, 7(S1):S49, 2006.

[134] J Bousquet, T Klein, M Solana, L Saminadayar, C Marcenat, and E Bustarret. Phase diagram of boron-doped diamond revisited by thickness-dependent transport studies. *Physical Review B*, 95(16):161301, 2017.

[135] EA Ekimov, VA Sidorov, AV Rakhmanina, NN Mel'nik, RA Sadykov, and JD Thompson. High-pressure synthesis and characterization of superconducting boron-doped diamond. *Science and Technology of Advanced Materials*, 7(sup1): S2–S6, 2006.

[136] Franck Dahlem, Philipp Achatz, Oliver Aneurin Williams, D Araujo, Hervé Courtois, and Etienne Bustarret. Nanocrystalline boron-doped diamond films, a mixture of bcs-like and non-bcs-like superconducting grains. *physica status solidi (a)*, 207(9):2064–2068, 2010.

[137] Soumen Mandal, Tobias Bautze, Oliver A Williams, Cécile Naud, Étienne Bustarret, Franck Omnes, Pierre Rodiere, Tristan Meunier, Christopher B´auerle, and Laurent Saminadayar. The diamond superconducting quantum interference device. *ACS nano*, 5(9):7144–7148, 2011.

[138] Tobias Bautze, Soumen Mandal, Oliver A Williams, Pierre Rodiere, Tristan Meunier, and Christopher B´auerle. Superconducting nano-mechanical diamond resonators. *Carbon*, 72:100–105, 2014.

[139] Alexandre Fiori, Jessica Bousquet, David Eon, Franck Omnès, E Bellet-Amalric, and Étienne Bustarret. Boron-doped superlattices and bragg mirrors in diamond. *Applied Physics Letters*, 105(8):081109, 2014.

[140] Soumen Mandal, Cécile Naud, Oliver A Williams, Étienne Bustarret, Franck Omnes, Pierre Rodiere, Tristan Meunier, Laurent Saminadayar, and Christopher Bäuerle. Nanostructures made from superconducting boron-doped diamond. *Nanotechnology*, 21(19):195303, 2010.

[141] RH Wentorf Jr and H Pt Bovenkerk. Preparation of semiconducting diamonds. *The Journal of Chemical Physics*, 36(8):1987–1990, 1962.

[142] FP Bundy. Direct conversion of graphite to diamond in static pressure apparatus. *The Journal of Chemical Physics*, 38(3):631–643, 1963.

[143] CM Huggins and P Cannon. Diamonds containing controllable impurity concentrations. *Nature*, 194(4831):829–830, 1962.

[144] HM Strong and RM Chrenko. Diamond growth rates and physical properties of laboratory-made diamond. *The Journal of Physical Chemistry*, 75(12): 1838–1843, 1971.

[145] RC Burns, Vesna Cvetkovic, CN Dodge, DJF Evans, Marie-Line T Rooney, PM Spear, and CM Welbourn. Growth-sector dependence of optical features in large synthetic diamonds. *Journal of Crystal Growth*, 104(2):257–279, 1990.

[146] VS Vavilov, MI Guseva, EA Konorova, KRASNOPE. VV, SERGIENK. VF, and VV Tutov. Semiconducting diamonds produced by ion bombardment, 1966.

[147] Sokrates T Pantelides. *Deep centers in semiconductors*. CRC Press, 1992.

[148] RG Farrer. On the substitutional nitrogen donor in diamond. *Solid State Communications*, 7(9):685–688, 1969.

[149] Johan F Prins. Ion implantation of diamond for electronic applications. *Semiconductor science and technology*, 18(3):S27, 2003.

[150] S Koizumi. Growth and characterization of phosphorus doped n-type diamond thin films. *physica status solidi (a)*, 172(1):71–78, 1999.

[151] Johan F Prins. Using ion implantation to dope diamond-an update on selected issues. *Diamond and related materials*, 10(9-10):1756–1764, 2001.

[152] Johan F Prins. Ion-implanted structures and doped layers in diamond. *Materials Science Reports*, 7(7-8):275–364, 1992.

[153] Johan F Prins. Ion-implanted n-type diamond: electrical evidence. *Diamond and related Materials*, 4(5-6):580–585, 1995.

[154] E Friedland and JPF Sellschop. Temperature dependence of critical damage energies in diamond. *Nuclear Instruments and Methods in Physics Research Section B: Beam Interactions with Materials and Atoms*, 191(1-4):17–21, 2002.

[155] H Weishart, F Eichhorn, V Heera, B Pécz, Á Barna, and W Skorupa. High-fluence si-implanted diamond: Optimum implantation temperature for sic formation. *Journal of applied physics*, 98(4):043503, 2005.

[156] Mildred S Dresselhaus and Rafael Kalish. *Ion implantation in diamond, graphite and related materials*, volume 22. Springer Science & Business Media, 2013.

[157] A Reznik, V Richter, and R Kalish. Kinetics of the conversion of broken diamond (s p 3) bonds to graphitic (s p 2) bonds. *Physical Review B*, 56(13): 7930, 1997.

[158] Ernest Rutherford and Thomas Royds. Xxi. the nature of the α particle from radioactive substances. *The London, Edinburgh, and Dublin Philosophical Magazine and Journal of Science*, 17(98):281–286, 1909.

[159] James F Ziegler and Jochen P Biersack. The stopping and range of ions in matter. In *Treatise on Heavy-Ion Science: Volume 6: Astrophysics, Chemistry, and Condensed Matter*, pages 93–129. Springer, 1985.

[160] J Lindhard and M Scharff. Energy dissipation by ions in the kev region. *Physical Review*, 124(1):128, 1961.

[161] JF Ziegler and JM Manoyan. The stopping of ions in compounds. *Nuclear Instruments and Methods in Physics Research Section B: Beam Interactions with Materials and Atoms*, 35(3-4):215–228, 1988.

[162] Jens Lindhard, Morten Scharff, and Hans E Schiøtt. *Range concepts and heavy ion ranges*, volume 33. Munksgaard Copenhagen, 1963.

[163] R Kalish. Ion implantation in diamond for quantum information processing (qip): doping and damaging. In *Quantum Information Processing with Diamond*, pages 36–67. Elsevier, 2014.

[164] C Uzan-Saguy, C Cytermann, R Brener, V Richter, M Shaanan, and R Kalish. Damage threshold for ion-beam induced graphitization of diamond. *Applied Physics Letters*, 67(9):1194–1196, 1995.

[165] Alan T Collins and Isaac Kiflawi. The annealing of radiation damage in type ia diamond. *Journal of Physics: Condensed Matter*, 21(36):364209, 2009.

[166] R Kalish, A Reznik, S Prawer, D Saada, and J Adler. Ion-implantation-induced defects in diamond and their annealing: experiment and simulation. *physica status solidi (a)*, 174(1):83–99, 1999.

[167] A Reznik, V Richter, and R Kalish. The re-arrangement of broken bonds in damaged diamond: graphitization versus annealing back to diamond. *Diamond and related materials*, 7(2-5):317–321, 1998.

[168] Peter Deák, Bálint Aradi, Moloud Kaviani, Thomas Frauenheim, and Adam Gali. Formation of nv centers in diamond: A theoretical study based on calculated transitions and migration of nitrogen and vacancy related defects. *Physical review B*, 89(7):075203, 2014.

[169] Ariful Haque and Sharaf Sumaiya. An overview on the formation and processing of nitrogen-vacancy photonic centers in diamond by ion implantation. *Journal of Manufacturing and Materials Processing*, 1(1):6, 2017.

[170] Yuhei Seki, Yasushi Hoshino, and Jyoji Nakata. Remarkable p-type activation of heavily doped diamond accomplished by boron ion implantation at room temperature and subsequent annealing at relatively low temperatures of 1150 and 1300Â° c. *Applied Physics Letters*, 115(7), 2019.

[171] Claus Feldmann, Thomas Jüstel, Cees R Ronda, and Peter J Schmidt. Inorganic luminescent materials: 100 years of research and application. *Advanced Functional Materials*, 13(7):511–516, 2003.

[172] Timothy H Gfroerer. Photoluminescence in analysis of surfaces and interfaces. *Encyclopedia of analytical chemistry*, 67:3810, 2000.

[173] Xiaoyong Huang, Sanyang Han, Wei Huang, and Xiaogang Liu. Enhancing solar cell efficiency: the search for luminescent materials as spectral converters. *Chemical Society Reviews*, 42(1):173–201, 2013.

[174] CL Anderson and CR Crowell. Threshold energies for electron-hole pair production by impact ionization in semiconductors. *Physical Review B*, 5(6): 2267, 1972.

[175] RC Alig and SJPR l Bloom. Electron-hole-pair creation energies in semiconductors. *Physical review letters*, 35(22):1522, 1975.

[176] David Tuschel. Photoluminescence spectroscopy using a raman spectrometer. *Spectroscopy*, 31(9):14–21, 2016.

[177] Clarence Karr. *Infrared and Raman spectroscopy of lunar and terrestrial materials*. Acad. Press, 1975.

[178] Peter Brüesch. *Phonons: Theory and experiments I: Lattice dynamics and Models of interatomic forces*, volume 34. Springer Science & Business Media, 2012.

[179] GJ Phelps. Dopant ion implantation simulations in 4h-silicon carbide. *Modelling and Simulation in Materials Science and Engineering*, 12(6):1139, 2004.

[180] Sun Guanqing, Liu Zhongyang, Zheng Sioxiao, Wang Beilu, Liao Xiaodong, and Jang Jinyun. An implantation facility for surface modification of metals. 1998.

[181] Lienhard Wegmann. The historical development of ion implantation. *Ion Implantation Science and Technology*, pages 3–49, 1984.

[182] SR Walther, BO Pedersen, and CM McKenna. Ion sources for commercial ion implanter applications. In *Conference Record of the IEEE Particle Accelerator Conference. DOI*, volume 10, 1991.

[183] Emily Aradi, SR Naidoo, RM Erasmus, B Julies, and TE Derry. Investigations on the characterization of ion implanted hexagonal boron nitride. *Nuclear Instruments and Methods in Physics Research Section B: Beam Interactions with Materials and Atoms*, 307:214–217, 2013.

[184] Nazmul Huda, M Akbar Rhamdhani, Geoffrey A Brooks, BJ Monaghan, and L Prentice. Aluminium production route through carbosulfidation of alumina utilising h2s. 2013.

[185] Johan F Prins. Annealing effects when activating dopant atoms in ion-implanted diamond layers. *Nuclear Instruments and Methods in Physics Research Section B: Beam Interactions with Materials and Atoms*, 59:1387–1390, 1991.

[186] Matthias Werner. Diamond metallization for device applications. *Semiconductor science and technology*, 18(3):S41, 2003.

[187] Matthias Werner, Otto Dorsch, H-U Baerwind, Emst Obermeier, Colin Johnston, Paul R Chalker, and Simon Romani. The effect of metallization on the ohmic contact resistivity to heavily b-doped polycrystalline diamond films. *IEEE transactions on electron devices*, 42(7):1344–1351, 1995.

[188] MRAAWRCPR Werner, R Job, A Denisenko, A Zaitsev, WR Fahrner, C Johnston, PR Chalker, and IM Buckley-Golder. How to fabricate low-resistance metal-diamond contacts. *Diamond and related materials*, 5 (6-8):723–727, 1996.

[189] John XJ Zhang and Kazunori Hoshino. *Molecular sensors and nanodevices: principles, designs and applications in biomedical engineering*. Academic Press, 2018.

[190] Milton Ohring. *Materials Science of Thin Films: Depositon and Structure*. Elsevier, 2001.

[191] Sabeur Msolli, Joel Alexis, and Heungsoo Kim. Mechanical behavior and adhesion of the ti/cr/au metallization scheme on diamond substrate. *Advanced Engineering Materials*, 19(8):1700109, 2017.

[192] WP Leroy, Christophe Detavernier, RL Van Meirhaeghe, and C Lavoie. Thin film solid-state reactions forming carbides as contact materials for carbon-containing semiconductors. *Journal of Applied Physics*, 101(5), 2007.

[193] Rudolf Kinder, Miroslav Mikolášek, Daniel Donoval, Jaroslav Kováč, and Marek Tlaczala. Measurement systemwith hall and a four point probes for characterization of semiconductors. *Journal of Electrical Engineering*, 64(2): 106–111, 2013.

[194] Toru Matsumura, Yuichi Sato, et al. A theoretical study on van der pauw measurement values of inhomogeneous compound semiconductor thin films. *Journal of Modern Physics*, 1(05):340–347, 2010.

[195] O Philips'Gloeilampenfabrieken. A method of measuring specific resistivity and hall effect of discs of arbitrary shape. *Philips Res. Rep*, 13(1):1–9, 1958.

[196] Keithley Instruments. Low level measurements handbook. *Precision DC Current, Voltage and Resistance Measurements, 7th ed.; Keithley Instruments Inc.: Cleveland, OH, USA*, page 245, 2013.

[197] Congmian Zhen, Yinyue Wang, Shanhu He, Qiufen Guo, Zhijun Yan, and Yuejiao Pu. Ohmic contacts to boron-doped diamond. *Optical Materials*, 23 (1-2):117–121, 2003.

[198] F Fontaine, E Gheeraert, and A Deneuville. Conduction mechanisms in boron implanted diamond films. *Diamond and related materials*, 5(6-8):752–756, 1996.

[199] Takashi Sugino, Yasuaki Muto, Junji Shirafuji, and Koji Kobashi. Electrical conduction mechanisms in polycrystalline chemically vapour-deposited diamond films. *Diamond and Related Materials*, 2(5-7):797–802, 1993.

[200] Takashi Inushima, Takahiro Matsushita, Seishirou Ohya, and Hiromu Shiomi. Hopping conduction via the excited states of boron in p-type diamond. *Diamond and Related Materials*, 9(3-6):1066–1070, 2000.

[201] S Kono, T Teraji, H Kodama, K Ichikawa, S Ohnishi, and A Sawabe. Direct determination of the barrier height of ti-based ohmic contact on p-type diamond (001). *Diamond and Related Materials*, 60:117–122, 2015.

[202] E Baskin, A Reznik, D Saada, Joan Adler, and R Kalish. Model for the defect-related electrical conductivity in ion-damaged diamond. *Physical Review B*, 64(22):224110, 2001.

[203] H Wang, M Bruna, Paolo Olivero, S Borini, Federico Picollo, O Budnyk, Federico Bosia, Ž Pastuovic, N Skukan, M Jakšič, et al. Space charge limited current (sclc) as observed on diamond surface damaged by mev ion implantation. In *IOP Conference Series: Materials Science and Engineering*, volume 16, page 012004. IOP Publishing, 2010.

[204] Sana Salami, Stéphane Pailhès, Christophe Adessi, Valentina M Giordano, Nyiku Mahonisi, Zuko Mthwesi, Stéphane Vignoli, Régis Debord, Rémy Fulcrand, Nicholas Blanchard, et al. Phonon-drag in a graphite channel buried in diamond. *Available at SSRN 4658686*.

[205] C Ramaswamy. Raman effect in diamond. *Nature*, 125(3158):704–704, 1930.

[206] Robert Robertson, John Jacob Fox, and Albert E Martin. Two types of diamond. *Philosophical Transactions of the Royal Society of London. Series A, Containing Papers of a Mathematical or Physical Character*, 232(707-720): 463–535, 1933.

[207] L Bergman, MT McClure, JT Glass, and RJ Nemanich. The origin of the broadband luminescence and the effect of nitrogen doping on the optical properties of diamond films. *Journal of applied physics*, 76(5):3020–3027, 1994.

[208] SA Grudinkin, NA Feoktistov, KV Bogdanov, AV Baranov, and VG Golubev. Effect of boron doping on luminescent properties of silicon–vacancy and germanium–vacancy color centers in diamond particles obtained by chemical vapor deposition. *Phys. Solid State*, 64(1506):10–21883, 2022.

[209] JA Freitas Jr, K Doverspike, PB Klein, YL Khong, and AT Collins. Luminescence studies of nitrogen-and boron-doped diamond films. *Diamond and Related Materials*, 3(4-6):821–824, 1994.

[210] Tresor B Matindi, Shunmugam R Naidoo, and Odireleng M Ntwaeaborwa. Luminescence induced by no ion implantation into diamond. *Diamond and Related Materials*, 96:11–19, 2019.

[211] Alexander M Zaitsev. *Optical properties of diamond: a data handbook*. Springer Science & Business Media, 2013.

[212] AP Yelisseyev, A Ya Khrenov, and VP Afanasiev. Photoluminescence spectra of impact diamonds formed by solid-state graphite-to-diamond transition. *JOSA B*, 33(3):B43–B48, 2016.

[213] Estela Pereira et al. Spin forbidden transitions in diamond. *Journal of luminescence*, 60:614–617, 1994.

[214] Federico Picollo, Paolo Olivero, F Bellotti, Ž Pastuović, N Skukan, A Lo Giudice, Giampiero Amato, M Jakšić, and Ettore Vittone. Formation of buried conductive micro-channels in single crystal diamond with mev c and he implantation. *Diamond and related materials*, 19(5-6):466–469, 2010.

[215] PN Vishwakarma and SV Subramanyam. Hopping conduction in boron doped amorphous carbon films. *Journal of Applied Physics*, 100(11), 2006.

[216] Julien Pernot, Pierre-Nicolas Volpe, Franck Omnès, Pierre Muret, Vincent Mortet, Ken Haenen, and Tokuyuki Teraji. Hall hole mobility in boron-doped homoepitaxial diamond. *Physical Review B-Condensed Matter and Materials Physics*, 81(20):205203, 2010.

[217] Shisheng Lin, Xutao Yu, Minhui Yang, Huikai Zhong, and Jiarui Guo. Superconductivity and metallic behavior in heavily doped bulk single crystal diamond and graphene/diamond heterostructure. *arXiv preprint arXiv:2403.00359*, 2024.

[218] DoE Soule. Magnetic field dependence of the hall effect and magnetoresistance in graphite single crystals. *Physical Review*, 112(3):698, 1958.

[219] JP Jay-Gerin and R Maynard. Phonon drag in graphite. *Journal of Low Temperature Physics*, 3:377–392, 1970.

[220] C Ayache, A De Combarieu, and JP Jay-Gerin. Observation of a new anomaly in the low-temperature thermoelectric power of graphite: Interpretation by a phonon-drag effect acting on the h-point minority holes. *Physical Review B*, 21 (6):2462, 1980.

[221] C Uher. Thermopower of exfoliated graphites between 1.7 and 300 k. *Physical Review B*, 25(6):4167, 1982.

[222] Y Hishiyama and A Ono. Low temperature anomalies in thermoelectricity of highly oriented graphite in relation to sample quality. *Carbon*, 23(4):445–448, 1985.

[223] T Takezawa, T Tsuzuku, A Ono, and Y Hishiyama. Thermoelectric power of single-crystal graphite at low temperatures. *Philosophical Magazine*, 19(159): 623–628, 1969.